UiO : University of Oslo

Petter Vollestad

Experimental investigations of two-phase flows

Dynamics of stratified and particle-laden flows in pipes and flumes

Thesis submitted for the degree of Philosophiae Doctor

Department of Mathematics
Faculty of Mathematics and Natural Sciences

2020

© Petter Vollestad, 2020

Series of dissertations submitted to the
Faculty of Mathematics and Natural Sciences, University of Oslo
No. 2325

ISSN 1501-7710

All rights reserved. No part of this publication may be
reproduced or transmitted, in any form or by any means, without permission.

Cover: Hanne Baadsgaard Utigard.
Print production: Reprosentralen, University of Oslo.

Preface

This thesis is submitted in partial fulfillment of the requirements for the degree philosophiae doctor (Ph.D.), at the University of Oslo (UiO). The work has been performed from September 2016 to September 2020, under the supervision of Professor Atle Jensen, Dr. Anis Awal Ayati, Associate Professor Luiza Angheluta and Professor Joseph Henry LaCasce.

Most of the experimental work has been conducted at the Hydrodynamics Laboratory at UiO, studying stratified air-water flows. The experience gained with the optical measurement technique applied was then transferred to a pipe flow setup at the DNV GL headquarters (Høvik), studying particle-laden air-sand pipe flow. This work was part of a paid industry projected, funded by TechnipFMC and headed by DNV GL.

The thesis consists of an introduction to the main topics under investigation, and the experimental setups applied. Seven papers make up the main part of the thesis. Five of these are related to stratified gas-liquid pipe flows, one to wind-wave interactions in a combined wind-wave flume, and finally a note documenting the work performed at DNV GL is presented.

I am the first author of all papers, and have been involved in all stages of the experimental work and analysis, with the exception of paper II, which is based on the experimental data stemming from my supervisor Dr. Anis Awal Ayati.

The work was done as part of the strategic research initiative *EarthFlows* at the Faculty of Mathematics and Natural Sciences, UiO.

Petter Vollestad
Oslo, September 2020

Acknowledgements

I would like to thank my main supervisor Professor Atle Jensen for always finding time to listen to the many concerns and problems I have faced during the course of this work. Also, your many ideas and contributions to the experimental work has been invaluable to me in this process.

I am extremely grateful for the help and support I have gotten from my co-supervisor Dr. Anis Awal Ayati. This work is in many ways a continuation of the work performed by Anis during his Ph.D., and I really enjoyed (and benefited from) the close collaboration and many discussions we had, especially during the first two years of this work.

I also would like to thank my co-supervisors Associate Professor Luiza Angheluta and Professor Joseph LaCasce. Through our discussions, and the EarthFlows meetings, I have gained insights into, and seen connections to other branches of physics and geophysical flows.

There are many people in the Hydrodynamics Laboratory who deserve a big thanks. Thanks to Dr. Jostein Kolaas for helping me out in the beginning of the project, giving me an introduction to his HydroLab PIV software and labview. I would also like to thank Dr. Jean Rabault for many fruitful discussions throughout the years. A special thank is also directed to our lab engineer Olav Gundersen. Whether I need help setting the correct IP address for my PIV cameras, or advice on some renovations at home, I can always count on you!

I would also like to thank Igor Braga de Paula and Luis Fernando A. Azevedo at Pontifical Catholic University of Rio de Janeiro for inviting me and Anis to stay in their laboratory, and discuss both the physics and experimental setups used to study gas-liquid pipe flows. I thoroughly enjoyed my weeks in Brazil, and hope I will be back.

Finally, I would like to thank my wife and family for support. These years have really gone by in a flash, and while I will remember my time at Blindern with fondness, the greatest and most important achievements have all come in my private life. Coming home to Mari and baby Ingrid has been my most important motivation during this work.

Petter Vollestad
Oslo, September 2020

Contents

Chapter 1

Introduction

1.1 Multiphase flows and the present thesis

Multiphase flow is the interactive and simultaneous flow of two or more immiscible phases. Such flows occur all around us in nature, and is an integral part of virtually any industrial process. Any combination of gas, liquid and/or solid component can constitute a multiphase flow. In the present work, the focus is primarily on two-phase gas-liquid flows. A typical configuration is the stratified flow configuration, where the two phases are separated by a continuous interface, and the lighter gaseous phase flows above the heavier liquid phase. This flow configuration occurs when wind blows over water waves in the ocean, and for horizontal gas-liquid pipe flows at moderate flow rates.

This thesis represents an effort to conduct detailed measurements in order to gain further insight into the physical mechanisms that govern stratified free surface flows. While the bulk of the work considers stratified gas-liquid pipe flows, airflow over waves in a combined wind-wave flume is also investigated. The project is a part of the EarthFlows strategic research initiative at the University of Oslo ("EarthFlows", 2020), where the goal is to investigate the interaction of geophysical flows, such as the interaction between the ocean and atmosphere, hence the link between the results obtained in a controlled pipe flow configuration and the physical processes occurring in the ocean is of interest. It was also concluded in the Ph.D. thesis of my co-supervisor, Anis A. Ayati that *"... observations made during the course of this work, suggest that it is worthwhile to further investigate oceanography literature for a better understanding of the physics that control the exchange of energy between the phases in stratified wavy [pipe] flows"* (Ayati, 2015).

Some of the overarching goals of the present thesis can be summarized as:

- Further develop optical measurement techniques and analysis methods applied to stratified gas-liquid (pipe) flows.
- Gain further insight into the mechanisms that control stratified air-water flows, with focus on momentum transfer both between, and within, the two phases.
- Provide experimental data that can be used in the validation of numerical models for stratified gas-liquid pipe flows.

Throughout this work, experimental results obtained in the two-phase pipe flow configuration are compared with literature on air-sea interactions, and the following question has been asked:

- What parallels can we draw between stratified gas-liquid pipe flows and the air-sea interactions occurring in the ocean? And what are the limitations?

The experimental technique used to study stratified gas-liquid flows has also been applied to measure the solid phase of a gas-sand pipe flow (in paper VII). While active particles in a particle-laden flow is somewhat separated from the main theme of the thesis, the study illustrates the applicability of the measurement technique to other physical systems.

An introduction to gas-liquid pipe flow, with focus on the stratified regime is presented in section 1.2, while an introduction to the relevant topics within air-sea interactions is provided in section 1.3. The purpose is to present relevant terms and topics that are investigated in the papers which form the bulk of the thesis. A summary of the main findings is provided in section 1.4.

1.2 Gas-liquid pipe flows

Gas-liquid pipe flows play an important part in many industrial processes, such as heat exchangers and nuclear reactors. It is also an integral part of the petroleum industry. Accurate prediction of the flow conditions is vital for safe and reliable production, and as the industry pushes the boundaries to go deeper, further offshore and to explore increasingly complex fields, understanding this multiphase flow configuration becomes both increasingly complicated and important.

Two-phase pipe flows are typically divided into flow regimes, where the flow structure changes in some qualitative way between the different regimes. The main flow regimes in horizontal gas-liquid pipe flows are illustrated in figure 1.1. An overview of flow regimes in two-phase flows is provided by Wallis (1969) and Brennen (2005). Predicting the flow regime for a given flow configuration remains one of the main challenges related to flow assurance in the oil and gas industry (Bratland, 2010). Mandhane et al. (1974) collected experimental data from different test rigs, considering air-water flow in horizontal pipes. Two-dimensional flow maps where the superficial gas and liquid velocities (the volumetric flow rate of each phase divided by the pipe cross-sectional area, denoted U_{sg} and U_{sl} respectively) formed the axis were found to be suitable to differentiate the main flow regimes observed. A similar flow regime map is presented in figure 1.1.

It is noted that the flow regime map presented in figure 1.1 represents a significant simplification, both in the description of the regimes and the transitions between them. While the boundaries between the different regimes are typically depicted as solid lines, regime transitions are in practice more gradual, and will occur at different flow rate combinations for different test rigs (even when the same fluids are applied). The visual characterization of the flow regimes also leads to significant discrepancies between different studies (Ayati et al., 2015; Spedding and Spence, 1993; Strand, 1993).

In the present work, focus is limited to the stratified smooth and wavy flow regime, considering air-water pipe flow at atmospheric pressure.

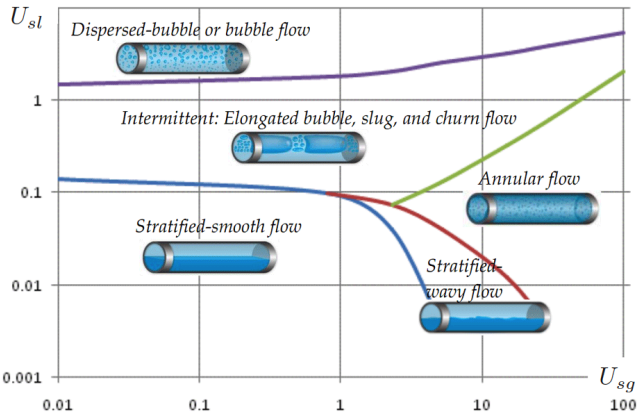

Figure 1.1: Example flow regime map for horizontal gas-liquid pipe flow. Axes are superficial gas (U_{sg}) and liquid (U_{sl}) velocities (in m/s). Image credit: Bratland (2010).

1.2.1 Wave regimes in horizontal air-water pipe flows

Further subdivision of the stratified regime depicted in figure 1.1 has been performed by several researchers (Andritsos and Hanratty, 1987; Ayati et al., 2015; Birvalski, 2015; Espedal, 1998; Newton and Behnia, 2001; Spedding and Spence, 1993; Strand, 1993; Tzotzi and Andritsos, 2013).

Andritsos and Hanratty (1987) and Tzotzi and Andritsos (2013) discussed four sub-regimes within stratified flow:

A. Smooth regime (no waves).

B. Two-dimensional (2D) wave regime. Interface is covered by small amplitude, regular disturbances.

C. Large amplitude (Kelvin-Helmholtz) waves regime.

D. Atomization regime, where droplets are torn of the crest of large amplitude waves and deposited on the pipe walls.

Increasing the gas superficial velocity in the stratified smooth regime, the first waves are initiated as pressure and shear work on the waves overcome the viscous dissipation (Taitel and Dukler, 1976). According to Tzotzi and Andritsos (2013), the transition to the 2D wave regime can be estimated based on the sheltering hypothesis by Jeffreys (1925) (see section 1.3.1), modified for two-phase pipe flow by Taitel and Dukler (1976), while the transition to large amplitude 'K-H' regime is governed by a Kelvin-Helmholtz mechanism. Hence, while the 2D waves are associated with pressure variations in phase with the wave slopes, the K-H waves are caused by pressure variations in phase with the wave crests, as

the suction force above individual wave crests overcome the stabilizing effect of gravity.

Tzotzi and Andritsos (2013) evaluated the transition from '2D' to 'large amplitude' waves based on visual observations and analysis of the film thickness recordings. 2D waves were associated by well-defined periodicity, and appeared relatively two-dimensional, while the film tracings of the 'large amplitude' waves were much more irregular. These waves are characterized by steep fronts and a gradually sloping back, and are observed to continuously change their shape as they propagate (Andritsos, 1986). They are also referred to as 'roll waves' in the literature (Spedding and Spence, 1993; Tzotzi and Andritsos, 2013), as they resemble the roll waves observed in channel flow, characterized by Hanratty and Engen (1957) as *"A slug of liquid" ... "picked up and carried over the top of the liquid surface by the gas at a very rapid rate."*. While no strict criterion for the periodicity of the film tracing signal was defined, Tzotzi and Andritsos (2013) presented semi-empirical correlations for the transition to 2D and large amplitude wave regime. Andritsos and Hanratty (1987) associated the transition to large amplitude waves with the kurtosis of the interface elevation exceeding 3.

Strand (1993) performed an extensive study of characterizing the gas-liquid interface by use of conductance wave probes in the same flow loop used in the present work. Strand defined six subregions within the stratified regime:

1. Smooth regime (no waves).
2. Small amplitude 2D wave region.
3. Large amplitude 2D wave region. Characterized by maximum amplitude towards the wall. The maximum amplitude is dependent on liquid flow rate (higher wave amplitude for higher liquid flow rates).
4. 3D wave region. The interface becomes increasingly agitated with increasing gas flow rates.
5. Pebbly wave region. High frequency, low *rms* amplitude.
6. Unstable large amplitude 2D waves. Long wavelengths, high wave speed. No significant variation across the pipe.

In figure 1.2, the flow map presented by Strand (1993) is presented. Overlaid the original figure by Strand are the regime transitions described by Tzotzi and Andritsos (2013) (red lines and letters), as well as scatter plots of the experimental cases considered by Strand, indicating whether the kurtosis is smaller (o) or larger (×) than 3 (representing the transition to the 'large amplitude' wave regime proposed by Andritsos and Hanratty (1987)).

Figure 1.2 illustrates some of the difficulties that arise when comparing different wave regime maps/definitions. While the transitions from a smooth interface to the first 2D waves are found to coincide fairly well comparing the flow regime maps, the transition from '2D' to 'large amplitude' waves does not

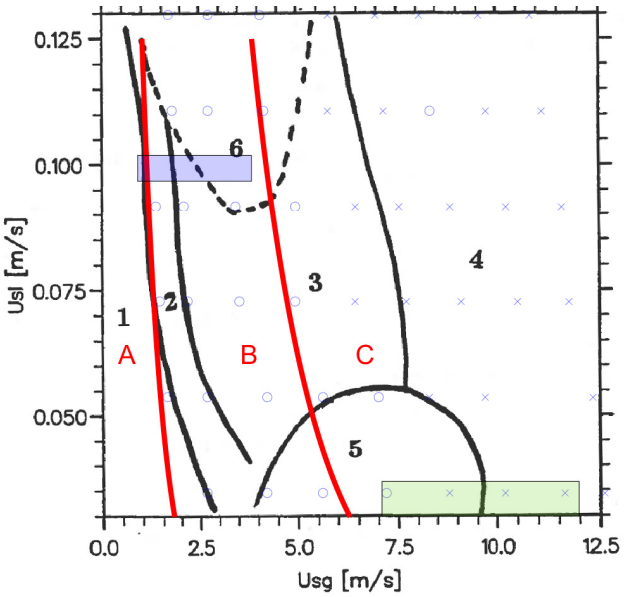

Figure 1.2: Wave regime map for horizontal air-water pipe flow. Image adapted from Strand (1993). Black lines and numbers: flow regimes from Strand (1993). Red lines and letters: Flow regimes from Tzotzi and Andritsos (2013). 'o'/'×': Experimental case from Strand (1993) where the kurtosis of the interface elevation was smaller/larger than 3. Blue and green rectangles: Regions in the flow map under investigation in the present work.

correspond to any of the transitions defined by Strand (1993). As the number of subdivisions are not the same, this is to be expected. The predicted transition from '2D' to 'large amplitude' waves is found go through regime 3, 5 and 6 defined by Strand, and separate regime 3 more or less in the middle. This illustrates that the regime transitions are not sharp borders which can be easily defined based on visual inspection, but gradual transitions from the periodic 2D waves at low U_{sg}, to a chaotic and highly three-dimensional regime at high U_{sg}. While the transition from experimental cases where the kurtosis is smaller/larger than 3 is seen to follow the same trend as the transitions to regime 4 defined by Strand and regime C by Tzotzi and Andritsos, it does not correspond to either of the flow regime transitions, but is located somewhere in between.

Espedal (1998) divided the stratified regime into 5 subregimes, based the work of Andritsos (1986) and Strand (1993). Espedal did not include the pebbly wave regime (regime 5 in figure 1.2), as it was difficult to distinguish. Newton and Behnia (2001) classified stratified wavy regime into rippled, 2D and roll waves. The rippled wave regime was characterized by high frequency, low amplitude waves, observed at moderate gas flow rates and low liquid holdup (probably equivalent to the 'pebbly' regime by Strand (1993)).

Ayati and Carneiro (2018) (considering the same flow loop used in the present work) analyzed the wave statistics measured by conductance wave gauges, and proposed a subdivision of the 2D wave regime based on the (non)linearity of the wave field. Increasing the gas flow rate beyond the onset of 2D waves, the rms of the interface elevation fluctuations (η_{rms}) was observed to increase until a regime of 'amplitude saturation' was observed. This transition was also noted in the work of Strand (1993) and Ayati et al. (2015). Ayati and Carneiro found that in the 'amplitude growth' regime the wave field closely followed Gaussian statistics, while the more irregular 'amplitude saturation' regime was characterized by nonlinear behavior. The authors note that in the latter regime, the increased energy input by higher gas flow rates does not result in increased wave energy. This could be caused by reduced energy transfer rates due to modifications of the airflow structure and/or dissipative mechanisms such as small-scale wave breaking, or interactions with the turbulent bulk flow.

The wave regimes observed in the present work are well described by the classifications of Strand (1993) and Ayati et al. (2015). This is to be expected, as the experiments are performed in the same two-phase flow loop. Example images from the two-phase flow loop, illustrating some of the flow regimes discussed are presented in figure 1.3.

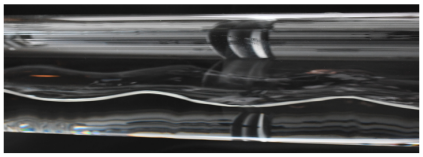

- Regular, '2D' waves
- Maximum wave amplitude increases with liquid height

a) $U_{sl} = 0.10$ m/s, $U_{sg} = 1.90$ m/s.

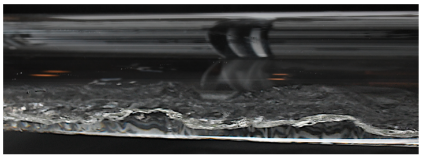

- 3D, high frequency wave pattern
- Large, irregular disturbances spanning the width of the pipe

b) $U_{sl} = 0.10$ m/s, $U_{sg} = 8.50$ m/s.

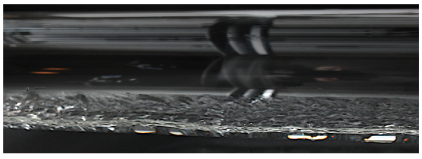

- 3D, high frequency wave pattern
- Surface roughness is fairly constant, both in time and space

c) $U_{sl} = 0.03$ m/s, $U_{sg} = 8.50$ m/s.

Figure 1.3: Images illustrating flow regimes observed in the experimental setup. a) 2D waves. b) 3D waves with intermittent 'large amplitude' (roll) waves. c) Pebbly wave regime.

In characterizing different regimes of two-phase gas-liquid pipe flow, focus has traditionally been on the behavior and visual characteristics of the liquid phase. This is understandable, as details of the gas flow are more difficult to

observe. However, recent studies (Ayati, 2015; Birvalski et al., 2015) has provided new insight into, and emphasized the importance of, the structure of the gas phase. In the present thesis, experiments are performed within the two different regions of the flow map, illustrated by the green and blue rectangles in figure 1.2. Focus is on the coupling between the phases, and whether specific dissipative mechanisms or changes in the flow structure of the gas and/or liquid phase can help explain the observed transitions.

- The effect of interface roughness on the secondary flow structure (see section 1.2.2) in the gas phase is analyzed within the flow region indicated by the green rectangle.
- The transition from 'amplitude growth' to 'amplitude saturation' within the 2D wave regime observed by Ayati et al. (2015) is analyzed, considering whether intermittent airflow separation and/or wave breaking can be linked to the transition observed (region indicated by blue rectangle in figure 1.2).

1.2.2 Turbulence and secondary flows in the air-phase

Turbulence is a state of fluid flow, characterized by chaotic, three-dimensional vorticity, and rapid fluctuations both in time and space. The counterpart of turbulent flow is laminar flow, where fluid particles flow along ordered paths, with little or no mixing. The classical view of turbulent flows is a cascade of vortical structures, or eddies, embedded in the mean flow. Turbulence is generated at the larger scales, and successively break up into smaller eddies until the length scales are small enough for viscosity to be important, leading to viscous dissipation of the turbulent kinetic energy. The process is known as the turbulent energy cascade.

Analyzing statistically steady turbulent flows, a standard method of analysis is the Reynolds decomposition, where an instantaneously measured value is decomposed into the time-averaged mean and fluctuating component, $u(\boldsymbol{x}, t) = U(\boldsymbol{x}) + u'(\boldsymbol{x}, t)$. Here u' is a turbulent fluctuation, and by analyzing a time series the turbulent Reynolds stresses (such as $-\rho\overline{u'u'}$, $-\rho\overline{v'v'}$ and $-\rho\overline{u'v'}$, where the overbar indicates time-averaging) can be evaluated.

When a turbulent fluid flows through a non-circular geometry, it has a profound, and perhaps surprising, effect on the velocity field. Considering laminar flow through a straight, non-circular cross-section, where the axial velocity is directed in the z-direction, there will be no velocity components in the x- or y-directions. The fluid will flow in an orderly fashion, and the only velocity component is directed in the z-direction. However, when the flow is turbulent, secondary flows (mean flow structures in the plane perpendicular to the axial flow direction) will form. These were observed in the early works of Prandtl (1927) and Nikuradse (1926), considering turbulent single-phase flows through non-circular cross-sections. The theory describing the occurrence of secondary flows is presented by Speziale (1982). It is shown that secondary flows will form

in non-circular ducts when the axial mean velocity results in $-\rho\overline{u'u'} \neq -\rho\overline{v'v'}$, i.e. when the in-plane normal Reynolds stresses exhibit anisotropic behavior.

In single-phase flows, secondary flow structures are known to result from non-circular cross sections (Prandtl, 1927), and/or due to roughness variations around the circumference (Hinze, 1967). Example secondary flow patterns resulting from the two effects are illustrated in figure 1.4. While secondary flows typically represent 1-2 % of the mean axial velocity, they can have a significant effect on the axial velocity profile, as momentum is transferred towards the corners in the case of a non-circular cross-section (figure 1.4 a), and towards the rough interface in the geometry presented in figure 1.4 b.

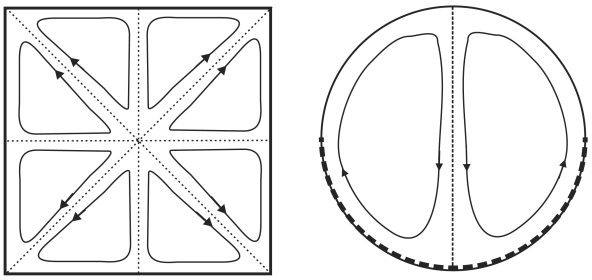

Figure 1.4: Secondary flow patterns observed due to non-circular cross-section (a) and due to non-uniform roughness (b) (lower half of pipe is rougher than the upper half). Image credit: Belt et al. (2012), Cambridge University Press.

Secondary flows are also known to form in multiphase flows, both considering gas-liquid (Dykhno et al., 1994; Meknassi et al., 2000; Strand, 1993) and particle-laden (Belt et al., 2012) flows. Considering the gas phase in stratified gas-liquid pipe flow, it is clear that it experiences a non-circular cross section as well as roughness variations around the circumference, as the liquid interface will have a different roughness than the pipe walls. These effects are known to give rise to secondary flow structures, symmetric about the centerplane of the pipe. The relative importance of the two effects (the non-circular cross section and the enhanced local roughness associated with interfacial disturbances), and how the secondary flow field develops with increasing surface roughness and for different wave regimes remains an open question, and will be investigated considering the stratified smooth, as well as the 'pebbly'/'3D' wave regime in the present work. As the secondary flows displace the mean axial velocity profile up or down in the pipe (depending on the direction of the secondary flows), they can significantly modify the airflow close to the interface, and indirectly the development of the interfacial wave pattern. This implies a complex two-way coupling between the interfacial wave pattern and the turbulent airflow.

It is noted that secondary flows will also form in the liquid phase of stratified gas-liquid flows. Here, the secondary flows are generated both due to turbulence anisotropy and the interaction between the wave orbital motion and the mean

axial velocity profile (Nordsveen, 1995). Secondary flows in the liquid phase are not investigated in the present work.

1.2.3 Prediction models for stratified gas-liquid pipe flow

While the focus of the present work is on experimental analysis of gas-liquid pipe flow, an overview of the main modeling approaches, and challenges are presented in this section.

1.2.3.1 Mechanistic approach

The most widely used model for stratified gas-liquid flow is the one-dimensional two-fluid model, based on mass, momentum and energy balances of the two phases (Bratland, 2010; Ishii and Mishima, 1984). For fully developed, incompressible, stratified flow, the momentum equations for the gas and liquid phase can be written as (Tzotzi and Andritsos, 2013):

$$-A_g\Big(\frac{dp}{dx}\Big) - \tau_{wg}S_g - \tau_i S_i - \rho_g A_g g \sin\theta = 0, \tag{1.1}$$

$$-A_l\Big(\frac{dp}{dx}\Big) - \tau_{wl}S_l + \tau_i S_i - \rho_l A_l g \sin\theta = 0. \tag{1.2}$$

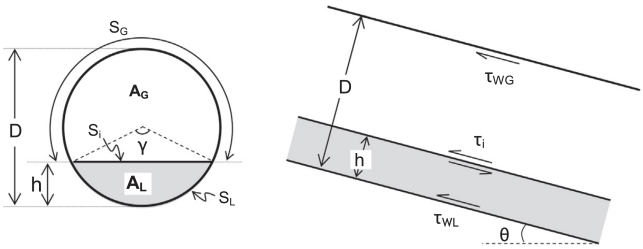

Figure 1.5: Geometrical and physical properties in the two-fluid model for stratified gas-liquid flow. Reprinted from Tzotzi and Andritsos (2013), with permission from Elsevier.

τ_{wl} and τ_{wg} are the liquid and gas wall shear stresses respectively, and τ_i is the interfacial shear stress. While τ_{wl} and τ_{wg} are generally accepted to be reasonably modeled using (modified) single-phase correlations, such as the Blasius or Colebrook-White equations (see Espedal (1998), Kowalski (1987), Schulkes (2011), and Spedding and Hand (1997)), the main challenge is to accurately predict the interfacial shear stress τ_i. This is typically related to the interfacial friction factor f_i by:

$$\tau_i = \frac{1}{2}\rho_g(U_{bg} - U_{bl})|(U_{bg} - U_{bl})|f_i, \tag{1.3}$$

where U_{bg} and U_{bl} are the bulk gas and liquid velocities. Taitel and Dukler (1976) assumed that the interface could be considered smooth, and applied $f_i \approx f_{wg}$ (where f_{wg} is the gas wall friction factor). It is however well known that the interface structure, and the presence of waves greatly modifies the interface friction factor. Several (semi-) empirical correlations for the interfacial friction factor within the stratified wavy regime has been proposed (summaries provided by Espedal (1998), Schulkes (2011), and Xiao and Shoham (1991)). These are also known to be related to the different wave regimes present in stratified two-phase flows. Large increases of the interfacial friction factor are associated with the transition to the 'large amplitude' wave regime (Tzotzi and Andritsos, 2013).

While correlation studies yielding interfacial friction factors provide a useful tool for evaluating stratified gas-liquid flows, they are not suitable for inferring the physical processes which make up the momentum exchange between the phases. Understanding how the presence of waves/enhanced surface roughness modifies the airflow in two-phase pipe flow is an important step towards reliable two-phase flow models.

1.2.3.2 CFD

Computational Fluid Dynamics (CFD), employing finite volume methods to evaluate the governing equations of the flow has been applied by several researchers analyzing stratified two-phase pipe flow (a recent review is provided by Ali (2017)). Due to the computational cost associated with two-phase flow simulations, focus has been on evaluating the gas and liquid flow fields using the RANS (Reynolds-averaged Navier-Stokes) equations. When reviewing the literature, two primary challenges are noted in modeling stratified gas-liquid pipe flows using CFD:

- Accurate prediction of the interfacial wave pattern/interface friction.
- Accurate evaluation of anisotropic Reynolds stress distribution and resulting secondary flows.

Related to the first challenge; one approach is to prescribe boundary conditions to the gas-liquid interface based on empirical values of the interfacial shear stress or interface roughness (Meknassi et al., 2000; Newton and Behnia, 2001). A more general approach is to model the development of the wave field directly. Ali (2017) calculated the development of the two-phase flow using a volume-of-fluid (VOF) CFD code. Here, the interfacial waves are allowed to develop, and the resulting interfacial friction factors and wave field are a result of the simulation. Both Meknassi et al. (2000) and Ali (2017) compare their numerical results to the experimental results of Strand (1993). The results by Meknassi et al. (2000) are found to be in better agreement with the experimental results, but as discussed by Ali (2017), this was achieved as empirical information from the measurements was taken as an input to the modelling of the interfacial

shear. For this reason, the validity of the model of Meknassi et al. (2000) for other flow configurations is unknown.

As discussed in section 1.2.2, secondary flows will form in non-circular channels when there is a non-zero difference in the in-plane normal Reynolds stresses. Accurate prediction of anisotropic turbulence represents a significant modeling challenge. In particular, the standard k-ϵ model is not able to predict the secondary flow patterns resulting in two-phase pipe flows (Speziale, 1982). Higher order Reynolds stress models, or modified RANS turbulence models specifically modeling the anisotropic terms are needed to accurately determine the secondary flow structures.

Chinello et al. (2019) compared the experimental results of Ayati (2015) (obtained in the same pipe loop used in the present work) with results from a VOF RANS simulation, using the k-ω SST turbulence model. Significant discrepancies, both considering the statistics of the wave field and velocity profiles were observed. While turbulence damping terms at the interface were observed to yield somewhat improved results, the authors concluded that *"In its current form, however, RANS with $k-\omega$ turbulence model is still not able to give an accurate prediction of the velocity profiles and of the interface waves"*.

This brief overview highlights the need for relevant experimental data on the interface structure and flow fields of gas-liquid flows. In particular, detailed experimental data on the secondary flow patterns and Reynolds stress distributions, coupled with statistics of the interface structure are assessed to be important for development and validation of CFD codes.

1.2.3.3 Commercial flow assurance models

To ensure safe and reliable production of oil and gas, a number of highly sophisticated, commercial, flow assurance models are available. Examples include OLGA (Bendiksen et al., 1991) and LedaFlow (Goldszal et al., 2007).

While multidimensional capabilities are available, the bulk of these models are based on a 1D approach (similar to the two-fluid model). They can describe both the transient and spatial development of the flow and take into account effects such as terrain, flow regime changes and heat exchange with the environments. The models are based on a large number of empirical closure relations, which highlights the need to further develop measurement techniques suitable to study multiphase pipe flows.

1.2.4 Experimental methods applied to gas-liquid pipe flows

A large number of experimental investigations of gas-liquid pipe flows have been performed. The most commonly measured quantities are the mean liquid holdup and pressure drop (see e.g. Hart et al. (1989), Spedding and Hand (1997), and Tzotzi and Andritsos (2013)). These are the main variables needed to evaluate the interfacial friction factor, when the gas or liquid wall friction factors are evaluated using empirical correlations (ref. section 1.2.3.1). Measurements of the wall friction has been performed using hot-film anemometry, in both the gas

(Kowalski, 1987) and liquid (Espedal, 1998) phases, providing support for the correlations used.

The mean liquid holdup has been evaluated by the use of quick-closing valves (Espedal, 1998), essentially trapping the liquid within a section of the pipe. Detailed measurement of the temporal and spatial evolution of the interface characteristics has been measured using conductance wave gauges positioned at different spanwise and streamwise locations of the pipe (Strand, 1993), high resolution photography (Sanchis, Johnson, et al., 2011), X-ray tomography (Smith, 2018) and gamma densitometry (Vestøl, 2013) techniques.

The velocity profiles in the gas phase has been measured by traversing pitot tube measurements (Newton and Behnia, 2001; Strand, 1993) and by hot-wire anemometry (Ayati et al., 2016). A limitation of these intrusive measurement techniques is that it is very difficult to measure in the trough-to-crest region of the stratified wavy regime, as this would require a wave-following traversing system, which can adapt quickly to the highly fluctuating flow. Hence, measurements are restricted to the region above the highest wave crest. An alternative, non-intrusive point-measurement technique is Laser Doppler Anemometry (LDA), which has been applied to measure the velocity profiles in the gas and liquid phase of stratified flow by Paras et al. (1998) and Strand (1993).

Recently, Particle Image Velocimetry (PIV) has been applied to study stratified gas-liquid pipe flows. In its basic form, PIV is an optical measurement technique which measures the two-dimensional velocity field on a thin plane, typically along the centerplane of the pipe. Vestøl (2013) analyzed the velocity fields in the gas and liquid phases separately, considering flows ranging from stratified smooth, to slug flow. Considering the stratified smooth and 2D wave regime, Ayati (2015) performed simultaneous PIV measurements in the gas and liquid phases (referred to as simultaneous two-phase PIV, S2P-PIV). Spatio-temporally averaged mean and fluctuating velocity profiles, as well as intriguing evidence of intermittent vortex shedding over steep waves, which could be linked to the energy spectra evaluated by hot-wire anemometry were presented. The ability to extract instantaneous, two-dimensional flow structures is one of the advantages of the PIV technique compared with the other point-measurements used to evaluate velocity profiles. The technique can also be applied to measure the instantaneous velocity field in the trough-to-crest region.

Simultaneous evaluation of the gas and liquid velocity fields using PIV has recently also been performed by Birvalski (2015) and Farias (2019). Farias analyzed the growth of artificially generated monochromatic waves compared with the growth-rates predicted by linear stability theory, while Birvalski analyzed naturally occurring waves generated by the airflow. Both of these investigations present phase-averaged results, where the gas and liquid velocities are averaged at a given wave phase. These analysis techniques provide further insight into the wave-turbulence interactions investigated by Ayati et al. (2016).

In the present work, different PIV techniques (including the S2P-PIV technique by Ayati (2015)) are applied together with conductance wave gauges and photographic interface detection to evaluate both the interface structure and gas/liquid flow fields. Details are presented in chapter 2.

1.3 Air-sea interaction

The formation, growth and breaking of wind waves plays an important role in the exchange of heat, momentum and chemical components between the ocean and atmosphere. In this section, some of the main concepts related to wave generation and dissipation are presented, referring to the air-sea literature.

An important hypothesis going into this work was that many the underlying physical mechanisms, considering stratified air-water pipe flows, are similar to the processes occurring in the ocean. Hence, the concepts introduced in this section are later discussed and analyzed considering the 2D wave regime of stratified air-water pipe flows.

Figure 1.6: Ocean wind-waves. Image credit: Pexels (2015).

1.3.1 Wave generation and growth

"The causal relationship between the wind and ocean waves is obvious to even the most casual of observers" (Young, 1999). Despite this obvious relationship, and considerable efforts put into the development of models for wave growth, there is still no unified model that can predict the growth of surface waves under the action of wind.

Considering a turbulent airflow over still water, Phillips (1957) proposed that the first water ripples were produced by a resonance mechanism between turbulent pressure fluctuations and the free modes of the gas-liquid interface. As the wave field has started to develop, waves can grow due to tangential (shear) and normal (pressure) stress variations acting on the water surface (Young, 1999). As a wave field is established, it is generally accepted that the dominant contribution to wave growth is the form drag associated with a phase shift of the pressure field relative to the wave form (Young, 1999). The physical mechanisms

leading to the phase shift of the pressure field has been an area of significant research.

Jeffreys (1925) was one of the first to propose a physical mechanism and mathematical model to explain wave growth. Jeffreys proposed that *"... the main air current, instead of flowing steadily down into the troughs and over the crest, merely slides over each crest and impinges on the next wave at some point intermediate between the trough and the crest."*. Such a flow would result in higher pressure on the windward face, and lower pressure on the leeward face of the wave, and hence a net energy transfer to the waves. The theory has been referred to as the sheltering hypothesis.

As ocean waves typically have gentle slopes, Belcher (1999) argued that airflow separation will not be a frequent event, but that turbulent stresses on the leeward side of the wave cause a reduction of the airflow velocity on the leeward side. This results in an asymmetric displacement of the streamlines relative to the wave shape, with an associated asymmetric pressure field. Belcher and Hunt (1993) refer to this wave growth mechanism as 'non-separated sheltering'.

Miles (1957) proposed a quasi-laminar model, where the role of the turbulent stresses was confined to producing the logarithmic velocity profile, characteristic of wall-bounded turbulent flow. The height where the wind speed matches the wave speed is referred to as the critical height. Owing to sinusoidal pressure variations in phase with the wave form, a region of recirculating flow forms around the critical height. As explained by Lighthill (1962), this results in a 'vortex force' which transfers energy from wind to waves.

While a review of eight mechanisms responsible for energy transfer from wind to slowly moving waves is presented by Belcher and Hunt (1993), the non-separated sheltering mechanism of Belcher and Hunt and the critical layer mechanism of Miles (expanded and modified in later works; Janssen 2004; Miles 1993) remain the most widely accepted mechanisms/models for wave growth by wind (Buckley and Veron, 2016). As waves in the ocean have wavelengths spanning more than five orders of magnitude, vary in steepness and are exposed to different wind conditions, it is not surprising that no one single mechanism is found to be responsible for wave growth. Both analytical (Belcher and Hunt, 1998) and computational (Kihara et al., 2007) models have indicated that different mechanisms dominate within different wave age regimes, where the wave age is expressed as C_p/u_*, where C_p is the phase speed of the waves at the peak of the spectrum, while u_* is the air friction velocity. Considering waves at moderate slopes, the non-separated sheltering mechanism is assessed to dominate considering young ($C_p/u_* \lessapprox 10$) and old ($C_p/u_* \gtrapprox 20$) waves, while the Miles mechanism is found to be effective for intermediate wave ages.

There still exist significant discrepancies between model predictions and experimental results for the growth rate of waves (Sullivan and McWilliams, 2010). While the majority of the ocean wave energy is contained in long waves with small slopes, the ocean surface is also covered by a continually evolving pattern of small scale (order 1 meter or less), steep, intermittently breaking waves. As discussed by Sullivan and McWilliams (2010), airflow separation from these small-scale waves introduce a mechanism for energy transfer which is not

considered in the non-separated sheltering or critical layer models. This could represent an important missing mechanism in the most used models for wave growth (Donelan et al., 2006; Sullivan and McWilliams, 2010).

It is noted that airflow separation over wind waves is not easy to define, and has caused some discussions in the literature (Banner and Melville, 1976; Gent and Taylor, 1977; Kawai, 1982; Sullivan, Banner, et al., 2018; Weissman, 1986). In the present work, the airflow is considered separated when the high vorticity shear layer characteristic of an attached boundary layer is ejected away from the surface, leaving a region of low speed/recirculating flow on the leeward side of the crest (similarly to the studies of Reul et al. (2008) and Buckley and Veron (2016)). This is assessed to cause a considerable phase-shift of the wave-coherent pressure field, and resulting enhanced momentum transfer to the waves compared with the non-separated case.

1.3.2 Wave breaking

Wave breaking is characterized by fluid elements near the crest of a wave which achieve a velocity greater than the propagation speed of the wave, resulting in a turbulent flow and transfer of momentum and energy from the waves to the underlying currents. In the literature, the process is typically divided into shallow water breaking, where the waves break due to changes in the water depth (Peregrine, 1983), and deep water breaking (Banner and Peregrine, 1993), where the breaking process is independent of changes in the bathymetry. Wave breaking serves to limit the wave height, generate ocean currents and near-surface turbulence and enhance the gas transfer rates between the ocean and atmosphere (Melville, 1996).

Predicting the onset of breaking has been a field of study for a long time (see Perlin et al. 2013 for a review). While significant developments have taken place since the geometric breaking criterion based on Stokes' theory, which predicts wave breaking to occur as the wave steepness ak grows to 0.443, there is still no unified model which can predict the onset of wave breaking. As the wave field in the ocean is highly three-dimensional, spans several orders of magnitude and is influenced by both wind and currents, it is perhaps not surprising that no single breaking criterion has been established.

At deep waters, wave breaking is separated into categories according to their severity and visual characteristics. Babanin (2011) separates wave breaking into plunging, spilling and microbreaking. While wave breaking is often referred to as "whitecapping", and associated with the more energetic plunging and spilling events which result in air-entrainment, wave breaking also occurs at small scales, where surface tension prevents the jet formation and air entrainment associated with larger breaking waves (Tulin and Landrini, 2001).

Banner and Phillips (1974) referred to the breaking of these short, wind-generated gravity waves as "micro-breaking". Microscale breaking waves are generally described as $\mathcal{O}$(0.1-1) m in length, and a few cm in height (Jessup et al., 1997). They are identified by parasitic capillary waves on the leeward side of the wave crest, which are displaced downstream as the spilling process is

initiated (Turney, 2016). Wave breaking is known to disrupt the thermal skin layer of the ocean surface, which can be identified by infrared imaging. As the visual characteristics of microscale breaking are weak, it is suggested by Jessup et al. (1997) that the disruption of the thermal skin layer may serve as practical means of defining the phenomenon. The characteristic features of microscale breaking waves discussed are illustrated in figure 1.7.

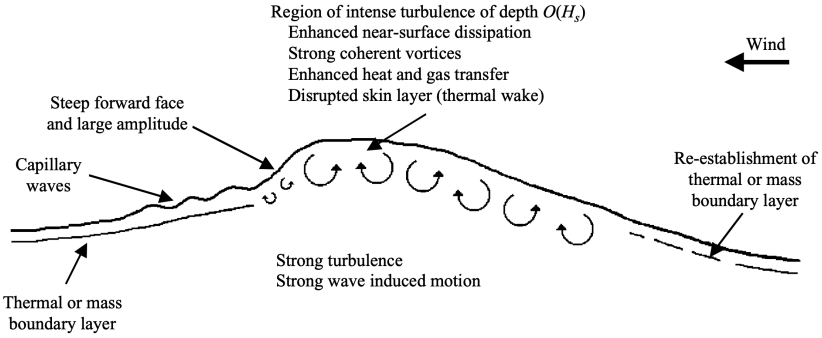

Figure 1.7: Characteristic features of microscale breaking waves. Image credit: Siddiqui and Loewen (2007), Cambridge University Press.

Due to the high frequency of microscale breaking in the ocean, it is assessed that they significantly contribute to the heat and gas fluxes across the interface (Jessup et al., 1997; Melville, 1996). Recent field experiments (Sutherland and Melville, 2013; Sutherland and Melville, 2015) have indicated that these small-scale breaking waves, with no or very little air entrainment, can account for as much as 20-90 % (depending on the wave age) of the dissipation by breaking in the ocean. The conclusion was supported by the identification of a thin layer of high dissipation rates near the surface. The relative importance of microscale breaking waves on the total dissipation rate is however still a subject under debate (Banner and Morison, 2016).

In the present work, microscale wave breaking will be analyzed in a pipe flow setup. Modifications of the airflow structure over steep and intermittently breaking waves will also be investigated both in a pipe and wind-wave flume, in light of the aerodynamic sheltering mechanism past the wave crests, caused by separated or non-separated sheltering.

1.4 Main developments and findings

Referring to the objectives presented in section 1.1, and the introduction provided to the subject of stratified gas-liquid flows, a summary is provided of the main developments and findings presented in the papers included in this work.

During the course of this work, the experimental methods applied have been developed to improve the measurement accuracy, obtain measurements from new parts of the flow field and facilitate new analysis techniques. While details of

the experimental techniques are presented in chapter 2, these developments can be summarized as:

- Stereoscopic PIV has been applied to measure all three velocity components in the cross section of the pipe occupied by the gas phase (paper I).
- The simultaneous two-phase PIV (S2P-PIV) method by Ayati (2015) has been modified and improved (paper IV and V):
  - Conditional sampling of the velocity fields based on a triggering system, detecting incoming waves.
  - Improved accuracy close to the interface owing to use of fluorescent liquid particles in combination with bandpass filters on the cameras.
  - Enhanced imaging due to Scheimpflug adapters and modifications to the optical corrections applied.
- PIV is applied to measure the mean particle velocity profile in a dilute air-sand pipe flow (paper VII).

The analysis performed has revealed new insight into the physics of stratified gas-liquid pipe flows, and some relations to processes occurring in the ocean (relevant for measurements in the '2D' wave regime):

- Secondary flows in the air-phase are measured over flat and rough (considering the 'pebbly' and '3D' wave region as defined by Strand (1993), ref. figure 1.2) interfaces (paper I). The interphase morphology is seen to govern the direction of the secondary flows, as the direction is reversed when interfacial disturbances are allowed to form. The secondary flow structures are found to be well predicted by the dominant gradients of the in-plane normal Reynolds stresses, measured in the pipe cross-section.

  The experimental data is considered suitable for validation of numerical models. It is noted that detailed velocity profiles from the experiments are provided in Appendix A of this thesis.
- Measurements of small-scale wave breaking in a two-phase pipe flow is performed, and the inception of this phenomena is associated with the 'amplitude saturation' regime (paper III). As the waves are breaking without air entrainment, and as the wavelengths/heights are in the range reported for microscale breaking waves in the air-sea literature, these are referred to as microbreaking/microscale breaking waves.

  A scheme is proposed to detect actively breaking waves based on the rms vorticity in the crest region, and it is found that the features of these small breaking waves are similar to the microbreakers considered to play a significant role in the air-sea interactions. In the stratified pipe flow configuration, these breaking events are assessed to play an important role in transferring energy and momentum to the underlying liquid flow, reducing the liquid holdup as the gas velocity is increased.

- The sheltered area on the leeward side of actively breaking and non-breaking waves is found to be well correlated with the crest front-face steepness of the waves, considering waves both in the stratified pipe flow (paper V) and wind-wave flume (paper VI) configuration. Airflow separation is found to be a frequent event in the 'amplitude saturation' regime, indicating that the momentum transfer mechanism is modified as the superficial gas velocity is increased into this regime (paper II).

  The link between small-scale wave breaking and airflow separation is investigated. Considering moderate airflow rates in the pipe flow setup, active wave breaking is seen to reduce the extent of the sheltered area, compared with non-breaking waves at similar steepness (paper V). A similar relationship was not found in the wind-wave flume, considering spilling breaking waves over a submerged step (paper VI).

Chapter 2

Experimental work

In this chapter an overview of the experimental setups used and measurement techniques applied are presented.

During the course of the work, modifications were made to the specifics of the measurement setups applied (in particular, to the PIV setup). While this chapter presents the main measurement techniques applied, and the aspects that are common for the different investigations, full details of the measurements are presented in each of the papers documenting the experimental work.

2.1 Experimental facilities

Measurements have been performed within three different experimental rigs:

- Air-water pipe loop at the Hydrodynamics Laboratory, UiO (paper I, II, III, IV and V).
- Wind-wave flume at the Hydrodynamics Laboratory, UiO (paper VI).
- Air-sand pipe flow loop at DNV GL (paper VII).

Details of the DNV GL pipe loop are not presented in this chapter, as the focus of this work (paper VII) is primarily on the application of the measurement technique to dilute particle-laden flows. Some details of the measurement setup are presented in paper VII.

2.1.1 Air-water pipe loop

The bulk of the experiments have been conducted in the two-phase pipe flow loop at the Hydrodynamics laboratory, University of Oslo. The experimental setup consists of a 31 meter long, horizontal, 10 cm inner diameter, transparent acrylic pipe made up of 11-13 (depending on the experimental equipment applied) sections that are tightly connected and clamped to an aluminium beam. An overview of the experimental setup is presented in figure 2.1.

Air and water is supplied by a frequency regulated fan and pump respectively. Both phases are circulated from the gas-liquid discharge tank back to the inlet section. The air is circulated through a 40 meter long, 160 mm diameter circular duct, through the fan which is connected to a 12 meter long circular duct before entering the pipe inlet. Water was recirculated through a 56 mm diameter pipe. The air and water flow rates are measured in the recirculating loops, using Emerson Micromotion and Endress Hauser Promass Coriolis flow meters respectively. As both phases are recirculated through the system, the fluids are at room temperature. The main measurement section was located approximately

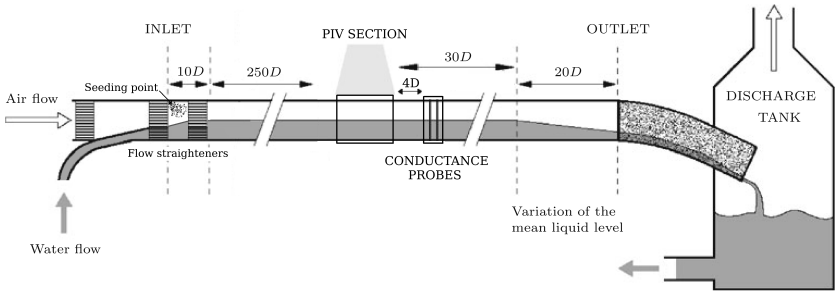

Figure 2.1: Overview of experimental setup.

26 meters from the pipe inlet. This includes a PIV section and conductance wave gauges (details provided in section 2.2.1 and 2.2.2). The pressure drop in the air phase was measured using a smarLD301 differential pressure gauge.

Figure 2.2 presents details of the inlet section. Air flow is directed from above, while water is provided from below. The inlets are separated by a plate directing the water in the horizontal direction, before the two phases are allowed to mix. Figure 2.2 illustrates the location of flow straighteners used. These have a honeycomb pattern, with an inner diameter of approximately 4.5 mm.

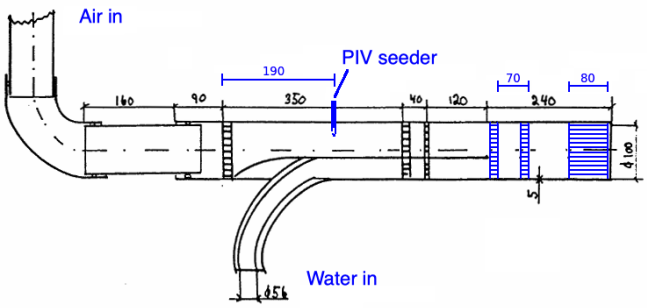

Figure 2.2: Details on the inlet section, adapted from Strand (1993). Blue lines/text indicate changes from Strand (1993). Length scales in *mm*.

Figure 2.2 also illustrates the location of the air-phase spray seeder, used to seed the gas phase with small water droplets for PIV (see section 2.2.1). In the work of Ayati (2015), the seeder was placed behind the last honeycomb illustrated in figure 2.2, and an additional honeycomb was placed 3 meters downstream, to dampen and "restart" the wavefield at this location. However, tests with this configuration indicated that the wave field could be significantly modified by the water spray. The water spray introduces momentum to the flow, and the tests performed indicated that the configuration did not adequately dampen the

disturbances introduced.

For this reason, the air-phase seeder was moved to the location indicated in figure 2.2. Here, the momentum of the spray is directed towards the plate separating the gas and liquid inlet, and does for this reason not induce the same disturbance to the wave field. The wave spectrum (evaluated by conductance wave gauges at the location indicated in figure 2.1) with and without spray was compared, and found to be relatively unaffected by the spray generation (see comparison for one relevant case in figure 2.3 a).

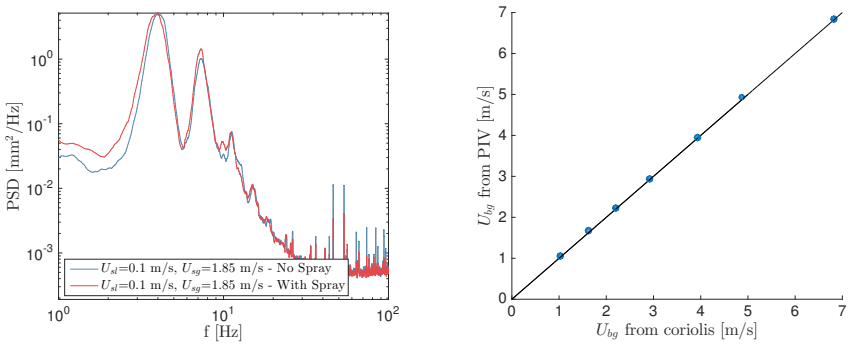

a) b)

Figure 2.3: a) Frequency spectra evaluated by conductance wave probes, with and without the spray generator. b) Flow rate measurements by Coriolis flow meter vs. PIV after correction of the Coriolis flow meter zero point. U_{bg} is the bulk gas velocity.

A significant fraction of the liquid spray generated by the air-phase seeder is assessed to accumulate to larger droplets as the air passes through the downstream flow straighteners, and become part of the liquid phase. As this water does not pass through the liquid-phase Coriolis flow meter, it is not included in the reported U_{sl}. However, water flow rate from the seeder is small relative to the liquid flow rate through the pipe, and represents less than 1 % of the liquid flow rate applied in the present work.

As the experimental work started, the zero-point of the air-phase Coriolis flow meter was found to be incorrect. After correction, measurements by the Coriolis flow meter were compared with PIV measurements of the pipe centerline, considering single-phase air flow through the pipe. Assuming axis-symmetric flow, the centerplane velocity profiles were integrated to provide the volumetric flow rate in the PIV section. A comparison of the flow rate evaluated by the Coriolis flow meter and PIV is presented in figure 2.3 b). As can be seen, the PIV results are in good agreement with the Coriolis flow meter (average deviation of 1.5 %), which is a validation both of the PIV system and the Coriolis flow meter after adjustment. A similar validation of the liquid phase Coriolis flow meter was performed in the master thesis of Gyllengahm (2019), which ran in parallel with the present Ph.D. work. No adjustments were needed to the liquid

flow meter.

It should be noted that the first analysis performed during this doctoral work (paper II) was performed on the experimental data stemming from the work of Ayati (2015). Hence, the adjustments to the spray generator location and the air-phase Coriolis flow meter were not taken into consideration for this study. The adjustment of the zero-level corresponded to a $\Delta U_{sg} \approx 0.29$ m/s (the zero-level was adjusted up, from negative values). While we cannot assess with certainty if the Coriolis flow meter was ill adjusted during the work of Ayati (2015), a comparison of the onset of wave formations and the 'amplitude saturation' regime observed indicates that the zero-point was likely set to a negative value for these studies. This should be kept in mind when comparing results from paper II with the other analysis in the present work, as well as when results are compared with the work of Ayati (2015).

2.1.2 Combined wind-wave flume

For the analysis presented in paper VI, the large wave tank at the Hydrodynamics Laboratory at the University of Oslo has been modified to a wind-wave flume. A schematic illustration of the setup is presented in figure 2.4. The flume is 25 meters long, 0.5 meters wide and 98 cm high.

Air is provided by two construction fans (Heylo FD4000, each with an adjustable flow rate from 0.8 to 1.15 m^3/s when used as standalone) positioned at the opposite end of the wavemaker, which suck air through the flume. An image of the fans, as well as a typical wind-sea analyzed is presented in figure 2.5. Further details of the experimental setup in the combined wind-wave flume is presented in paper VI.

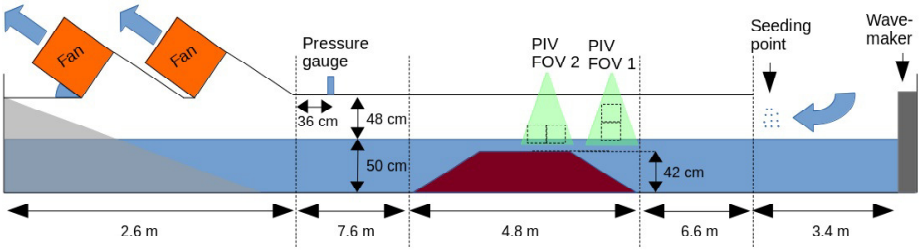

Figure 2.4: Schematic view of combined wind-wave flume.

It can be noted that the intention was to apply a high speed (1000 Hz) PIV system to analyze the transient behavior of airflow over breaking waves in the combined wind-wave tank. However, due to technical problems with two different high speed lasers, a much slower laser (maximum 16 Hz) was applied, somewhat limiting the scope of the investigations.

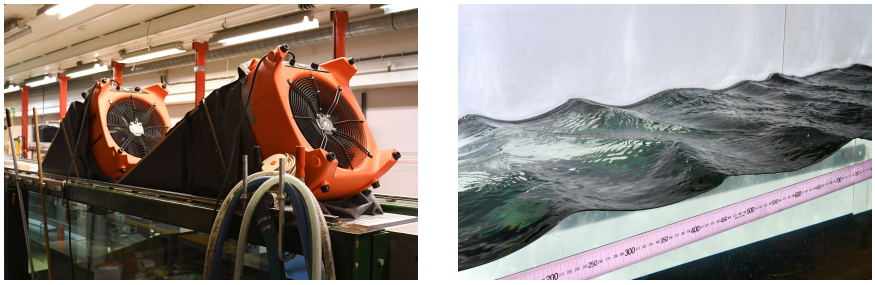

Figure 2.5: Left: Fans applied for wind-generation in wind-wave flume. Right: Typical wind-sea observed at the measurement section. Ruler scale is in mm.

2.2 Experimental techniques and analysis

2.2.1 Particle image velocimetry

Particle image velocimetry (PIV) is an optical measurement technique where particles acting as passive tracers in the fluid of interest are imaged within an illumination region. By acquiring images separated by a known Δt, cross-correlation techniques are used on subwindows within related images to evaluate the instantaneous velocity field. Details of the PIV measurement technique are presented in the books of Raffel et al. (2018) and Adrian et al. (2011).

Through the work, different PIV setups and techniques were applied. The main principles and challenges associated with the methods are presented in the following sections.

2.2.1.1 Standard planar PIV

The standard planar PIV technique measures two velocity components on a two-dimensional cross-section of the flow. Typically, a double-pulsed laser is used to illuminate a planar illumination region, and a single camera acquires images for cross-correlation. The process is illustrated in figure 2.6. The method is referred to as 2D2C-PIV, 2C-PIV (Raffel et al., 2018), 2D-PIV (Dabiri, 2006) and planar PIV (Adrian et al., 2011; Westerweel et al., 2013) by different authors.

As the present work considers the simultaneous flow of air and water, care must be taken in the choice of seeding particles for the air phase. In addition to the standard requirements to seeding particles (e.g. a low Stokes number to ensure passivity and suitable light scattering behavior), it is critical that the particles do not influence the fluid mechanical properties of the liquid phase (e.g. viscosity and surface tension), as this would modify the wave generation process and resulting wind-wave interaction under investigation. For this reason, small water droplets generated by a high-pressure atomizing nozzle attached to a wind-tunnel seeder are used as seeding particles in the air phase (similar to the work of Ayati (2015)). In the liquid phase, polyamid particles from

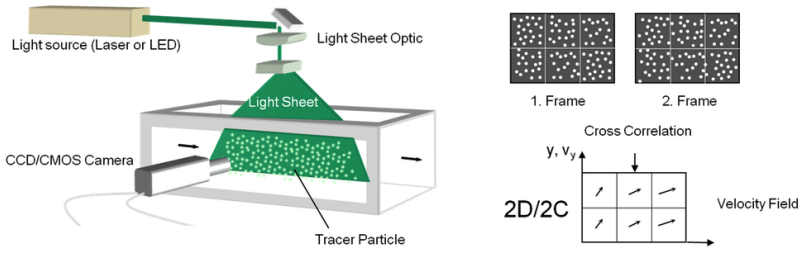

Figure 2.6: Schematic illustration of planar PIV. Image credit: Optolution (2020).

Dantec Dynamics (paper III) and fluorescent particles made from a commercially available acrylic paint (paper IV and V) are used.

Several sources of error are present in PIV. These arise from the calibration images acquired (and resulting coordinate transforms applied), alignment of the laser light sheet, passivity of the tracer particles applied and unpaired particles due to in-plane motions, to name just a few sources of error. A summary of the main measurement uncertainties of planar PIV in pipe flow is presented by Ayati et al. (2014). While it was important to use water droplets as seeding particles in the gas phase, it is noted that their light scattering properties and small size (relative to the field of view of the cameras) are not ideal for PIV, as they are prone to induce peak-locking effects, where integer values of the pixel displacements are over-represented by the cross-correlation calculations. In the present work, a validation of the 2D PIV setup, and the application of the water droplet seeding particles, was performed by comparing the single-phase flow of air with DNS results by Wu and Moin (2008). Example results are presented in figure 2.7, further details are presented in Appendix A of paper I.

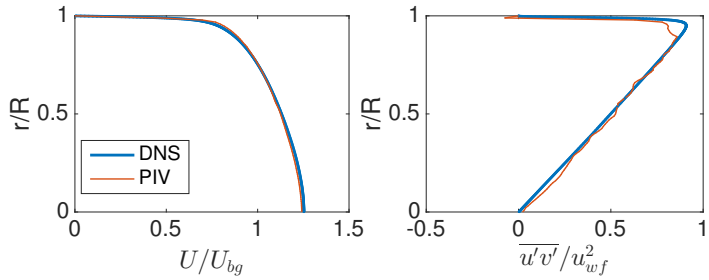

Figure 2.7: Comparison of 2D PIV results of single-phase air flow with DNS results by Wu and Moin (2008). Results from pipe centerline to top wall.

2.2.1.2 Simultaneous two-phase PIV

The simultaneous two-phase PIV (S2P-PIV) method introduced by Ayati (2015) (ref. section 1.2.4) is used in paper IV and V of the present thesis. The method is an extension of the standard PIV technique, as separate cameras are used to acquire images and two-dimensional velocity fields for the gas and liquid phases, which are illuminated from above by a single double-pulsed laser. A schematic illustration of the technique is presented in figure 2.8.

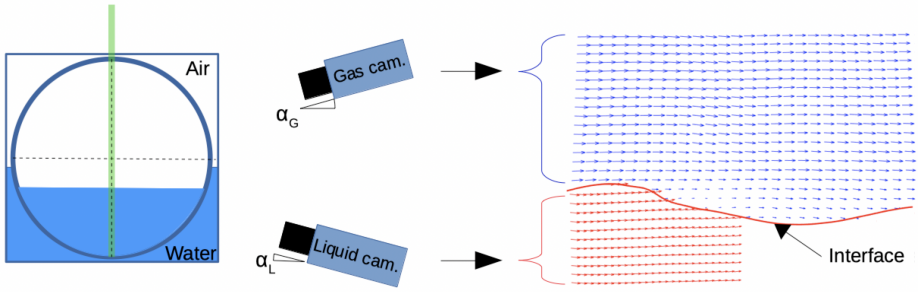

Figure 2.8: Schematic illustration of the S2P-PIV setup and resulting two-dimensional velocity field for the gas (blue vectors) and liquid (red vectors) phase. Red line indicates interface.

Limitations of the S2P-PIV technique applied include: (i) the use of a single (common) Δt for the exposure of the gas and liquid phases; (ii) refraction of the laser light sheet as it enters the liquid phase; (iii) the need for the cameras to be tilted at an angle relative to the pipe centerline, due to the crescent shape of the waves and the wetting of the pipe by passing crests.

Limitation (i) and (ii) imply that the ratio of the gas and liquid velocities should not be too large (and/or that the field of view of the cameras are adjusted independently, as indicated in figure 2.8), to ensure that the particle displacement (in pixels/Δt) in both the gas and liquid phase is suitable for accurate cross-correlation, and that the spanwise gradients of the interface elevation are not too large, as this would significantly modify the position of the laser light sheet in the liquid phase. Considering these limitations, it is clear that the method is most suitable for the smooth and 2D-wave regime of stratified flow, and it will only be applied to these regimes in the present thesis. The error source associated with point (iii) will be discussed in more detail towards the end of this section.

The S2P-PIV measurements by Ayati (2015) are used in paper II (considering only the air-phase velocity fields), while new S2P-PIV measurements performed are presented in paper IV and V. Compared with the measurements performed by Ayati (2015), a number of modifications and improvements were made to acquire higher quality PIV data, and to enable new analysis techniques to be applied to the S2P-PIV data presented:

- Ayati (2015) employed the same optical correction box used in the present work, filled with isopar. Replacing the isopar with water, and reducing the liquid level to approximately 50% (so that only the liquid-phase PIV camera looked through the liquid phase in the optical correction box, see figure 2.8) significantly improved the gas-phase PIV images.
- The liquid-phase camera field of view (FOV) was reduced relative to the gas-phase FOV (indicated in figure 2.8). This ensured that the ratio of the gas- and liquid-phase particle displacements (in pixels/Δt) was reduced.
- The angles of the liquid- and gas-phase cameras were modified.
- Scheimpflug adaptors were added to the PIV cameras to ensure that the full pipe cross section was in focus, despite the high downward/upward looking angles of the cameras.
- Thin strips of black tape were placed on the inside of the pipe to remove reflections introduced by the interface and the pipe walls.
- Fluorescent liquid particles were combined with a gas-phase bandpass filter (centered at the wavelength of the laser light) to improve PIV accuracy near the interface (see paper IV for details).
- A third 'large-field-of-view' camera was applied to measure the instantaneous interface elevation extending outside the PIV FOV. This enables instantaneous interface statistics of a full wave profile to be coupled with velocity measurements performed over a smaller section of the wave.
- A system was designed to trigger the PIV acquisition as waves passed the PIV section, enabling conditional sampling of the velocity fields (details in paper IV).

Prior to the measurements, a coordinate system was inserted into the pipe centerline (coincident with the laser sheet) and nonlinear coordinate transforms (from pixel to 'world' coordinates) were created for each camera applied. When imaging the coordinate system by the liquid-phase camera, the pipe was filled with water. A semi-circular mounting frame was designed and 3D-printed with a mini jack lift that could be extended to secure the coordinate system in position, ensuring that the coordinate system did not move as water was introduced. The optical correction box and coordinate system is presented in figure 2.9. The gas-liquid interface was detected based on gradients in the light intensity observed by either the gas-phase PIV camera (paper II), or by a designated interface detection camera (paper III, IV, V). The interface was transferred to the PIV images by the coordinate transforms, and the regions above/below the detected interface were masked prior to the cross-correlation procedure (see paper IV for further details).

Towards the end of the doctoral work, it was realized that the oblique viewing angle of the PIV cameras introduced an error source which was not previously analyzed in work with the S2P-PIV technique. This error source is present

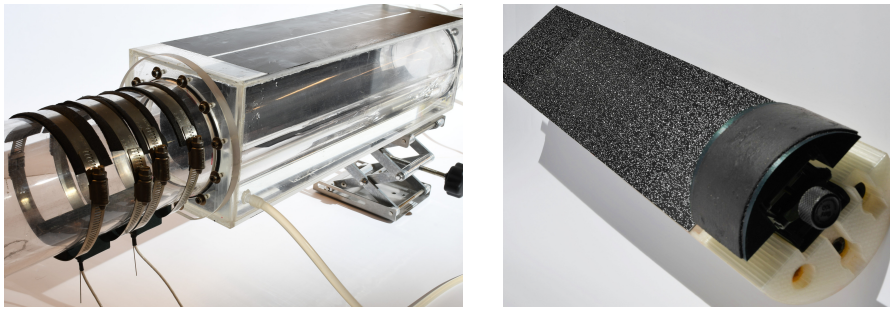

Figure 2.9: Left: Optical correction box used. Right: Coordinate system with mounting frame used for 2D PIV calibration.

whenever a camera tilted relative to the normal of the laser plane is used to evaluate 2D PIV from a three-dimensional flow. Considering the gas-phase camera tilted at an angle α_G relative to the normal of the laser light sheet (ref. figure 2.8), an in-plane velocity v_z would be interpreted as a velocity in the vertical (y) direction, with the magnitude $v_z \tan(\alpha_G)$. As the method is applied only in the centerplane of the pipe, there are no mean in-plane velocities which would cause a bias in the mean vertical velocity profile. Turbulent in-plane velocities will however influence the instantaneous velocity profiles, and turbulent statistics (vertical component). The most notable impacts of this error source in the present work are assessed to be:

- Vertical component of instantaneous vector plots, and instantaneous vorticity (such as figure 11 in paper II, figure 8 and 9 in paper III and figure 5 in paper V) are influenced by $v_z \tan(\alpha)$.
- Root-mean-squared (rms) vorticity on the leeward side of the waves, used to detect signs of wave breaking (paper III, IV and V) and airflow separation (paper IV, V) will have been influenced, as turbulent in-plane motions will add to the rms vorticity.

Overall, the error associated with the oblique viewing angle is not assessed to influence any of the main findings in the present work, but it should be considered for future analysis, especially as turbulent statistics from S2P-PIV results are used to validate numerical models (e.g. in the work of Chinello et al. (2019), analyzing the data of Ayati (2015)).

Quantifying the overall uncertainties related to the S2P-PIV technique is difficult, as some of the sources of uncertainty are directly linked to the presence of the two-phase flow (such as intermittent light reflections from the interface, refraction of the light through the interface and the interface detection procedure), which a single-phase validation (like the one presented in figure 2.7) will not evaluate. In the present work, the S2P-PIV methodology is applied to identify

specific events, such as wave breaking and signs of intermittent airflow separation, where the velocity field over a larger section of the wave is used. Hence, small localized errors will not dominate the evaluation of the physical processes. For such studies, the S2P-PIV technique is assessed to provide valuable new insight into the simultaneous flow of air and water. Further development of the method should include the use of separate laser pulses for the gas and liquid phases (which has already been applied by Birvalski (2015) in a similar setup), and the use of stereoscopic PIV to evaluate (and avoid the erroneous influence of) the in-plane velocity component. This will however significantly enhance the complexity of the method, and introduce new sources of error.

2.2.1.3 Stereoscopic PIV

Stereoscopic PIV applies many of the same principles as standard planar PIV, together with a stereoscopic viewing arrangement of two cameras to obtain all three velocity components on a two-dimensional plane. The method is often referred to as 3C-2D PIV. Details of stereoscopic PIV has been presented by Prasad (2000), Raffel et al. (2018), and Soloff et al. (1997). Here, only the fundamental part of the geometric reconstruction of the 3-C velocity field from the two 2D measurements are described.

Consider a light sheet in the XY-plane, and a camera arrangement as indicated in figure 2.10. The cameras are tilted at an angle α in the XZ-plane relative to the Z-axis, and at an angle β in the YZ-plane. The two cameras observe the displacement $\vec{V}$ as (u_1,v_1) and (u_2,v_2) for camera 1 and 2 respectively. The components of $\vec{V}$ can then be evaluated as (Raffel et al., 2018):

$$U = \frac{u_1 \tan\alpha_2 + u_2 \tan\alpha_1}{\tan\alpha_1 + \tan\alpha_2}, \tag{2.1}$$

$$V = \frac{v_1 \tan\beta_2 + v_2 \tan\beta_1}{\tan\beta_1 + \tan\beta_2}, \tag{2.2}$$

$$W = \frac{u_1 - u_2}{\tan\alpha_1 + \tan\alpha_2}. \tag{2.3}$$

Stereoscopic PIV has previously been used to evaluate the velocity components in the cross-section of single-phase pipe flows by Van Doorne and Westerweel (2007) and in the liquid phase of partially filled pipes by Henry et al. (2018). Common for these investigations is that stereoscopic PIV is performed in the liquid phase. In paper I, stereoscopic PIV is applied to the air phase of stratified air-water pipe flow. To the authors' knowledge, this is the first time stereoscopic PIV has been applied to measure velocity fields in the gas phase of a single- or two-phase pipe flow.

In paper I, stereoscopic PIV is performed using LaVision DaVis 10. As the curved pipe geometry introduces optical distortions, a simple pinhole camera model is not suitable, and a third order polynomial fitted to multiple levels of a translated calibration grid is applied to convert from pixel locations to 'world' coordinates. The stereoscopic PIV setup was validated by comparing

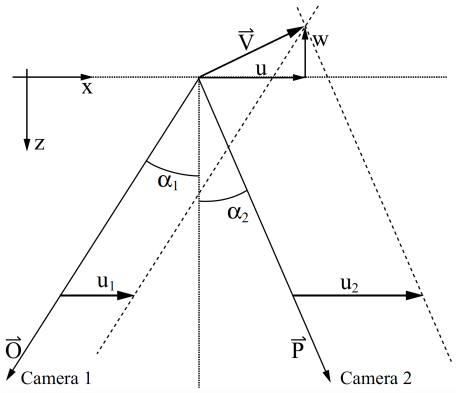

Figure 2.10: Stereo viewing geometry in XZ-plane. Reprinted from Raffel et al. (2018), by permission from Springer Nature.

results from single phase experimental results with DNS from Wu and Moin (2008). Example calibration images and velocity fields are presented in figure 2.11, while details are presented in Appendix B of paper I. It is noted that errors in the in-plane velocity components, assessed to be a result of inaccuracies in the calibration, were observed and corrected for (see paper I for details).

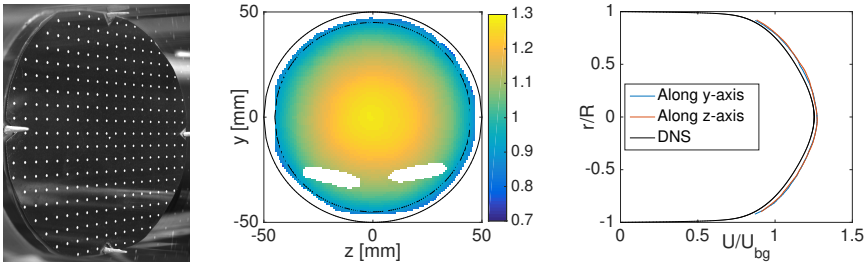

a) b) c)

Figure 2.11: a) Stereoscopic calibration grid as observed by one of the two PIV cameras. b-c) Results for U/U_{bg} from stereoscopic PIV validation, and comparison with DNS results by Wu and Moin (2008) (c).

2.2.1.4 PIV applied to dilute air-sand flow

While conventional PIV relies on the use of passive tracer particles to measure the fluid flow velocity, the cross-correlation technique can also be applied on active particles, which due to their size and/or density difference to the ambient fluid do not passively follow the fluid flow. In paper VII, the standard planar PIV technique is modified to evaluate the mean velocity profiles of dilute sand particles in an air-sand pipe flow experiment.

The paper documents the work conducted as part of a paid industry project for TechnipFMC, focusing on the erosion rates of gas-solid pipe flows. It is noted that the PIV technique has also previously been used to evaluate the particle velocity in air-sand flows, with the focus on erosion rates due to particle impingement (Arabnejad et al., 2015; Lin et al., 2018; Vieira et al., 2016).

While somewhat separated from the rest of this thesis, the paper illustrates how the PIV technique can be applied to study the solid phase of particle-laden pipe flows. In the petroleum industry, stratified gas-liquid flows are often accompanied by solid particles, which pose a challenge due to erosion. It is noted that the S2P-PIV technique can be extended to simultaneously measure the gas, liquid and solid phase immersed in the gas-phase of stratified flow, if separate cameras are used for the three phases, and if fluorescent PIV particles are used in the air phase, enabling filtration of the signal from the gas-phase PIV particles and the solid material.

2.2.2 Interface elevation measurements

2.2.2.1 Interface detection in the PIV section

As PIV is performed above/below a wavy gas-liquid interface, it is necessary to detect the instantaneous interface elevation in the PIV images, and to mask the regions below/above the detected interface for the gas and liquid phase PIV images respectively.

The interface was detected either directly from the gas-phase PIV camera (paper II and VI), or by a designated interface detection camera, focused on the interface III, IV and V). The interface was detected by separating the image into vertical sections, identifying the gradients in light intensity associated with the gas-liquid interface (example images shown in paper IV). Detecting the gas-liquid interface based on the Radon transform of the liquid-phase images, as proposed by Sanchis and Jensen (2011) was also tested during the work, but found to be less reliable.

2.2.2.2 Conductance wave gauges

Conductance wave gauges (see figure 2.12) were used to measure the interface elevation in the pipe centerline considering the 2D wave regime in the two-phase pipe loop. The wave gauge consists of four parallel wire probes, made from 0.3 mm thick platinum wires, separated by 4 mm. However, in the present work only two parallel probes in the pipe centerline, separated by 6 cm in the streamwise direction are used. The interface elevation was sampled at a frequency of 500 Hz, enabling evaluation of the power spectrum of the interface elevation, as well as the mean water level and *rms* interface elevation. Further details of the wave gauge are presented by Ayati et al. (2015).

The wave gauges were calibrated positioned in the main pipe section. The end of the pipe section was lifted to control the liquid holdup in the pipe, while water was recirculated slowly through the system. A separate ultrasonic wave probe (U-Gage S18U) was attached to the top of the pipe, just upstream of the

wave gauge. This measured the height of the air gap between the water level and the top of the pipe (and thus indirectly the liquid level) simultaneously with the voltage readouts from the conductance wave probes (note that the ultrasonic wave probe was first calibrated by traversing it relative to a block outside of the pipe loop). 10 liquid levels covering the full range of liquid heights (crest to trough) for a specific experiment were measured, and a third order polynomial was fitted to the relation between the measured liquid level, and probe voltage readout.

While the ultrasonic wave probe was found to yield reliable measurements when the water surface was flat, considerable dropouts were observed when it was tested in the wavy regime. Hence, it could not be used to measure the instantaneous surface elevation directly.

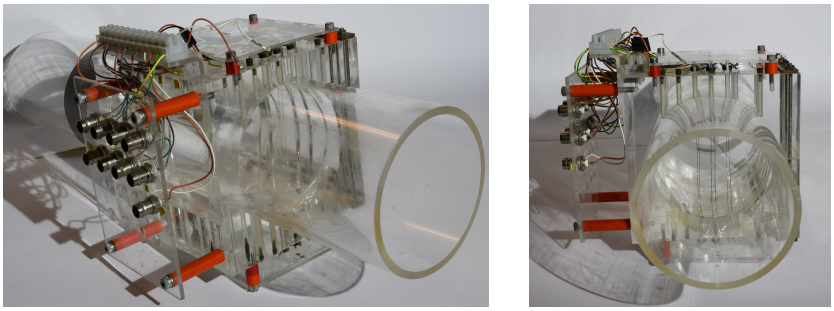

Figure 2.12: Images of the conductance wave probes used.

2.2.2.3 Ultrasonic wave probes

In the wind-wave flume, the surface elevation was measured using an array of four ultrasonic wave probes (Ultralab USS 02/HFP), placed along the centerline of the tank. A known disadvantage to ultrasonic wave probes is that they are unable to measure very steep waves, as the emitted signal is not reflected back to the probe. This limited the accuracy of the ultrasonic wave probes for the steepest waves under investigation, and meant that the probes could not reliably measure breaking waves.

2.2.3 Phase averaging of PIV results

As wind blows over waves, and as waves propagate on a turbulent liquid layer, velocity fluctuations measured in a single point (in the gas or liquid phase) are generated by two different mechanisms: the wave-coherent velocity fluctuations and turbulence. Separation of the wave- and turbulence-induced velocity fluctuations is of interest, as it provides insight into the mechanisms that govern wave growth and momentum transfer within and between the phases.

Considering measurements of a flow property f at the position $\boldsymbol{x}$, influenced by a monochromatic wave and turbulent fluctuations, the instantaneous velocity

component $f(\boldsymbol{x},t)$ can be separated into a time-averaged mean ($\overline{f}$), wave-coherent ($\tilde{f}$) and turbulent (f') component, according to (Hussain and Reynolds, 1970):

$$f(\boldsymbol{x},t) = \overline{f}(\boldsymbol{x}) + \tilde{f}(\boldsymbol{x},t) + f'(\boldsymbol{x},t). \tag{2.4}$$

The wave-coherent fluctuations can be evaluated by subtracting the time-averaged mean from the phase-averaged mean ($\langle f \rangle$), defined as

$$\langle f(\boldsymbol{x},t)\rangle = \lim_{N\to\infty} \frac{1}{N+1} \sum_{n=0}^{N} f(\boldsymbol{x}, t+n\tau), \tag{2.5}$$

where τ is the period of the wave. The separation presented in equation 2.4 is only valid when there is only a single wave component, or when all the wave components present are a multiple of the lowest frequency component (Nordsveen, 1995). This is obviously not the case for wind generated waves in either the open ocean or in a two-phase pipe flow.

Evaluating the airflow above wind-waves, there are two main approaches used to separate the wave and turbulence induced fluctuations. Either the wave induced velocities are assumed to be related in some way to the interface elevation, or the frequency spectra of the wave and turbulence components are assumed to be sufficiently distinct, enabling the use of bandpass filters to separate the two components (Peirson, 1998). The second approach is problematic, as the length scale of the waves and the largest turbulent eddies are assessed to be of similar order in a two-phase pipe flow (note however that a variation of this approach is used to separate the wave induced fluctuations from the small scale turbulent fluctuations due to microscale breaking in paper III). Related to the first approach, the simplest way to separate the wave-induced and turbulent fluctuations is to assume a linear relationship between the wave-coherent component and the instantaneous interface elevation (Benilov et al., 1974; Cheung and Street, 1988). Another approach is to apply the Hilbert transform to the temporal interface elevation measurements, and perform the phase-averaging for constant wave phase (Hristov et al., 1998).

While the above-mentioned techniques consider time-resolved point measurements, the PIV measurements provide low-frequency velocity field data. It is also desirable to describe the phase-averaged flow field within the trough-to-crest region. Considering a simple Cartesian coordinate system, the time-averaged mean air/water velocity will not be defined in this region, as a single point will intermittently be located above/below the interface. Hence, a wave-following coordinate system is required. An illustration of the wave-following coordinate systems (separate coordinate systems in the gas and liquid phase) applied in the present work are presented in figure 2.13. The wave phase θ is based on a zero-crossing procedure, where the crest, trough, zero down/up crossings of an individual wave is defined as 0°, 180°, 90° and 270° respectively, while the phases in between are linearly distributed. This is similar to the procedure used by Birvalski (2015) and Siddiqui and Loewen (2010). An alternative approach based on the spatial Hilbert transform is presented by Buckley and Veron (2016).

The wave-following vertical coordinate ζ is evaluated somewhat differently in the gas and liquid phase, as indicated in figure 2.13.

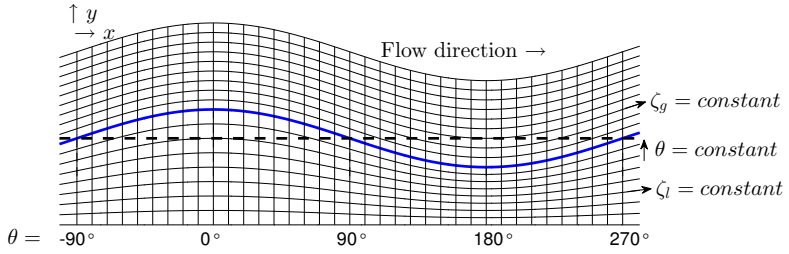

Figure 2.13: Illustration of the wave-following coordinate system used. Blue line indicate interface. Dashed line represents mean water level.

Sampling and averaging a series of instantaneous velocity fields in the (θ, ζ) coordinate system, the phase-averaged velocity field is obtained. This can be used to evaluate the mean (averaged over θ) and wave-coherent velocity fields, and the instantaneous velocity can be decomposed as indicated in equation 2.6. The phase-averaging technique is applied in the gas phase in paper II, liquid phase in paper III, and in both the gas and liquid phases in paper V, considering the 2D wave regime of stratified gas-liquid flow. Full details of the methods are described in each of the papers where the method is used. Here, some of the limitations to the method are discussed.

$$q(x, y, t) = \overline{q}(\zeta) + \tilde{q}(\theta, \zeta) + q'(\theta, \zeta, t) \tag{2.6}$$

The phase-averaging technique applied suffers from the same limitations as the time-resolved approaches described above. As we consider a (relatively) broad banded wave spectrum, the phase-averaged flow field is not representative for all waves, and the deviations from the phase-average will be a combination of turbulent and wave-coherent fluctuations, which are not accurately predicted by the phase-averaging procedure. Hence, the residual fluctuations q' should be interpreted as the sum of turbulence, wave-coherent velocities not accurately filtered by the method, and random measurement errors. As the wave-coherent velocity fluctuations can be considerable compared to the turbulent velocity fluctuations, the method is not assessed to be robust in evaluating turbulent statistics such as phase-averaged Reynolds stresses for the wavy regimes under investigation. A discussion on this topic related to the velocity field below wind generated microscale breaking waves is provided by Siddiqui and Loewen (2007).

While the phase-averaged velocity fields obtained are not representative for all waves, they are considered to provide valuable information on the average flow structure over a representative wave in the system. In the present work, the focus is on comparing the phase-averaged flow fields considering different airflow rates (paper II), and non-breaking vs. breaking waves (paper III and V). For this application, the phase-averaging technique is assessed to provide valuable insights

into the relative differences between the cases under investigation, although direct application of the results should be analyzed with care, considering the range of different wave components present in the system.

Bibliography

Adrian, L., Adrian, R. J., and Westerweel, J. (2011). *Particle image velocimetry*. 30. Cambridge university press.

Ali, I. T. (2017). "CFD Prediction of Stratified and Intermittent Gas-Liquid Two-Phase Turbulent Pipe Flow Using RANS Models". PhD thesis. University of Manchester.

Andritsos, N. and Hanratty, T. J. (1987). "Interfacial instabilities for horizontal gas-liquid flows in pipelines". In: *International journal of multiphase flow* vol. 13, no. 5, pp. 583–603.

Andritsos, N. (1986). "Effect of pipe diameter and liquid viscosity on horizontal stratified flow". PhD thesis. University of Illinois, Urbana.

Arabnejad, H., Mansouri, A., Shirazi, S., and McLaury, B. (2015). "Development of mechanistic erosion equation for solid particles". In: *Wear* vol. 332, pp. 1044–1050.

Ayati, A. A. (2015). "Dynamics of stratified gas/liquid pipe flow". Ph.D. thesis from the University of Oslo. University of Oslo.

Ayati, A. A. and Carneiro, J. N. E. (2018). "Statistical characterization of interfacial waves in turbulent stratified gas-liquid pipe flows". In: *International Journal of Multiphase Flow* vol. 103, pp. 94–105.

Ayati, A. A., Kolaas, J., Jensen, A., and Johnson, G. W. (2014). "A PIV investigation of stratified gas-liquid flow in a horizontal pipe". In: *International Journal of Multiphase Flow* vol. 61, pp. 129–143.

— (2015). "Combined simultaneous two-phase PIV and interface elevation measurements in stratified gas/liquid pipe flow". In: *International Journal of Multiphase Flow* vol. 74, pp. 45–58.

— (2016). "The effect of interfacial waves on the turbulence structure of stratified air/water pipe flow". In: *International Journal of Multiphase Flow* vol. 78, pp. 104–116.

Babanin, A. (2011). *Breaking and dissipation of ocean surface waves*. Cambridge University Press.

Banner, M. L. and Melville, W. K. (1976). "On the separation of air flow over water waves". In: *Journal of Fluid Mechanics* vol. 77, no. 04, pp. 825–842.

Banner, M. L. and Peregrine, D. H. (1993). "Wave breaking in deep water". In: *Annual Review of Fluid Mechanics* vol. 25, no. 1, pp. 373–397.

Banner, M. L. and Phillips, O. M. (1974). "On the incipient breaking of small scale waves". In: *Journal of Fluid Mechanics* vol. 65, no. 4, pp. 647–656.

Banner, M. L. and Morison, R. P. (2016). "On the upper ocean turbulent dissipation rate due to very short breaking wind-waves". In: *arXiv preprint arXiv:1602.06649*.

Belcher, S. E. (1999). “Wave growth by non-separated sheltering”. In: *European journal of mechanics. B, Fluids* vol. 18, no. 3, pp. 447–462.

Belcher, S. E. and Hunt, J. C. R. (1993). “Turbulent shear flow over slowly moving waves”. In: *Journal of Fluid Mechanics* vol. 251, pp. 109–148.

— (1998). “Turbulent flow over hills and waves”. In: *Annual Review of Fluid Mechanics* vol. 30, no. 1, pp. 507–538.

Belt, R., Daalmans, A., and Portela, L. (2012). “Experimental study of particle-driven secondary flow in turbulent pipe flows”. In: *Journal of Fluid Mechanics* vol. 709, pp. 1–36.

Bendiksen, K. H., Maines, D., Moe, R., Nuland, S., et al. (1991). “The dynamic two-fluid model OLGA: Theory and application”. In: *SPE production engineering* vol. 6, no. 02, pp. 171–180.

Benilov, A. Y., Kouznetsov, O., and Panin, G. (1974). “On the analysis of wind wave-induced disturbances in the atmospheric turbulent surface layer”. In: *Boundary-Layer Meteorology* vol. 6, no. 1-2, pp. 269–285.

Birvalski, M. (2015). “Experiments in stratified gas-liquid pipe flow”. PhD thesis. TU Delft, Delft University of Technology.

Birvalski, M., Tummers, M., Delfos, R., and Henkes, R. (2015). “Laminar-turbulent transition and wave-turbulence interaction in stratified horizontal two-phase pipe flow”. In: *Journal of Fluid Mechanics* vol. 780, pp. 439–456.

Bratland, O. (2010). “Pipe flow 2: multi-phase flow assurance”. In: *Ove Bratland Flow Assurance Consulting, Chonburi, Thailand*.

Brennen, C. E. (2005). *Fundamentals of multiphase flow*. Cambridge university press.

Buckley, M. P. and Veron, F. (2016). “Structure of the airflow above surface waves”. In: *Journal of Physical Oceanography* vol. 46, no. 5, pp. 1377–1397.

Cheung, T. K. and Street, R. L. (1988). “The turbulent layer in the water at an air—water interface”. In: *Journal of Fluid Mechanics* vol. 194, pp. 133–151.

Chinello, G., Ayati, A. A., McGlinchey, D., Ooms, G., and Henkes, R. (2019). “Comparison of Computational Fluid Dynamics Simulations and Experiments for Stratified Air-Water Flows in Pipes”. In: *Journal of Fluids Engineering* vol. 141, no. 5.

Dabiri, D. (2006). “Cross-correlation digital particle image velocimetry—a review”. In: *Turbul. ABCM Curitiba*, pp. 155–199.

Donelan, M. A., Babanin, A. V., Young, I. R., and Banner, M. L. (2006). “Wave-follower field measurements of the wind-input spectral function. Part II: Parameterization of the wind input”. In: *Journal of physical oceanography* vol. 36, no. 8, pp. 1672–1689.

Dykhno, L., Williams, L., and Hanratty, T. (1994). “Maps of mean gas velocity for stratified flows with and without atomization”. In: *International journal of multiphase flow* vol. 20, no. 4, pp. 691–702.

"EarthFlows" (2020). *Interface Dynamics in Geophysical Flows - EarthFlows*. Accessed 13.03.2020. URL: http://www.mn.uio.no/geo/english/research/groups/earthflows/index.html.

Espedal, M. (1998). “An experimental investigation of stratified two-phase pipe flow at small inclinations”. PhD thesis. Norwegian University of Science and

Technology (NTNU), Department of Applied Mechanics, Thermo- and Fluid Dynamics.

Farias, P. S. C. (2019). "Experimental characterization of linear interfacial waves in a stratified turbulent gas-liquid pipe flow using Particle Image Velocimetry". PhD thesis. Pontifical Catholic University of Rio de Janeiro (PUC-Rio), Department of Mechanical Engineering.

Gent, P. R. and Taylor, P. A. (1977). "A note on 'separation' over short wind waves". In: *Boundary-Layer Meteorology* vol. 11, no. 1, pp. 65–87.

Goldszal, A. et al. (2007). "LedaFlow 1D: Simulation results with multiphase gas/condensate and oil/gas field data". In: *13th International Conference on Multiphase Production Technology*. BHR Group.

Gyllengahm, S. (2019). "In depth PIV analysis of turbulent single phase pipe flow". MA thesis. Department of Mathematics, University of Oslo.

Hanratty, T. J. and Engen, J. M. (1957). "Interaction between a turbulent air stream and a moving water surface". In: *AIChE Journal* vol. 3, no. 3, pp. 299–304.

Hart, J., Hamersma, P. J., and Fortuin, J. M. H. (1989). "Correlations predicting frictional pressure drop and liquid holdup during horizontal gas-liquid pipe flow with a small liquid holdup". In: *International Journal of Multiphase Flow* vol. 15, no. 6, pp. 947–964.

Henry, C.-H., Cregan Hope, L., Dodds, J. M., Poole, R. J., and Dennis, D. J. (2018). "Partially filled pipes: experiments in laminar and turbulent flow". In: *Journal of Fluid Mechanics* vol. 848, pp. 467–507.

Hinze, J. (1967). "Secondary currents in wall turbulence". In: *The Physics of Fluids* vol. 10, no. 9, S122–S125.

Hristov, T., Friehe, C., and Miller, S. (1998). "Wave-coherent fields in air flow over ocean waves: Identification of cooperative behavior buried in turbulence". In: *Physical review letters* vol. 81, no. 23, p. 5245.

Hussain, A. K. M. F. and Reynolds, W. C. (1970). "The mechanics of an organized wave in turbulent shear flow". In: *Journal of Fluid Mechanics* vol. 41, no. 2, pp. 241–258.

Ishii, M. and Mishima, K. (1984). "Two-fluid model and hydrodynamic constitutive relations". In: *Nuclear Engineering and design* vol. 82, no. 2-3, pp. 107–126.

Janssen, P. (2004). *The interaction of ocean waves and wind*. Cambridge University Press.

Jeffreys, H. (1925). "On the formation of water waves by wind". In: *Proc. R. Soc. Lond. A* vol. 107, no. 742, pp. 189–206.

Jessup, A., Zappa, C. J., and Yeh, H. (1997). "Defining and quantifying microscale wave breaking with infrared imagery". In: *Journal of Geophysical Research: Oceans* vol. 102, no. C10, pp. 23145–23153.

Kawai, S. (1982). "Structure of air flow separation over wind wave crests". In: *Boundary-Layer Meteorology* vol. 23, no. 4, pp. 503–521.

Kihara, N., Hanazaki, H., Mizuya, T., and Ueda, H. (2007). "Relationship between airflow at the critical height and momentum transfer to the traveling waves". In: *Physics of Fluids* vol. 19, no. 1, p. 015102.

Kowalski, J. (1987). "Wall and interfacial shear stress in stratified flow in a horizontal pipe". In: *AIChE journal* vol. 33, no. 2, pp. 274–281.

Lighthill, M. (1962). "Physical interpretation of the mathematical theory of wave generation by wind". In: *Journal of Fluid Mechanics* vol. 14, no. 3, pp. 385–398.

Lin, N., Arabnejad, H., Shirazi, S., McLaury, B., and Lan, H. (2018). "Experimental study of particle size, shape and particle flow rate on erosion of stainless steel". In: *Powder Technology* vol. 336, pp. 70–79.

Mandhane, J., Gregory, G., and Aziz, K. (1974). "A flow pattern map for gas—liquid flow in horizontal pipes". In: *International Journal of Multiphase Flow* vol. 1, no. 4, pp. 537–553.

Meknassi, F., Benkirane, R., Liné, A., and Masbernat, L. (2000). "Numerical modeling of wavy stratified two-phase flow in pipes". In: *Chemical engineering science* vol. 55, no. 20, pp. 4681–4697.

Melville, W. K. (1996). "The role of surface-wave breaking in air-sea interaction". In: *Annual review of fluid mechanics* vol. 28, no. 1, pp. 279–321.

Miles, J. (1993). "Surface-wave generation revisited". In: *Journal of Fluid Mechanics* vol. 256, pp. 427–441.

Miles, J. W. (1957). "On the generation of surface waves by shear flows". In: *Journal of Fluid Mechanics* vol. 3, no. 2, pp. 185–204.

Newton, C. H. and Behnia, M. (2001). "A numerical model of stratified wavy gas–liquid pipe flow". In: *Chemical Engineering Science* vol. 56, no. 24, pp. 6851–6861.

Nikuradse, J. (1926). Ph.D. thesis, Göttingen. Also as Verein Deutscher Ingenieure Forschungsheft 281, Berlin (1926).

Nordsveen, M. (1995). "Modelling of wave and turbulence induced secondary currents in stratified duct flow". PhD thesis. University of Oslo, Oslo, Norway.

Optolution (2020). *Measurement principle of the Particle Image Velocimetry (PIV)*. Accessed 17.03.2020. URL: https://www.optolution.com/en/measuring-principles/piv-principle/.

Paras, S., Vlachos, N., and Karabelas, A. (1998). "LDA measurements of local velocities inside the gas phase in horizontal stratified/atomization two-phase flow". In: *International journal of multiphase flow* vol. 24, no. 4, pp. 651–661.

Peirson, W. L. (1998). "On the dynamics and kinetics of microscale-breaking wind waves." PhD thesis. University of New South Wales, Australia.

Peregrine, D. H. (1983). "Breaking waves on beaches". In: *Annual Review of Fluid Mechanics* vol. 15, no. 1, pp. 149–178.

Perlin, M., Choi, W., and Tian, Z. (2013). "Breaking waves in deep and intermediate waters". In: *Annual review of fluid mechanics* vol. 45, pp. 115–145.

Pexels (2015). Accessed 02.04.2020. URL: https://www.pexels.com/photo/landscape-photograph-of-body-of-water-1001682/.

Phillips, O. M. (1957). "On the generation of waves by turbulent wind". In: *Journal of fluid mechanics* vol. 2, no. 5, pp. 417–445.

Prandtl, L. (1927). *Turbulent flow*. International Congress for Applied Mechanics, Zurich 1926. Also as N.A.C.A. Tech Memo 435.

Prasad, A. K. (2000). “Stereoscopic particle image velocimetry”. In: *Experiments in fluids* vol. 29, no. 2, pp. 103–116.

Raffel, M., Willert, C. E., Scarano, F., Kähler, C. J., Wereley, S. T., and Kompenhans, J. (2018). *Particle image velocimetry: a practical guide*. Springer.

Reul, N., Branger, H., and Giovanangeli, J.-P. (2008). “Air flow structure over short-gravity breaking water waves”. In: *Boundary-layer meteorology* vol. 126, no. 3, pp. 477–505.

Sanchis, A., Johnson, G. W., and Jensen, A. (2011). “The formation of hydrodynamic slugs by the interaction of waves in gas-liquid two-phase pipe flow”. In: *International Journal of Multiphase Flow* vol. 37, no. 4, pp. 358–368.

Sanchis, A. and Jensen, A. (2011). “Dynamic masking of PIV images using the Radon transform in free surface flows”. In: *Experiments in fluids* vol. 51, no. 4, pp. 871–880.

Schulkes, R. (2011). *An introduction to Multiphase Pipe Flow*.

Siddiqui, M. H. K. and Loewen, M. R. (2007). “Characteristics of the wind drift layer and microscale breaking waves”. In: *Journal of Fluid Mechanics* vol. 573, pp. 417–456.

— (2010). “Phase-Averaged Flow Properties Beneath Microscale Breaking Waves”. In: *Boundary-Layer Meteorology* vol. 134, no. 3, pp. 499–523.

Smith, L. (2018). “Experiments of Breaking Waves in Pipes and Flumes”. PhD thesis. University of Oslo, Norway.

Soloff, S. M., Adrian, R. J., and Liu, Z.-C. (1997). “Distortion compensation for generalized stereoscopic particle image velocimetry”. In: *Measurement science and technology* vol. 8, no. 12, p. 1441.

Spedding, P. L. and Hand, N. P. (1997). “Prediction in stratified gas-liquid co-current flow in horizontal pipelines”. In: *International journal of heat and mass transfer* vol. 40, no. 8, pp. 1923–1935.

Spedding, P. L. and Spence, D. R. (1993). “Flow regimes in two-phase gas-liquid flow”. In: *International journal of multiphase flow* vol. 19, no. 2, pp. 245–280.

Speziale, C. G. (1982). “On turbulent secondary flows in pipes of noncircular cross-section”. In: *International Journal of Engineering Science* vol. 20, no. 7, pp. 863–872.

Strand, O. (1993). “An experimental investigation of stratified two-phase flow in horizontal pipes”. PhD thesis. University of Oslo, Oslo, Norway.

Sullivan, P. P., Banner, M. L., Morison, R. P., and Peirson, W. L. (2018). “Turbulent Flow over Steep Steady and Unsteady Waves under Strong Wind Forcing”. In: *Journal of Physical Oceanography* vol. 48, no. 1, pp. 3–27.

Sullivan, P. P. and McWilliams, J. C. (2010). “Dynamics of winds and currents coupled to surface waves”. In: *Annual Review of Fluid Mechanics* vol. 42.

Sutherland, P. and Melville, W. K. (2013). “Field measurements and scaling of ocean surface wave-breaking statistics”. In: *Geophysical Research Letters* vol. 40, no. 12, pp. 3074–3079.

Sutherland, P. and Melville, W. K. (2015). "Field measurements of surface and near-surface turbulence in the presence of breaking waves". In: *Journal of Physical Oceanography* vol. 45, no. 4, pp. 943–965.

Taitel, Y. and Dukler, A. (1976). "A model for predicting flow regime transitions in horizontal and near horizontal gas-liquid flow". In: *AIChE journal* vol. 22, no. 1, pp. 47–55.

Tulin, M. P. and Landrini, M. (2001). "Breaking waves in the ocean and around ships". In: *23rd Symposium on Naval Hydrodynamics*. The National Academies Press., pp. 713–745.

Turney, D. E. (2016). "Coherent motions and time scales that control heat and mass transfer at wind-swept water surfaces". In: *Journal of Geophysical Research: Oceans* vol. 121, no. 12, pp. 8731–8748.

Tzotzi, C. and Andritsos, N. (2013). "Interfacial shear stress in wavy stratified gas-liquid flow in horizontal pipes". In: *International Journal of Multiphase Flow* vol. 54, pp. 43–54.

Van Doorne, C. and Westerweel, J. (2007). "Measurement of laminar, transitional and turbulent pipe flow using stereoscopic-PIV". In: *Experiments in Fluids* vol. 42, no. 2, pp. 259–279.

Vestøl, S. (2013). "Detailed measurements of gas/liquid flow with low liquid fractions in horizontal and near horizontal pipes". PhD thesis. Norwegian University of Science and Technology (NTNU), Faculty of Engineering Science and Technology, Department of Energy and Process Engineering.

Vieira, R. E., Mansouri, A., McLaury, B. S., and Shirazi, S. A. (2016). "Experimental and computational study of erosion in elbows due to sand particles in air flow". In: *Powder technology* vol. 288, pp. 339–353.

Wallis, G. B. (1969). *One-dimensional two-phase flow*. McGraw-Hill.

Weissman, M. A. (1986). "Observations and measurements of air flow over water waves". In: *Wave dynamics and radio probing of the ocean surface*. Springer, pp. 335–352.

Westerweel, J., Elsinga, G. E., and Adrian, R. J. (2013). "Particle image velocimetry for complex and turbulent flows". In: *Annual Review of Fluid Mechanics* vol. 45, pp. 409–436.

Wu, X. and Moin, P. (2008). "A direct numerical simulation study on the mean velocity characteristics in turbulent pipe flow". In: *Journal of Fluid Mechanics* vol. 608, pp. 81–112.

Xiao, J. J. and Shoham, O. (1991). "Evaluation of interfacial friction factor prediction methods for gas/liquid stratified flow". In: *SPE Annual Technical Conference and Exhibition*. Society of Petroleum Engineers.

Young, I. R. (1999). *Wind generated ocean waves*. Elsevier.

Chapter 3

Summary of Papers

Paper I

P. Vollestad, L. Angheluta and A. Jensen, 'Experimental study of secondary flows above rough and flat interfaces in horizontal gas-liquid pipe flow'. In: *International Journal of Multiphase Flow* **125** (2020), 103235.
DOI: 10.1016/j.ijmultiphaseflow.2020.103235.

This paper investigates secondary flows in the gas phase above rough (considering the pebbly and 3D wave regime) and flat interfaces in air-water pipe flow, using planar and stereoscopic PIV.

Paper II

P. Vollestad, A. A. Ayati, L. Angheluta, J. H. LaCasce and A. Jensen, 'Experimental investigation of airflow above waves in a horizontal pipe'. In: *International Journal of Multiphase Flow* **110** (2019), pp. 37–49.
DOI: 10.1016/j.ijmultiphaseflow.2018.08.008.

Analysis of the airflow over waves within the 2D wave regime. Conditional phase-averaging of velocity fields and swirling events reveal changes in the airflow structure as the gas flow rate is increased into the 'amplitude saturation' regime.

Paper III

P. Vollestad, A. A. Ayati and A. Jensen, 'Microscale wave breaking in stratified air-water pipe flow'. In: *Physics of Fluids* **31** (2019), 032101.
DOI: 10.1063/1.5082607.

PIV analysis of the liquid phase in the 2D wave regime. Analysis of the inception of, and modifications of the flow structure resulting from microscale wave breaking.

Paper IV

P. Vollestad and A. Jensen, 'Microbreaking and airflow separation in stratified air-water pipe flow - PIV setup and initial results'. In: *Proceedings of the 13th International Symposium on Particle Image Velocimetry* (2019), pp. 1435–1444.

Presents the experimental setup and initial experimental results from the modified simultaneous two-phase PIV setup.

Paper V

P. Vollestad, A. A. Ayati and A. Jensen, 'Experimental investigation of intermittent airflow separation and microscale wave breaking in wavy two-phase pipe flow'. In: *Journal of Fluid Mechanics* **878** (2019), pp. 796–819.
DOI: 10.1017/jfm.2019.660.

Simultaneous two-phase PIV measurements, analyzing the relationship between active microscale wave breaking and the airflow structure above the waves in two-phase pipe flow. At a moderate U_{sg}, the sheltered region is reduced due to active breaking. At higher gas velocities, the geometric properties of the waves are found to govern the airflow structure.

Paper VI

P. Vollestad and A. Jensen, 'Modification of the airflow structure due to wave breaking on a submerged topography'. Under review.

Results from the modified wind-wave flume at the Hydrodynamics Laboratory. An analysis of the extent of the sheltered region of steep breaking and non-breaking waves is presented. Results indicate that the geometrical properties, and not state state of breaking, governs the sheltered region.

Paper VII

P. Vollestad and A. Jensen, 'A note on PIV measurements of dilute air-sand pipe flow'. In preparation.

Documents the measurement setup, analysis method and main results from a PIV analysis of dilute air-sand pipe flow, performed for TechnipFMC. The plan is to combine this note with results from CFD (performed by TechnipFMC) for a future publication.

The published papers are reprinted with permission from Elsevier, American Institute of Physics and Cambridge University Press.

Papers

Paper I

Experimental study of secondary flows above rough and flat interfaces in horizontal gas-liquid pipe flow

Petter Vollestad, Luiza Angheluta, Atle Jensen

Published in *International Journal of Multiphase Flow* **125** (2020), 103235.
DOI: 10.1016/j.ijmultiphaseflow.2020.103235.

Experimental study of secondary flows above rough and flat interfaces in horizontal gas-liquid pipe flow

P. Vollestad[1,*], L. Angheluta[2], A. Jensen[1]

[1] *Department of Mathematics, University of Oslo, P. O. Box 1053, 0316 Oslo, Norway*

[2] *PoreLab, The Njord Centre, Department of Physics, University of Oslo, P. O. Box 1048, 0316 Oslo, Norway*

[*] *Corresponding author: pettervo@math.uio.no*

Abstract

We perform an experimental analysis of stratified, co-current gas-liquid flow in a straight pipe, with the aim of investigating secondary flow structures in the gas-phase. Planar PIV (particle image velocimetry) of the pipe centerline as well as stereoscopic PIV of the pipe cross section is performed, considering cases where the interface is either rough (wavy) or flat.

Results demonstrate that the interface morphology determines the direction of the secondary flow patterns. Over a flat interface, the secondary flow cells are directed up along the pipe centerline and down along the pipe walls. When the interface is rough (wavy), the direction of the secondary flow cells is reversed. Normalized by the peak axial velocity, the vertical velocity profile in the pipe centerline is seen to collapse to a common curve when the interface is flat, while results indicate that the normalized strength of the secondary flows increase with increasing surface roughness.

An assessment of the Reynolds stresses in the cross section is performed, and the direction of the secondary flow cells are found to be well predicted by the dominant gradients of the radial and circumferential Reynolds stresses (τ_{rr} and $\tau_{\theta\theta}$) in the radial and circumferential direction respectively.

Keywords: Gas-liquid pipe flow, Stratified flow, Secondary flows, Particle image velocimetry

1. Introduction

As a turbulent fluid flow is directed through a pipe or channel, it is possible (and in fact common) to induce secondary flows (i.e. mean-flow vortical structures perpendicular to the axial flow direction), which can impact the axial velocity profile as well as the pressure drop through the pipe/channel. Secondary flows are conventionally divided into secondary flows of the first and second kind (Belt *et al.*, 2012; Bradshaw, 1987), where the first kind refers to secondary flows driven by pressure variations in the cross-section, e.g. flow in a bend, while secondary flows of the second kind are generated by turbulence anisotropy and divergence of the Reynolds stresses in the cross-section. In this work we consider a straight pipe section, and hence secondary flows of the second kind, which were first documented by Prandtl (1927). Prandtl (1927) observed that in a turbulent flow through non-circular channels, fluid is flowing into corners along the middle of the corner angle, and out of the corners along the channel walls. Such secondary flows through non-circular pipes have later been studied by Speziale (1982), and are typically found to be 1-3% of the axial mean velocity in magnitude. While Prandtl (1927) and Speziale (1982) considered channels of uniform roughness, secondary flows can also be generated due to non-uniform distribution of the surface roughness of the pipe/channel walls (Van't Westende *et al.*, 2007; Hinze, 1967, 1973).

In two-phase pipe flow through a straight circular pipe, secondary flows in the gas phase are generated both from the non-circular cross section occupied by the gas phase, and by variations in

surface roughness/shear between the pipe walls and the gas-liquid interface (Dykhno *et al.*, 1994). Secondary flows have been observed in the gas-phase of stratified (Birvalski, 2015; Dykhno *et al.*, 1994; Liné *et al.*, 1996; Meknassi *et al.*, 2000; Strand, 1993) and annular (Flores *et al.*, 1995) flow regimes. Droplet deposition/atomization can also induce secondary flows due to uneven droplet deposition in the cross-section (Dykhno *et al.*, 1994; Belt *et al.*, 2012; Alletto & Breuer, 2013).

As shown by Speziale (1982) and Belt *et al.* (2012), secondary flows of the second kind result from the divergence of Reynolds stresses on the plane perpendicular to the axial flow direction. Van't Westende *et al.* (2007) studied the flow in a pipe with varying wall roughness, imposing the maximum roughness on the pipe bottom and minimum at the top. In this configuration, $\overline{u'_\theta u'_\theta}$ (where u'_θ is the velocity fluctuation in the circumferential direction) varies along the pipe wall similarly the wall roughness, resulting in a secondary flow directed from the high roughness/$\overline{u'_\theta u'_\theta}$ zone (pipe bottom) towards the low roughness/$\overline{u'_\theta u'_\theta}$ zone (top of the pipe) along the pipe walls, and down through the pipe center. Numerical results by Van't Westende *et al.* (2007) are in agreement with experimental findings by Darling & McManus (1968). Belt *et al.* (2012) and Alletto & Breuer (2013) also identified the circumferential gradient of $\overline{u'_\theta u'_\theta}$ as the driving force of the secondary flows for particle laden pipe flow.

As the gas phase of stratified gas-liquid pipe flow experiences variable roughness around its circumference, there are clear analogies to the single phase flow studied by Van't Westende *et al.* (2007). However, characteristics of interfacial waves and the non-circular gas cross section may change the secondary flows in a qualitative manner. Liné *et al.* (1996) investigated stratified flow in a rectangular channel. Here, the wave amplitude, and hence the interfacial roughness, increased towards the channel walls, resulting in secondary flows from the walls towards the center, and upwards at the channel center. Similar qualitative behavior of the secondary flow structure was observed by Dykhno *et al.* (1994), Belt *et al.* (2012) and Alletto & Breuer (2013), studying flows with significant atomization. However, analyzing stratified pipe flow without atomization, Dykhno *et al.* (1994) found that the secondary flows were directed downwards in the pipe centerline. This is similar to the results obtained by Meknassi *et al.* (2000), simulating flow over a wavy interface in two-phase pipe flow. Numerical results by Meknassi *et al.* (2000) were found to be in good agreement with experimental results by Strand (1993).

Recently, PIV (particle image velocimetry) has been applied to study both the gas and liquid phase of two-phase pipe flows (Ayati *et al.*, 2014; Birvalski *et al.*, 2016). Birvalski *et al.* (2016) found a shift in the gas-phase secondary flow pattern of stratified gas-liquid pipe flow as the wave field transitioned from 3D small amplitude, to larger 2D waves. Large 2D waves were observed to create a secondary flow pattern matching the observations by Liné *et al.* (1996) (upward flow in the pipe center), while small amplitude waves created a more complex secondary flow pattern, indicating four flow cells with the flow along the pipe centerline directed downwards near the upper wall, and upwards near the interface. The secondary flow structures were found to result in a displacement of the peak horizontal velocity upwards/downwards for the large 2D and smaller 3D waves respectively. Similar displacement of the mean velocity profiles associated with secondary flows have been reported by Meknassi *et al.* (2000); Dykhno *et al.* (1994); Alletto & Breuer (2013). Henry *et al.* (2018) investigated the flow in the liquid phase of partially filled pipes using stereoscopic PIV. Secondary flow cells with downwards velocity in the pipe center were observed to displace the peak streamwise velocity some distance below the interface.

In this paper we present results of an experimental analysis of stratified air-water pipe flow. Focus is on investigating the secondary flow structures in the gas phase, and the influence of the surface roughness. In order to modify the surface roughness, small quantities of DEHS (dioctyl sabacate) is added to the water for some experimental cases. This is observed to dampen the ripple formation at moderate gas flow rates, producing a smooth interface between the phases. It is well known that the addition of an oily surface film will help calm waves at sea, by damping out high

frequency capillary waves (Davies & Vose, 1965). Hand *et al.* (1992) investigated the impact of a silicone-based surfactant in water on the flow patterns in a 0.0935 m diameter pipe, and found that the surfactant had the effect of increasing the volumetric gas rate required to produce ripples on the interface. Hence, the stratified smooth regime was extended in the flow map.

Both the non-circular cross section and the variable shear experienced by the gas phase will give rise to secondary flows. Figure 1 presents the highly simplified flow patterns assessed to result from the different mechanisms. Considering the non-circular cross section, a secondary flow pattern with two pairs of corner vortices, resembling the pattern in figure 1 a) is expected (see also experimental results by Dykhno *et al.* (1994), and numerical results by Larsson *et al.* (2011)). Increased roughness/shear in the top/lower half of a circular pipe is expected to result in secondary flow patterns seen in figure 1 b) and c) (Belt *et al.*, 2012).

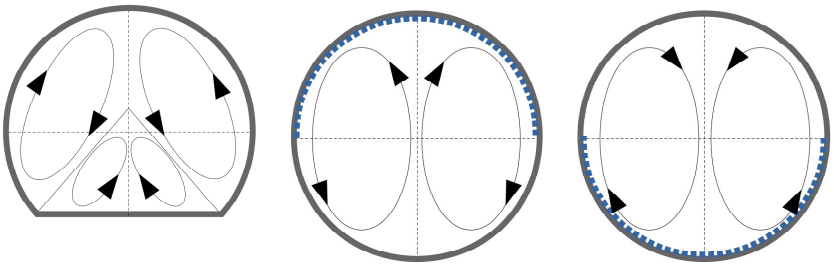

Figure 1: Simplified sketches of idealized secondary flow structures due to effect of non-circular cross-section (a), effect of variable wall roughness (b and c). Higher roughness on top (b) and bottom (c) of pipe.

When the gas-liquid interface is smooth, the wall-shear can dominate the interfacial shear (due to the co-current flow configuration), and conceptually the flow can be described as a combination of figure 1 a) and b). In the present work, the primary secondary flow pattern over a flat gas-liquid interface is found to be well described by the pattern illustrated in figure 2 a). The most energetic secondary flow cells are found to be restricted to the lower region of the gas-space. One interpretation of this result is that in the upper region of the pipe, the secondary flow cells in figure 1 a) and b) act in the opposite direction, and hence cancel each-other out. Considering a rough gas-liquid interface, the flow can be describes as a combination of figure 1 a) and c). As will be seen in the results presented in this work, the secondary flow structure for this case are well described by the pattern illustrated in figure 2 b). Here, the largest secondary flow structures due to the non-circular cross-section and the uneven distribution of the roughness in figure 1 a) and c) are seen to be directed in the same direction, resulting in large secondary flow cells occupying the full height of the gas-space.

In addition to 2D PIV measurements of the pipe centerplane, stereoscopic PIV (S-PIV) is applied to describe the secondary flow patterns in the full cross-section of the pipe. S-PIV in the cross-section of a pipe represents a significant observational challenge, as the dominant flow component is directed normal to the lasersheet. Van Doorne & Westerweel (2007) considered single phase pipe flow, and measured the velocity in the cross section using S-PIV. A similar setup was used by Henry *et al.* (2018), measuring the liquid phase in partially filled pipes. Common for both of these investigations is that the measurements were performed in water. In this work, stereoscopic measurements of the air-phase is performed. To the authors' knowledge, this is the first time S-PIV in the cross-section of a pipe has been applied to measure velocity fields in the gas-phase. For this reason, we combine the results from S-PIV with 2D (planar) PIV, which has previously been reported on and validated (Ayati *et al.*, 2014) in the same experimental setup.

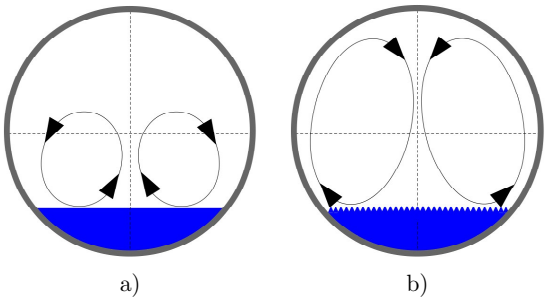

Figure 2: Sketches of the primary secondary flow cells observed in the present work for the case of a flat (a) and rough (b) gas-liquid interface.

2. Experimental setup

The experiments were conducted at the Hydrodynamics Laboratory, at the University of Oslo. The facility consists of a 31 meter long, 10 cm inner diameter (11 cm outer diameter) transparent acrylic pipe, which is made up 11 individual pipe sections. An overview of the experimental setup is presented in figure 3. Air and water flow is provided by a frequency regulated fan and pump respectively, and the gas and liquid flow rates are measured using Coriolis flow meters (Emerson Micromotion and Endress Hauser Promass for the gas and liquid phase respectively). At the inlet, a series of honeycomb flow straighteners are used to dampen secondary flows and turbulent fluctuations introduced at the inlet. The pressure drop in the air-phase is measured over a 12.4 meter section of the pipe using a Smar LD301 differential pressure gauge.

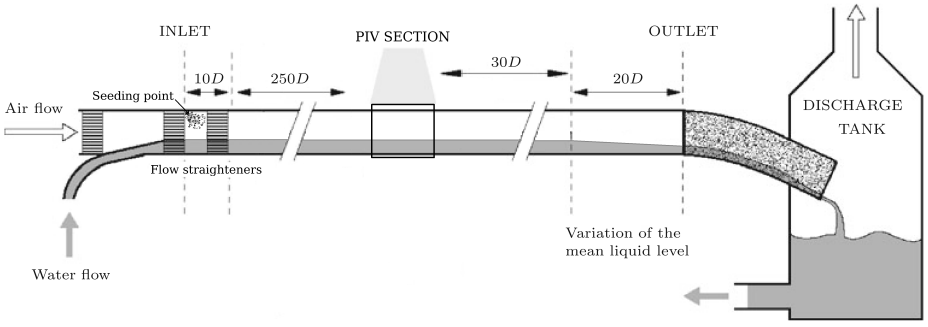

Figure 3: Overview of experimental setup.

A PIV measurement section was placed 260 D from the pipe inlet. In the present work, two different PIV setups were employed. First, planar (2D) PIV was performed, imaging the centerplane of the pipe. Additionally, stereoscopic measurements were performed, imaging the full cross section of the pipe. For both PIV setups, the air was seeded with small water droplets, generated from a high pressure atomizer. According to the manufacturer, 72 % of the droplets generated will have a diameter < 6 μm (Ayati *et al.*, 2014). Details of the two PIV measurement setups are described in the following sections. For further details on the experimental setup the reader is referred to Vollestad *et al.* (2019); Ayati *et al.* (2016).

50

2.1. Planar PIV

Planar PIV was performed along the pipe centerline, with a PCO.4000 camera (4008x2672 pixels) directed perpendicular to the measurement plane. The field of view (FOV) of the camera was 15 cm in width and 10 cm in height. A laser light sheet with a thickness of approximately 1 mm was generated from a double pulse Nd:YAG laser (maximum 147 mJ per pulse), positioned above the measurement section. The setup is illustrated in figure 4.

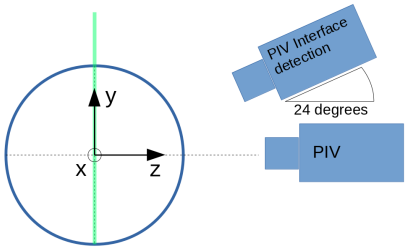

Figure 4: Schematic view of 2D PIV setup. Looking in the streamwise direction. x-axis is directed into the plane. Green line indicate laser light sheet.

In order to provide statistics of the interface structure, a second PCO.4000 camera was used to detect the interface in the measurement plane (note that this was only applied for the cases where waves were observed on the interface). This was tilted at an angle of 24°, looking downwards and focused on the interface, with a width of the FOV of 12 cm. For efficient interface detection, Rhodamine B was added to the liquid phase, and a B+W 041 filter was used on the interface detection camera.

Nonlinear coordinate transforms (from pixel to world coordinates) were created for both cameras by imaging a coordinate system in the pipe centerline prior to the experiments. The coordinate system applied has previously been described by Ayati *et al.* (2015). Cross correlation of the double images acquired were performed in Digiflow by Dalziel research partners, using a cascade of cross correlation passes with a final subwindow size of 64x32 pixels, and 50 % overlap, which translates to a spatial resolution of approximately 1.2 and 0.6 mm in the x-and y-direction respectively. A validation of the planar PIV setup is provided in Appendix A.

2.2. Stereoscopic PIV

The stereoscopic PIV setup is illustrated in figure 5. The lasersheet (produced by the same laser and optics as used for 2D PIV) was directed from above, illuminating a cross section of the pipe. The lasersheet was assessed to have a thickness of approximately 1 mm at the top of the pipe, and 2 mm at the bottom. The two PCO.4000 cameras were positioned at either side of the pipe, at an angle of approximately 40° to the measurement plane. To optimize the FOV of the cameras, these were positioned sideways, so that there were 4008 pixels in the y- and 2672 pixels in the z-direction. Scheimpflug adapters were added to the two cameras to ensure that the entire measurement plane was in focus. Initial analysis using an acrylic pipe in the PIV measurement section revealed that small-scale imperfections in the pipe caused considerable optical distortions, which could not be accounted for in the stereoscopic calibration. To overcome this issue, a one-meter section of the acrylic pipe in the PIV measurement section was replaced with a glass section of the same inner (and outer) diameter.

The stereoscopic PIV was processed using LaVision Davis 10. Calibration images were obtained by traversing a circular, single-level calibration grid with dots separated by 5 mm in the vertical (y) and crosswise (z) direction (example calibration image provided in Appendix B). The grid was

traversed in the streamwise (x) direction using a high precision translation stage, with an accuracy of 2 μm per 25 mm of travel. Nine images, each separated by 0.25 mm were used in the stereoscopic calibration, and a third order polynomial was used to create a mapping function for each of the x-positions recorded. A cascade of cross correlation passes with a final subwindow size of 64x64 pixels, using 50 % overlap was used in the analysis. This translates to a spatial resolution of 0.86 mm in the y-and z-direction respectively. For both 2D and stereoscopic PIV, new pair(s) of double images used for PIV were acquires at a rate of 0.3 Hz. A validation of the stereoscopic PIV setup is presented in Appendix B.

The coordinate system used is indicated in figure 4 and 5. Velocities in the x-, y- and z-direction are denoted u, v and w respectively. In section 4.2, velocities are also decomposed into a cylindrical coordinate system, where the velocities in the x- (streamwise), r- (radial) and θ- (circumferential) direction are denoted u_x, u_r and u_θ ((r,θ) located in the yz-plane).

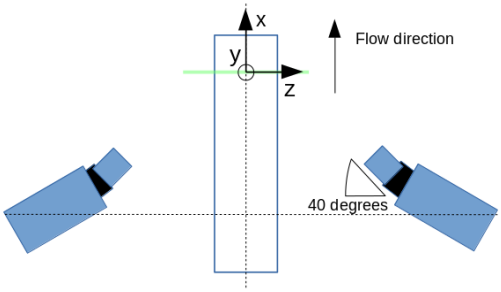

Figure 5: Schematic view of the stereoscopic PIV setup. Seen from above. y is directed out of the plane. Cameras on same height (y-coordinate) as pipe centerline. Green line indicate laser light sheet.

3. Methodology

3.1. Experimental cases

An overview of the experimental cases is presented in table 1. The main input parameters to the experimental system is the gas and liquid superficial velocity, U_{sg} and U_{sl}. The superficial velocities are related to the bulk velocity of each phase by $U_{sf} = U_{bf}A_f/A$, where A is the pipe cross-sectional area, A_f is the area occupied by phase f and U_{bf} is the bulk velocity of phase f. The primary focus is on the effect of increasing U_{sg}. U_{sl} was modified to keep the liquid level relatively constant for the different cases considered, hence U_{sl} is increased slightly with U_{sg} for all cases.

In table 1 the interface is characterized as 'flat' or 'rough' for the different cases. For the flat cases, DEHS (dioctyl sebacate) was added to the liquid phase at a concentration of ≈ 3 mg/L. DEHS was atomized and added to the liquid phase discharge tank (ref. figure 3) prior to the experiments. A circulation pump in the discharge tank kept the water and DEHS well-mixed, and ensured that water and DEHS circulated together through the pipe section. DEHS is an oily, colorless liquid, frequently used as seeding particles in the air phase for PIV analysis. As DEHS is not soluble in water, and has a density of 0.9 kg/m^3, it creates a thin oily film on the surface which prevents the growth of capillary waves. While the first interfacial waves (at $U_{sl} = 0.025$ m/s) were observed at $U_{sg} \approx 2.2$ m/s for pure water, the interface remained flat up until $U_{sg} \approx 8.8$ m/s with the addition of DEHS. The liquid water spray providing particles for PIV was not observed to impact on the ability of the DEHS to maintain a flat interface. For simplicity, the experimental cases are referred to by the superficial gas velocity, and whether the interface is 'flat' or 'rough' in the remainder of

the paper. $\overline{h}$ and η_{rms} is the mean water level and rms (root mean square) of the interface elevation fluctuations in the pipe centerline (details presented in section 3.2).

From table 1, the pressure drop is seen to be significantly enhanced when the interface is rough. Comparing the two cases at $U_{sg} = 7.2$ m/s, the pressure drop is increased by 35 % when the interface is rough. At higher gas flow rates, η_{rms} is increased, further enhancing the pressure drop for the rough interface cases. It can be noted that the liquid level is increased as a result of the addition of DEHS (comparing the two $U_{sg} = 7.2$ m/s cases), resulting in a lower bulk liquid velocity compared with the pure water cases. The gas Reynolds number $Re_{D_h,g}$ (based on the hydraulic diameter D_h) illustrates that the gas flow is turbulent for all cases considered. This is important, as the secondary flows under consideration are a result of the turbulent Reynolds stresses, and would not be present for laminar flows.

Table 1: Overview of experimental cases. N_{2D} and N_{st} is the number of 2D and stereoscopic velocity fields analyzed respectively. *: While the interface appeared flat with no measurable waves, light patterns revealed disturbances in the liquid phase. Close to the transition of large amplitude waves.

U_{sl} $[m/s]$	U_{sg} $[m/s]$	Inter-face	$\overline{h}$ $[mm]$	η_{rms} $[mm]$	$\lvert\Delta P/\Delta x\rvert$ $[Pa/m]$	U_{bl} $[m/s]$	U_{bg} $[m/s]$	$Re_{D_h,l}$ $[-]$	$Re_{D_h,g}$ $[-]$	N_{2D}	N_{st}
0.018	5.2	flat	13.8	NA	4.9	0.21	5.65	7 600	34 900	500	NA
0.023	7.2	flat	14.6	NA	8.5	0.25	7.90	9 600	48 400	500	1000
0.024	8.7	flat*	13.5	NA	11.3	0.29	9.51	10 500	58 500	1000	NA
0.025	7.2	rough	12.2	0.98	11.5	0.36	7.74	11 500	48 200	500	NA
0.030	9.5	rough	12.4	1.12	18.7	0.42	10.20	13 700	63 500	500	NA
0.035	11.5	rough	10.2	1.71	31.2	0.65	12.15	17 700	76 600	1000	2300

3.2. Interface structure

The interface was detected on the images acquired from the interface detection camera. A manual detection of 30 images per experimental case was performed to acquire the interface statistics (η_{rms} and $\overline{h}$) presented in table 1. Secondly, a maximum intensity map was created based on all the images from the interface detection camera, from which the maximum liquid height for each case was found. This is indicated in the results presented in section 4.

The stratified regime can be subdivided based on the characteristics of the interfacial waves generated. Newton & Behnia (2001) classified the stratified wavy regime into rippled, 2D and roll waves. Rippled flow (also referred to as 'pepply' by other researchers (Hanratty & Engen, 1957; Strand, 1993)) occurs at moderate gas flow rates and low liquid hold-up. It is characterized by high frequency disturbances on the gas-liquid interface. 2D waves occur at higher liquid holdup, and are characterized by low frequency (< 10 Hz) waves, spanning the cross-section of the pipe. For the low liquid holdup/high gas flow rates considered in this work, we do not experience 2D waves. As discussed by Andritsos & Hanratty (1987*b*) and Tzotzi & Andritsos (2013), wave generation in stratified two-phase pipe flow is governed by different mechanisms as the gas flow rate is increased. Gradually increasing U_{sg}, the first interfacial waves are generated and grow due to pressure variations in phase with the wave slope. At higher gas flow rates, irregular 'large amplitude' waves are generated by pressure variations 180° out of phase with the wave profile (Tzotzi & Andritsos, 2013). These are often referred to as 'roll waves' (Spedding & Spence, 1993; Hand *et al.*, 1992; Newton & Behnia, 2001), as they resemble the roll waves observed in channel flow, characterized as *"a slug of liquid" ... "picked up and carried over the top of the liquid surface by the gas at a very rapid rate"* (Hanratty & Engen, 1957). Following the expression proposed by Tzotzi & Andritsos (2013) for predicting the transition to the 'large amplitude' (roll wave) regime, this is expected to occur at $U_{sg} \approx 7$ m/s for the liquid flow rates used. In the experimental setup used the transition is observed for somewhat higher U_{sg}.

In figure 6, typical interface profiles for the three rough interface cases are presented. At U_{sg} = 7.2 m/s the interface appeared covered by small ripples. At the highest gas flow rate case (U_{sg} = 11.5 m/s), larger, intermittent, surface disturbances (fitting the description of 'roll waves') were observed (see figure 6 d). For the intermediate flow rate case, the disturbances appeared somewhat more irregular than for the U_{sg} = 7.2 m/s case, and a few examples of large amplitude waves were observed, but these were less frequent and of a slightly lower amplitude than what was observed for the U_{sg} = 11.5 m/s case. Hence, the rough interface cases considered were seen to transition from the 'ripple'/'pebbled' to 'large amplitude'/'roll wave' regime of stratified flow (this is in line with the observations by Strand (1993), made in the same experimental setup). We observed that with the addition of DEHS, the transition to rippled/2D waves was essentially eliminated, and the flow field appeared to transition directly from a flat interface to the roll wave regime for $U_{sg} > 8.8$ m/s (similar to the observations by Hand *et al.* (1992)).

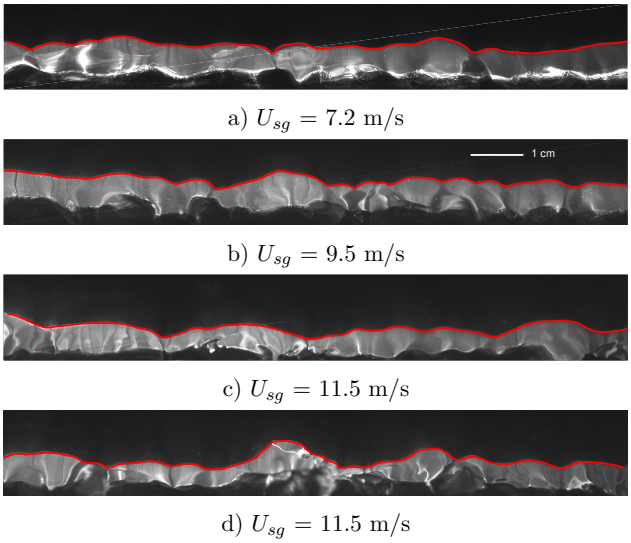

a) U_{sg} = 7.2 m/s

b) U_{sg} = 9.5 m/s

c) U_{sg} = 11.5 m/s

d) U_{sg} = 11.5 m/s

Figure 6: Example interface structures observed for the rough interface cases. Red line shows detected interface. Length scale (1 cm) included in figure b).

It should be noted that the interface elevation is only recorded in the pipe center. From visual inspection of the flow, the interface roughness appeared to be relatively evenly distributed in the crosswise direction, but no quantitative measurements were performed to verify this. Strand (1993) measured the surface elevation at different crosswise planes of the pipe using conductance wave probes (using the same flow loop applied in the present work). At the lowest liquid flow rate applied by Strand (U_{sl} = 0.04 m/s), and for U_{sg} in the range of 7.2 to 11.50 m/s (corresponding to the rough interface cases investigated in the present work), Strand reports a region in the pipe center (approximately -30 mm $\leq z \leq$ 30 mm) where η_{rms} is (close to) constant, and a reduction in η_{rms} closer to the pipe walls. While this was difficult to verify visually for the present work, a similar behavior is expected for the rough interface cases investigated. From visual inspection the mean liquid layer appeared flat, both for the rough and flat interface cases, and we did not observe liquid creeping up on the pipe walls due to secondary flows for any of the cases under investigation.

4. Results

4.1. Results from planar PIV

Spatio-temporally averaged results from the planar PIV are presented in figure 7 and 8. To better visualize the relative differences between the experimental cases, the vertical coordinate is normalized as $y* = (y - \overline{h})/(D - \overline{h})$, where $\overline{h}$ is the mean water level, y is the height relative to the pipe bottom, and D is the pipe diameter, while the mean velocity is normalized by the peak horizontal velocity. For the experimental cases where the interface is rough, the maximum liquid level is indicated by a dashed horizontal line. Results below this line should be interpreted with care, as intermittent wave structures passing the PIV section will impact the results in this region (these were not masked out from the images, and are assessed to result in increased noise in the calculated velocity profiles, and an overprediction of the turbulent stresses reported below the line). Note that due to light reflections near the upper pipe wall and gas-liquid interface, small regions of nonphysical discontinuities were observed in the PIV velocity profiles (this was also observed by Ayati *et al.* (2014)). For readability, these sections were removed from the velocity profiles in figure 7 and 8, and replaced by cubic interpolation.

From figure 7 b), it can be observed that for the flat interface cases, the vertical velocity is directed up along the pipe centerline, with a peak vertical velocity at $y* \approx 0.2$. As the flow is symmetric around the y-axis, this implies that the secondary flow field is dominated by two vortical structures located in the lower half of the gas-space. The upwards flow in the pipe centerline is seen to have the effect of displacing the peak horizontal velocity up in the pipe, to $y^* \approx 0.58$ (see figure 7 a). Dykhno *et al.* (1994) placed solid inserts in the bottom of a circular pipe to simulate the effect of a flat gas-liquid interface. While Dykhno *et al.* (1994) found evidence of an upward flow in the lower half of the pipe center, the peak horizontal velocity remained in the center of the gas-space. This implies that the co-current flow configuration applied in the present work enhances the upwards secondary flows observed over a solid, flat interface. For the rough interface cases, the vertical velocity is primarily directed downwards in the pipe centerline, resulting in a lower position of the peak horizontal velocity. Small regions of positive vertical velocity near the interface for the two lowest rough interface cases indicate additional secondary flow cells near the interface, in the opposite direction to the primary structures.

It can be noted that while the normalized horizontal and vertical velocity profiles are seen to collapse onto the same curve for the flat interface cases, we see a development of the intensity of the secondary flow structure for the rough interface cases. Increasing U_{sg} (and hence η_{rms}) is seen to result in stronger secondary flow structures. It can be noted that while the intensity of the secondary flow structures increase with increasing U_{sg}, the position of the peak horizontal velocity is not seen to be reduced as one might expect. The occurrence of large amplitude (roll) waves is assessed to be a possible reason why the position of the peak horizontal velocity is increased with increasing U_{sg}, as this will push the flow up relative to the mean water level, counteracting the downwards oriented secondary flow in the pipe centerline.

Figure 8 presents $\overline{u'v'}$ as well as the rms of the fluctuating velocity components, normalized by the wall friction velocity. It should be noted that the recorded velocity fluctuations are a result of turbulent fluctuations as well as perturbations due to the wavy gas-liquid interface. Separating these fluctuations (turbulence and wave/ripple induced fluctuations) is outside the scope of the present work, and all fluctuations about the mean values recorded in figure 7 are reported as turbulent fluctuations. Again, the flat interface cases are seen to exhibit similar profiles, while a clear evolution of the turbulence intensity in the lower half of the pipe is seen when increasing U_{sg} for the rough interface cases.

The wall friction velocity u_{wf} was estimated by extrapolating the (close to) linear part of the shear stresses ($\overline{u'v'}$) above the inflection point of the peak horizontal velocity to the top of the pipe, giving an estimate for u_{wf}^2 (similar to Birvalski *et al.* (2016)). The wall shear stress was

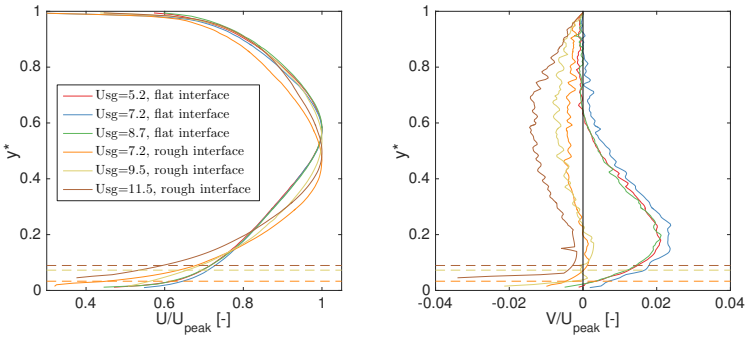

a) U/U_{peak} b) V/U_{peak}

Figure 7: Mean flow structures evaluated from planar PIV, normalized by peak horizontal velocity. Dashed horizontal lines represents maximum water level (crest height) observed (only relevant for the rough interface cases). U_{peak} = 7.13, 9.81, 11.73, 10.02, 12.79, 15.40 m/s for the cases respectively (in same order as legend).

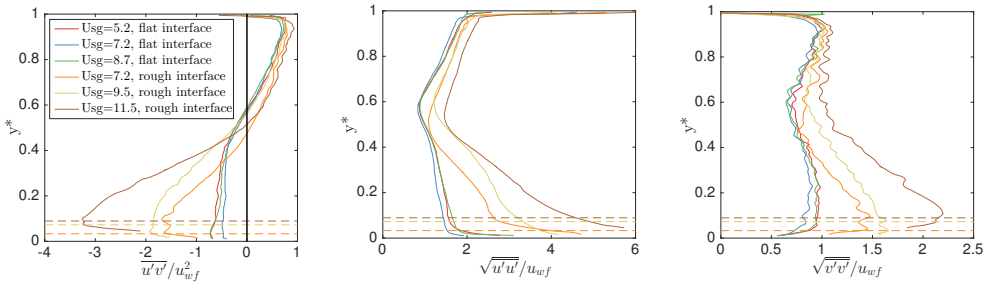

a) $\overline{u'v'}/u_{wf}^2$ b) $\sqrt{\overline{u'u'}}/u_{wf}$ c) $\sqrt{\overline{v'v'}}/u_{wf}$

Figure 8: Turbulent velocity profiles, normalized by wall friction velocity. Dashed horizontal lines represents maximum water level (crest height) observed (only relevant for the rough interface cases).

then calculated as $\tau_w = u_{wf}^2 \rho_g$. This allowed the interfacial shear stress τ_i and friction velocity u_{if} ($u_{if} = \sqrt{|\tau_i|/\rho_g}$) to be estimated by a simple force balance on the gas phase, applying the measured pressure drop and mean liquid height $\overline{h}$. It should be noted that these are rough estimates of the friction velocities, as circumferential variations in the wall friction and streamwise variations in the flow field are not accounted for in the estimate of u_{wf}. It is however assessed that these calculations give reasonable estimates for the relative importance of the wall and interfacial shear stresses. Results for u_{if}/u_{wf} are presented in figure 9 a), along with the measured pressure drop (figure 9 b). It is seen that for all the flat interface cases, the wall friction dominates the interfacial friction, while the opposite is true for the rough interface cases. This trend can also be inferred from the shear stresses presented in figure 8 a), as extrapolating the normalized shear stresses to the interface provides an estimate of the shear stresses in the pipe center to be lower/higher than the wall shear stresses for the flat/rough interface cases respectively. A higher relative velocity at the wall due to the co-current flow configuration is assessed to be the reason why the wall shear dominates the interfacial shear for the flat interface cases.

Wave/ripple formations on the gas-liquid interface is known to significantly enhance the interfacial friction, with the result that it dominates the wall friction (Andritsos & Hanratty, 1987*a*). A large number of (semi-) empirical correlations for the interfacial friction factor exists in the literature (Xiao & Shoham, 1991; Espedal, 1998). When comparing experimental results to existing

correlations, it is important to consider correlations created for the relevant flow regime.

Tzotzi & Andritsos (2013) presented semi-empirical correlations for the ratio of the interfacial and gas wall friction factors (f_i/f_{wg}) for wavy flows, using separate correlation for 2D and 'large amplitude' waves. Within the 2D waves regime, the following relation is proposed

$$\frac{f_i}{f_{wg}} = 1 + 0.35\Big(\frac{\overline{h}}{D}\Big)^{0.5}(U_{sg} - U_{sg,2D}), \tag{1}$$

while within the 'large-amplitude' regime (considering air-water flow) the relation is given by

$$\frac{f_i}{f_{wg}} = 2\Big(\frac{\overline{h}}{D}\Big)^{0.1} + 4\Big(\frac{\overline{h}}{D}\Big)^{0.5}(U_{sg} - U_{sg,KH}). \tag{2}$$

In equation 1 and 2, $U_{sg,2D}$ and $U_{sg,KH}$ is the superficial gas velocity at which the regime transitions to 2D and 'large amplitude' waves occur (for a given U_{sl}) respectively. Tzotzi & Andritsos (2013) provide expressions for these transitions, but (as discussed in section 3.2) these do not coincide directly with the transitions observed in the present experimental setup. Hence, we set $U_{sg,2D} = 2.2$ m/s and $U_{sg,KH} = 8.8$ m/s, corresponding to the transitions observed in the present experimental work. Results from these correlations (using the flow properties presented in table 1, and converting from f_i/f_{wg} to u_{if}/u_{wg} by using the relations provided by Tzotzi & Andritsos (2013)) are included in figure 9 a) for the rough interface cases. It is seen that the correlation for 2D waves underpredict u_{if}/u_{wf} for all cases considered (also for the lowest gas flow rate where 'large amplitude' waves are not observed), while good agreement between the experimental results and equation 2 is observed for the two highest gas flow rate cases. The under-prediction of u_{if}/u_{wf} for the lowest gas flow rate case could be related to the distinction between the rippled and 2D wave pattern, which was not addressed by Tzotzi & Andritsos (2013). As discussed in section 3.2, we do not observe 2D waves at the low liquid holdup and high gas flow rates considered, and the wave field before the onset of intermittent large amplitude roll waves is better described as 'rippled'.

Hart *et al.* (1989) proposed a correlation for the interfacial friction factor for flows with low liquid holdup (< 0.06)

$$f_i = 9.26 \cdot 10^{-3} f_{wl} Re_{sl}^{0.726}. \tag{3}$$

Here, Re_{sl} is the superficial liquid Reynolds number and f_{wl} is the friction factor between the liquid phase and the pipe wall. The rough interface cases considered have liquid hold-up in the range of 0.05 - 0.07, and only for the highest gas flow rate case the liquid holdup is < 0.06.

Based on experimental data from several researchers, Spedding & Hand (1997) proposed a model for the interfacial friction factor based both on the gas and liquid superficial velocities

$$f_i = 0.046 Re_{sg}^{-0.2} \cdot \left(1.76\Big(\frac{U_{sg}}{6}\Big) + 2.7847 \log\Big(\frac{U_{sl}}{U_{sl}+6}\Big) + 7.8035\right), \tag{4}$$

where Re_{sg} is the superficial gas Reynolds number. Estimating f_{wl} and f_{wg} using the Blasius friction factor (see Tzotzi & Andritsos (2013)), equation 3 and 4 is used to calculate u_{if}/u_{wf} for the rough interface cases. Results included in figure 9 a) indicate that both equation 3 and 4 overpredicts f_i for the two lowest gas flow rates, while good agreement in seen for $U_{sg} = 11.5$ m/s. This is to be expected for equation 4, as this is primarily valid within the roll wave regime (Spedding & Hand, 1997).

The comparison with existing correlations illustrate the difficulty in accurately predicting the interfacial friction in stratified two-phase flows, especially in regions of the flow map where regime transitions occur. The comparison does however illustrate that the ratio of the interfacial and wall friction velocities calculated for the rough interface cases are reasonable compared with existing

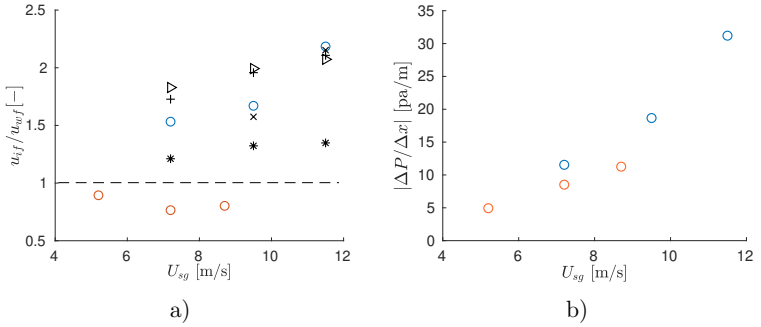

Figure 9: a) Ratio of interface and wall friction velocity, u_{if}/u_{wf}. Circles represent measurements performed in the present work. Blue circles: Rough interface. Red circles: Flat interface. $*$: evaluated by equation 1. $\times$: evaluated by equation 2 (only relevant for $U_{sg} > 8.8$ m/s). $\triangleright$: evaluated by equation 3. $+$: evaluated by equation 4. b) Average pressure drop over 12.4 m pipe section, $|\Delta P/\Delta x|$. Blue icons: Rough interface. Red icons: Flat interface.

correlations. As discussed in the introduction, the secondary flows are driven by the divergence of the Reynolds stress tensor, and the qualitative change in the direction of the secondary flow structures observed can be related to the relative importance of the wall and interfacial friction. This will be investigated further in section 4.2.1.

4.2. Results from stereoscopic PIV

Two cases are analyzed using the stereoscopic PIV setup; the medium flow rate of the flat interface cases ($U_{sl} = 0.023$ m/s, $U_{sg} = 7.2$ m/s) and the maximum gas flow rate case with rough interface ($U_{sl} = 0.035$ m/s, $U_{sg} = 11.5$ m/s). The second case was chosen from the rough interface cases as this is where we, in section 4.1, observed that the relative strength of the secondary flows were the highest, hence the secondary flows can be measured with a higher relative accuracy.

Example raw images from one of the PIV cameras are shown in figure 10. At the lower left a reflection is observed in both images. A similar reflection was observed also for the opposite camera, then located at the lower right part of the pipe. These regions were masked from the images prior to the stereoscopic processing, and hence no velocity measurements are obtained within these regions. Reflection near the pipe walls (especially noticeable near the top of the pipe) caused unreliable results close to the pipe walls. A manual masking of the images at approximately $r = 45$ mm was performed, omitting these regions from the analysis.

As discussed in Appendix B, the accuracy of the in-plane stereoscopic PIV measurements were found to be approximately 2 % of the bulk gas velocity, similar to the magnitude of the secondary flows found in section 4.1. The error is assessed to be caused by the calibration, and due to optical distortions not adequately taken care of by the third-order coordinate transform applied. However, as this is assessed to be a calibration error, and as the error is known in the single phase flow measurements, it should be possible to remove, or at least reduce it. Here we choose to correct the mean in-plane velocities by subtracting the mean in-plane velocity component measured in a single-phase run at the same U_{sg} (analyzing 1000 velocity fields for each case), weighted by the ratio of the local mean streamwise velocity (U) between the two-phase ($2p$) and the single phase (sp) measurements. Hence, we go from the measured V and W components (V_{2p} and W_{2p}) to $V_{corrected}$ and $W_{corrected}$ by the following relations:

$$V_{corrected}(y,z) = V_{2p}(y,z) - \frac{U_{2p}(y,z)}{U_{sp}(y,z)} V_{sp}(y,z), \tag{5}$$

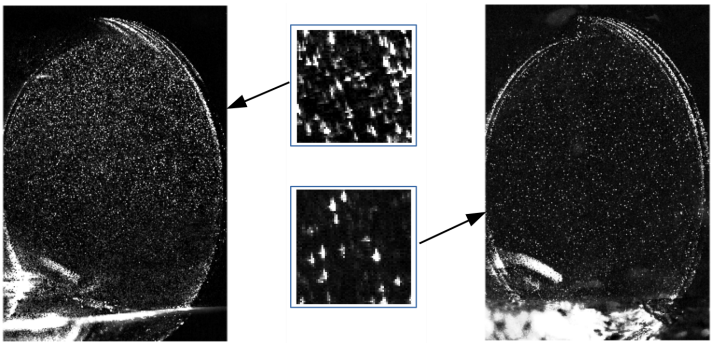

Figure 10: Example raw PIV images of the U_{sg} = 7.2 m/s flat interface case (left) and the U_{sg} = 11.5 m/s, rough interface case (right). In the center, 64x64 px^2 regions of the images are included to illustrate the typical particle density.

$$W_{corrected}(y,z) = W_{2p}(y,z) - \frac{U_{2p}(y,z)}{U_{sp}(y,z)} W_{sp}(y,z). \tag{6}$$

Applying equation 5 and 6 was found to result in a much more symmetric velocity profile, and a better agreement with the vertical velocity profiles obtained from 2D PIV (see figure 12). Further discussion and an example velocity field before and after correction is included in Appendix B.

Mean flow results for the stereoscopic PIV analysis are presented in figure 11. For both experimental cases, clear coherent in-plane flow structures symmetric about the y-axis are observed. For the flat interface case, the secondary flow cells are seen to be predominantly present in the lower half of the space occupied by the gas (up to $y \approx 10$ mm), directed up in the pipe centerline and down at the pipe walls close to the interface. The development of the secondary flow patterns will be investigated in more detail in section 4.2.1, but it is interesting to note that the secondary flow patterns in figure 11 a) are seen to be drastically reduced near the top of the pipe. Referring to figure 1 a) and b), the secondary flow patterns caused by the non-circular cross section and the variable surface shear (low shear at the interface) are directed in the opposite direction in this region. This may explain why the secondary flows are seen to be significantly reduced in this region, and the main flow cells are restricted to the lower half of the gas-space.

For the rough interface case, the secondary flow cells are seen to be directed downwards at the pipe centerline, and upwards along the pipe walls. Referring to figure 1 a) and c), it can be seen that the two effects responsible for the secondary flows (non-circular cross section and high interface roughness compared to wall roughness) are expected to result in the same primary secondary flow pattern, similar to what we observed in figure 11 b). The smaller secondary flow structure associated with the non-circular cross section is however not observed.

While the largest in-plane velocities are observed at the pipe centerline (at $y \approx$ -20 mm) for the flat interface case, and represents 3.2 % of the bulk gas velocity, the maximum in-plane velocities for the rough interface case is observed near the pipe walls (at $y \approx$ -15 mm), and represents approximately 6 % of the bulk velocity.

In figure 12 the mean flow results from the stereoscopic and 2D PIV are compared. While it is observed that the vertical velocity profile of the flat interface case and the streamwise velocity of both cases match well with the 2D PIV measurements, some discrepancies (approximately 0.5 % of U_{sg}) are observed for the vertical velocity component of the rough interface case. Also here the general shape of the secondary flow signature is the same for the 2D and stereoscopic measurements, but it is assessed that the in-plane correction described in equation 5 and 6 results in some errors.

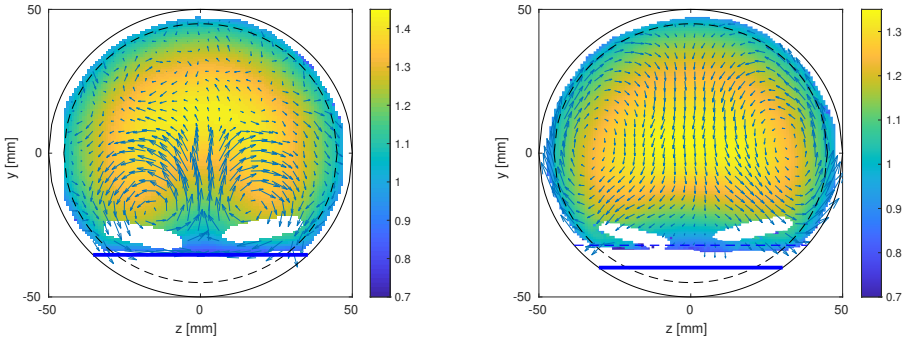

a) $U_{sg} = 7.2$ m/s, flat int. b) $U_{sg} = 11.5$ m/s, rough int.

Figure 11: Results for mean flow from stereoscopic PIV analysis. Contour plot of mean streamwise velocity normalized by U_{sg} (U/U_{sg}), and vector plots of mean in-plane velocity components V and W (showing 1/4 vectors). Full black circle represents pipe walls, dashed circle represents $r = 45$ mm. Thick blue horizontal line represents mean water level, and dashed blue line represents maximum wave amplitude observed, if applicable (from 2D PIV measurements of the same case).

While the results in figure 12 illustrate that there are uncertainties related to the secondary flows recorded by stereoscopic PIV, the comparison illustrates that the main flow structures observed in figure 11 are well described by the stereoscopic PIV setup.

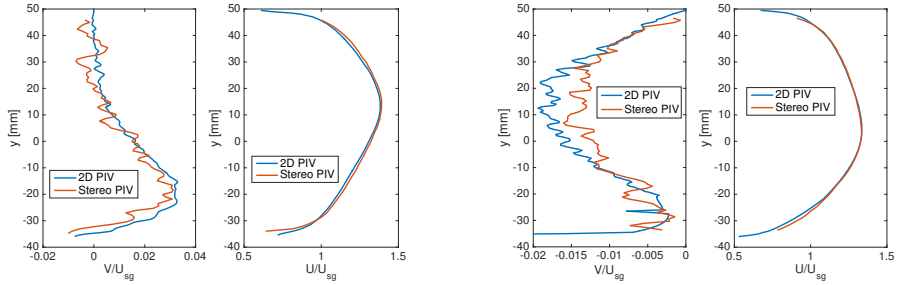

a) $U_{sg} = 7.2$ m/s, flat int. b) $U_{sg} = 11.5$ m/s, rough int.

Figure 12: Comparison of mean-flow velocity components obtained from 2D and stereoscopic PIV. Vertical and streamwise velocity components in the pipe centerline.

The turbulent kinetic energy ($k = 0.5 \cdot (\overline{u'u'} + \overline{v'v'} + \overline{w'w'})$) and the Reynolds shear stresses $-\overline{u'_x u'_r}$ (where u'_x and u'_r are turbulent velocity fluctuations in the streamwise and radial direction respectively), are presented in figure 13. As expected, k and $-\overline{u'_x u'_r}$ are seen to be symmetric about the y-axis. The distribution of the turbulent kinetic energy and the turbulent momentum flux towards the pipe center is qualitatively different comparing the flat and rough interface cases. While the turbulent kinetic energy and turbulent momentum flux is highest near the pipe wall for the flat interface case, the region above the rough interface is seen to dominate the momentum flux for the rough interface case.

A comparison of the Reynolds shear stresses measured by stereoscopic and 2D PIV is presented in figure 14. While very good agreement is seen between the 2D and stereoscopic measurements near the pipe center, some deviations are observed close to the interface/upper wall, and the stereo-

60

scopic PIV is seen to under predict the Reynolds shear stresses compared with the 2D PIV results. However, overall the comparison illustrates that the stereo PIV captures the qualitative features of the Reynolds shear stress distribution.

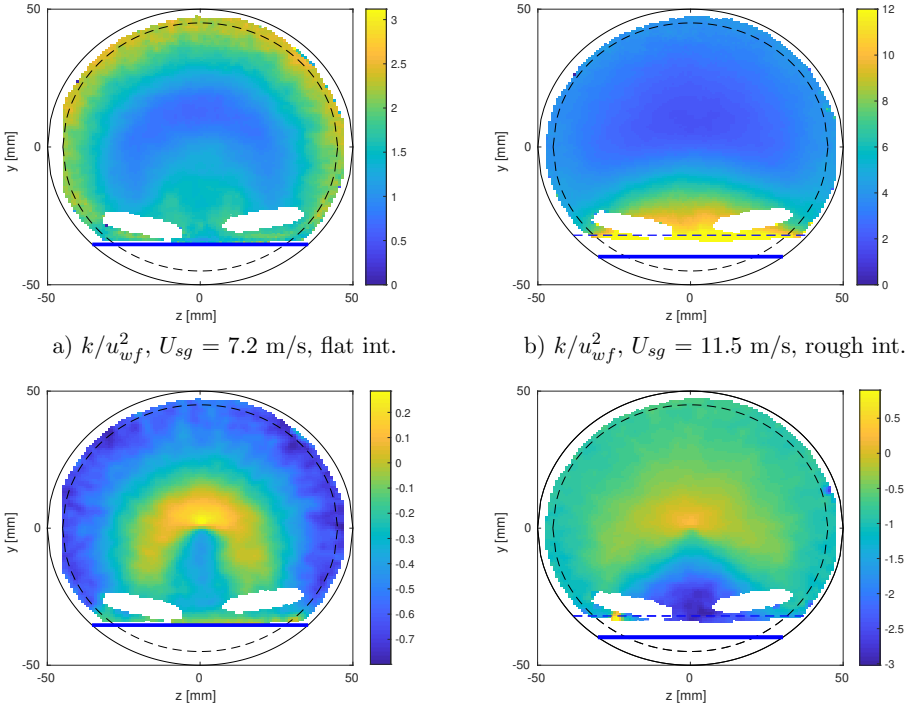

a) k/u_{wf}^2, $U_{sg} = 7.2$ m/s, flat int.

b) k/u_{wf}^2, $U_{sg} = 11.5$ m/s, rough int.

c) $-\overline{u_x'u_r'}/u_{wf}^2$, $U_{sg} = 7.2$ m/s, flat int.

d) $-\overline{u_x'u_r'}/u_{wf}^2$, $U_{sg} = 11.5$ m/s, rough int.

Figure 13: Results from stereoscopic PIV analysis. a-b) Turbulent kinetic energy normalized by u_{wf}^2 (evaluated based on 2D PIV results). c-d) Reynolds shear stresses ($-\overline{u_x'u_r'}$) normalized by u_{wf}^2. Full cicle represents pipe walls, dashed circle represents $r = 45$ mm. Thick blue horizontal line represents mean water level, dashed blue line represents maximum wave amplitude observed, if applicable (from 2D PIV measurements of the same case).

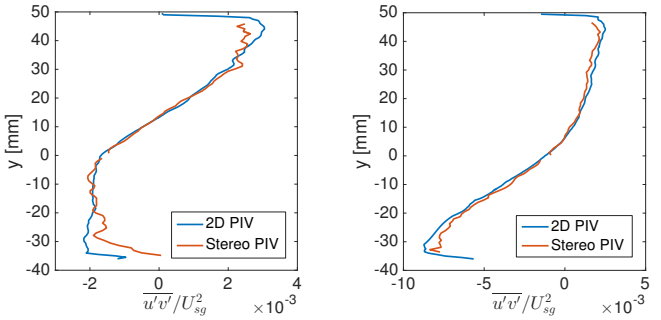

a) $U_{sg} = 7.2$ m/s, flat int.

b) $U_{sg} = 11.5$ m/s, rough int.

Figure 14: Comparison of shear stresses $\overline{u'v'}$ along the pipe centerline obtained from 2D and stereoscopic PIV.

4.2.1. Assessment of secondary flow structures and driving mechanisms

The theory describing the occurrence of secondary flows has previously been presented by Speziale (1982) and Belt *et al.* (2012). Secondary flows of the second kind result from anisotropy of the Reynolds stresses, and the divergence of the Reynolds stress tensor ($\boldsymbol{\nabla} \cdot \tilde{\boldsymbol{\tau}}$) in the cross-section represents the driving mechanism. Hence, the direction of the secondary flows can be inferred by the (divergence of the) Reynolds stresses. In cylindrical coordinates, the divergence of the Reynolds stress tensor in the pipe cross-section is given by

$$(\boldsymbol{\nabla} \cdot \tilde{\boldsymbol{\tau}})_r = \frac{\partial \tau_{rr}}{\partial r} + \frac{1}{r}\frac{\partial \tau_{r\theta}}{\partial \theta} + \frac{\tau_{rr} - \tau_{\theta\theta}}{r}, \tag{7}$$

and

$$(\boldsymbol{\nabla} \cdot \tilde{\boldsymbol{\tau}})_\theta = \frac{1}{r}\frac{\partial \tau_{\theta\theta}}{\partial \theta} + \frac{\partial \tau_{r\theta}}{\partial r} + \frac{2\tau_{r\theta}}{r}, \tag{8}$$

in the radial and circumferential direction respectively. The Reynolds stresses in equation 7 and 8 are given as

$$\tau_{\theta\theta} = -\rho\overline{u'_\theta u'_\theta}; \quad \tau_{rr} = -\rho\overline{u'_r u'_r}; \quad \tau_{r\theta} = -\rho\overline{u'_r u'_\theta}. \tag{9}$$

Analyzing a particle laden flow, Belt *et al.* (2012) found that the first term of equation 7 and 8 dominated, and that the pattern of the secondary flow structures could be inferred from these two terms. By plotting the different terms in equation 7 and 8, this was seen to be the case for the results obtained in the present work as well. Hence, it should be possible to infer (in a qualitative manner) the direction of the secondary flow structures by considering $-\partial\overline{u'_\theta u'_\theta}/\partial\theta$ and $-\partial\overline{u'_r u'_r}/\partial r$. Note that this is different from single phase flow in square pipes, where the shear stresses in the cross-section are known to play a significant role in the generation of secondary flows (Belt *et al.*, 2012; Demuren & Rodi, 1984). As the flow is symmetric about the y-axis, we only need to consider half of the flow field to analyze these terms.

Figure 15 shows contour plots of the Reynolds stresses in the circumferential ($-\overline{u'_\theta u'_\theta}$, for z = [-50 mm: 0 mm]) and radial ($-\overline{u'_r u'_r}$ for z = [0 mm: 50 mm]) direction (normalized by u^2_{wf}), for the two cases under investigation. Vector plots of the secondary flow structures are overlaid the contour plots. It is observed that the distribution of $-\overline{u'_\theta u'_\theta}$ and $-\overline{u'_r u'_r}$ closely matches the distribution of the turbulent kinetic energy (although with a change in sign) shown in figure 13, and that the radial stresses are somewhat weaker than the stresses in the circumferential direction, especially near the pipe wall. This is a result of the radial restriction imposed by the boundary. Also included in figure 15 are arrows indicating the most prominent gradients of $-\overline{u'_\theta u'_\theta}$ in the θ-direction and $-\overline{u'_r u'_r}$ in the r-direction respectively. Similar plots were provided by Belt *et al.* (2012) to infer the direction of the secondary flow structures in a particle laden pipe flow.

For the flat interface case (figure 15 a), we observe that at the intersection between walls and the interface, gradients of $-\overline{u'_\theta u'_\theta}$ pushes the flow downwards near the wall. Note that these gradient are not fully visualized, as we are not able to obtain accurate stereoscopic measurements very close to the wall, and it is assessed that the gradients would be more pronounced had the measurements extended all the way to the pipe walls. Due to symmetry, the flow is forced upwards near the interface at $z = 0$. Above the interface, gradients in $-\overline{u'_\theta u'_\theta}$ and $-\overline{u'_r u'_r}$ are seen to divert the flow outwards again, and to restrict the secondary flow structure from expanding into the upper part of the gas-space, as strong gradients of $-\overline{u'_r u'_r}$ towards the pipe center are observed at $r \approx 30$ mm.

For the rough interface case (figure 15 b), the dominant gradients in the θ-direction are all in the same direction, resulting in an upwards flow at the pipe walls. Except for near the interface, where gradients of $-\overline{u'_r u'_r}$ are directed upwards, decelerating the flow as it is diverted down through the pipe center, gradients of $-\overline{u'_r u'_r}$ in the r-direction are seen to be relatively weak, and assessed

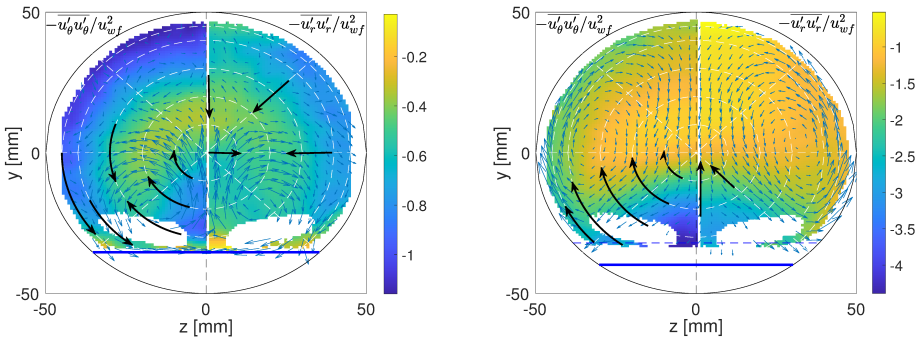

a) $U_{sg} = 7.2$ m/s, flat int. b) $U_{sg} = 11.5$ m/s, rough int.

Figure 15: Contour plots of the Reynolds stresses in the circumferential ($-\overline{u'_\theta u'_\theta}$, for z = [-50 mm: 0 mm]) and radial ($-\overline{u'_r u'_r}$ for [z = 0 mm: 50 mm]) direction, normalized by u^2_{wf}. Blue vectors shows mean secondary flow field. Black arrows included to illustrate the most significant gradients of $-\overline{u'_\theta u'_\theta}$ in the θ-direction, and $-\overline{u'_r u'_r}$ in the r-direction on the left and right side of the centerline respectively. White dashed lines: lines of constant θ or r.

not to influence the flow in the same way as seen for the flat interface case. Hence, the secondary flow structures generated by gradients in $-\overline{u'_\theta u'_\theta}$ are seen to occupy the entire gas-space.

Both Belt *et al.* (2012) and Alletto & Breuer (2013), studying secondary flows in particle laden pipe flow found that the direction of the secondary flow pattern could be inferred from $-\partial\overline{u'_\theta u'_\theta}/\partial\theta$ at the wall. We also observe that the gradients of $-\partial\overline{u'_\theta u'_\theta}/\partial\theta$ at the intersection between the pipe wall and liquid interface correctly predicts the direction of the secondary flow structures. The restriction of the secondary flow structures observed for the flat interface case does however require an analysis of the stresses everywhere in the pipe cross section.

5. Discussion and concluding remarks

The results presented in this work provide new insights into the origin and structure of secondary flows in stratified gas-liquid pipe flow, and experimental data to which numerical models can be validated. Both the non-circular area occupied by the gas, and the variable roughness around the gas circumference is assessed to be important for setting up the secondary flows. We observe that when the gas-liquid interface is flat, secondary flow structures directed upwards in the pipe centerline, and down at the walls are generated, while the direction of the secondary flow structures are reversed as interfacial disturbances are allowed to form on the interface. The qualitative change in the secondary flow patterns considering a flat or rough gas-liquid interface is well explained by the gradients of the radial and circumferential Reynolds stresses in the radial and circumferential direction respectively, and particularly the circumferential gradients of $-\overline{u'_\theta u'_\theta}$ at the intersection between the wall and the interface are assessed to be important in setting up the secondary flow structures. This is related to the gradients of the circumferential shear/roughness, which is lower (higher) at the gas-liquid interface compared with the wall for the flat (rough) interface cases respectively.

Stratified gas-liquid pipe flow is of engineering importance for many applications, especially within the petroleum industry. Correctly predicting the interfacial friction and pressure drop is the primary challenge in the modelling. Results in this work illustrate that changes in the interface structure significantly impacts the secondary flow structures and pressure drop in stratified gas-liquid pipe flow. It is well known (Speziale, 1982; Meknassi *et al.*, 2000) that flow geometries inducing strong secondary flows represent a significant challenge for turbulence modelling. Due to the computational cost associated with accurately simulating two-phase flows, simplified numerical models

(see e.g Meknassi *et al.* (2000)) have been specifically developed to predict the three-dimensional flow pattern of the gas phase in stratified gas-liquid pipe flow. The data presented in this work should be suitable for further validation of these numerical models.

While planar PIV has previously been used to analyze both the gas and liquid phase of stratified gas-liquid pipe flow, results presented here represents (to the author's knowledge) the first analysis of the gas phase in a pipe cross-section using stereoscopic PIV. While the single phase validation and comparison with 2D PIV illustrate that care must be taken in using the stereoscopic results directly, it is assessed that the method is able to describe the main features of the secondary flow structures, and the distribution of the Reynolds stresses in a satisfactory manner.

Acknowledgement

The authors wish to acknowledge the strategic research initiative EarthFlows at the Faculty of Mathematics and Natural Sciences at the University of Oslo. Laboratory Head Engineer O. Gundersen is gratefully acknowledged for the technical assistance he provided during the experimental work. We also want to thank Professor J. R. Dawson at the Norwegian University of Science and Technology for his assistance with the stereoscopic PIV software applied.

Appendix A: Planar (2D) PIV validation

The planar (2D) PIV setup was validated by comparing results for single phase gas flow with DNS results by Wu & Moin (2008). A similar validation has previously been conducted by Ayati *et al.* (2014), using the same flow loop and a similar experimental setup.

Results presented in figure 16 (analyzing 500 PIV velocity fields) show good agreement between the experimental and DNS results. Close to the pipe wall ($r/R > 0.9$) the results are less favorable, and particularly the results for the streamwise and shear Reynolds stresses are seen to deviate from the DNS close to the pipe walls. Significant optical distortion and large velocity gradients near the pipe walls are assessed to be the reason for sub-optimal results in this region. This was also observed by Ayati *et al.* (2014). It can be noted that we observed slightly larger values of the streamwise Reynolds stresses than the DNS. One possible explanation for this is slight fluctuations in the volumetric flow rate provided by the fan, resulting in mean flow variations that will be interpreted as turbulence when a single mean is subtracted from the flow field. The vertical velocity along the pipe center was found to fluctuate around zero, with an absolute velocity $|v| < 0.01$ m/s in the region with reliable PIV results ($r/R < 0.9$), which is less than 0.15% of the bulk velocity. This is within the uncertainty of the PIV measurements, and the deviations from a zero mean vertical velocity are assessed to be caused by uncertainty in the PIV measurements rather than secondary flows in the pipe.

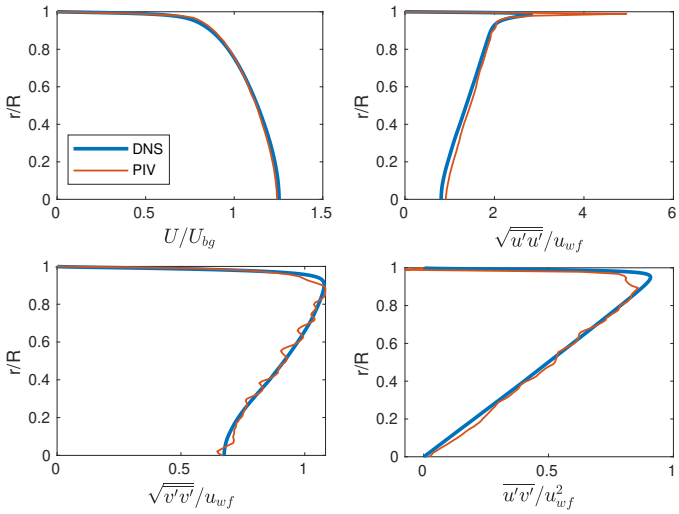

Figure 16: Planar PIV results of single phase (air) flow at Re=44k, and comparison with DNS results by Wu & Moin (2008). Results presented from pipe center and up to the top-wall.

Appendix B: Stereoscopic PIV validation

Similarly to the 2D PIV setup, the stereoscopic PIV setup was validated by comparing the results of single phase gas flow at Re = 44k (relevant for the current application, ref. table 1) with the DNS results of Wu & Moin (2008). Example images of the coordinate system used (details presented in section 2.2) and an example PIV image from the single phase validation is presented in figure 17, while results from the analysis is presented in figure 18, 20 and 21. 1000 velocity fields

were obtained and analyzed. This was found to give a qualitative convergence, suitable for the present analysis.

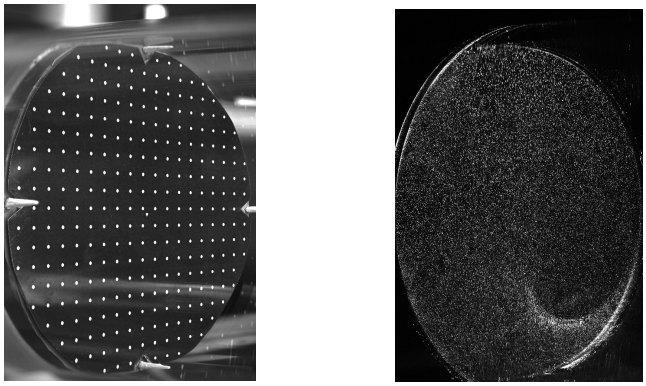

a) b)

Figure 17: Calibration image (a) and raw PIV image from single phase stereoscopic PIV validation (b). The four spikes on the upper/lower/left/right side of the calibration grid (figure a) were painted using a fluorescent paint, and used to accurately align the lasersheet with the calibration plate.

Figure 18 illustrates the mean flow field. The streamwise velocity component is seen to be symmetric, and matches the DNS results from Wu & Moin (2008) both along the y- and z-axis, although the results indicate that the stereo PIV slightly over predicts the streamwise velocity. It is seen that the mean velocity in the y- and z-directions are not zero, as would be expected for single phase flow in a straight pipe. As seen in figure 18, the maximum mean velocities in the in-plane directions are approximately 2 % of the bulk velocity. Referring to section 4.1, this is similar to the magnitude of the secondary flows observed in the centerplane using 2D PIV. While in-plane mean velocities observed in figure 18 could be interpreted as secondary flows, we assess that the velocities are primarily an artifact of the calibration. Hence, we apply the correction described in section 4.2 to correct the in-plane velocities measured in the two-phase cases. The reason why we assess these velocities to be primarily an artifact of the calibration can be summarized as: i) the patterns of V and W from the single phase validation is not consistent with a secondary flow pattern in the pipe, as it does not fulfill continuity in the pipe cross section. ii) Correcting the measured velocities result in a secondary flow pattern which is symmetric around the pipe centerline. This is consistent with the symmetric distribution of the Reynolds stresses, which are responsible for secondary flows (and which are unaffected by the correction applied). iii) Correcting the velocities resulted in a better agreement between the vertical velocity component in the pipe centerline measured by 2D and stereoscopic PIV. iv) Analyzing the PIV validation images with a different set of calibration images resulted in a qualitative change in the V and W patterns (although the peak values of the components remained roughly constant).

An example of the in-plane velocities before and after correction is shown in figure 19. Before correction, the secondary flows are seen to be non-symmetric and exhibiting a nonphysical distribution, as continuity in the cross section is not fulfilled (the flow appears to be introduced at the right edge of the pipe).

Figure 20 shows the rms of the streamwise, radial and circumferential velocity fluctuations, as well as the shear stress $(\overline{u'_x u'_r})$ along the y- and z-axis. Results are normalized by the wall friction velocity u_{wf} (evaluated by a control volume analysis based on the measured pressure drop), and

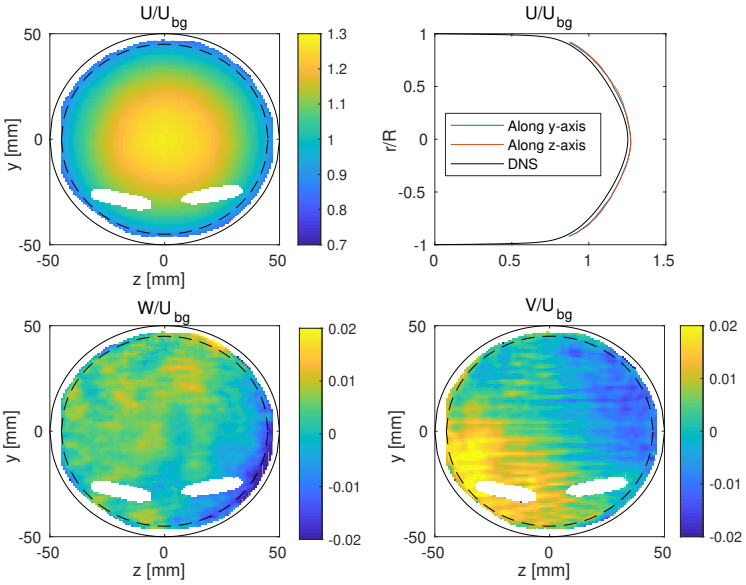

Figure 18: Mean flow results from stereoscopic PIV validation. Contour plots of streamwise (U), crosswise (W) and vertical (V) components, and comparison between the streamwise component and DNS by Wu & Moin (2008). All velocity components normalized by the bulk velocity U_{bg}.

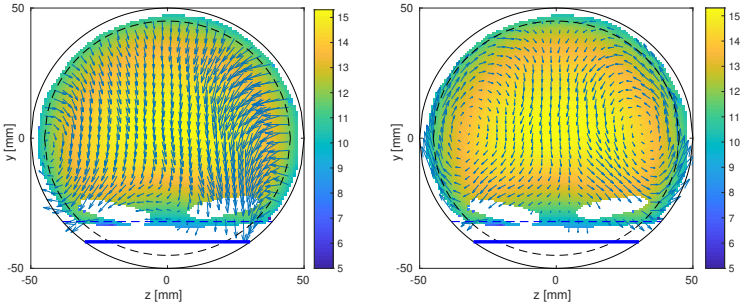

Figure 19: Comparison of velocity field before (a) and after (b) in-plane velocity correction by equation 5 and 6 for the $U_{sg} = 11.5$ m/s rough interface case.

compared with DNS results by Wu & Moin (2008). Figure 21 plots the distribution of the Reynolds shear stresses as well as the turbulent kinetic energy k in the cross section.

In general, we observe a fair agreement between the experimental results and the DNS by Wu & Moin (2008). It is noted that the velocity fluctuations in the radial direction along the y-axis, and circumferential direction along the x-axis are somewhat lower (approximately 10 %) than predicted by the DNS, owing to an underestimation of the velocity fluctuations in the y-direction compared with the DNS. The reason for this is not completely understood, but it is assessed that it will not have a significant impact on the analysis of the dominant gradients performed in section 4.2.1, as gradients of the stresses are well represented.

The contour plots in figure 21 illustrate that the distribution of $-\overline{u'_x u'_r}$ and k is close to circle-symmetric, although lower turbulence levels are observed near the pipe bottom. This is also seen in the $\sqrt{\overline{u'_\theta u'_\theta}}$, $\sqrt{\overline{u'_r u'_r}}$ and $\overline{u'_x u'_r}$ plots along the y-axis presented in figure 20. One possible explanation for this behavior is the development of a thin liquid film at the pipe bottom, caused by settling of the seeding particles (water droplets), which reduces the local shear. For the two-phase flows presented, this effect will not influence the results, as the region is already occupied by water, and omitted from the PIV calculations.

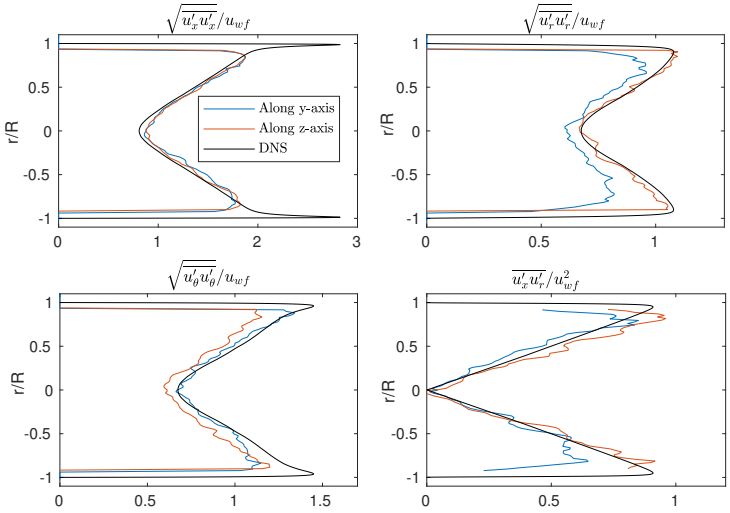

Figure 20: Comparison of experimental results of single phase flow at Re=44k and DNS results by Wu & Moin (2008). Results for rms of velocity fluctuations in the streamwise ($\sqrt{\overline{u'_x u'_x}}$), radial ($\sqrt{\overline{u'_r u'_r}}$) and circumferential ($\sqrt{\overline{u'_\theta u'_\theta}}$) direction, as well as shear stresses ($\overline{u'_x u'_r}$) (all normalized by wall friction velocity u_{wf}).

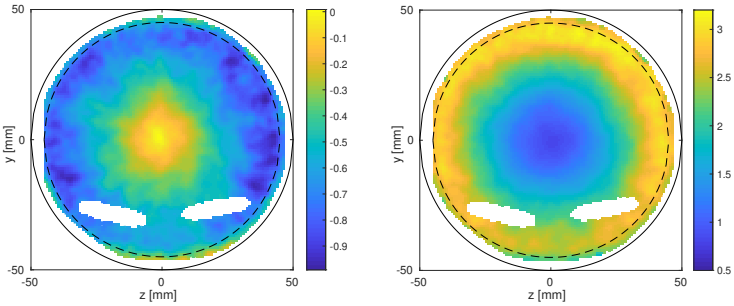

a) $-\overline{u'_x u'_r}/u^2_{wf}$ b) k/u^2_{wf}

Figure 21: Contour plots of Reynolds shear stresses ($-\overline{u'_x u'_r}$) and turbulent kinetic energy k (normalized by the wall friction velocity u_{wf}) in the pipe cross section.

References

Alletto, M. & Breuer, M. 2013 Prediction of turbulent particle-laden flow in horizontal smooth and rough pipes inducing secondary flow. *International Journal of Multiphase Flow* **55**, 80–98.

Andritsos, N. & Hanratty, T. J. 1987*a* Influence of interfacial waves in stratified gas-liquid flows. *AIChE journal* **33** (3), 444–454.

Andritsos, N. & Hanratty, T. J. 1987*b* Interfacial instabilities for horizontal gas-liquid flows in pipelines. *International journal of multiphase flow* **13** (5), 583–603.

Ayati, A. A., Kolaas, J., Jensen, A. & Johnson, G. W. 2014 A PIV investigation of stratified gas-liquid flow in a horizontal pipe. *International Journal of Multiphase Flow* **61**, 129–143.

Ayati, A. A., Kolaas, J., Jensen, A. & Johnson, G. W. 2015 Combined simultaneous two-phase PIV and interface elevation measurements in stratified gas/liquid pipe flow. *International Journal of Multiphase Flow* **74**, 45–58.

Ayati, A. A., Kolaas, J., Jensen, A. & Johnson, G. W. 2016 The effect of interfacial waves on the turbulence structure of stratified air/water pipe flow. *International Journal of Multiphase Flow* **78**, 104–116.

Belt, R. J., Daalmans, A. C. L. M. & Portela, L. M. 2012 Experimental study of particle-driven secondary flow in turbulent pipe flows. *Journal of Fluid Mechanics* **709**, 1–36.

Birvalski, M. 2015 *Experiments in stratified gas-liquid pipe flow*. TU Delft, Delft University of Technology.

Birvalski, M., Tummers, M. J. & Henkes, R. A. W. M. 2016 Measurements of gravity and gravity-capillary waves in horizontal gas-liquid pipe flow using PIV in both phases. *International Journal of Multiphase Flow* **87**, 102 – 113.

Bradshaw, P. 1987 Turbulent secondary flows. *Annual review of fluid mechanics* **19** (1), 53–74.

Darling, R. S. & McManus, H. N. 1968 Flow patterns in circular ducts with circumferential variation of roughness: a two-phase flow analog. In *Proceedings of the 11th Mid-Western Mechanics Conference Developments in Mechanics*, , vol. 5, pp. 153–170.

Davies, J. T. & Vose, R. W. 1965 On the damping of capillary waves by surface films. *Proceedings of the Royal Society of London. Series A. Mathematical and Physical Sciences* **286** (1405), 218–234.

Demuren, A. O. & Rodi, W. 1984 Calculation of turbulence-driven secondary motion in non-circular ducts. *Journal of Fluid Mechanics* **140**, 189–222.

Dykhno, L. A., Williams, L. R. & Hanratty, T. J. 1994 Maps of mean gas velocity for stratified flows with and without atomization. *International journal of multiphase flow* **20** (4), 691–702.

Espedal, M. 1998 An experimental investigation of stratified two-phase pipe flow at small inclinations. PhD thesis, Norwegian University of Science and Technology (NTNU), Department of Applied Mechanics, Thermo-and Fluid Dynamics.

Flores, A. G., Crowe, K. E. & Griffith, P. 1995 Gas-phase secondary flow in horizontal, stratified and annular two-phase flow. *International Journal of Multiphase Flow* **21** (2), 207–221.

Hand, N. P., Spedding, P. L. & Ralph, S. J. 1992 The effect of surface tension on flow pattern, holdup and pressure drop during horizontal air-water pipe flow at atmospheric conditions. *The Chemical Engineering Journal* **48** (3), 197–210.

Hanratty, T. J. & Engen, J. M. 1957 Interaction between a turbulent air stream and a moving water surface. *AIChE Journal* **3** (3), 299–304.

Hart, J., Hamersma, P. J. & Fortuin, J. M. H. 1989 Correlations predicting frictional pressure drop and liquid holdup during horizontal gas-liquid pipe flow with a small liquid holdup. *International Journal of Multiphase Flow* **15** (6), 947–964.

Henry, C.-H., Cregan, H. L. F., Dodds, J. M., Poole, R. J. & Dennis, D. J. C. 2018 Partially filled pipes: experiments in laminar and turbulent flow. *Journal of Fluid Mechanics*

848, 467–507.

Hinze, J. O. 1967 Secondary currents in wall turbulence. *The Physics of Fluids* **10** (9), S122–S125.

Hinze, J. O. 1973 Experimental investigation on secondary currents in the turbulent flow through a straight conduit. *Applied Scientific Research* **28** (1), 453–465.

Larsson, I. A. S., Lindmark, E. M., Lundström, T. S. & Nathan, G. J. 2011 Secondary flow in semi-circular ducts. *Journal of Fluids Engineering* **133** (10), 101206.

Liné, A., Masbernat, L. & Soualmia, A. 1996 Interfacial interactions and secondary flows in stratified two-phase flow. *Chemical Engineering Communications* **141** (1), 303–329.

Meknassi, F., Benkirane, R., Liné, A. & Masbernat, L. 2000 Numerical modeling of wavy stratified two-phase flow in pipes. *Chemical Engineering Science* **55** (20), 4681–4697.

Newton, C. H. & Behnia, M. 2001 A numerical model of stratified wavy gas–liquid pipe flow. *Chemical Engineering Science* **56** (24), 6851–6861.

Prandtl, L. 1927 Turbulent flow. International Congress for Applied Mechanics, Zurich 1926. Also as N.A.C.A. Tech Memo 435.

Spedding, P. L. & Hand, N. P. 1997 Prediction in stratified gas-liquid co-current flow in horizontal pipelines. *International journal of heat and mass transfer* **40** (8), 1923–1935.

Spedding, P. L. & Spence, D. R. 1993 Flow regimes in two-phase gas-liquid flow. *International journal of multiphase flow* **19** (2), 245–280.

Speziale, C. G. 1982 On turbulent secondary flows in pipes of noncircular cross-section. *International Journal of Engineering Science* **20** (7), 863–872.

Strand, O. 1993 An experimental investigation of stratified two-phase flow in horizontal pipes. *Dr. Scient. Thesis, University of Oslo. Oslo, Norway* .

Tzotzi, C. & Andritsos, N. 2013 Interfacial shear stress in wavy stratified gas-liquid flow in horizontal pipes. *International Journal of Multiphase Flow* **54**, 43 – 54.

Van Doorne, C. W. H. & Westerweel, J. 2007 Measurement of laminar, transitional and turbulent pipe flow using stereoscopic-piv. *Experiments in Fluids* **42** (2), 259–279.

Van't Westende, J. M. C., Belt, R. J., Portela, L. M., Mudde, R. F. & Oliemans, R. V. A. 2007 Effect of secondary flow on droplet distribution and deposition in horizontal annular pipe flow. *International journal of multiphase flow* **33** (1), 67–85.

Vollestad, P., Ayati, A. A., Angheluta, L., LaCasce, J. H. & Jensen, A. 2019 Experimental investigation of airflow above waves in a horizontal pipe. *International Journal of Multiphase Flow* **110**, 37–49.

Wu, X. & Moin, P. 2008 A direct numerical simulation study on the mean velocity characteristics in turbulent pipe flow. *Journal of Fluid Mechanics* **608**, 81–112.

Xiao, J. J. & Shoham, O. 1991 Evaluation of interfacial friction factor prediction methods for gas/liquid stratified flow. In *SPE Annual Technical Conference and Exhibition*. Society of Petroleum Engineers.

Paper II

Experimental investigation of airflow above waves in a horizontal pipe

II

Petter Vollestad, Anis Awal Ayati, Luiza Angheluta, Joseph Henry LaCasce, Atle Jensen

Published in *International Journal of Multiphase Flow* **110** (2019), pp. 37–49.
DOI: 10.1016/j.ijmultiphaseflow.2018.08.008.

Experimental investigation of airflow above waves in a horizontal pipe

P. Vollestad[1,*], A.A. Ayati[1], L. Angheluta[2], J.H. LaCasce[3], A. Jensen[1]

[1] *Department of Mathematics, University of Oslo, Norway*

[2] *Department of Physics, University of Oslo, Norway*

[3] *Department of Geosciences, University of Oslo, Norway*

[*] *Corresponding author. E-mail: pettervo@math.uio.no.*

Abstract

We investigate the effect of waves on the airflow in horizontal two-phase pipe flow. Velocity fields in the gaseous phase were acquired by particle image velocimetry (PIV), while interfacial elevation was measured with conductance wave probes. The velocity fields were sampled on a wave-following coordinate system which allows for a decomposition of the velocity field into a mean, wave-coherent and fluctuating component by means of a three-component Reynolds decomposition. Additionally, coherent vortical structures were identified by the swirling strength criterion, and their distribution along the waves is investigated.

Results suggest that the interaction between turbulent airflow and propagating waves in a pipe has a number of features reminiscent of wind-wave interaction in open systems. Above waves generated by sufficiently high gas flow rates, there is a distinct region of sheltered airflow, and a lifting of the critical layer on the leeward side of the crest. Streamlines of the phase-averaged flow field show a cat's eye structure located close to the crest in this region. Above waves of moderate steepness, we observe a shear layer that remains adjacent to the wave surface. Above steeper waves and higher gas flow rate, this layer detaches from the surface just downstream of the crest. Shear layer separation above waves is traditionally linked to the onset of wave breaking, and it is interesting to note that the case where we observe a separated shear layer in the phase-averaged vorticity field is in a regime of amplitude saturation.

The swirling strength criterion reveals that vortical structures are shed from the interface and populate the detached shear layer above the trough. Below the detached shear layer, there is a region populated by counter-rotating vortices. The critical height coincides with the border between these two regions.

Keywords: Two-phase pipe flow, Stratified flow, PIV, Vortical structures

1. Introduction

The interaction between a turbulent gas flow and propagating waves on a liquid layer plays an important role in the exchange of mass, momentum and heat across the interface. It is therefore an important problem to a wide range of research areas ranging from air-sea interactions to gas-liquid flow in pipes. The latter is relevant to engineering applications in petroleum, nuclear and process industries.

On the ocean surface, the rate at which momentum is exchanged between wind and waves depends on the wind to wave speed ratio (wave age). In situations where the waves are young, momentum is transferred from wind to waves by the action of form drag and viscous stresses, leading to wave growth and onset of surface currents (Grare *et al.*, 2013). Proper understanding and modelling of these mechanisms is important to weather- and climate models as they rely on

the parametrization of scalar and momentum fluxes across the air-sea interface (Janssen, 2004). A large number of experimental (e.g. Buckley & Veron (2016); Grare *et al.* (2013); Banner & Peirson (1998); Reul *et al.* (2008)) and numerical studies (including LES (Large Eddy Simulations) and DNS (Direct Numerical Simulations, e.g. Sullivan *et al.* (2018); Hara & Sullivan (2015); Yang & Shen (2010)) has significantly improved our understanding of wind-wave interaction over the past decades. DNS has also been applied to study the initial development and growth of the wave-field under the action of wind (Lin *et al.*, 2008; Zonta *et al.*, 2015, 2016), where the wavenumber spectra of the initial capillary waves forming are found to follow the results from wave-turbulence theory (Deike *et al.*, 2014; Pan & Yue, 2014).

Turbulent gas-liquid flow in long pipes or channels includes many different flow regimes, from stratified to annular flow. The stratified regime occurs when gas and liquid velocities are relatively low; below the threshold for intermittent flow. If the gas velocity is sufficiently high, waves appear on the interface as a result of similar interfacial mechanisms as at the air-sea interface. The presence of waves leads to a complex two-way interaction between themselves and the turbulent gas flow. Depending on the gas-liquid velocity combination, different wavy flow patterns (sub-regimes) can be observed. Numerous investigators have studied and categorized the different sub-regimes, see for instance Tzotzi & Andritsos (2013) and Fernandino & Ytrehus (2006).

The main engineering aspect of the stratified regime consists of predicting flow parameters such as the pressure drop and liquid hold-up, as well as finding criteria for transition to slug flow. Engineers rely upon multiphase flow simulators (e.g. OLGA, see Bendiksen & Espedal (1992) and LedaFlow) to simulate the flow inside pipelines over large distances. Naturally, the inherent complexity of the flow calls for significant simplifications of the problem in exchange for computational efficiency. The most common modelling approach is the so-called one-dimensional two-fluid model, that is, the velocity field in each phase is considered one-dimensional. Conservation equations are solved separately for each phase and connected at the interface through relevant kinematic and dynamic boundary conditions. This approach depends on closure relations for the interfacial friction. This particular step is a source of significant discrepancies between model predictions and experimental or field measurements. As a consequence, a large number of proposed friction factor correlations can be found in the literature, e.g. Andritsos & Hanratty (1987) and Biberg (2007).

There is also a significant disparity in proposed mechanisms explaining interfacial wave growth and transition to slug flow. These include; i) linear stability of a stratified two-layer flow, e.g. one-dimensional viscous Kelvin-Helmholtz instability (Barnea & Taitel, 1993) or two-dimensional Orr-Sommerfeld analysis (Barmak *et al.*, 2016; Kaffel & Riaz, 2015), ii) local instability on top of a growing long wave (Kordyban & Ranov, 1970; Woods *et al.*, 2000) or, iii) non-linear wave interaction (Sanchis *et al.*, 2011; Campbell & Liu, 2016).

The lack of consensus on the subject calls for additional phenomenological studies exploring mechanisms that do not feature in present models. One of such mechanisms is flow separation above steep waves (Gent & Taylor, 1977; Banner & Melville, 1976). It is well known that airflow separation may have an important impact on interfacial momentum fluxes in turbulent gas-liquid flows (Makin & Kudryavtsev, 2002; Banner & Peirson, 1998).

Recent experimental studies using Particle Image Velocimetry (PIV) have led to a better understanding of the structure of the two-dimensional flow field in air-water flow in pipes (Ayati *et al.*, 2014; Birvalski *et al.*, 2014), and in large wind-wave channels (Reul *et al.*, 2008; Veron *et al.*, 2007; Buckley & Veron, 2016). In previous studies, Ayati *et al.* (2014, 2015, 2016) combined PIV, conductance probing and hot-wire anemometry in order to acquire two-dimensional (2D) spatially resolved simultaneous measurements of both the gaseous and liquid flow fields, interfacial elevation statistics, and velocity fluctuations in the gaseous phase. The main outcome from the PIV measurements were presented in the form of spatio-temporally averaged velocity profiles. Such base flow profiles provide interesting flow information and can be used to conduct realistic stability analysis studies.

However, they do not provide insight on the phase-dependency of the flow structure. This can only be achieved by conducting phase-locked measurements (Ayati *et al.*, 2017) or by performing conditional-averaging techniques on statistically independent velocity fields. The latter is the scope of this paper.

Thus, in this study, we extend previous works by Ayati *et al.* by performing conditional phase-averaging on the gas-phase flow field, similar to the technique employed by Birvalski *et al.* (2014) and Siddiqui & Loewen (2010) on the liquid phase. This enables us to decouple the wave-coherent fluctuations from residual fluctuations (turbulence and noise), and to study the phase-dependency of the velocity field and the distribution of vortical structures along an average wave profile. Note that some alternative results from this analysis has been presented in a conference proceeding (Ayati *et al.*, 2018), highlighting main results from different studies on the topic of two-phase stratified pipe flow.

In order to keep the paper concise, we conduct a detailed comparison of two different flow cases in which the liquid superficial velocity is kept constant at $U_{sl} = 0.1$ m/s, whilst the gas velocity increases from $U_{sg} = 1.5$ in case A, to 2.1 m/s in case B. These cases were selected as they feature in two different sub-regimes, as shown by Ayati & Carneiro (2018). Case A belongs to a region of flow conditions in which waves grow as a consequence of increasing gas flow rates. In this regime, interfacial elevation statistics are well described by the Gaussian wave model (Onorato *et al.*, 2013), indicating that these waves behave quasi linearly. Meanwhile, case B belongs to a regime in which wave amplitudes remain more or less constant within a wide range of gas velocities above $U_{sg} = 1.75$ m/s. In this regime, the waves are steeper and their statistical distributions deviate strongly from Gaussian statistics, implying the presence of non-linear processes (Ayati & Carneiro, 2018). Similar results have been reported by Toffoli *et al.* (2017) for a circular, fetch-unlimited wind-wave tank. They also observed that waves in a growth regime were well represented by Gaussian statistics, while strong deviations from Gaussian statistics were observed as the wave field reached a stationary state.

Saturation of wave growth in confined gas-liquid flows has been addressed by several investigators, see for instance Jurman *et al.* (1992) and Campbell *et al.* (2016). They both attributed this phenomenon to non-linear energy transfer from linearly unstable to stable interfacial modes through sub-harmonic and triadic resonances. Although these are sophisticated approaches, they do not address the role of modified momentum flux due to changes in the gas flow structure. Thus, a more specific motivation for this study is to investigate whether the proposed phase-averaging technique can reveal new dynamics in the gas flow field that may further explain this sub-regime transition.

This paper is organized as follows; the experimental setup and data processing methodology are presented in section 2. Results and discussions are presented in section 3, which includes instantaneous and phase-averaged flow fields and an investigation of the phase-distribution of vortical structures. Finally, concluding remarks are outlined in section 4.

2. Experimental setup and methodology

2.1. Experimental setup

The data under investigation were acquired during an experimental campaign conducted at the Hydrodynamics Laboratory, University of Oslo. The experimental techniques (PIV, conductance probing and hot-wire anemometry) were combined to study air-water flow in pipes (Ayati *et al.*, 2014, 2015, 2016). Here, we will primarily focus on the data stemming from PIV in the air phase, and use some of the results from the wave gauges.

A 31 m long horizontal acrylic pipe with internal diameter D = 100 mm was used in the experiments, the test fluids were air and water at atmospheric pressure. Fluorescent dye (Rhodamine B) was added to the water in order to increase the intensity jump across the interface (enabling

efficient interface detection from the PIV images) and minimize local light reflections. Both fluids were introduced at the pipe inlet using frequency-regulated pump and fan, for the water and gas, respectively. A plate separating the two phases at the inlet caused the liquid phase to be introduced without waves, these developed along the pipe due to the airflow above the liquid interface. For each experimental case considered the gas and liquid flow rates were kept constant for some time before the measurements started, ensuring that the statistical properties of the flow were constant at the measurement section during the experiments. The water and air mass flow rates were measured with an Endress Hauser Promass and an Emerson MicroMotion Coriolis flow meter, with 0.2 % and 0.05 % of maximum measured values in accuracy, respectively. A schematic view of the experimental setup is shown in figure 1.

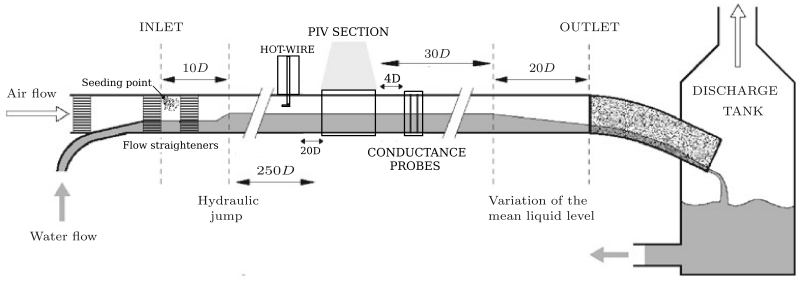

Figure 1: Schematic view of the experimental setup in use. Figure from Ayati *et al.* (2016).

A wave gauge was placed approximately 270D downstream from the pipe inlet. The gauge consisted of two double-wire probes made of platina wires of 0.3 mm diameter and separated by 4 mm. Both probes were placed in the center of the pipe with a distance $d = 60$ mm in the streamwise direction, enabling calculation of the wave speed through cross-correlation methods. Interface elevation was measured with a relatively high temporal resolution of 500 Hz. For more details about the interface elevation measurements, the reader is referred to Ayati *et al.* (2015).

Simultaneous two-phase PIV (S2P-PIV) was conducted along the pipe centerline in a PIV section located approximately 260D downstream from the pipe inlet. A double-pulsed Nd:YAG laser of 135 mJ illuminated a vertical plane along the pipe centerline from above. The images were recorded with two 14-bit PCO.4000 cameras (one for each phase). The gas-phase camera was located 15 cm above the pipe centerline, tilted 15° downwards, with a horizontal field of view (FOV) of 90 mm. The gas phase was seeded with small water droplets, injected at the pipe inlet using a high-pressure atomizing nozzle. The nozzle produces small particles (according to the manufacturers specifications, 72 % of the droplets are below 6 μm), which are found to behave as passive tracers for the flow rate combinations under investigation (Ayati *et al.*, 2014). Double images with a time delay of 250-300 μs (depending on the flow rate combinations) were acquired at a rate of 0.3 Hz. For each experimental case, 1000 image pairs were obtained from the experiments. The S2P-PIV has been described in more detail by Ayati *et al.* (2014). In the present work only the images of the air-phase are analyzed.

For the present study the air phase PIV images have been re-analyzed using an in-house PIV routine based on cross-correlation (Kolaas, 2016). A cascade of cross-correlation passes with increasingly fine subwindow sizes was applied. The final subwindow size was 40x20 pixels, with 75 % overlap. This resulted in a spatial resolution of approximately 0.25x0.25 mm^2. Subpixel interpolation is performed with a 3x3 gaussian subpixel estimator, and outliers are detected and replaced by means of a 3x3 local median filter. The fraction of spurious vectors were maximum near the interface, typically in the range of 15 %. The results from the present cross-correlation procedure

has been compared with the results obtained by Ayati *et al.* (2016). The results for the mean flow structures are similar, and no qualitative differences are found on the phase-averaged velocities presented in this paper comparing the two sets of results. However, due to higher spatial resolution, it is possible to extract more details of the small scale vortical structures from the updated velocity profiles, presented in section 3.3.

2.2. Conditional phase-averaging procedure

In this section the conditional phase-averaging routine is described. The first step in the analysis is to detect the interface between the gas and liquid phase. The methodology used by Ayati *et al.* (2015), in which the interface is detected from the differences in light intensity across the water interface of the PIV images was used also here, and a manual control of all the detected interfaces was performed.

The field of view, which was 90 mm in width, was not wide enough to fully resolve the dominant wavelengths present. These were in the range of 1.8 to 2.5 times the FOV width. For this reason the interface was divided into wave quadrants, and the averaging was performed for a sequence of velocity fields related to the same quadrant. A similar approach was employed by Siddiqui & Loewen (2010) and Birvalski *et al.* (2014), averaging the liquid phase beneath a wavy interface.

Wave quadrants were identified by means of a zero-crossing procedure. Between two consecutive zero-crossings, global maxima/minima were identified as crests/troughs. If a local maxima/minima (which is not on the edge of the PIV image) is detected to the left (right) of the first (last) zero-crossing of a PIV image, this is also assessed to be a crest/trough of a wave. The region in between a zero-crossing and a crest/trough was then classified as a wave quadrant according to the definition in figure 2. A minimum wave amplitude of 1 mm was used as a threshold in order to limit the influence of measurement uncertainties close to the interface (due to strong light reflections near the interface, see Ayati *et al.* (2014)). This threshold also governs that the minimum wavelength considered is approximately 50 mm, ensuring that all waves considered are gravity dominated waves (Birvalski *et al.*, 2015).

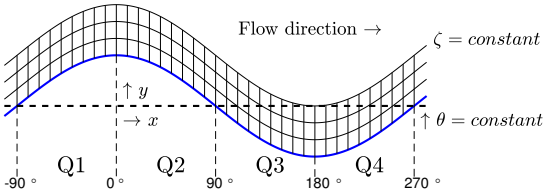

Figure 2: Definition of wave quadrants and illustration of wave-following coordinate system applied. Blue line: Water interface. Dotted horizontal line: Mean water level. Wave following coordinate system (θ, ζ) illustrated above the water interface.

The air domain was subjected to a coordinate transformation from Cartesian (x, y) to wave-following coordinates (θ, ζ). The crest, trough and zero-crossings were assigned phases of 0°, 180° and +/- 90°, respectively (see figure 2), whilst phases in between were linearly distributed. The vertical coordinate $\zeta = (y - \eta(x))/\eta_c$ is the dimensionless height above the interface, normalized by the crest height. The resulting coordinate system is illustrated in figure 2. Velocity fields above the identified wave quadrants are sampled from $\zeta = 0$ to 5. For each quadrant observed, all variables of the flow field (u, v, vorticity etc.) were sampled at the equally distributed (θ, ζ) coordinates, with 180 points in the θ-direction and 100 points ζ-direction.

The normalization of the vertical coordinate ensures that points in the trough-to-crest region are averaged with other points located at the same relative position in the trough-to-crest region. Outside of this region, where the wave amplitude is no longer a characteristic length scale of the flow,

the normalization is less relevant. For this reason, the phase-averaging performed in the present work is mostly valuable in the crest-to-trough region. Alternative wave-following coordinate systems have been applied by, amongst others Buckley & Veron (2016); Hara & Sullivan (2015); Hsu *et al.* (1981), for flow above water waves in open channels. The advantage of these systems is that the vertical coordinate becomes horizontal when far away from the interface, i.e., $\zeta \to y$ as y becomes large. This removes artificial wave-coherent fluctuations far from the interface, caused by the varying vertical position of the wave-following coordinate system in the undisturbed region of the flow. As in the present study we are primarily interested in the region very close to the interface, the proposed coordinate system is assessed to be suitable.

As the wave field consists of a spectrum of wave components with varying heights, lengths and steepnesses (see figure 3), a criterion is employed prior to averaging. The wave steepness is known to have a significant impact on the airflow above waves, affecting the critical layer thickness, streamline patterns and potential for airflow separation above the waves (Gent & Taylor, 1977; Reul *et al.*, 2008). For this reason, quadrant steepness was chosen as the averaging criterion in this study. The steepness of each observed quadrant is defined as $\epsilon = \eta_{ct}/\lambda_q$, where λ_q is the quadrant length and η_{ct} is crest/trough height relative to the mean water level. Typical scatter plots of quadrant lengths and crest/trough heights are shown in figure 3. Wave quadrants of equal steepness are found along straight lines from the origin. Thus, by averaging over realizations along different lines, we may evaluate the influence of steepness on the airflow. In order to achieve a valuable number of averaging realizations, a steepness range is defined as $\epsilon_0 \pm \alpha\epsilon_0$, where α represents fractional variation in steepness. In the present study, α was adjusted such that a minimum of 40 quadrant observations were included in each averaging window. This was found to be a sufficient number for achieving a qualitative convergence of the velocity fields.

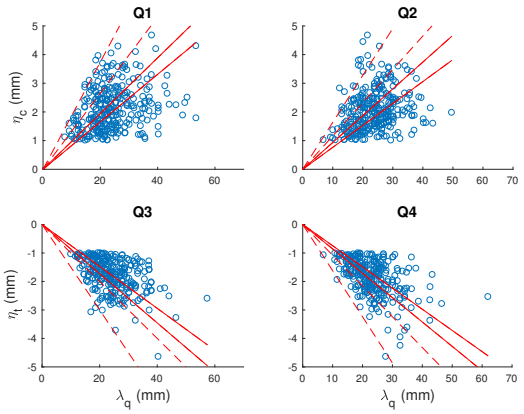

Figure 3: Typical scatter plot of quadrant lengths and crest/trough heights for one experimental case. Red lines indicate two ranges of steepness criteria; median steepness (solid lines) and high/maximum steepness (dashed lines).

Typical interface profiles selected on the basis of the steepness criteria are shown in figure 4. The variability in the interfaces detected is clearly visible. These variations have the effect of inducing an additional fluctuation into the fluctuating component of the decomposed velocity field (see section 2.3).

2.3. Three-component Reynolds decomposition

A three-component Reynolds decomposition is applied on the averaged velocity fields (Hsu *et al.*, 1981; Birvalski *et al.*, 2014; Buckley & Veron, 2016). For a given variable $q(x, y, t)$ in the flow field,

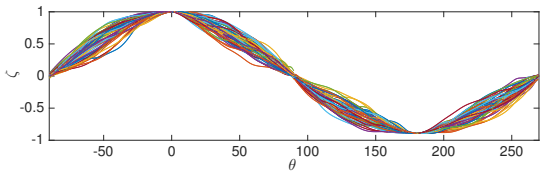

Figure 4: Quadrant interface profiles selected by means of the steepness criteria. Interfaces normalized according to wave-following coordinate system.

the variable is decomposed into a phase independent mean $\overline{q}(\zeta)$, a wave-induced field $\tilde{q}(\theta,\zeta)$ and a fluctuating component $q'(\theta,\zeta,t)$:

$$q(x,y,t) = \overline{q}(\zeta) + \tilde{q}(\theta,\zeta) + q'(\theta,\zeta,t) \tag{1}$$

The decomposition is illustrated in figure 5 for the horizontal velocity component u in a single Q2 observation. The phase-averaged variable $\langle q \rangle$ ($\langle q \rangle = \overline{q} + \tilde{q}$) is obtained by averaging several instantaneous velocity fields selected by the steepness criterion. $\overline{q}$ is evaluated based on $\langle q \rangle$ for all four wave quadrants. The wave-coherent component is then given as $\tilde{q} = \langle q \rangle - \overline{q}$, while the fluctuating component is evaluated as $q' = q - \langle q \rangle$. The fluctuating quantities u' and v' are often referred to as turbulent fluctuations (Birvalski *et al.*, 2014; Buckley & Veron, 2016). However, as the averaging is performed over a spectrum of waves the fluctuations should rather be interpreted as a combination of turbulence and fluctuations caused by variations of the air-water interface and the coordinate system applied.

Our focus will be on the phase-averaged ($\langle q \rangle$) and wave induced ($\tilde{q}$) components of the velocity field above the waves. The influence of interface variations on the fluctuating velocity components, coupled with a limited dataset, means that the Reynolds stresses (e.g. $\overline{u'v'}$) are not considered to provide a reliable measure for the turbulence. In order to get an impression of the variations of the small scale turbulent fluctuations along the wave, we extract vortical structures and investigate their variations over the waves (see section 3.3).

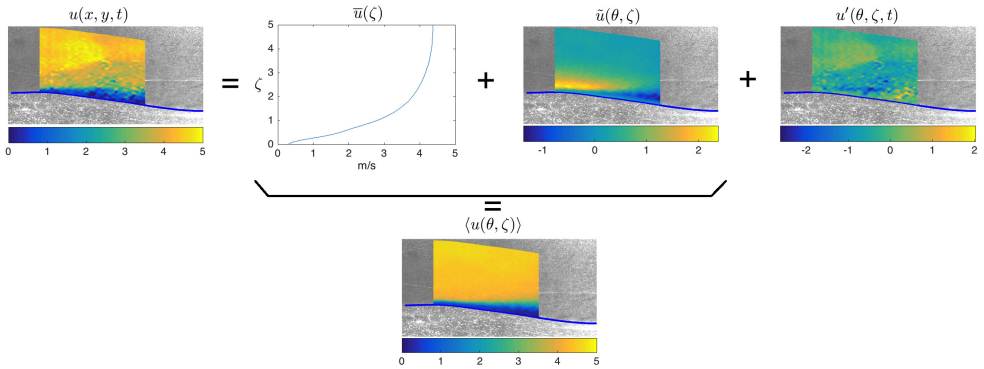

Figure 5: Illustration of the three-component decomposition of the horizontal velocity field applied in the study. Colorbars are in m/s. Velocity fields of identified quadrant overlaid original PIV image.

2.4. Experimental cases

Two experimental cases performed by Ayati *et al.* (2016) are revisited. The main characteristics of the two experimental cases are presented in table 1. Here U_{sf}, U_{bf}, Re_{Df}, with subscript $f = g, l$

Exp. case	U_{sl} [m/s]	U_{sg} [m/s]	U_{bl} [m/s]	U_{bg} [m/s]	Re_{Dg} [-]	Re_{Dl} [-]	η_{rms} [mm]	c [m/s]	λ_p [m]	$\overline{H}_w$ [mm]	c/u_* [-]
A	0.1	1.5	0.26	2.44	11 200	25 200	1.25	0.71	0.16	42	2.7
B	0.1	2.1	0.26	3.49	15 800	24 900	3.00	0.81	0.22	41	2.1

Table 1: Experimental cases under investigation.

indicating gas or liquid, are the superficial velocities, bulk velocities and Reynolds numbers which are based on the bulk velocity and hydraulic diameter. The relationship between bulk and superficial velocity is $U_{bf} = U_{sf}A/A_f$, where A_f is the cross-sectional area occupied by fluid f. Furthermore, η_{rms}, c, λ_p, $\overline{H}_w$ and c/u_*, are the root-mean-squared interface elevation relative to the mean water level (interface evaluated from PIV images), characteristic wave celerity given by means of cross-correlation of conductance probe signal, dominant wave-length based on the peak interfacial spectral density and wave celerity, mean liquid height and wave age, respectively.

The wave age c/u_* indicates that the waves are young, wind driven waves (Buckley & Veron, 2016; Belcher & Hunt, 1998). The friction velocity $u_* = \sqrt{\tau_i/\rho_g}$ was determined through the momentum balance equation, in which interfacial shear stress τ_i is balanced by the pressure drop and wall-friction. The pressure drop was measured over a 12.3 m section of the pipe, while the wall friction was estimated fitting a logarithmic profile to the mean velocity profile in the log-layer near the upper pipe wall ($30 < y^+ < 80$). Different methods for calculating the interfacial friction exists, providing slightly different results. Estimating the wall friction based on the Colebrook-White equation resulted in a 10 % deviation from the present method. While the calculated u_* is assessed to give a reasonable estimate for the wave age, and display clearly that we are in a regime of young, wind driven waves ($c/u_* < 5$ considered young waves), u_* should be used with care, as crosswise and spanwise variations in the wavefield means that the interface friction will vary along the pipe section. As the interface friction is estimated based on a pressure drop evaluated over a 12.3 m section of the pipe, this represents a characteristic interface friction for the system, rather than for the centerplane of the PIV section.

Detailed analysis of the evolution of the wave field with different U_{sl}/U_{sg}-combinations has previously been performed by Ayati *et al.* (2015) and Ayati & Carneiro (2018). Here it has been demonstrated that case A is in a region of the flow map where η_{rms} increases with increasing gas flow rates, while case B is in a region of "amplitude saturation", where η_{rms} is independent of the gas flow rate. Example time-series of the interface elevation measurements are presented in figure 6 a-b), while frequency spectra of the two experimental cases is presented in figure 6 c). Turbulence spectra in the air-phase (evaluated by hot-wire anemometry) has previously been presented by Ayati *et al.* (2016). These reveal an inertial range (-5/3 log-law), characteristic of a turbulent flow, and distinct low-frequency peaks related to the propagating waves.

From the two experimental cases, a total of three averaging cases (based on quadrant steepness) are analyzed. These are referred to as A1, A2 and B1. Details on the averaging cases are presented in table 2 and 3. Note that the experimental case A has two averaging cases, where A1 represents wave quadrants with median steepness, and A2 represents waves with the maximum steepness observed. Case B only has one averaging case (B1), representing waves with the median steepness.

From table 3, it can be seen that the waves at $U_{sg} = 1.50$ m/s (case A1 and A2) are fairly symmetric around the mean, whereas at $U_{sg} = 2.1$ m/s (case B1), they have tall and narrow crests and long and shallow troughs. This indicates that in case B1, the waves have some degree of non-linearity. This is in line with the characterization of the wave field by Ayati & Carneiro (2018), where it is found that the $U_{sg} = 1.50$ m/s case behaves according to Gaussian statistics, while the $U_{sg} = 2.1$ m/s case deviates significantly from linear theory. Furthermore, the second quadrant of case B1 is considerably shorter and steeper than the other quadrants. While case A2 has a higher

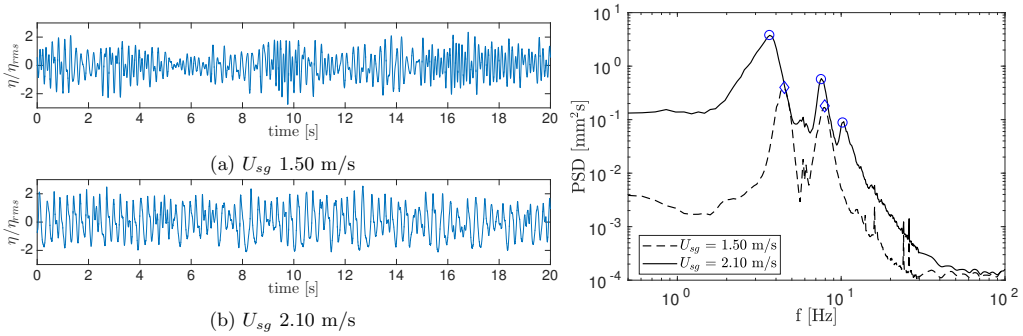

(a) U_{sg} 1.50 m/s

(b) U_{sg} 2.10 m/s

(c) Frequency spectra

Figure 6: a-b) Example interfacial elevation measurements for the two experimental cases. Normalized by η_{rms}. c) Interfacial power spectral density (PSD) for the two experimental cases

wave steepness (ak) than case B1, the Q2 steepness is higher for case B1. This is considered to be particularly important to airflow separation and possible microscale breaking events.

Avg. case	U_{sl}	U_{sg}	Q1			Q2			Q3			Q4		
			ϵ_0	α	N_{av}	ϵ_0	α	N_{av}	ϵ_0	α	N_{av}	ϵ_0	α	N_{av}
A1 - median ϵ	0.1	1.5	0.09	8 %	46	0.09	10 %	49	-0.08	8 %	47	-0.08	7 %	47
A2 - max ϵ	0.1	1.5	0.16	17 %	42	0.14	17 %	43	-0.12	20 %	40	-0.13	20 %	40
B1 - median ϵ	0.1	2.1	0.14	11 %	46	0.17	10 %	46	-0.09	10 %	44	-0.09	14 %	43

Table 2: Overview of three averaging cases. Quadrant observations with steepness within $\epsilon_0 \pm \alpha\epsilon_0$ used in averaging. N_{av}: number of wave quadrants within the selected limits.

Avg. Case	U_{sl}	U_{sg}	$\overline{\eta}_c$ [mm]	$\overline{\eta}_t$ [mm]	$\overline{\lambda}_{q,1}$ [mm]	$\overline{\lambda}_{q,2}$ [mm]	$\overline{\lambda}_{q,3}$ [mm]	$\overline{\lambda}_{q,4}$ [mm]	ak
A1 - median ϵ	0.1	1.5	2.0	-1.8	22.8	23.2	22.9	22.4	0.13
A2 - max ϵ	0.1	1.5	2.6	-2.5	17.1	18.1	19.6	18.3	0.22
B1 - median ϵ	0.1	2.1	5.5	-3.4	39.7	30.8	38.7	36.8	0.19

Table 3: Mean crest and trough elevation ($\overline{\eta}_t$, $\overline{\eta}_c$), and mean length $\overline{\lambda}_q$ of each quadrant for averaging cases considered. $ak = \pi(|\overline{\eta}_c| + |\overline{\eta}_t|)/(\overline{\lambda}_{q,1} + \overline{\lambda}_{q,2} + \overline{\lambda}_{q,3} + \overline{\lambda}_{q,4})$

3. Results and discussion

The results section is divided into three parts. First, instantaneous velocity fields for each averaging cases are presented in section 3.1. Secondly, phase-averaged velocity fields are shown in section 3.2, and lastly, the distribution of vortical structures along an average wave profile is investigated in section 3.3.

3.1. Instantaneous flow fields and intermittent airflow separation

In figure 7 the horizontal velocity and the spanwise vorticity over waves with a Q2 steepness matching the intervals used for the three averaging cases are presented. Figure 7 a) and b) demonstrate the flow field dependency on the Q2 steepness. At low steepness, both the velocity and vorticity fields are relatively unaffected by the wave, except for a small region at x = [30-40] mm where a small undulation induces extra vorticity. This particular observation is interesting as it

shows the effect of surface roughness caused by small waves riding on top of long waves. In general, the shear layer is seen to remain adjacent to the water surface. At higher steepness but same air velocity (figure 7 b), a region of sheltered flow is more visible behind the crest. The vorticity field shows sign of detachment at $x \approx 0$ mm. These features are more pronounced in figure 7 c), where both the air velocity and wave steepness are higher. Herein, the region of sheltered flow is considerable and negative axial airflow is observed on the leeward side of the crest. The negative vorticity layer is seen to separate from the crest and a region of positive vorticity is seen above the trough, between the water surface and the separated shear layer. The phase-averaged statistics of the vorticity field will be investigated in section 3.3.2.

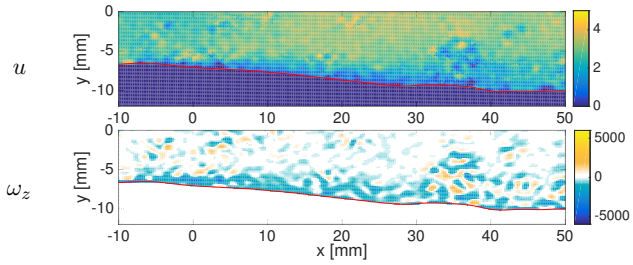

a) U_{sg} 1.50 m/s, $\epsilon_{Q2} \approx 0.08$ (Case A1)

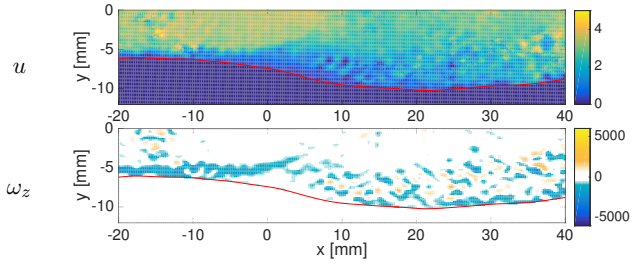

b) U_{sg} 1.50 m/s, $\epsilon_{Q2} \approx 0.14$ (Case A2)

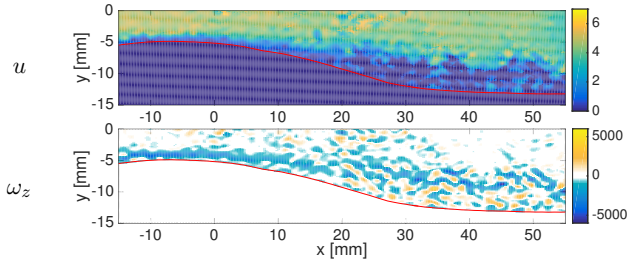

c) U_{sg} 2.10 m/s, $\epsilon_{Q2} \approx 0.16$ (Case B1)

Figure 7: Contour plot of horizontal velocity [m/s] (top) and spanwise vorticity [s^{-1}] (bottom) for three instantaneous PIV velocity fields. Representative flow field for the three averaging cases: a) median steepness U_{sg} 1.50 m/s (case A1), b) maximum steepness U_{sg} 1.50 m/s case (case A2), c) median steepness U_{sg} 2.10 m/s (case B1).

Airflow separation has traditionally been linked to the onset of wave breaking (Gent & Taylor, 1977; Banner & Melville, 1976; Reul *et al.*, 2008). Recent experimental (Veron *et al.*, 2007) and numerical (Sullivan *et al.*, 2018) analysis does however indicate that while airflow separation is a sufficient criterion for separation, it is not a necessary criterion, as airflow separation has been reported over non-breaking waves.

Buckley & Veron (2016) considered the airflow as separating "if the near-surface, high vorticity layer characteristic of an attached boundary layer is ejected away from the water surface and the surface vorticity is near zero or negative"[1]. Figure 7 c) demonstrates that (instantaneous) separation of the shear layer occurs for case B1. While no strong breaking (breaking with air entrainment) was observed during the experiments, we are currently not able to assess whether weak forms of wave breaking (microscale breaking) coincides with the airflow separation observed in figure 7 c). The steep wave-fronts observed for the U_{sg} 2.10 m/s case (ref. section 2.4) is a strong indicator of wave breaking, and visual observations of the waves at $U_{sg} = 2.10$ m/s indicate that weak forms of wave breaking is intermittently occuring. However, as demonstrated by Siddiqui & Loewen (2006), while microbreaking is well correlated with high wave steepness, the maximum wave slope is not a sufficient criterion for detecting breaking. Hence, at this stage we are not able to quantify the frequency of small-scale wave breaking in the system, or relate these events directly to the observed airflow separation.

3.2. Phase-averaged velocities

The phase-averaged horizontal ($\langle u \rangle$), vertical ($\langle v \rangle$), mean horizontal ($\overline{u}$) and the wave-coherent horizontal velocity ($\tilde{u}$) for averaging cases A1, A2 and B1 are presented in figure 8, plotted above the mean interface evaluated for each averaging case. The critical height z_i (defined as the height where $\langle u \rangle = c$) is indicated by a red-dotted line in the $\langle u \rangle$ fields. Note that the mean vertical velocity profile and vertical wave-coherent field are not shown to avoid overcrowding the figures. The former is nearly zero, and as $\tilde{v} = \langle v \rangle - \overline{v}$ it will be nearly equal to $\langle v \rangle$.

Figure 8 a) and b) show that with constant wind conditions, higher wave steepness affects both the phase-averaged vertical velocity $\langle v \rangle$ and the wave-coherent horizontal velocity $\tilde{u}$. Larger steepness induces stronger positive $\langle v \rangle$ upstream of the crest and stronger negative $\langle v \rangle$ above the trough. Also $\tilde{u}$ is stronger above the crest and trough.

As expected from the instantaneous flow fields (section 3.1), a significant sheltered region is observed behind the crest of case B1 (figure 8 c). Furthermore, while the critical height is adjacent to the wave surface in both case A1 and A2, it lifts at approximately $\theta = 30°$, and reattaches at approximately $\theta = -50°$ in case B1. Note that the critical height is based on the characteristic wave speed c for each experimental case (ref. section 2.4). While some variations in the wave speed was observed considering the cross correlation of individual wave components, these were relatively small, and selecting a different characteristic wave speed within the range observed will not qualitatively change the evolution of the critical height plotted in figure 8.

The wave-coherent mode of case B1 contains, in its peak, almost 50% of the mean flow velocity. The wave-coherent velocities are directly related to the low frequency peak fluctuations measured by the hot-wire probes presented by Ayati *et al.* (2016).

Note that while case A1 and B1 provide relatively smooth transitions between the four wave quadrants, case A2 exhibits more abrupt transitions. This indicates that the steepness combination chosen for case A2 is not characteristic of the waves in the system. While the averaging illustrates how the (high) steepness affects the flow in each individual quadrant, the combination of the four quadrants presented in figure 8 b) does not necessarily represent the typical flow over steep waves in the system. For these reasons, we will focus on the cases A1 and B1 in the following.

When comparing cases A1/A2 and B1, it should be recalled that as the vertical coordinate ζ is normalized by the crest amplitude, the maximum ζ value in case B1 represents a larger physical distance from the interface compared with case A1/A2. In fact, $\zeta = 5$ in case B1 is approximately midway between the interface and upper wall. For this reason, the mean velocity profile in case B1

[1]Due to a difference in the coordinate system applied, there is a sign change in the vorticity when comparing the results of this study with the study of Buckley & Veron (2016)

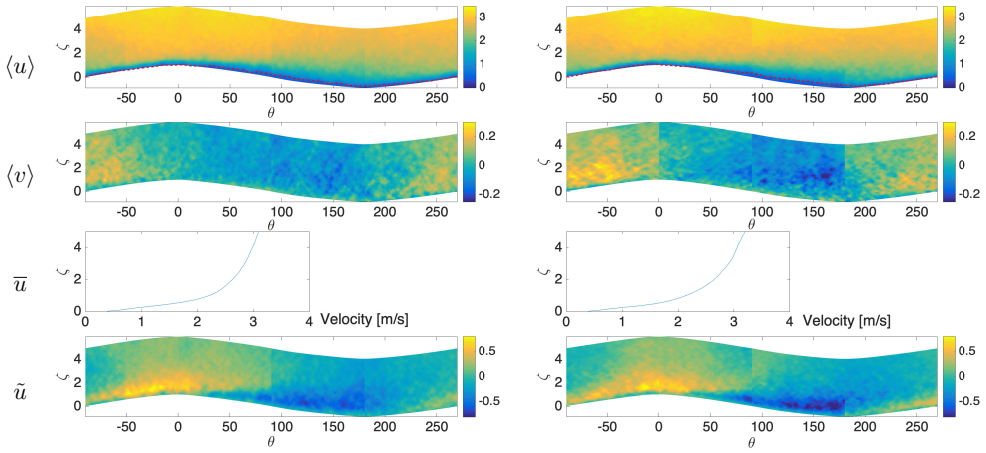

a) U_{sg} 1.50 m/s, $ak = 0.13$ (case A1) b) U_{sg} 1.50 m/s, $ak = 0.22$ (case A2)

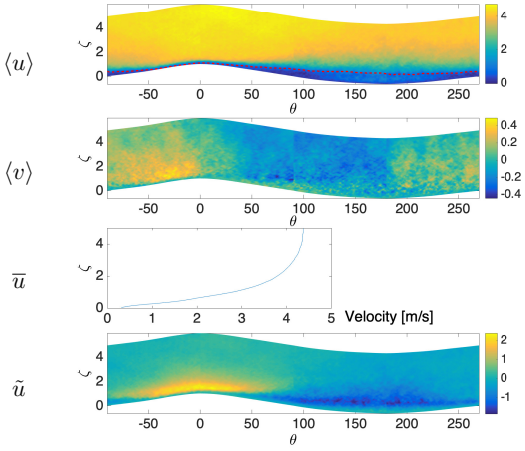

c) U_{sg} 2.10 m/s, $ak = 0.19$ (case B1)

Figure 8: Mean flow structure of the three averaging cases investigated. All velocities are in [m/s]. Red-dashed line of the $\langle u \rangle$ plot indicates the location of the critical height z_i

reaches its centerline value at $\zeta = 5$, while this does not happen for cases A1 and A2. Nonetheless, the mean velocity profiles provide valuable information concerning the boundary layer, i.e. the region with strong velocity gradient. It stretches up to $\zeta \approx 1$ in cases A1 and A2 and to $\zeta \approx 2$ in case B1. This indicates that large amplitude waves induce a thicker boundary layer, i.e., momentum is pushed away from the interface. This effect is related to the wave induced stress $-\tilde{u}\tilde{v}$. The results of the phase averaged velocities presented in figure 8 are qualitatively in agreement with the results presented by Buckley & Veron (2016) for airflow over slow waves in an open system. As discussed by Buckley & Veron, the airflow pattern gives rise to a negative wave induced momentum flux, transporting horizontal momentum away from the interface.

In figure 9, the streamlines of the phase-averaged velocity field, seen in a frame of reference moving with the representative wave speed, is plotted for cases A1 and B1. The streamlines are coloured with the kinetic energy of the phase averaged flow field $(0.5(\langle u \rangle^2 + \langle v \rangle^2)$.

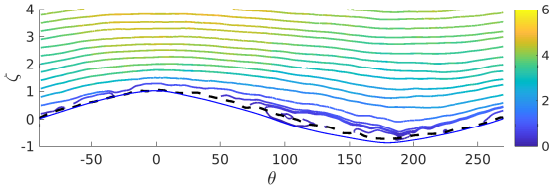

a) U_{sg} 1.50 m/s, $ak = 0.13$ (case A1)

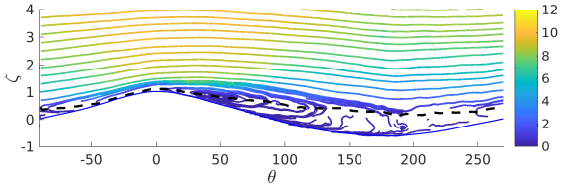

b) U_{sg} 2.10 m/s, $ak = 0.19$ (case B1)

Figure 9: Streamlines of $\boldsymbol{u} - c$ for averaged flow field. Colorbar represents kinetic energy of the mean flow divided by fluid density ($0.5(\langle u \rangle^2 + \langle v \rangle^2)$ $[m^2/s^2]$. Dashed line indicates the position of the critical layer.

In case A1, the streamlines closely follow the average wave profile, except near the critical layer, where two small regions of closed streamlines can be seen at $\theta = 100°$ and $180°$.

In case B1, a distinct cat's eye (Lighthill, 1962) is observed slightly downstream of the crest ($\theta = 50°$). The position of the cat's eye implies that on average the waves experience a co-moving pocket of air located slightly downwind of the crest. The streamlines adjacent to crest are pushed away from the wave surface and the shape of the streamlines above the cat's eye structure are shifted approximately 40°compared with the wave profile. This asymmetry of the flow field is believed to produce an asymmetric pressure distribution along the wave.

The results for case B1 are qualitatively similar to the LES results by Hara & Sullivan (2015), investigating a linear wave in open channel flow under strong wind forcing, with $c/u_* = 1.6$ and wave steepness $ak = 0.226$. As demonstrated by Hara & Sullivan, such an asymmetry in the critical layer causes the peak pressure to move downstream from the wave trough to the Q4 region. Here the high pressure pushes on the positive surface slope and contributes to the air-water momentum flux, pushing the wave in the flow direction. This effect is related to the sheltering effect by Jeffreys (1925), and the nonseparated sheltering by Belcher & Hunt (1998). Although there are differences between an open air-sea system and a closed pipe section, a similar effect is expected to apply in our experimental cases, and particularly in case B1 where a significant lifting of the critical height and asymmetry between the wave shape and streamlines above the wave is observed. The distribution of the mean flow kinetic energy (indicated by the colouring of the streamlines in figure 9) indicate that this is the case, as the horizontal position of the peak kinetic energy (associated with low-pressure zone) is seen to be located on the leeward side of the crest for case B1.

3.3. Vortical structures

The distribution of vortical structures gives insight into the turbulence of the flow, being one of the main features of turbulent wall-bounded flow (Chen *et al.*, 2014). The swirling strength criterion proposed by Adrian *et al.* (2000) is employed to identify vortical motion on the 2D PIV plane. The criterion discriminates regions of swirling motion from regions of shear, ensuring that coherent regions of swirling strength will contain rotational flow structures. A directional swirling strength is given as follows (Wu & Christensen, 2006):

$$\Lambda_{ci} = \lambda_{ci} \frac{\omega_z(x,y)}{|\omega_z(x,y)|}, \tag{2}$$

where λ_{ci} is the imaginary part of the complex eigenvalue of the velocity-gradient tensor and $\omega_z(x,y)$ is the spanwise vorticity. Λ_{ci} will be referred to as the swirling strength in the remainder of the paper. Using this definition, vortical structures with clockwise rotation will have a negative swirling strength, while vortical structures with an anti-clockwise rotation will have a positive swirling strength. Furthermore, the sign-dependent normalization scheme proposed by Chen *et al.* (2014) is applied to remove the wall-normal dependence of the swirling strength

$$\Lambda_n = \begin{cases} \frac{\Lambda_{ci}(x,y)}{\Lambda^+_{avg}(y)} & \text{if } \Lambda_{ci} > 0 \\ \frac{\Lambda_{ci}(x,y)}{|\Lambda^-_{avg}(y)|} & \text{if } \Lambda_{ci} < 0, \end{cases} \tag{3}$$

where $\Lambda^+_{avg}(y) = \langle \Lambda_{ci}(y) | \Lambda_{ci}(y) > 0 \rangle$ and $\Lambda^-_{avg}(y) = \langle \Lambda_{ci}(y) | \Lambda_{ci}(y) < 0 \rangle$. Λ_n is referred to as the normalized swirling strength.

As the flow is bounded by two boundaries (upper pipe wall and water interface), the normalization in equation 3 is modified slightly. Separate $\Lambda^+_{avg}(y)$ and $\Lambda^-_{avg}(y)$ are calculated for the region above and below the air center (midpoint between the mean interface and upper pipe wall). Above the air center y is the distance to the stationary upper wall, and below the air center y is the distance to the interface. Λ^+_{avg} and Λ^-_{avg} was evaluated for all available velocity fields (independent of wave quadrant dependency) for the two experimental cases investigated. Results are presented in figure 10. The profiles of Λ^+_{avg} and Λ^-_{avg} are seen to be continuous across the mean air centreline.

As the velocity gradient near the upper wall is larger than near the moving interface, the characteristic strength of vortical structures near the upper wall is higher than at the interface (see figure 10). Case A exhibits a narrow region of energetic structures close to the interface, resembling the (inverse) profile at the upper wall. Meanwhile, case B exhibits a thicker layer of strong vortices near the interface. This indicates that while the airflow in case A behaves approximately as the flow over a flat wall, vortical structures are considerably affected by the larger waves in case B.

In order to extract coherent regions of swirling motion, a non-zero threshold of $|\Lambda_n|$ has to be used. Chen *et al.* (2014) used a threshold of $|\Lambda_n| > 1$, this is also applied here. To reduce the probability of including vortical structures generated by errors in the PIV, a minimum of three vectors across is required for a region to constitute a vortical structure.

When evaluating the swirling strength, a 7x7 finite difference filter was applied. The filter acts to smooth out the calculated swirling strength field and small PIV errors. The filter also dictates the size of structures to be extracted, as a larger filter will identify larger regions of swirling motion, and hence extract larger structures. The filter size was chosen to ensure that the vortical structures extracted had a single vortex core, when a Galilean decomposition of the local velocity field was applied (see section 3.3.1). As we are mostly interested in the distribution of vortical structures in the crest-to-trough region, it was necessary to select a filter size able to extract structures smaller than the wave amplitude.

3.3.1. Instantaneous swirling events

In figure 11 instantaneous vector plots of the individual swirling events (coherent regions with $|\Lambda_n| > 1$) are plotted using a local Galilean decomposition of the velocity field. The normalization of the swirling strength ensures that vortical structures are identified throughout the pipe cross section, but the structures close to the interface and upper pipe wall are in general more energetic than at the pipe centre. Note that the region of the pipe from y = 20 to 30 mm is heavily influenced by local light reflections, hence this region is omitted from figure 10 and should not be trusted in figure 11.

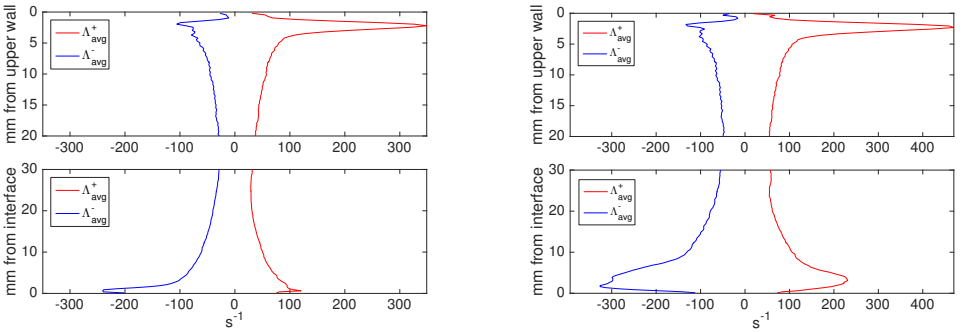

a) U_{sg} 1.50 m/s (case A). b) U_{sg} 2.10 m/s (case B).

Figure 10: Λ^{+}_{avg} and Λ^{-}_{avg} $[s^{-1}]$ evaluated above (top) and below (bottom) the mean air centerline for the two experimental cases. a) U_{sg} 1.50 m/s, and b) U_{sg} 2.10 m/s.

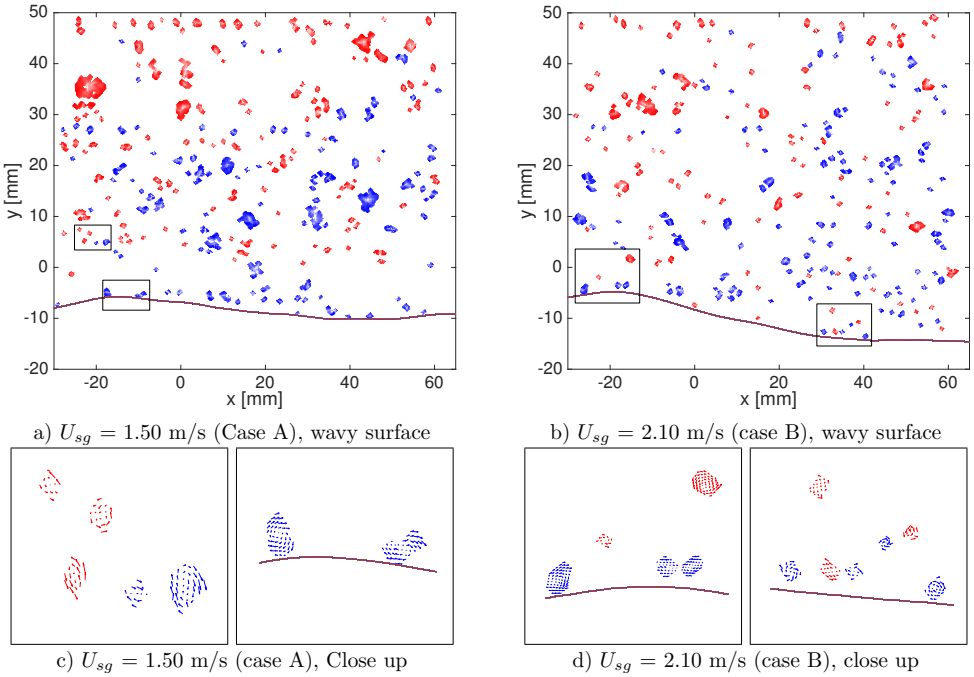

a) U_{sg} = 1.50 m/s (Case A), wavy surface b) U_{sg} = 2.10 m/s (case B), wavy surface

c) U_{sg} = 1.50 m/s (case A), Close up d) U_{sg} = 2.10 m/s (case B), close up

Figure 11: Local Galilean decomposition of the instantaneous flow field showing vector plots of each identified swirling event. Positive (counter-clockwise rotation) swirling events coloured in red. Negative (clockwise rotation) in blue. Flow direction from left to right. a-b) Instantaneous vortices for case A (a) and case B (b). c,d) Close up of vortical structures in figure a and b (location indicated by black box in a and b).

Figure 11 reveals a significant number of rotating structures of the flow. From the close-up section of figure 11 (c and d) it can be seen that the identified structures exhibit a rotating motion, when a local Galilean decomposition of the velocity field is used. Close to the top wall, positive vortices dominate. This is to be expected as the flow is directed from left to right in the plots. Close to the interfaces the identified vortices are small, ranging from approximately 1 to 3 mm in

diameter. Away from the interfaces some larger (up to 6 mm diameter) regions of positive (above the air center) and negative (below the air center) swirling events are observed. As a cut-off value ($|\Lambda_n| > 1$) is used, these size estimates are not absolute, but relate to the size of the high energy core of the vortex.

In case A (figure 11 a) the region above the interface is mainly populated by negative vortices. This is analogous to the vortices observed close to the top wall. For case B, positive vortices are observed close to the interface in the crest-to-trough region (figure 11 b). From the crest and along the streamwise direction, a number of negative swirling events are observed, suggesting that vortical structures on the windward side of the crest are shed locally. A similar observation was made by Ayati *et al.* (2016), analyzing instantaneous velocity fields like the ones presented in figure 11. More evidence of this behavior is seen in the next section.

3.3.2. Phase dependency of swirling events

During the phase-averaging procedure, the normalized peak strength and location of each identified swirling event was registered. Scatter plots of all swirling events for cases A1 and B1 are presented in figure 12 a) and b). In the middle part of figure 12 a) and b), the average number of swirling events within $0 \leq \zeta \leq 1$ and $0 \leq \zeta \leq 3$ is plotted as a function of wave phase. At the bottom, the average peak Λ_n within these intervals is plotted, also as a function of wave phase.

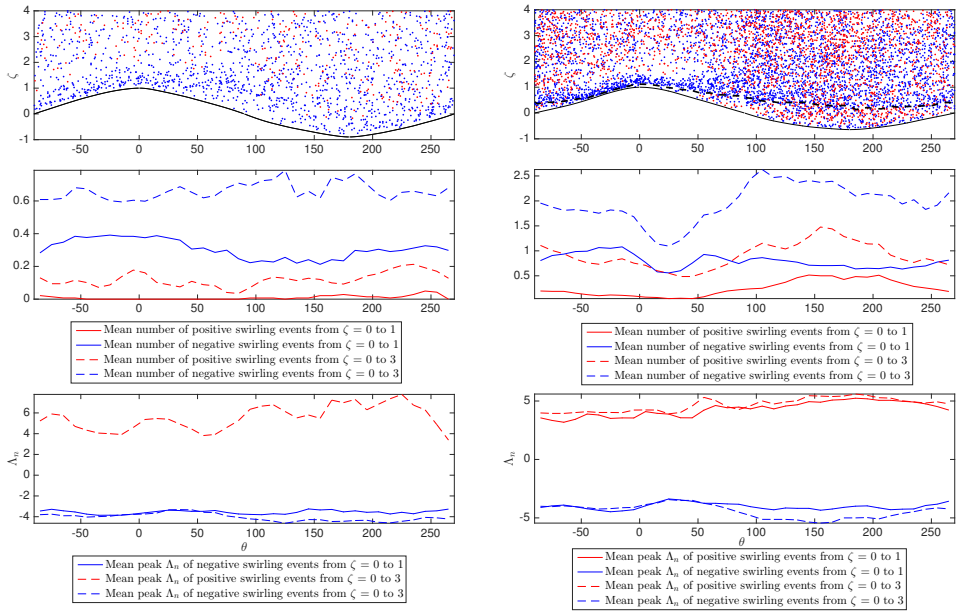

a) $U_{sg} = 1.50$ m/s, (case A1)

b) $U_{sg} = 2.10$ m/s, (case B1)

Figure 12: Phase dependency of swirling events for the two median steepness cases. Top: Scatter plot of all positive (red) and negative (blue) swirling events. Black dotted line represents critical height. Middle: Mean number of positive (red) and negative (blue) swirling events ($N_{sw}/(N_q \Delta\theta)$) from $\zeta = 0$ to 1 (full line) and from $\zeta = 0$ to 3 (dashed line). Bottom: Mean peak normalized swirling strength of positive (red) and negative (blue) swirling structures detected from $\zeta = 0$ to 1 (full line) and from $\zeta = 0$ to 3 (dashed line).

In case A1, the distribution of swirling events (figure 12 a) reveals only a weak phase dependence. Close to the interface ($0 \leq \zeta \leq 1$), there are slightly more negative swirling events above the crest

than on the leeward side of the wave. Note that the mean strength of positive vortices within $0 \leq \zeta \leq 1$ is not included in figure 12 a) since no positive swirling events were observed here. In general, case A1 exhibits a weak phase dependency in both registered swirling events and phase-averaged swirling strength, indicating that the waves do not significantly alter the distribution of vortical structures.

In case B1, a clear phase dependence of swirling events is observed (figure 12 b). Close to the interface ($0 \leq \zeta \leq 1$), a large concentration of negative swirling events is observed on the windward side of the wave, between the reattachment point of the critical layer to the crest ($-50° < \theta < 0°$). These vortices are then shed from the crest of the wave. Slightly downstream at θ=50°, the number of positive swirling events close to the interface increases, and reaches a maximum above the trough. These observations are further elucidated by the middle plot of figure 12 b), which clearly shows that there is a considerably higher concentration of vortices where the critical layer is lifted from the surface. The total number of swirling events (positive and negative combined) is maximum above the trough, indicating a highly turbulent region, characteristic of a separated shear layer (Buckley & Veron, 2016).

The bottom plot of figure 12 b) shows that although the variations in mean peak strength (Λ_n) are more subtle than the variation in number of swirling events, the vortices (both positive and negative) are more energetic above the trough.

The phase-averaged vorticity field $\langle \omega_z \rangle$ is plotted for all three averaging cases in figure 13. The vorticity field is seen to follow the critical height in case B1, and the criterion for shear layer separation is fulfilled for the phase-averaged vorticity field (ref. section 3.1). Below the critical height is a region dominated by positive vorticity. This is related to the high concentration of positive swirling events observed below the critical height (ref. figure 12 b).

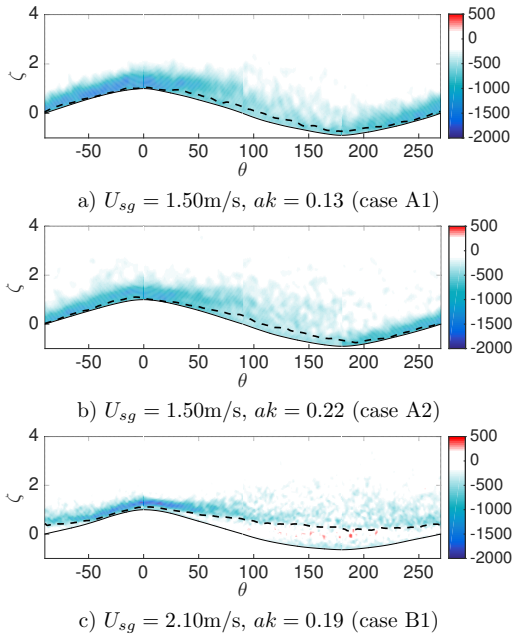

a) $U_{sg} = 1.50$m/s, $ak = 0.13$ (case A1)

b) $U_{sg} = 1.50$m/s, $ak = 0.22$ (case A2)

c) $U_{sg} = 2.10$m/s, $ak = 0.19$ (case B1)

Figure 13: Phase averaged vorticity field ($\langle \omega_z \rangle$) for the three averaging cases under investigation

It is interesting to note that shear layer separation is observed for case B1, as this experimental case is in the regime of "amplitude saturation" (ref. section 2.4). As discussed in section 3.1,

airflow separation above waves is traditionally linked to the onset of wave breaking, and while new experimental (Buckley & Veron, 2016) and numerical (Sullivan *et al.*, 2018) results indicate that separation may occur above waves without active wave breaking, the shear layer separation observed in case B1 is assessed to be a strong indication of dissipative mechanisms in the waves (microbreaking or spilling) which may help explain the amplitude saturation observed in previous studies (Ayati *et al.*, 2015).

In both A1 and A2 the high intensity vorticity field remains adjacent to the wave surface. Based on the instantaneous vorticity plots presented in figure 7 this is to be expected for A1, but for A2 the instantaneous vorticity field (figure 7 b) indicated a slight separation behind the crest. While a clear separation like the results observed for case B1 are not observed in either case A1 or A2, there is a marked reduction in the shear layer intensity along the third quadrant of the wave, and the phase averaged vorticity field is observed to extend further away from the interface in this region, indicating that intermittent airflow separation occurs also for these two cases, but that the frequency of occurrence is significantly lower than for case B1.

4. Concluding remarks

We present an experimental investigation of air-water flow in a horizontal pipe. Two experimental cases with $U_{sl} = 0.1$ m/s are investigated, increasing U_{sg} from 1.5 to 2.1 m/s. The first case contains small, moderate-steepness waves ($\eta_{rms} = 1.25$ mm, $ak \sim 0.13$ (median steepness)), whilst the second case contains higher and steeper waves ($\eta_{rms} = 3.00$ mm, $ak \sim 0.19$ (median steepness)).

The conditional phase-averaging procedure reveals that the velocity field at $U_{sg} = 2.10$ m/s displays a thicker region of sheltered airflow on the leeward side of the crest, compared with the flow at $U_{sg} = 1.50$ m/s. In this region the critical layer is seen to lift from the interface for the $U_{sg} = 2.10$ m/s case. In a wave co-moving frame of reference, the phase-averaged streamlines form a closed pattern (cat's eye) around the critical height and slightly downwind of the crest. This implies that the typical wave crest has a pocket of circulating air in its front. This is assessed to impact on the pressure field above the waves, resulting in increased form drag along the wave profile.

The analysis of small scale vortical structures and the evaluation of the average shear layer along the wave reveals significant differences between the two experimental cases. At $U_{sg} = 1.50$ m/s (considering both median and maximum wave steepness), we observe a shear layer dominated by negative vorticity that remains adjacent to the wave surface along the entire wave profile. At $U_{sg} = 2.10$ m/s, this layer detaches from the surface just downstream of the crest. The swirling strength criterion reveals that below the detached layer of negative vorticity, there is a region dominated by opposite-signed vortices. The border between these regions coincides with the critical height.

Airflow separation is known to alter the wind-to-wave momentum transfer, and while further analysis is needed to quantify the impact of separation on the momentum transfer (and wave-growth), it is interesting to note that the $U_{sg} = 2.10$ m/s case is in the region of amplitude saturation (Ayati *et al.*, 2015). Future studies will investigate whether the onset of separation is related to the amplitude saturation observed by Ayati *et al.* for superficial gas velocities above 1.75 m/s. To assess this question it will be necessary to obtain an improved understanding of how airflow separation, possible wave breaking and other dissipative mechanisms interact, considering the closed geometry and pressure driven flow which is characteristic of the two-phase pipe flow. This is the subject of current investigations.

Acknowledgement

The authors wish to acknowledge the strategic research initiative EarthFlows and the Academia program at the Faculty of Mathematics and Natural Sciences at the University of Oslo. Thanks to

Jostein Kolaas for help with the HydroLab PIV code. Laboratory Head Engineer Olav Gundersen is gratefully acknowledged for the technical assistance he provided for the experimental work.

References

Adrian, R. J., Christensen, K. T. & Liu, Z. C. 2000 Analysis and interpretation of instantaneous turbulent velocity fields. *Experiments in fluids* **29** (3), 275–290.

Andritsos, N. & Hanratty, T. J. 1987 Influence of interfacial waves in stratified gas-liquid flows. *AIChE Journal* **33**, 444–454.

Ayati, A.A., Kolaas, J., Jensen, A. & Johnson, G.W. 2014 A PIV investigation of stratified gas-liquid flow in a horizontal pipe. *International Journal of Multiphase Flow* **61**, 129 – 143.

Ayati, A.A., Kolaas, J., Jensen, A. & Johnson, G.W. 2015 Combined simultaneous two-phase PIV and interface elevation measurements in stratified gas-liquid pipe flow. *International Journal of Multiphase Flow* **74**, 45 – 58.

Ayati, A.A., Kolaas, J., Jensen, A. & Johnson, G.W. 2016 The effect of interfacial waves on the turbulence structure of stratified air-water pipe flow. *International Journal of Multiphase Flow* **78**, 104 – 116.

Ayati, A. A. & Carneiro, J. N. E. 2018 Statistical characterization of interfacial waves in turbulent stratified gas-liquid pipe flows. *International Journal of Multiphase Flow* **103**, 94–105.

Ayati, A. A., Farias, P. S. C., Azevedo, L. F. A. & de Paula, I. B. 2017 Characterization of linear interfacial waves in a turbulent gas-liquid pipe flow. *Physics of Fluids* **29** (6), 062106.

Ayati, A. A., Vollestad, P. & Jensen, A. 2018 Detailed measurements of interfacial dynamics in air-water pipe flow. *Procedia IUTAM* **26**, 59–69.

Banner, M. L & Melville, W. K. 1976 On the separation of air flow over water waves. *Journal of Fluid Mechanics* **77** (04), 825–842.

Banner, M. L. & Peirson, W. L. 1998 Tangential stress beneath wind-driven air–water interfaces. *Journal of Fluid Mechanics* **364**, 115–145.

Barmak, I., Gelfgat, A., Vitoshkin, H., Ullmann, A. & Brauner, N. 2016 Stability of stratified two-phase flows in horizontal channels. *Physics of Fluids* **28** (4), 044101.

Barnea, D. & Taitel, Y. 1993 Kelvin-helmholtz stability criteria for stratified flow: viscous versus non-viscous (inviscid) approaches. *International journal of multiphase flow* **19** (4), 639–649.

Belcher, S. E. & Hunt, J. C. R. 1998 Turbulent flow over hills and waves. *Annual Review of Fluid Mechanics* **30** (1), 507–538.

Bendiksen, K. & Espedal, M. 1992 Onset of slugging in horizontal gas-liquid pipe flow. *International journal of multiphase flow* **18** (2), 237–247.

Biberg, D. 2007 A mathematical model for two-phase stratified turbulent duct flow. *Multiphase Science and Technology* **19**, 1–48.

Birvalski, M., Tummers, M. J., Delfos, R. & Henkes, R.A.W.M. 2014 PIV measurements of waves and turbulence in stratified horizontal two-phase pipe flow. *International Journal of Multiphase Flow* **62**, 161–173.

Birvalski, M., Tummers, M. J., Delfos, R. & Henkes, R. A. W. M. 2015 Laminar-turbulent transition and wave-turbulence interaction in stratified horizontal two-phase pipe flow. *Journal of Fluid Mechanics* **780**, 439456.

Buckley, M. P. & Veron, F. 2016 Structure of the airflow above surface waves. *Journal of Physical Oceanography* **46** (5), 1377–1397.

Campbell, B. K., Hendrickson, K. & Liu, Y. 2016 Nonlinear coupling of interfacial instabilities with resonant wave interactions in horizontal two-fluid plane couettepoiseuille flows: numerical and physical observations. *Journal of Fluid Mechanics* **809**, 438479.

Campbell, B. K. & Liu, Y. 2016 A nonlinear flow-transition criterion for the onset of slugging in horizontal channels and pipes. *Physics of Fluids* **28** (8), 082103.

Chen, Q., Zhong, Q., Wang, X. & Li, D. 2014 An improved swirling-strength criterion for identifying spanwise vortices in wall turbulence. *Journal of Turbulence* **15** (2), 71–87.

Deike, L, Fuster, D, Berhanu, M & Falcon, E 2014 Direct numerical simulations of capillary wave turbulence. *Physical review letters* **112** (23), 234501.

Fernandino, M. & Ytrehus, T. 2006 Determination of flow sub-regimes in stratified air-water channel flow using LDV spectra. *I.J. Multiphase Flow* **32**, 436–446.

Gent, P. R. & Taylor, P. A. 1977 A note on separation over short wind waves. *Boundary-Layer Meteorology* **11** (1), 65–87.

Grare, L., Peirson, W. L., Branger, H., Walker, J. W., Giovanangeli, J. P. & Makin, V. 2013 Growth and dissipation of wind-forced, deep-water waves. *Journal of Fluid Mechanics* **722**, 5–50.

Hara, T. & Sullivan, P. P. 2015 Wave boundary layer turbulence over surface waves in a strongly forced condition. *Journal of Physical Oceanography* **45** (3), 868–883.

Hsu, C. T., Hsu, E. Y. & Street, R. L. 1981 On the structure of turbulent flow over a progressive water wave: theory and experiment in a transformed, wave-following coordinate system. *Journal of Fluid Mechanics* **105**, 87–117.

Janssen, P. 2004 *The interaction of ocean waves and wind*. Cambridge University Press.

Jeffreys, H. 1925 On the formation of waves by wind ii. *Proc. Roy. Soc.* **110A**, 341–347.

Jurman, L. A., Deutsch, S. E. & McCready, M. J. 1992 Interfacial mode interactions in horizontal gasliquid flows. *Journal of Fluid Mechanics* **238**, 187–219.

Kaffel, A. & Riaz, A. 2015 Eigenspectra and mode coalescence of temporal instability in two-phase channel flow. *Physics of Fluids* **27** (4), 042101.

Kolaas, J. 2016 Getting started with HydrolabPIV v1.0. *Preprint series. Research Report in Mechanics* .

Kordyban, E. S. & Ranov, T. 1970 Mechanism of slug formation in horizontal two-phase flow. *Journal of Basic Engineering* **92** (4), 857–864.

Lighthill, M. J. 1962 Physical interpretation of the mathematical theory of wave generation by wind. *Journal of Fluid Mechanics* **14** (3), 385–398.

Lin, M., Moeng, C., Tsai, W., Sullivan, P. P. & Belcher, S. E. 2008 Direct numerical simulation of wind-wave generation processes. *Journal of Fluid Mechanics* **616**, 1–30.

Makin, V. K. & Kudryavtsev, V. N. 2002 Impact of dominant waves on sea drag. *Boundary-Layer Meteorology* **103** (1), 83–99.

Onorato, M., Residori, S., Bortolozzo, U., Montina, A. & Arecchi, F.T. 2013 Rogue waves and their generating mechanisms in different physical contexts. *Physics Reports* **528** (2), 47 – 89, rogue waves and their generating mechanisms in different physical contexts.

Pan, Y & Yue, D. K. P. 2014 Direct numerical investigation of turbulence of capillary waves. *Physical review letters* **113** (9), 094501.

Reul, N., Branger, H. & Giovanangeli, J.-P. 2008 Air flow structure over short-gravity breaking water waves. *Boundary-layer meteorology* **126** (3), 477–505.

Sanchis, A., Johnson, G.W. & Jensen, A. 2011 The formation of hydrodynamic slugs by the interaction of waves in gas-liquid two-phase pipe. *I. J. of Multiphase flow* **37**, 358–368.

Siddiqui, M. H. K. & Loewen, M. R. 2006 Detecting microscale breaking waves. *Measurement Science and Technology* **17** (4), 771.

Siddiqui, M. H. K. & Loewen, M. R. 2010 Phase-averaged flow properties beneath microscale breaking waves. *Boundary-Layer Meteorology* **134** (3), 499–523.

Sullivan, P. P., Banner, M. L., Morison, R. P. & Peirson, W. L. 2018 Turbulent flow over steep steady and unsteady waves under strong wind forcing. *Journal of Physical Oceanography*

48 (1), 3–27.

Toffoli, A, Proment, D, Salman, H, Monbaliu, J, Frascoli, F, Dafilis, M, Stramignoni, E, Forza, R, Manfrin, M & Onorato, Miguel 2017 Wind generated rogue waves in an annular wave flume. *Physical review letters* **118** (14), 144503.

Tzotzi, C. & Andritsos, N. 2013 Interfacial shear stress in wavy stratified gas-liquid flow in horizontal pipes ". *I. J. Multiphase Flow* **54**, 43 – 54.

Veron, F., Saxena, G. & Misra, S. K. 2007 Measurements of the viscous tangential stress in the airflow above wind waves. *Geophysical Research Letters* **34** (19).

Woods, B. D., Hurlburt, E. T. & Hanratty, T. J. 2000 Mechanism of slug formation in downwardly inclined pipes. *International journal of multiphase flow* **26** (6), 977–998.

Wu, Y. & Christensen, K. T. 2006 Population trends of spanwise vortices in wall turbulence. *Journal of Fluid Mechanics* **568**, 55–76.

Yang, D. & Shen, L. 2010 Direct-simulation-based study of turbulent flow over various waving boundaries. *Journal of Fluid Mechanics* **650**, 131–180.

Zonta, F, Onorato, M & Soldati, A 2016 Decay of gravity-capillary waves in air/water sheared turbulence. *International Journal of Heat and Fluid Flow* **61**, 137–144.

Zonta, F, Soldati, A & Onorato, M 2015 Growth and spectra of gravity–capillary waves in countercurrent air/water turbulent flow. *Journal of Fluid Mechanics* **777**, 245–259.

Paper III

Microscale wave breaking in stratified air-water pipe flow

Petter Vollestad, Anis Awal Ayati, Atle Jensen

Published in *Physics of Fluids* **31** (2019), 032101.
DOI: 10.1063/1.5082607.

III

Microscale wave breaking in stratified air-water pipe flow

P. Vollestad[1,*], A. A. Ayati[1], A. Jensen[1]

[1] *Department of Mathematics, University of Oslo, P. O. Box 1053, 0316 Oslo, Norway*

[*] *Corresponding author: pettervo@math.uio.no*

Abstract

We perform an experimental analysis of two-phase stratified wavy pipe flow, with the aim to detect and quantify the effect of small scale wave breaking. Particle image velocimetry is employed to analyze the velocity fields below individual waves, and a threshold for the vorticity on the leeward side of the crest is used to assess active wave breaking.

Keeping the liquid flow rate constant, we analyze five experimental cases with increasing gas flow rates. The cases span the flow map from when first interfacial waves are observed, to the "amplitude saturation" regime, where the rms interface elevation is independent of the gas flow rate. While some wave breaking events are observed also in the wavegrowth regime, wave breaking is found to be much more frequent when the gas flow rate is increased into the amplitude saturation regime, and 35-40 % of the waves passing the measurement section are assessed to be in a state of active breaking in this regime.

A conditional averaging of the flow field is performed, and the turbulent dissipation rate below breaking and non-breaking waves is estimated. The effect of microscale breaking is observed down to a depth of 10 mm below the water surface. Below the crest of microscale breaking waves the turbulent dissipation rate is increased by a factor 2.5 to 4 compared with non-breaking waves. This fraction increases with U_{sg}, implying that the breaking events become more energetic as the gas flow rate is increased.

1. Introduction

Wave breaking is characterized by fluid elements near the wave crest which achieve a velocity greater than the propagation speed of the wave, resulting in a reduction of the wave amplitude and increased turbulence levels in the liquid phase (Banner & Phillips, 1974; Jessup *et al.*, 1997; Khait & Shemer, 2018). Here we consider wave breaking at deep or intermediate depths, as discussed by Perlin *et al.* (2013), as opposed to depth-limited breaking, typically observed as water waves approach a beach (Peregrine, 1983). The phenomenon is typically divided into categories related to the severity and visual characteristics of the breaking process. Babanin (2011) separates wave breaking into plunging, spilling and microbreaking. While wave breaking is generally associated with the more energetic forms, producing whitecaps on the water surface as air is entrained into the liquid phase, microbreaking or microscale wave breaking is a weak form of wave breaking without air entrainment (Banner & Phillips, 1974). For these small scale wave breaking events, surface tension prevents the jet formation and overturning of the wave crest which results in air entrainment for larger scale breaking events (Tulin & Landrini, 2001; Duncan, 2001). Recent numerical analysis by Deike *et al.* (2015) demonstrates the effect of surface tension on the nature of the breaking process. As pointed out by Babanin (2011), while the external signature of microscale breaking waves are different to breaking waves that produce whitecapping, the fundamental physics is the same as for spilling breakers. Microscale breaking waves can also be referred to as small-wavelength spilling waves (Duncan, 2001; Tulin & Landrini, 2001). Due to the high frequency of microscale breaking

on the ocean surface (compared with the more energetic forms of breaking producing whitecaps), it is assessed that microscale breaking may have a significant impact on the air-sea exchange in the ocean (Peirson & Banner, 2003; Jessup *et al.*, 1997). Recent field experiments indicate that microscale breaking waves and breaking events with very little air-entrainment may contribute to 20-90 % (depending on the wind speed and wave age) of the total dissipation by wave-breaking (Sutherland & Melville, 2013, 2015).

Microscale breaking is reported to occur for wind forced waves with wavelengths in the order of decimeters. Jessup *et al.* (1997) report the wavelength to be in the range of 0.1 to 1 meters, while Caulliez (2013) identified microscale wave breaking as the dominant dissipative mechanism for wind forced waves from 0.1 to 0.2 m wavelength. The visual characteristics of microscale breaking waves are a bore-like crest and parasitic capillary waves on the forward face of the wave (Jessup *et al.*, 1997). As the breaking is initiated, a thin (< 2 mm) spilling region is formed on the leeward face of the wave (Peirson & Banner, 2003). This region disrupts the parasitic capillaries closest to the crest, while the smaller capillary waves located upstream of the toe of the spilling region may prevail during the breaking event (Zhang & Cox, 1999). Recently, the kinematic breaking criterion, which states that breaking occurs when fluid particles at the wave crest moves faster than the representative wave velocity, has received significant support (Banner *et al.*, 2014; Shemer & Liberzon, 2014; Khait & Shemer, 2018). Investigations of the initiation of breaking is however outside the scope of the present work, as we focus on detecting actively breaking waves and evaluating the properties of the liquid flow below actively breaking and non-breaking waves.

As microscale breaking waves do not cause air entrainment, they are more difficult to observe than breaking waves producing whitecaps. Different techniques have been applied to detect and quantify the effect of microscale breaking waves. Katsaros & Ataktürk (1992) used video recordings and a manual visual observation to detect and quantify microscale breaking waves in field conditions. Jessup *et al.* (1997) used infrared imagery and found that turbulence generated by the breaking process disrupts the thermal boundary layer of the microbreaking wave. According to Jessup *et al.* (1997), disruption of the thermal boundary layer and the infrared signature generated may serve as a practical means of defining microscale breaking waves. Siddiqui *et al.* (2001) used infrared imaging and subsurface particle image velocimetry (PIV) measurements and found that the disruption of the thermal boundary layer was well correlated with the presence of vortical structures and high levels of vorticity in the crest region of the wave. In a later work, Siddiqui & Loewen (2006) tested three different methods for detecting microscale breaking waves: wave steepness, infrared imagery and vorticity in the crest region evaluated by PIV. According to Siddiqui & Loewen (2006), PIV measurements of the vorticity field in the crest region was found to be the best predictor for detecting microscale breaking waves. In a later paper, Siddiqui & Loewen (2010) observed that below microscale breaking waves the turbulent dissipation rate increased by a factor two to three compared with non-breaking waves.

Peirson & Banner (2003) used PIV to evaluate the effect of microscale breaking waves. The spilling region was observed to remain compact and restricted to a limited portion of the overall waveform, downwind of the wave crest. Regions of intense shear were observed at the toe of the spilling region. In some PIV velocity fields, vorticity was also observed downwind of the spilling region. This was attributed to the parasitic capillary waves riding in front of the wave. As demonstrated by Longuet-Higgins (1992), capillary waves located on the leeward side of short gravity waves generate intense vorticity in a thin layer close to the interface, but following the results from Peirson & Banner (2003), the impact of these capillary ripples is much smaller than the effect of microscale breaking.

In two-phase pipe flow, different flow regimes may be present, depending on the properties of the fluids involved and flow rate combinations applied. The stratified regime occurs when the gas and liquid velocities are relatively low, and below the threshold for transition to slug flow. As

the gas velocity is increased, waves appear on the liquid interface. Within the stratified regime, several sub-regimes of wavy flow patterns exist, depending on the flow rate combinations (Tzotzi & Andritsos, 2013; Fernandino & Ytrehus, 2006; Coleman & Garimella, 1999; Strand, 1993).

The main engineering aspects of the stratified flow regime is related to predicting flow parameters such as the pressure drop and liquid hold-up, and finding criteria for transition to slug flow. Due to the inherent complexities of the flow, simplified two-fluid models are the main tools applied. This approach depends on closure relations for the interfacial friction. A large number of proposed friction factor correlations can be found in the literature (Andritsos & Hanratty, 1987; Biberg, 2007).

Recently, PIV has been applied to study the stratified regime in two-phase pipe flow (Ayati *et al.*, 2014, 2016; Birvalski *et al.*, 2014, 2016; Vollestad *et al.*, 2019). The main results from these studies are spatio-temporally and phase-averaged flow fields. While this has lead to an improved understanding of stratified gas-liquid pipe flow, the issue of microscale wave breaking has not yet been assessed in detail. Considering the significant impact of microscale wave breaking in the momentum budget at the atmosphere-ocean interface, it is assessed that small scale wave breaking may be an important mechanism also in the stratified wavy regime of two-phase pipe flow.

While some references to small scale wave breaking in two-phase pipe flow are found in the literature, no thorough analysis of the phenomenon has been performed to the authors' knowledge. Coleman & Garimella (1999) used high speed cameras and observed wave breaking in the stratified wavy regime for sufficiently large pipe diameters. The severity of breaking was however not reported, nor was the point of breaking onset in the flow map specified. Ayati & Carneiro (2018) analyzed the statistics from interfacial wave probes in two-phase stratified flow, considering the same experimental setup and flow rate combinations closely matching the cases under investigation in the present work. By comparing the wave statistics with Gaussian statistics (linear wave theory), they observed a clear transition from a quasi-linear regime to a non-linear regime, where linear wave theory considerably over predicts the maximum observed surface elevation η. The transition was linked to the onset of "amplitude saturation", reported previously by Ayati *et al.* (2015), where the rms surface elevation is found to be independent of the gas flow rate. Ayati & Carneiro (2018) mention microscale breaking as one of the possible mechanisms explaining the transition observed, but no further analysis was performed to assess whether the onset of microscale wave breaking corresponds with the observed transition.

In the present work, we perform a PIV analysis of the liquid phase in stratified gas-liquid pipe flow. Keeping the liquid superficial velocity constant at 0.1 m/s (the superficial velocity is the volumetric flow rate divided by the pipe cross-sectional area), the gas flow rate is varied and experimental cases covering the transition from the "wave growth" to the "amplitude saturation" regime observed by Ayati & Carneiro (2018) are considered. The goal is to identify where in the flow map microscale breaking waves first appear, and to quantify the effect of microscale wave breaking on the liquid phase flow field.

2. Experimental setup

The experiments were conducted at the hydrodynamics laboratory, University of Oslo. A horizontal, 31 m long transparent acrylic pipe with an internal diameter D = 100 mm is used. The fluids are air and water at atmospheric pressure. An overview of the experimental setup is presented in figure 1. Water is supplied at the inlet through a 50 mm diameter pipe. The water mass flow rate was controlled by a frequency regulated pump, and measured using an Endress Hauser Promass Coriolis flow meter. The air flow was supplied by a frequency regulated fan, and measured by an Emerson MicroMotion Coriolis flow meter. The water and air flow meters have an accuracy of ± 0.2 % and ± 0.05 % of maximum measured value, respectively. Honeycomb flow straighteners were placed at the inlet of the pipe section to dampen turbulent fluctuations introduced at the inlet. The

differential pressure in the air phase was measured over a 12.4 meter section, using a smar LD301 differential pressure gauge (±0.2 % of max. range in accuracy).

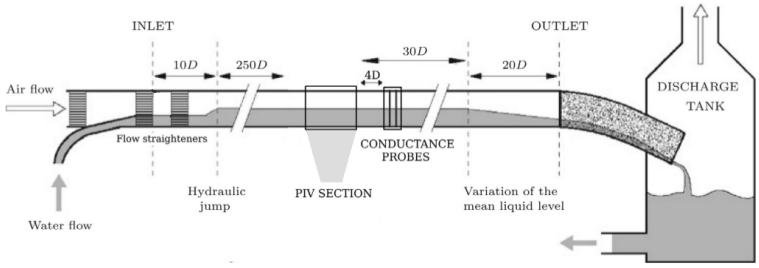

Figure 1: Schematic view of experimental setup.

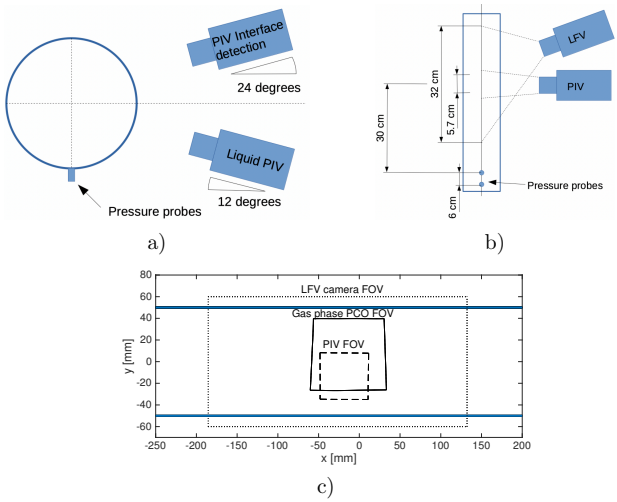

Figure 2: Schematic view of PIV setup. a) Looking downstream. The LFV (large field of view) camera is located at the same height as the gas phase PCO camera. b) Seen from above. The liquid phase PIV camera is located below the gas phase PCO camera. c) Field of view along the centerline of the pipe for the three cameras.

A PIV section was placed approximately 260 D downstream of the inlet. An optical correction box was placed covering the PIV section. The box was half filled with isopar which ensured that the optical distortion of the liquid phase PIV camera was reduced. A three-camera system was applied in the study. The camera specifications and their function in the experimental setup is summarized below. The placement of the cameras and their field of view (FOV) is illustrated in figure 2.

- Liquid phase PIV camera. A 14 bit PCO.4000 camera with 4008x2672 pixels, oriented upwards at an angle of 12°. The camera was fitted with an AF-S Teleconverter and a 100 mm lens. This enabled a relatively small FOV of 57 mm in the horizontal direction.
- PIV interface detection camera. Same type of camera as the liquid phase PIV camera, but fitted without the AF-S Teleconverter. Directed downward at an angle of 24°, focused on the interface. A high downward looking angle was necessary as the crescent shape of the waves

100

meant that the pipe wall was repeatedly wetted by the waves well above the mean liquid level. FOV of approximately 100 mm in the horizontal direction.

- Large-field of view (LFV) camera. A Nikon D7200 (4800x3200 pixels), equipped with a 28 mm lens was directed at an angle of approximately 30° downwards, looking upstream at an angle of approximately 31°. FOV of approximately 320 mm, which is longer than the dominant wavelengths of all experimental cases in the study. Images were used to identify the large scale properties (such as the wavelength and height) of the waves.

Prior to the experiments, a coordinate system was inserted into the pipe centerline, and cubic coordinate transforms (from pixel to world coordinates) were created for each of the three cameras. The coordinate system is identical to the one used by Ayati *et al.* (2015), but has been extended in the horizontal direction due to the larger FOV of the LFV camera.

A vertical plane in the pipe center was illuminated from below by a laser sheet, generated by a 147 mJ double pulsed ND:YAG laser. The head of the laser optics was placed 45 cm below the optical correction box. This enabled the laser light sheet to illuminate not only the FOV of the PIV, but the full FOV of the LFV camera. The two laser pulses were triggered with a Δt of 300 μs. The PCO cameras acquired double images (one image per laser pulse) used for PIV calculations, while the LFV camera was set to trigger before the first camera pulse, and has an exposure time which extends over the time period of both laser pulses. Hence, the LFV image is double exposed with a Δt of 300 μs. During this time delay the waves in the highest gas flow rate case will move approximately 0.25 mm, which is a negligible distance compared with the overall wave shape.

The liquid phase was seeded with 20 μm polyamide spheres. PIV was performed using a cascade of cross-correlation passes, with a final subwindow size of 32x32 pixels, and 50 % overlap. This translates to a spatial resolution of approximately 0.24x0.24 mm. Spurious vectors were detected by standard methods based on a local median filtering (Raffel *et al.*, 2018). Typically, 2-3 % of the vectors were found to be spurious, and replaced by cubic interpolation. Note that for microscale breaking waves, light reflections were detected at the interface of the spilling region. In order to avoid that these bright regions dominated the PIV results, these high intensity regions were masked from the raw images prior to the PIV analysis. Rhodamine B was added to the water at a concentration of approximately 0.1 mg/L to enhance the contrast between the liquid and gas phase, enabling efficient interface detection from the two gas-phase cameras.

A conductance wave gauge was placed 4 D downstream of the PIV section. This consists of two double-wire probes of 0.3 mm diameter separated by 4 mm. The two probes were placed in the center of the pipe with a distance 6 cm in the streamwise direction. The interface elevation was measured with a relatively high temporal resolution of 500 Hz. For more details about the wave-gauges the reader is referred to Ayati *et al.* (2015).

The data transfer rate between the cameras and the computer limited the frequency of data acquisition, and it was found necessary to reduce the PIV acquisition rate to maximum 0.2 Hz for the data transfer to be successful over long measurement series (i.e. a new set of double images could be acquired every 5 seconds). To overcome the limitation of the low PIV acquisition rate, and to ensure that the PIV system acquired images of value to the experimental investigation, a system to trigger the PIV acquisition was designed. Two pressure probes (Kulite XTL-190) mounted flush to the pipe bottom (position indicated in figure 2 a-b) detected as waves approached the PIV section, and triggered the PIV system, ensuring that the leeward side of the waves (where we expect to see the strongest indications of wave breaking) were regularly present within the PIV FOV. As we are interested in detecting breaking waves, the triggering system was set up to detect the relatively larger waves in the system, where breaking is assessed to be more probable. Details of the triggering system are presented in Appendix A: Trigging of PIV system.

3. Methodology

3.1. Description of experimental cases

Five experimental cases, where the liquid superficial velocity is kept constant at $U_{sl} = 0.1$ m/s, while the gas superficial velocity is increased from 1.5 to 2.4 m/s are analyzed. The main characteristics of the experimental cases are presented in table 1. U_{sf}, U_{bf} is the superficial and bulk velocities, where $f = g,l$ refers to the gas or liquid phase respectively. $U_{bf} = U_{sf}A/A_f$, where A is the total cross-sectional area of the pipe, while A_f is the area occupied by phase f. Re_{Df} is the Reynolds number based on the hydraulic diameter. The number of PIV images acquired for each case is presented in the right column of table 1. As we will analyze breaking and non-breaking waves separately, a larger number of velocity fields were acquired in the cases where wave breaking was present.

Table 1: Experimental cases under investigation. $U_{sl} = 0.1$ m/s for all cases. N_{PIV} is the number of PIV velocity fields acquired per experimental case.

U_{sg} $[m/s]$	U_{bl} $[m/s]$	U_{bg} $[m/s]$	Re_{Dg} $[-]$	Re_{Dl} $[-]$	N_{PIV}
1.50	0.26	2.44	11 400	23 800	500
1.70	0.27	2.75	13 000	23 100	500
1.80	0.27	2.95	13 700	24 200	1000
2.10	0.30	3.22	15 600	25 300	1000
2.40	0.30	3.67	17 800	25 200	1000

Additional information including the mean water level, rms of the interface elevation fluctuations (η_{rms}), characteristic wave speed C_p (calculated by cross-correlation of the conductance wave probes), and dominant wavelength λ_p (evaluated based on the spectral peak frequency and characteristic wave speed, $\lambda_p = C_p/f_p$), as well as mean pressure drop ($\Delta p/\Delta x$) is presented in graphical form in figure 3, while the normalized wave spectra for all five cases under investigation are presented in figure 4. Note that in figure 3 additional experimental cases with flow rates lower and higher than the cases investigated by PIV have been included, to better visualize the trends in the flow map. Here the PIV cases under investigation are marked by crosses.

Different regimes exist within two-phase stratified pipe flow, depending on the flow rate combinations applied, and the properties of the fluids. Andritsos & Hanratty (1987) and Tzotzi & Andritsos (2013) discussed four sub-regimes within stratified flow:

(i) Smooth regime (no waves).

(ii) Two-dimensional (2D) wave regime. Interface is covered by small amplitude, relatively regular disturbances.

(iii) Large amplitude (Kelvin-Helmoltz) waves regime.

(iv) Atomization regime.

Applying the expressions proposed by Tzotzi & Andritsos (2013) for predicting flow regime transitions, the 2D wave regime is predicted to be present for 1.1 m/s $< U_{sg} <$ 4.1 m/s in our experimental setup. This is in good agreement with visual observations of the flow field, although in the experimental setup we first observed waves when U_{sg} exceeded 1.3 m/s. Variations in pipe diameter, inlet conditions and pipe materials are however known to impact on the transition criteria. The three-dimensionality of the wavefield has previously been investigated by Strand (1993). Using the same experimental setup and liquid flow rate, he found that the spanwise cross-correlation was close to unity for $U_{sg} < 4$ m/s, indicating that the waves are well described as 2D waves. For higher

gas flow rates, Strand (1993) found that the spanwise cross-correlation was drastically reduced, indicating the transition to the large amplitude wave regime. We conclude that all experimental cases considered in this work are within the 2D wave regime.

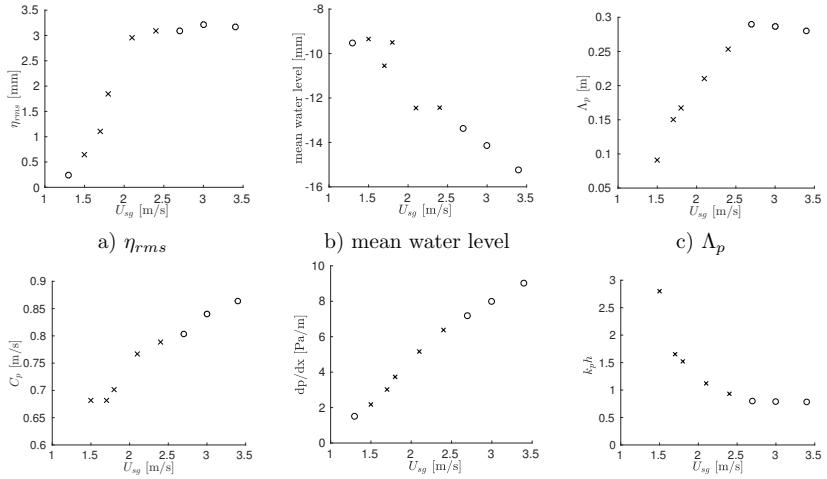

Figure 3: Data for the experimental cases. x: cases analyzed by PIV. Additional data points (o) included to visualize the trends in the flow map. a) η_{rms} is the rms interface elevation. b) mean water level (relative to the pipe centerline). c) Peak wavelength (λ_p, evaluated from spectra). d) Characteristic wave speed C_p. e) dp/dx, average pressure drop over 12.4 meter section of the pipe. f) $k_p h$ (h is mean water level in pipe center).

Figure 3 illustrates the dominant trends in the flow field as U_{sg} is increased. Starting with no waves ($\eta_{rms} \approx 0.2$ mm identified as electrical noise by Ayati *et al.* (2015)) at $U_{sg} = 1.30$ m/s, the wave field passes through a regime of amplitude growth, until the "amplitude saturation" regime is observed at $U_{sg} = 2.10$ m/s. Hence the five experimental cases under investigation cover the range from amplitude growth to saturation. Figure 3 b-d) shows that while also the dominant wavelength stabilizes as U_{sg} is increased, the mean water level is reduced (due to increased interfacial friction), while the wave speed and pressure drop is increased. The wave speed is observed to increase despite the fact that the geometrical features of the waves (amplitude and wavelength) and $k_p h$ are relatively constant above U_{sg} 2.70. This is related to the reduced water level and the increased bulk water velocity (as the volumetric liquid flow rate is constant for all cases).

3.2. Interface and wave phase detection

The liquid interface was first found from the LFV images, using a thresholding technique. Transforming this interface to the gas phase PCO images illustrated that while the interface detected by the LFV camera provided adequate accuracy to describe the large scale properties of the waves, improved accuracy of the interface in the PIV section could be obtained by the gas phase PCO images. Hence, and a region 100 pixels above/below the interface found by the LFV camera was scanned along the PCO images, using a combination of sobel edge detection and a threshold value of the light intensity to detect the interface. The interface was then converted to the liquid phase PIV images, and the region above the interface was masked and omitted from the PIV analysis. By analyzing original PIV images and the interfaces obtained, the accuracy of the interface detection is estimated to be 0.25 mm, equivalent to the PIV resolution.

The wave phase as a function of horizontal coordinate was calculated based on the LFV interfaces by a zero-crossing procedure. Crests, troughs and zero crossings were assigned a phase of 0°,

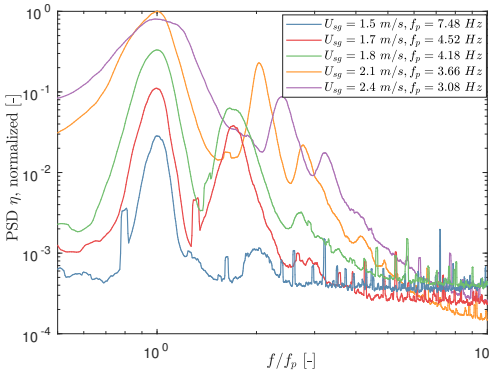

Figure 4: Normalized waveprobe frequency spectra for the five cases under investigation. y-axis normalized by the maximum spectral value, x-axis normalized by peak frequency f_p for each experimental case (included in figure legend).

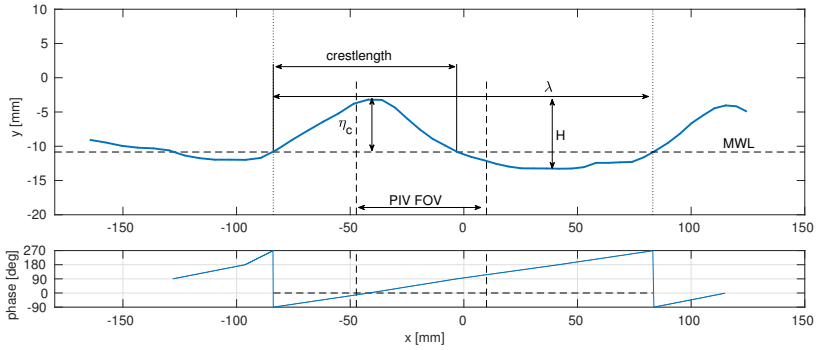

Figure 5: Example plot illustrating the interface detection (top) and wave phase determination (bottom). Thick blue line: Interface detected from LFV camera. PIV FOV and wave properties including η_c, λ and the crestlength indicated.

180° and ± 90° respectively, and the phases in between were linearly distributed. The process is illustrated in figure 5. This allows for statistics of the flow field located at the same relative location of the wave to be evaluated, and is a crucial step in the conditional phase-averaging procedure described in section 3.3, and the classification into breaking and non-breaking waves presented in section 4.2.

3.3. Phase-averaging procedure

A conditional averaging of all scalar fields (horizontal velocity, vertical velocity, vorticity, etc.) is performed on a wave-following coordinate system. For each velocity field, a coordinate transformation from (x, y) to (θ, ζ) is performed.

The wave-following coordinate system used is similar to the coordinate system applied by Birvalski *et al.* (2014) and Siddiqui & Loewen (2010). The wave phase θ determined by the LFV camera (ref. section 3.2) is used together with a relative height between the interface and the lower part of the PIV velocity field (located at y = -30 mm) to create a wave-following coordinate system (illustrated in figure 6). The height between the interface and y = -30 mm is divided into 100 equally spaced points, and the scalar fields are sampled at each of these 100 nondimensional ζ-coordinates and at each wave phase ($\Delta\theta = 1$) observed in the FOV.

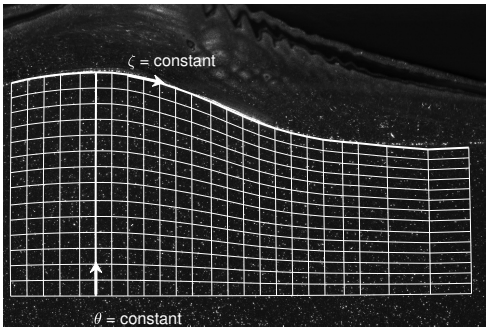

Figure 6: Illustration of the wave-following coordinate system applied, overlaid original PIV image. Vertical lines are lines of constant θ, near horizontal/wave-following lines are lines of constant ζ.

Once sampled, the identified velocity fields are ensamble-averaged (in the (θ, ζ) space). This ensures that the ensamble of velocity fields are averaged at constant wave phase and at a constant relative depth between the interface and the lower part of the PIV FOV. The phase-averaged interface elevation is evaluated simultaneously. When presenting the phase-averaged properties, the wave field is transformed from (θ, ζ) to (θ, y) by applying the mean interface elevation.

3.4. Estimation of turbulent dissipation rate

When sampling the velocity field in a wave-following coordinate system, a three-component Reynolds decomposition of the velocity field is typically applied (Hsu *et al.*, 1981; Birvalski *et al.*, 2014; Buckley & Veron, 2016). For a given variable q in the flow field, which varies in time and space, the variable is decomposed into a phase independent mean $\overline{q}(\zeta)$, a wave induced field $\tilde{q}(\theta, \zeta)$ and a fluctuating component $q'(\theta, \zeta, t)$:

$$q(x, y, t) = \overline{q}(\zeta) + \tilde{q}(\theta, \zeta) + q'(\theta, \zeta, t). \tag{1}$$

The phase-averaged component $\langle q \rangle$ is then

$$\langle q \rangle(\theta, \zeta) = \overline{q}(\zeta) + \tilde{q}(\theta, \zeta). \tag{2}$$

The above method is not able to fully decouple the wave-induced motions and the turbulence in a dispersive wave system (Birvalski *et al.*, 2014). As the system consists of a (relatively) broad banded spectrum of wave components, a significant amount of the wave-coherent velocity fluctuations will be included in the fluctuating velocity component. These errors will magnify when quantities such as the turbulent kinetic energy is calculated from the three-component Reynolds decomposition.

Siddiqui & Loewen (2007) introduced a spatial filtering technique to estimate the turbulent velocity fluctuations beneath microscale breaking waves. When the mean velocity $\overline{u}$ is subtracted from the instantaneous velocity field, we are left with the wave-coherent and turbulent fluctuations. This is referred to as u_{wt}. Wave-coherent fluctuations u_w are estimated by applying a spatial low-pass filter to the u_{wt} field, where the cut-off wavenumber is chosen to be lower than the wavenumber associated with the largest and most energetic turbulent structures. The rationale for this method is that the wave-coherent fluctuations occur over a larger spatial scale than the turbulent fluctuations generated by breaking. The turbulent fluctuations are then estimated as $u_t = u_{wt} - u_w$.

It is observed that beneath microscale breaking waves a turbulent region with high levels of vorticity is observed to extend typically 6 mm below the interface (see section 4.1). Based on this

observation, it is assessed that the most energetic turbulent structures generated by the breaking waves are in the range of 6 mm, and a spatial low-pass filter of 6x6 mm (top-hat) is applied. Note that changing the filter size in the range of 4x4 to 15x15 mm was tested and found to have only a small quantitative effect of the results. Figure 7 illustrates the effect of the low-pass filter, and the evaluation of u_t.

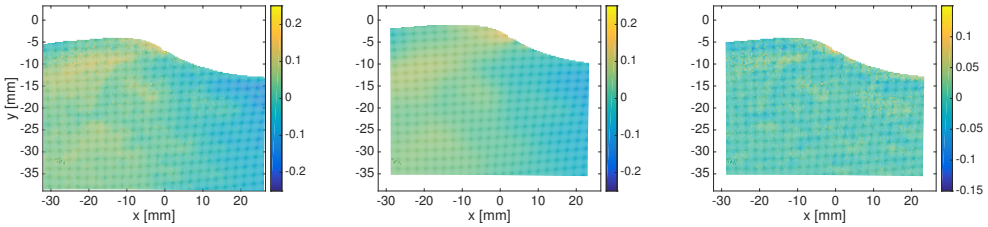

a) u_{wt} b) u_w c) u_t

Figure 7: Illustration of the spatial high-pass decomposition of the (horizontal) turbulent and wave-coherent velocity fluctuations. Colorbar in m/s.

The low-pass decomposition technique is not fully able to decouple the turbulent fluctuations from the wave-induced fluctuations (Siddiqui & Loewen, 2007). As the wave-induced fluctuations can be more than an order of magnitude higher than the turbulent fluctuations, including even small fractions of wave-coherent fluctuations into the turbulent fluctuations can lead to significant overestimation of quantities such as the turbulent kinetic energy. Hence, this method should not be applied to calculate the turbulent kinetic energy or Reynolds stresses.

The dissipation rate of turbulent kinetic energy can be estimated from a 2D velocity field using the following relation (Doron *et al.*, 2001; Siddiqui & Loewen, 2007):

$$\epsilon = 3\nu\left(\overline{\left(\frac{\partial u'}{\partial x}\right)^2} + \overline{\left(\frac{\partial v'}{\partial y}\right)^2} + \overline{\left(\frac{\partial u'}{\partial y}\right)^2} + \overline{\left(\frac{\partial v'}{\partial x}\right)^2} + 2\overline{\left(\frac{\partial u'}{\partial y}\frac{\partial v'}{\partial x}\right)} + \frac{2}{3}\overline{\left(\frac{\partial u'}{\partial x}\frac{\partial v'}{\partial y}\right)}\right), \tag{3}$$

where the overbar indicates time or ensamble average. As can be seen from equation 3, ϵ is only dependent on the spatial derivatives of the fluctuations, not on the magnitude of the fluctuations. In this work, the spatial derivatives of the fluctuations are evaluated by a 5x5 finite difference filter, considering the 50% overlap used in the PIV processing, and to reduce the influence of small errors in the PIV. Siddiqui & Loewen (2007) argue that as the spatial derivatives of u_t are higher than the spatial derivatives of u_w, the method outlined above can be applied to give a reasonable estimate for ϵ, as the inclusion of wave-coherent fluctuations into u_t will not significantly alter the spatial derivatives of u_t. In the experiments by Siddiqui & Loewen (2007), the turbulent velocity gradients were typically 2.5 times larger than the wave-induced velocity gradients in the crest region. Similar results were obtained in this study.

In order for the method to be accurate, PIV needs sufficient spatial resolution to resolve the shear responsible for the dissipation. The dissipation of turbulent kinetic energy occurs at the smallest scales of the flow, bounded by the Kolmogorov microscale η_ν. As discussed by Siddiqui & Loewen (2007), it is not necessary to fully resolve the Kolmogorov scale for the dissipation rates to be estimated with reasonable accuracy, as most of the dissipation occurs at scales larger than η_ν. The Kolmogorov length scale can be evaluated as $\eta_\nu = (\nu^3/\epsilon)^{0.25}$. As ϵ is the magnitude we are interested in, calculating η_ν a priori is not possible, and applying the obtained dissipation rates to estimate η_ν implies a circular argument. Here we use a simplified approach to estimate η_ν a priori. Using the triple decomposition described in equation 1, we estimate the turbulent kinetic energy in the flow field. For the highest gas flow rate case the maximum turbulent kinetic energy evaluated

directly below the wave crest was estimated to be $3.75 * 10^{-3}$ m^2/s^2. This implies a characteristic turbulent velocity u' of 0.05 m/s. Note that this is assessed to be a high estimate for the turbulence in the region, as wave-coherent velocities which were not accurately filtered by the three-component Reynolds decomposition will impact on the estimated turbulent kinetic energy. The region of high turbulence levels below the interface of microbreaking waves typically extended 6 mm below the interface. With this velocity and length scale we estimate a characteristic eddy turnover time for the most energetic eddies as $\tau_{turnover} = l/u'$. If it is further assumed that all the turbulent kinetic energy is dissipated within the time period $\tau_{turnover}$ (assessed to be a conservative assumption), $\epsilon \approx k/\tau_{turnover}$. Applying these assumptions we can provide an estimate of ϵ directly beneath the crest of 0.03 m^2/s^3 (this estimate is seen to be in fair agreement with results obtained in section 4.3.2), which results in an estimate of η_ν of 73 μm. The smallest structures which can be detected by the PIV are $\approx$ 480 μm (twice the PIV resolution), which gives $k\eta_\nu \approx 1$. From the normalized energy and dissipation rate spectra presented by Tennekes & Lumley (1972), it can be seen that almost all the dissipation($> 90\%$) occurs for $k\eta_\nu < 1$, indicating that the resolution of the PIV is sufficient for giving reasonable estimates for ϵ beneath the crest.

Using the estimate for ϵ, we can estimate the kolmogorov timescale as $\tau_k = (\nu/\epsilon)^{0.5}$, and find that the Δt in the PIV acquisition is more than an order of magnitude lower than τ_k. Hence we conclude that the spatial resolution, not the temporal resolution used to compute individual PIV velocity fields is the limiting factor in determining ϵ.

In the highly turbulent spilling region, the turbulence levels are observed to be an order of magnitude higher than directly below the crest. Here the high turbulence region is observed to be very thin, and it is assessed that the Kolmogorov length scale is smaller than what we are able to resolve with the current PIV method, making the estimated dissipation rate in this region unreliable.

4. Results

4.1. Instantaneous Velocity fields

In this section a few example plots of the velocity and vorticity fields of individual PIV results are presented.

Figure 8 illustrates a wave which is not in an active state of breaking. In figure 8 a), capillary ripples are observed on the leeward face of the wave, extending almost to the crest of the wave. A vector plot of the liquid phase (seen in a frame of reference moving with the wave speed) is presented in figure 8 b). Here it is seen that the wave speed is higher than the liquid velocity vectors. The vorticity contour plot presented in figure 8 c) shows that the vorticity is relatively constant along the wave profile. However, somewhat higher vorticity levels ($\approx$ -100 s^{-1}) are observed just beneath the wave crest. This is assessed to be caused by the higher wind forcing exerted on the interface in this region. As mentioned in the introduction, a bore-like crest and capillary ripples as observed in figure 8 a) and d) are characteristic of microscale breaking waves. However, following the discussion by Qiao & Duncan (2001) on the time development of small scale breaking waves, increased levels of vorticity and energy dissipation is first observed when the leading edge of the bulge of the crest starts to move downwards, creating a highly turbulent flow where water particles are observed to move at a velocity exceeding the wave speed. While the formation of the bulge and the parasitic capillaries can be associated with wave breaking, we will only refer to the wave as breaking when increased levels of vorticity are observed beneath the leeward side of the wave, i.e. when the bulge has started to move down the wave, resulting in a highly turbulent flow. The wave presented in figure 8 can be considered as incipient breaking. Note that the majority of the non-breaking waves do not exhibit the distinct bulge and capillary ripples presented in figure 8, as the non-breaking waves are typically much smoother.

It can be noted that no significant increase in vorticity is observed beneath the parasitic capillary waves observed in figure 8 a) and d). Following Longuet-Higgins (1992), very high levels of vorticity

is expected to be generated beneath small capillary waves. However, as discussed by Duncan (2001), the layer of increased vorticity directly generated by parasitic capillary waves will be very small, significantly smaller than what we are able to resolve using PIV. Our observations follow the results by Qiao & Duncan (2001) and Peirson & Banner (2003), and indicate that diffusion of vorticity from parasitic capillary waves into the interior of the wave field is a weak effect relative to the onset of wave breaking.

Figure 9 represents a wave which is breaking. The vector plots presented in figure 9 b) shows that the spilling region is highly turbulent, and the maximum horizontal velocities exceed the wave propagation speed. The capillary ripples which in figure 8 were observed to extend all the way to the crest are now confined to a small region below the spilling region. The vorticity contour plot presented in figure 9 c) shows that high levels of vorticity (peak vorticity of $\approx$ -1000 s^{-1}) are produced in the spilling region, and a turbulent wake of high vorticity is observed below the crest.

The PIV system will detect waves at different stages of the wave breaking process. From visual inspection of the flow field (also using high-speed video), and looking through many images similar to the ones presented in this section, it is assessed that the velocity field presented in figure 9 represents a typical wave in an intermediate stage of the breaking process. Here the shape of the wave is still relatively similar to the non-breaking wave presented in figure 8, and the region of highest vorticity is observed in a relatively thin layer (approximately 3 mm) along the leeward side. Towards the windward side of the wave, a marked reduction of the vorticity is observed.

Waves assessed to be in a later stage of the breaking process were frequently observed in the experimental data. These were characterized by a more irregular shape of the crest, and high levels of vorticity was observed throughout the crest, down to a depth of up to 10 mm beneath the free surface. Here the high vorticity region was observed to extend a significant distance in the upstream direction, possibly impacting the upstream wave as this overtakes the turbulent eddies left in the wake of the breaking wave (limitations in the PIV FOV meant that this effect could not be observed directly).

4.2. ROI statistics

Based on the instantaneous velocity fields obtained, a region of interest (ROI) was defined, and the flow properties in this region were monitored to detect the signature of breaking waves.

For all the waves where clear indications of active wave breaking was observed, high levels of vorticity was observed on the leeward side of the crest, associated with the spilling region of the wave. The full extent of this high vorticity region varied considerably, as different stages of the wave breaking process was detected. However, in the region from $20° < \theta < 80°$, from the interface and down to approximately 3 mm below the interface, high levels of vorticity were always present for the waves associated with wave breaking. This region was selected as the ROI (indicated in figure 10). All PIV velocity fields containing the ROI were analyzed (number of PIV velocity fields including the ROI presented in table 2), and statistics from the ROI analyzed. The main focus is on evaluating the rms vorticity (denoted ω_{rms}) and the maximum horizontal velocity in the ROI.

In figure 11 a), scatter plot of the maximum horizontal velocity divided by the wave velocity (u_{max}/c) versus ω_{rms} in the ROI is presented for all waves analyzed. The wave speed c is evaluated for each wave individually by a cross correlation of the upstream pressure probes, used to trigger the PIV system (ref. "Appendix A: Trigging of PIV system"). As the figure contains many overlapping data points, lines are included to indicate the maximum extent of the scatter points for each experimental case. In figure 11 b), ω_{rms} is binned with a bin size of 10, and the probability density function (PDF) of ω_{rms} within the ROI is presented. Figure 11 a) shows that the relationship between ω_{rms} and u_{max}/c can be divided into two regimes, and the transition between these occur at $u_{max}/c \approx 1$. Above this limit the slope of $\omega_{rms}(u_{max}/c)$ is seen to increase significantly. This result is to be expected, as wave breaking is characterized by fluid elements near the wave crest overtaking the general waveform, resulting in increased vorticity beneath the crest.

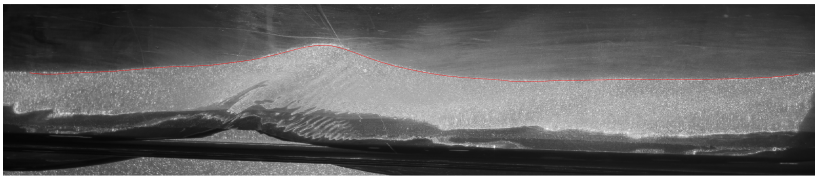

a)

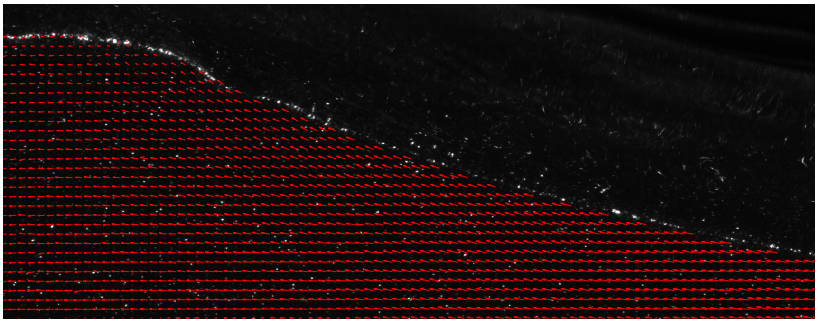

b)

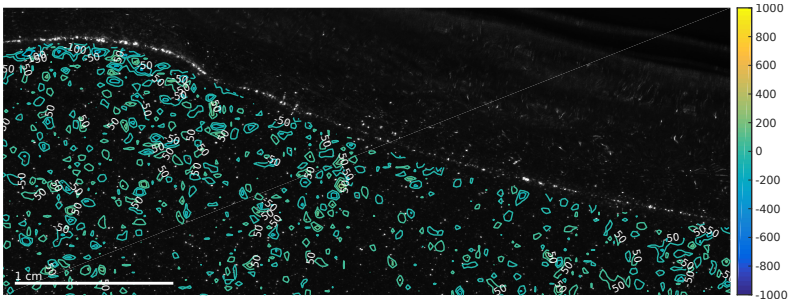

c)

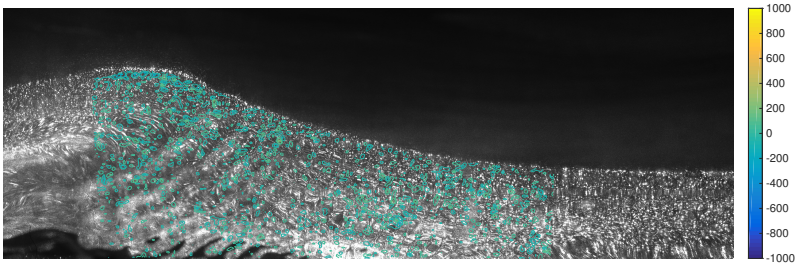

d)

Figure 8: Images and overlaid PIV velocity fields of a non-breaking wave. $U_{sl} = 0.1$, $U_{sg} = 2.40$. a) Interface seen from LFV camera. b) Vector plot seen in a frame of reference moving with the wave speed. c) Vorticity field below the crest (colorbar in $[s^{-1}]$). d) PIV interface detection camera with liquid phase vorticity field superimposed (colorbar in $[s^{-1}]$). Note that only a section of the liquid phase PIV images (b and c) are shown. In figure b, half of the vectors are shown. Flow from left to right.

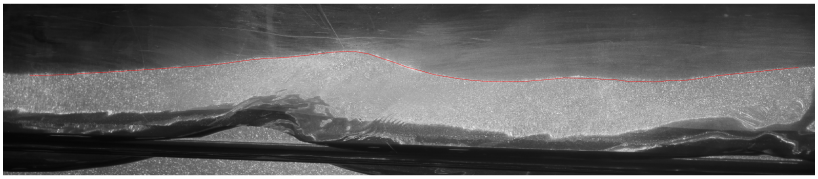

a)

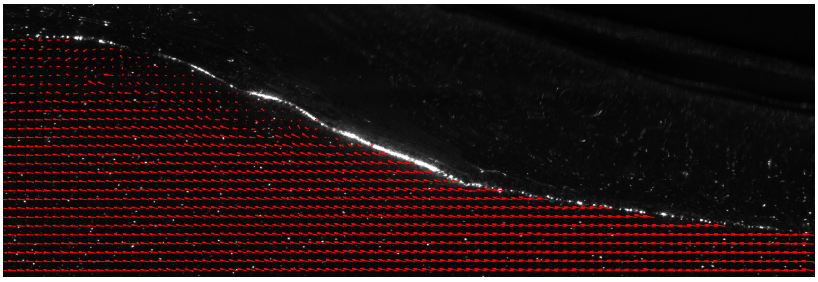

b)

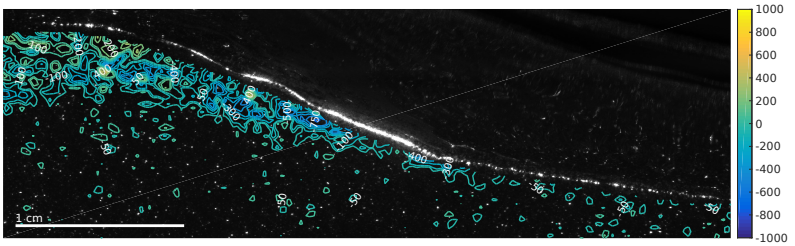

c)

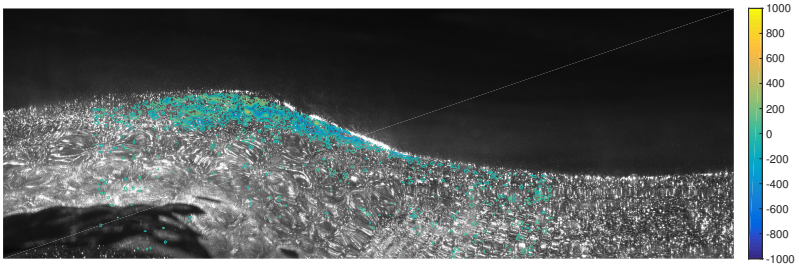

d)

Figure 9: Images and overlaid PIV velocity fields of a breaking wave. $U_{sl} = 0.1$, $U_{sg} = 2.40$. a) Interface seen from LFV camera. b) Vector plot seen in a frame of reference moving with the wave speed. c) Vorticity field below the crest (colorbar in $[s^{-1}]$). d) PIV interface detection camera with liquid phase vorticity field superimposed (colorbar in $[s^{-1}]$). Note that only a section of the liquid phase PIV images (b and c) are shown. In figure b, half of the vectors are shown. Flow from left to right.

110

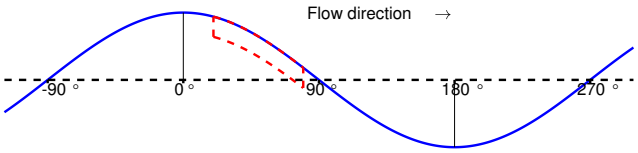

Figure 10: Illustration of the region of interest. Blue line represents water surface. Red dotted line contains the ROI.

In figure 11 b), it can be observed that for the two lowest flow rate cases, ω_{rms} is in the range of 20 to 60 for all waves, except for one observation of the U_{sg} 1.70 m/s case. For all experimental cases, a distinct peak is observed in the PDF at ω_{rms} of 30-50 s^{-1}. This peak is associated with non-breaking waves, and the vorticity levels observed can be viewed as a background vorticity in the flow. For the two highest flow rates, a secondary, although much wider, peak is observed in the PDF at ω_{rms} between 100 and 250 s^{-1}. These high levels of ω_{rms} are associated with wave breaking events. As the waves are captured by the PIV system at different stages of the wave breaking process, and as the waves are likely to break with different intensity, it is to be expected that this secondary peak is wider than the peak associated with non-breaking waves.

For the U_{sg} 1.80 m/s case, values of ω_{rms} significantly higher than the peak associated with the non-breaking peak are evident, although no secondary peak in the PDF is observed, indicating that the wave breaking events are rarer and less energetic than for the U_{sg} 2.10 and 2.40 m/s cases.

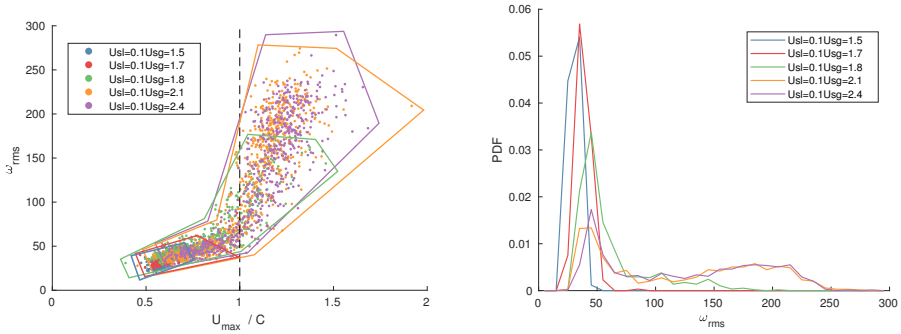

Figure 11: a) Scatter plot of maximum horizontal velocity divided by wave speed vs. rms vorticity $[s^{-1}]$ observed in ROI. Lines corresponding to color of each experimental case illustrates the maximum extent of the scatter points for each case. b) Probability distribution of rms vorticity $[s^{-1}]$ within the ROI.

In figure 12, scatter plots of ω_{rms} against two different steepness measures are presented. S_{max} is the maximum slope along the leeward side of the wave ($\max(|d\eta/dx|)$), while $ak = \pi H/\lambda$, where H and λ is the wave height and length, evaluated from the LFV camera. Note that the interface was detected for segments of approximately 1.3 mm along the wave profile, introducing a smoothing of the interface. Hence, the very high steepness associated with any capillary waves will not be resolved in the evaluation of S_{max}. The results show that there is no clear correlation between ω_{rms} and the wave steepness. There does however seem to be a limiting steepness below which no waves are breaking. This limit is approximately at $S_{max} \approx 0.2$ and $ak \approx 0.08$.

As our PIV system detects the waves at one instant in time, and at different stages of the

breaking process, these results are to be expected. Peirson & Banner (2003) applied a local slope threshold of 0.5 to separate breaking and non-breaking waves. However, as discussed by Siddiqui & Loewen (2006), there will be a significant overlap in the PDF of the wave steepness when comparing breaking and non-breaking waves. While it is observed from figure 12 that waves with a local steepness exceeding 0.5 are likely to be in a state of breaking (associated with high levels of ω_{rms}), it does not serve as an accurate criterion for detecting breaking waves in the present work.

While the current dataset is not suited to detect the onset of wave breaking (as this would require time-resolved measurements of individual waves going from a non-breaking to breaking state), the maximum steepness observed may be interpreted as a limiting steepness for the waves in the system. The maximum ak observed is ≈ 0.3. This is a typical steepness where wave-breaking in the ocean is assessed to occur (Sutherland & Melville, 2015).

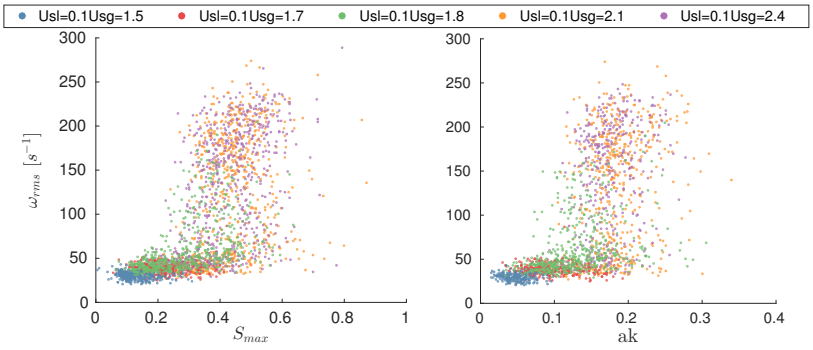

Figure 12: Scatter plot of ω_{rms} vs. maximum wave slope S_{max} and the wave steepness ak.

4.2.1. Breaking detection method

Based on the observations of the ROI statistics, a criterion for distinguishing breaking and non-breaking waves is introduced. Figure 13 illustrates the fraction of waves assessed to be breaking using different thresholds for ω_{rms}, and by applying $u_{max} > c$ as a criterion. This illustrates that the fraction of breaking waves is sensitive to the threshold applied, but that for the range of thresholds considered to be reasonable, the onset of wave breaking occurs at the same flow rate case ($U_{sg} =$ 1.8 m/s), and the trends in the observed breaking frequency do not vary considerably depending on the threshold applied.

In the rest of this analysis, waves with $\omega_{rms} < 60$ are assessed to be non-breaking, while waves with $\omega_{rms} > 100$ are assessed to be breaking. Referring to figure 11 a), this threshold ensures that virtually all waves assessed to be breaking has $u_{max}/c > 1$. Employing $u_{max}/c > 1$ as a criterion directly is not assessed to be robust, as this is only dependent on one vector in the ROI, and because of uncertainties related to determining the instantaneous wave speed. It should be noted that these thresholds are not general, and will depend on the PIV resolution of the measurements (as higher resolution implies that more of the shear is resolved).

The total number of PIV velocity fields, waves with ROI within the PIV FOV and waves assessed to be breaking and non-breaking are presented in table 2. Waves with $60 < \omega_{rms} < 100$ are not classified as either breaking or non-breaking. In table 2 they are classified as "intermediate". These might be waves at a very early/late stage of the breaking process, or it could be non-breaking waves passing through the turbulent wake of an upstream breaking wave. Inspection of the velocity fields related to these cases illustrated that it was sometimes difficult to assess whether the waves were breaking or not, and that setting a single threshold for separating breaking from non-breaking waves resulted in cases where non-breaking waves were assessed to be breaking and vice versa.

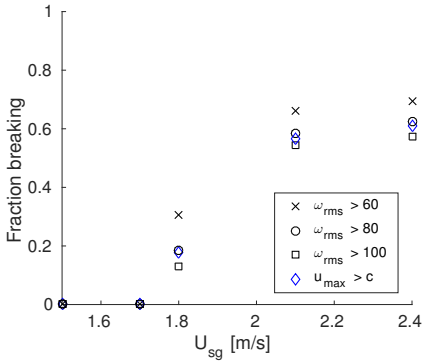

Figure 13: Fraction of waves that are considered breaking at different ω_{rms}-threshold values, and using $u_{max} > c$ as criterion for detecting wave breaking.

Siddiqui & Loewen (2006) also used a criterion based on the vorticity in the crest region to differentiate between breaking and non-breaking waves in an open channel system. They considered waves where the variance of the vorticity in the ROI (note that a different ROI was applied) was greater than 70 s^{-2} to be microscale breaking. The present study considers a different physical system than what was investigated by Siddiqui & Loewen (2006), and the geometrical properties of the waves vary somewhat between the two studies. Differences in the observed vorticity levels are for this reason to be expected. However, it is assessed that the primary reason for the significantly higher vorticity levels observed in the present work is the enhanced PIV resolution (resolution is a factor 8 times higher compared with Siddiqui & Loewen (2006)). The vorticity levels observed in this work resemble the results from Peirson & Banner (2003) and Duncan (2001), where the PIV resolution is similar to our analysis. The more focused ROI applied in the present work also means that a higher value of the vorticity threshold is suitable compared with the analysis performed by Siddiqui & Loewen (2006).

Table 2: Overview of waves analyzed by PIV, and fraction of breaking and non-breaking waves.

U_{sg} [m/s]	1.50	1.70	1.80	2.10	2.40
Number of PIV velocity fields	500	500	1000	1000	1000
Waves with ROI identified	345	306	582	696	654
Number (%) breaking	0 (0)	0 (0)	75 (12.8)	379 (54.5)	374 (57.2)
Number (%) intermediate	0 (0)	1 (0.3)	101 (17.3)	81 (11.6)	80 (12.2)
Number (%) non-breaking	345 (100)	305 (99.7)	406 (69.8)	236 (33.9)	200 (30.6)

4.3. Characteristics of breaking and non-breaking waves

Using the ω_{rms}-threshold for detecting breaking and non-breaking waves described in section 4.2.1, statistics of breaking and non-breaking waves are extracted and compared. As there are five experimental cases, for three of which we observe both non-breaking and breaking waves, a total of eight averaging cases are analyzed.

4.3.1. Average properties of breaking and non-breaking waves

In table 3, the mean of the maximum wave steepness ($\overline{S_{max}}$), $\overline{ak}$, ROI steepness ($\overline{S_{ROI}}$, evaluated as $|\Delta y/\Delta x|$ in the ROI) and average crest height ($\overline{\eta_c}$) for microbreaking and non-microbreaking waves are compared. Note that for $U_{sg} = 1.50$ and 1.70 m/s, no breaking waves were detected. It is observed that on average, the breaking waves are steeper than the non-breaking waves, evaluating

either of the three steepness measures. These results are similar to the results reported by Siddiqui & Loewen (2007), who observed that $\overline{S_{max}}$ increased by 30-50 % comparing breaking and non-breaking waves. Note that as discussed previously, there is a significant overlap in the steepness observed for breaking and non-breaking waves, hence the steepness in itself can not be used as a criterion for detecting breaking waves.

While Siddiqui & Loewen (2007) observed that microscale breaking waves on average had a higher crest than non-breaking waves (25 - 100 % higher), results for the two highest flow rates imply that there is very little difference in the crest height of breaking and non-breaking waves observed in the present work. The reason for this discrepancy is assessed to be the triggering system applied. While Siddiqui & Loewen (2007) evaluated all waves passing the PIV section as either breaking or non-breaking, the triggering system introduces a bias towards detecting larger amplitude waves. Including a large fraction of small amplitude, non-breaking waves into the dataset would result in the average crest height of non-breaking waves to be reduced, and our results would likely be more in accord with the results obtained by Siddiqui & Loewen (2007).

Table 3: Average properties of breaking and non-breaking waves. η_c is the crest height. Overbar indicates average properties.

U_{sg}	$\overline{S_{max}}$ [-]		$\overline{ak}$ [-]		$\overline{S_{ROI}}$ [-]		$\overline{\eta_c}$ [mm]	
	non-breaking	breaking	non-breaking	breaking	non-breaking	breaking	non-breaking	breaking
1.50	0.13	NA	0.049	NA	0.04	NA	0.8	NA
1.70	0.22	NA	0.096	NA	0.10	NA	2.1	NA
1.80	0.25	0.38	0.111	0.142	0.15	0.26	3.9	4.8
2.10	0.35	0.46	0.164	0.180	0.25	0.32	7.2	7.0
2.40	0.33	0.46	0.157	0.170	0.22	0.31	7.3	7.2

4.3.2. Phase-averaged properties of breaking and non-breaking waves

The conditional phase-averaging procedure described in section 3.3 was applied to all five experimental cases, separating breaking and non-breaking waves. In figure 14, phase-averaged properties for the $U_{sg} = 2.10$ m/s case are presented. These are representative for the results obtained also at $U_{sg} = 1.80$ and 2.40 m/s. The subfigures on the left illustrate phase-averaged properties beneath non-breaking waves, while the subfigures on the right illustrate properties of the breaking waves. The velocity fields are plotted in a region ensuring that at least 200 data points are used in the averaging of any variable in the (θ, ζ) coordinate system. When analyzing the phase-averaged results, it should be kept in mind that the averaging is performed over a relatively broad-banded wave spectrum, hence significant variability is expected also within each averaging case. However, the phase-averaged velocity fields are assessed to provide valuable information on the characteristic features of the waves, and how these evolve from non-breaking to active breaking.

Several distinct features of the flow fields can be observed in figure 14. Comparing figure 14 a) and b), it is observed that while the peak horizontal velocity for non-breaking waves is centered at the crest, this peak is shifted to the leeward side of the breaking waves, indicating a spilling region. This spilling region is also observed clearly in the $\langle V \rangle$ plots presented in figure 14 c) and d).

In figure 14 e) - h), the phase-averaged ω_z- and ϵ-fields reveal that while the vorticity is observed to be fairly constant over the wave form in the non-breaking case, significantly higher values (approximately one order of magnitude) are observed in the spilling region for the breaking waves. This is consistent with the instantaneous velocity fields analyzed in section 4.1. Also $\langle \epsilon \rangle$ is observed to have peak values one order of magnitude higher for the breaking than non-breaking waves. It can be noted that the maximum dissipation rate is observed on the leeward side of the wave, in the highly turbulent spilling region. Siddiqui & Loewen (2010) also calculated the phase distribution of

ϵ, and found that the peak values of ϵ were located directly below the wave crest. As the spilling region is very thin (typically less than 2 mm), it seems likely that this was not captured by the measurements of Siddiqui & Loewen (2010), as their PIV resolution was approximately 2 mm. The results presented in figure 14 are assessed to be qualitatively reasonable, as we expect high levels of energy dissipation in the spilling region. However, as discussed in section 3.4, we do not expect that the PIV resolution is sufficient to accurately estimate ϵ in this region, as the very high dissipation rates observed imply a Kolmogorov length scale significantly smaller than the PIV resolution.

In figure 15, the phase-averaged interface elevation η for breaking and non-breaking waves is presented in figure a). In figure 15 b) and c), $\langle\omega_z\rangle$ and $\langle\epsilon\rangle$ are depth-averaged over the top 2 mm of the wave (typical depth of the highly turbulent spilling region), and presented as a function of wave phase.

The phase-averaged interface elevation is calculated by the interface detected by the LFV camera; hence for all cases, a reliable average is obtained for all wave phases. As $\langle\omega_z\rangle$ and $\langle\epsilon\rangle$ is calculated by the PIV velocity fields, information on these parameters far from the ROI (20° to 80°) are not available. A cutoff in the data is made so that phase-averaged values with fewer than 50 data points are omitted from the results presented in figure 15. All breaking and non-breaking waves (numbers listed in table 2) will contain information of the wave phase from 20° to 80°, while the probability of detecting a wave phase away from the ROI decreases with distance from the ROI.

Consistent with the results for $\langle\eta_c\rangle$ presented in table 3, it can be observed that there is little to differentiate the observed crest heights of breaking and non-breaking waves of the two highest flow rates. However, the troughs of the breaking waves are significantly shallower. This is consistent with the results presented in table 3, where it was observed that the average wave steepness $\overline{ak}$ is higher for the breaking than for the non-breaking waves, indicating that the breaking waves (on average) has a higher degree of non-linearity.

The results for the depth-averaged $\langle\omega_z\rangle$ and $\langle\epsilon\rangle$ follow the same trends observed in figure 14 e)-h). Significantly higher levels of vorticity and turbulent dissipation is observed in the spilling region of breaking waves compared with the non-breaking waves.

In figure 16 a) and b), the phase-averaged horizontal velocity and turbulent dissipation rate below the crest (at θ=0°) is presented for all averaging cases. It is observed that for the U_{sg} 2.10 and 2.40 m/s cases, the phase-averaged horizontal velocity for breaking and non-breaking waves are very similar below a depth of approximately 6 mm from the interface. Closer to the interface, the horizontal velocity profiles of the breaking waves are observed to increase compared with the non-breaking waves.

The results for $\langle\epsilon\rangle$ beneath the crest of microscale breaking waves show that the turbulent dissipation rate is approximately $1.5 * 10^{-2}\ m^2/s^3$ close to the water surface. This is an order of magnitude higher than the results reported by Siddiqui & Loewen (2007). While there are differences in the physical system (comparing an open wind-wave tank and a closed two-phase pipe flow geometry), the higher PIV resolution in the present work is assessed to be an important reason for the enhanced turbulent dissipation rate calculated. Lee *et al.* (2017) reported values of ϵ below the crest of mechanically generated microscale breaking waves, and found values approaching $1 * 10^{-2} m^2/s^3$ near the interface, in line with the dissipation rates observed here. It should be noted that the calculation of ϵ is sensitive to errors in the PIV. These are (in absolute value) assessed to be relatively constant within the PIV FOV. As we see a clear evolution of ϵ with depth, and a significant increase in the turbulent dissipation rate for breaking waves, we assess that the turbulent dissipation rate near the interface (for breaking and non-breaking waves) is not dominated by noise from the PIV. Care should however be taken when evaluating the lowest dissipation rates observed, as these may be significantly influenced by noise in the PIV measurements.

The black dashed lines in figure 16 b) indicate that for the non-breaking cases, and below the depth where the increased dissipation rate associated with wave breaking is observed, $\epsilon \propto \xi^{-0.7}$,

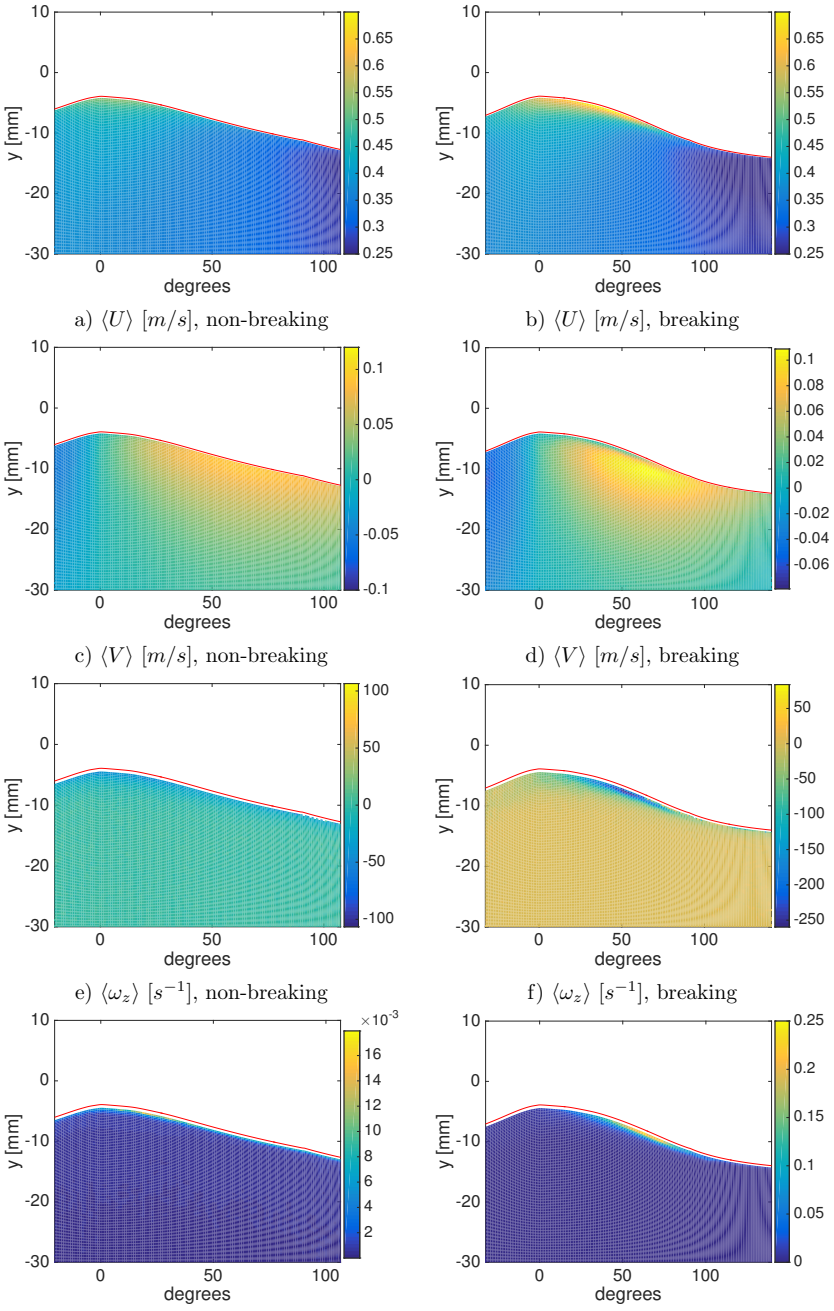

a) $\langle U \rangle$ $[m/s]$, non-breaking

b) $\langle U \rangle$ $[m/s]$, breaking

c) $\langle V \rangle$ $[m/s]$, non-breaking

d) $\langle V \rangle$ $[m/s]$, breaking

e) $\langle \omega_z \rangle$ $[s^{-1}]$, non-breaking

f) $\langle \omega_z \rangle$ $[s^{-1}]$, breaking

g) $\langle \epsilon \rangle$ $[m^2/s^3]$, non-breaking

h) $\langle \epsilon \rangle$ $[m^2/s^3]$, breaking

Figure 14: Comparison of phase-averaged fields for non-breaking (left side) and breaking (right side) waves observed in the U_{sg} 2.10 m/s case.

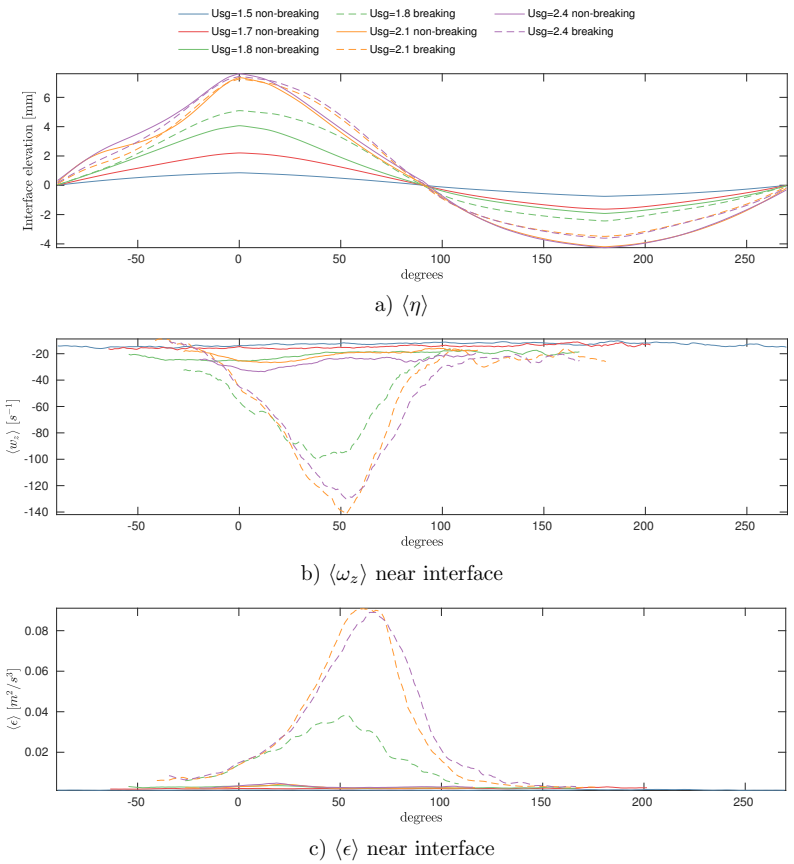

Figure 15: a) Mean interface elevation as function of wave phase. b) and c) Phase-averaged properties averaged within the top 2 mm of the interface.

where ξ is the distance from the interface. In the region directly affected by wave breaking, the dissipation rate is found to scale approximately as $\epsilon \propto \xi^{-2}$. Based on analysis of field experiments conducted in Lake Ontario, Terray *et al.* (1996) proposed a three-layer scaling of the dissipation rate below breaking waves. Terray *et al.* (1996) proposed that breaking directly injects energy to a depth z_b, and the dissipation rate was assumed to be constant between the surface and z_b. Below this upper layer was an intermediate layer which was found to scale as $\epsilon \propto \xi^{-2}$, similar to the behavior observed in figure 16 b). Below the transition layer was a region which would behave as a normal wall-layer. Terray *et al.* (1996) identified the "breaking depth" as $z_b \approx 0.6H_s$, where H_s is the significant waveheight. The constant dissipation rate above the breaking depth is not observed in the data presented in figure 16 b). However, it should be kept in mind that there are significant differences to the physical systems analyzed, and the breaking severity of microscale and larger scale breaking waves. Lee *et al.* (2017) reports $\epsilon \propto \xi^{-2}$ beneath the crest of breaking waves, and while a constant dissipation rate layer at the scale of the significant wave height was not observed, the dissipation was found to scale as $\epsilon \propto \xi^{-1}$ close to the surface (for depths less than ≈ 0.3 times the wave amplitude). For the U_{sg} 2.10 and 2.40 m/s cases (considering breaking waves), we also observe a change in the depth-dependence of ϵ close to the free surface, although we do not observe the

same scaling as reported by Lee *et al.* (2017).

From figure 16 b), the effect of microscale breaking is observed down to a depth of approximately 10 mm below the interface for the two highest gas flow rate cases. This is consistent with the results from Siddiqui & Loewen (2007), who found that the effect of microscale breaking waves could be observed to a depth of one significant waveheight ($H_s = 4\eta_{rms}$, is approximately 12 mm for these cases). To obtain a more global estimate of the effect of breaking on the turbulent dissipation rate, $\langle\epsilon\rangle$ is depth-averaged from the interface down to 10 mm below the interface at the crest ($\theta = 0°$). The results are presented in figure 16 c). It is observed that $\langle\epsilon\rangle$ remains relatively constant below non-breaking waves as the gas flow rate is increased above the onset of wave breaking. However, below breaking waves, the dissipation rate is observed to increase as the gas velocity is increased, indicating that the breaking events become more energetic. Comparing the depth-averaged dissipation rate of breaking and non-breaking waves, it is observed that the dissipation rate is 2.5-4 times higher for the breaking cases. These results are comparable to the results presented by Siddiqui & Loewen (2010), who reported an increase in turbulent dissipation rate by a factor 2-3 beneath the crest of microscale breaking waves.

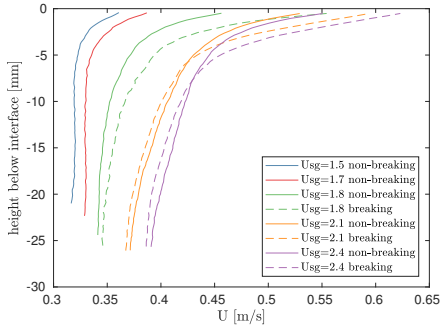

a) $\langle U\rangle$ at $\theta = 0$

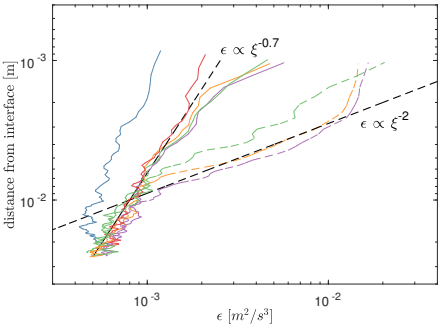

b) $\langle\epsilon\rangle$ at $\theta = 0$

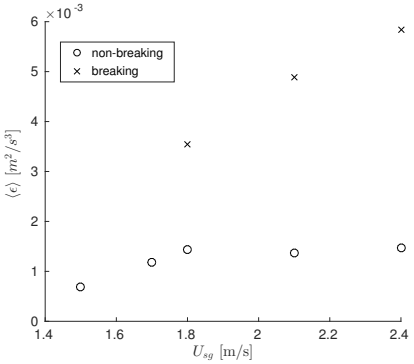

c) depth-averaged $\langle\epsilon\rangle$ at $\theta = 0$

Figure 16: a) Phase-averaged horizontal velocity below the crest. b) Turbulent dissipation rate $\langle\epsilon\rangle$ below crest. c) Depth-averaged $\langle\epsilon\rangle$ below the crest, from interface to 10 mm below interface.

4.4. Estimation of total breaking frequency

The breaking frequencies presented in figure 13 and table 2 represent the breaking frequencies observed in the PIV data acquired by the pressure probe trigging. As shown in Appendix A: Trigging

of PIV system, the trigging system results in a bias towards detecting and acquiring data for the higher amplitude waves in the system. To estimate a total breaking frequency for all waves, the breaking probability within each 0.5 mm crest height bin observed by the PIV was evaluated, using the threshold of $\omega_{rms} > 100$. The number of observations within each crest height bin observed by the wave probes was then used to estimate the total breaking frequency for each experimental case. Results are presented in figure 17.

For the two highest gas velocity cases, there are no observed wave crests with a surface elevation below 3.5 mm in the PIV dataset. Here the breaking probability is assumed to be zero. This is assessed to be a reasonable estimate as for the two height bins from 3.5 to 4.5 mm, a marked reduction in the breaking probability (approximately 50 % reduction) was observed compared with the higher amplitude waves for both cases. Extrapolating these results, and also considering the fact that no cases of wave breaking was observed for crest heights below 2.5 mm in the U_{sg} 1.80 m/s case, it seems reasonable that only a small fraction of the waves with a crest height below 3.5 mm in the $U_{sg} = 2.10$ and 2.40 m/s cases will be breaking.

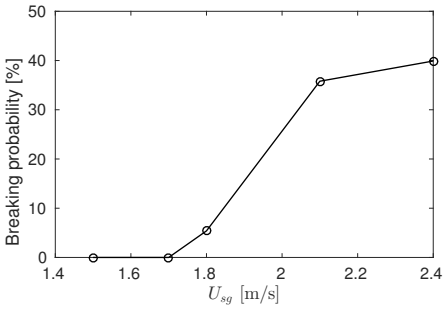

Figure 17: Estimated total breaking probability.

It should be noted that there are other biases which may impact on the total breaking probability estimated. One of these is the method employed to detect breaking, which requires the region from 20° to 80° to be visible in the PIV FOV. This results in a bias towards detecting waves where the leeward side of the crest is steeper, and the distance from the wave crest to the zero-down crossing (at 90°) is short. As seen in section 4.3.1, steeper waves are more likely to be in a state of breaking, hence this effect may result in a bias towards detecting a higher fraction of breaking waves. The threshold of ω_{rms} also impacts the total breaking frequency. This has a relatively higher impact on the $U_{sg} = 1.80$ m/s case, as seen in figure 13.

From visual inspection of the wave field and analysis of high speed video of the experiments, the breaking probabilities presented in figure 17 are assessed to be reasonable. The initial occurrence of breaking waves at U_{sg} 1.80 m/s coincides with the visual impression obtained from the experiments.

5. Concluding remarks

In this paper, detailed PIV measurements of waves in two-phase pipe flow are performed, in order to detect where in the flow-map small-scale wave breaking is first observed, and to quantify the impact of these small-scale breaking events.

Keeping the superficial liquid velocity constant at 0.1 m/s, the first signs of wave breaking are observed at $U_{sg} = 1.8$ m/s. This implies that microscale wave breaking occurs before the onset of the amplitude saturation regime reported by Ayati *et al.* (2015). As the gas flow rate is increased into the amplitude saturation regime, a significant fraction of the waves are observed to be in

a state of active breaking, and it is estimated that 35 - 40 % of the waves passing through the measurement section are breaking. Although small scale breaking is also observed before the onset of the amplitude saturation regime, the results presented in this study support the suggestions by Ayati & Carneiro (2018) that microscale breaking is an important mechanism as the gas velocity is increased and the wave amplitude is observed to saturate.

The effect of microscale wave breaking is observed down to a depth of approximately 10 mm below the interface for the highest gas flow rate case ($U_{sg} = 2.40$ m/s). The analysis reveals that below the crest of microscale breaking waves, the dissipation rate is 2.5 to 4 times higher than below non-breaking waves. The turbulence levels below breaking waves are observed to increase for increasing gas flow rates, indicating that the wave breaking events become more energetic as the gas flow rate is increased.

Acknowledgement

The authors wish to acknowledge the strategic research initiative EarthFlows at the Faculty of Mathematics and Natural Sciences at the University of Oslo. Laboratory Head Engineer Olav Gundersen is gratefully acknowledged for the technical assistance he provided for the experimental work.

Appendix

Appendix A: Trigging of PIV system

Two pressure probes (Kulite XTL-190) were mounted flush to the pipe bottom, upstream of the PIV section (ref. figure 2). The pressure probes sampled the pressure at a frequency of 2000 Hz. The raw data was low-pass filtered and normalized by a normalization filter based on the previous 30 seconds of measurement time. The output from the normalization filter is centered around 0 with standard deviation 1. Assuming that the measured pressure is directly related to the hydrostatic pressure above the probes (neglecting dynamic pressure and pressure variations in the air-phase above the wavy interface), and further that this is related to the interface elevation in the center of the pipe, the output from the normalization filter represents the number of standard deviations around the mean water level of the current interface elevation. Note that it is generally observed that the water level is higher towards the pipe walls (especially for the higher gas flow rate cases), which is assessed to impact on the pressure probe data, making a direct link between the measured pressure and the interface height in the center of the pipe inaccurate.

The trigger is set up to activate when a normalized pressure peak higher than some threshold value σ is detected by the downstream pressure probe. When a valid pressure peak is detected, cross correlation is performed between the two pressure probes, evaluating the previous 1 second of data. The peak of the cross-correlation is used to estimate the wave propagation speed c. The distance from the pressure probes to the PIV section (approximately 28 cm) and the wave propagation speed is used to evaluate the required delay time until the system is triggered. The system ensures that the section of the wave that is of interest (the leeward side of the wave crest in this study) is repeatedly present in the FOV when the PIV system is triggered, and the double images used for PIV are obtained. As seen in table 2, $\approx$ 65 % of all PIV images acquired included the ROI, and could be used in the statistical analysis of the flow field performed in this work. A minimum time delay between two trigger pulses of 5 seconds was implemented to prevent problems with the data transfer to the computer (ref. section 2).

In the present study, the focus was on detecting the larger amplitude waves, where wave breaking is assessed to be more probable. For this reason, a threshold value of σ =1.6 was used. This ensures that the relatively higher amplitude waves are detected and evaluated. The triggering of the PIV

system described in this section introduces a bias towards including waves with a higher crest height in the PIV dataset. This bias is illustrated in figure 18, where the wave crest heights observed by the conductance wave probes (performing continuous measurements for the full experimental time period) and by the PIV system are binned in 0.5 mm bins, and their frequency of occurrence in the dataset is presented.

The trigging of the PIV system was applied for all experimental cases, except for the lowest gas flow rate (U_{sg} = 1.5 m/s). Here the waves were very small, and the cross correlation from the pressure probes was dominated by noise, providing unreliable estimates for the trigging delay. For this reason, the PIV system was triggered at a constant frequency of 0.2 Hz. Note that as the waves at this flow rate were much shorter than for the higher gas flow rate cases (ref. figure 3 c), and as the wave field was observed to be more regular (ref. figure 4), the pressure probe trigging was less important for this experimental case. It can be noted from figure 18 a) that the the PDF of η_c observed by the wave probes and PIV system closely match, as no bias is introduced by the triggering. For the remaining four cases where the pressure probe trigging was applied, it is clear that the waves triggering the PIV system represent the larger waves in the system.

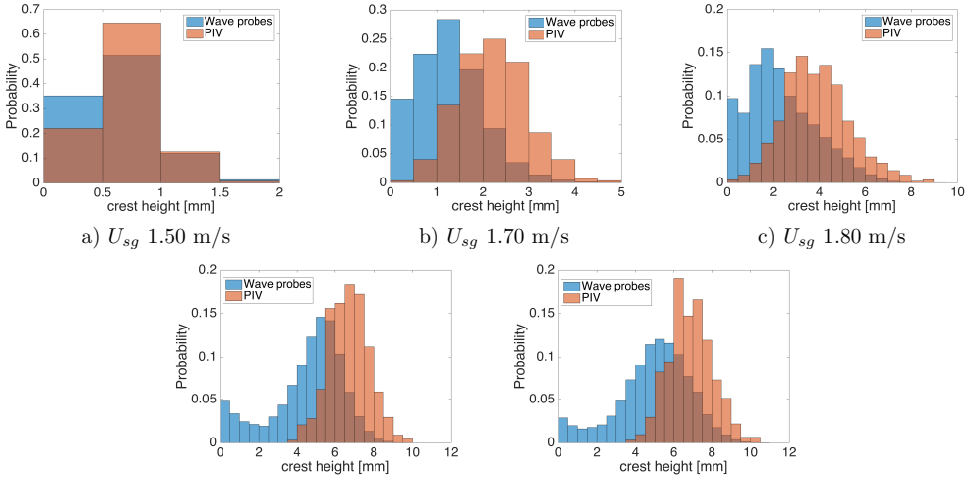

a) U_{sg} 1.50 m/s b) U_{sg} 1.70 m/s c) U_{sg} 1.80 m/s

d) U_{sg} 2.10 m/s e) U_{sg} 2.40 m/s

Figure 18: Bar chart indicating the frequency of occurrence for crest height within 0.5 mm bins. Observed by wave probes (including all waves during the experimental runs) and by PIV system.

References

Andritsos, N. & Hanratty, T.J. 1987 Influence of interfacial waves in stratified gas-liquid flows. *AIChE journal* **33** (3), 444–454.

Ayati, A.A. & Carneiro, J.N.E. 2018 Statistical characterization of interfacial waves in turbulent stratified gas-liquid pipe flows. *International Journal of Multiphase Flow* **103**, 94–105.

Ayati, A.A., Kolaas, J., Jensen, A. & Johnson, G.W. 2014 A PIV investigation of stratified gas-liquid flow in a horizontal pipe. *International Journal of Multiphase Flow* **61**, 129–143.

Ayati, A.A., Kolaas, J., Jensen, A. & Johnson, G.W. 2015 Combined simultaneous two-phase PIV and interface elevation measurements in stratified gas/liquid pipe flow. *International Journal of Multiphase Flow* **74**, 45–58.

Ayati, A.A., Kolaas, J., Jensen, A. & Johnson, G.W. 2016 The effect of interfacial waves on the turbulence structure of stratified air/water pipe flow. *International Journal of Multiphase Flow* **78**, 104–116.

Babanin, A. 2011 *Breaking and dissipation of ocean surface waves*. Cambridge University Press.

Banner, M.L. & Phillips, O.M. 1974 On the incipient breaking of small scale waves. *Journal of Fluid Mechanics* **65** (4), 647–656.

Banner, M. L., Barthelemy, X., Fedele, F., Allis, M., Benetazzo, A., Dias, F. & Peirson, W. L. 2014 Linking reduced breaking crest speeds to unsteady nonlinear water wave group behavior. *Physical review letters* **112** (11), 114502.

Biberg, D. 2007 A mathematical model for two-phase stratified turbulent duct flow. *Multiphase Science and Technology* **19**, 1–48.

Birvalski, M., Tummers, M.J., Delfos, R. & Henkes, R.A.W.M. 2014 PIV measurements of waves and turbulence in stratified horizontal two-phase pipe flow. *International Journal of Multiphase Flow* **62**, 161–173.

Birvalski, M., Tummers, M.J. & Henkes, R.A.W.M. 2016 Measurements of gravity and gravity-capillary waves in horizontal gas-liquid pipe flow using PIV in both phases. *International Journal of Multiphase Flow* **87**, 102 – 113.

Buckley, M.P. & Veron, F. 2016 Structure of the airflow above surface waves. *Journal of Physical Oceanography* **46** (5), 1377–1397.

Caulliez, G. 2013 Dissipation regimes for short wind waves. *Journal of Geophysical Research: Oceans* **118** (2), 672–684.

Coleman, J.W. & Garimella, S. 1999 Characterization of two-phase flow patterns in small diameter round and rectangular tubes. *International Journal of Heat and Mass Transfer* **42** (15), 2869–2881.

Deike, L., Popinet, S. & Melville, W.K. 2015 Capillary effects on wave breaking. *Journal of Fluid Mechanics* **769**, 541–569.

Doron, P., Bertuccioli, L., Katz, J. & Osborn, T.R. 2001 Turbulence characteristics and dissipation estimates in the coastal ocean bottom boundary layer from PIV data. *Journal of Physical Oceanography* **31** (8), 2108–2134.

Duncan, J.H. 2001 Spilling breakers. *Annual review of fluid mechanics* **33** (1), 519–547.

Fernandino, M. & Ytrehus, T. 2006 Determination of flow sub-regimes in stratified air–water channel flow using LDV spectra. *International journal of multiphase flow* **32** (4), 436–446.

Hsu, C.-T., Hsu, E.Y. & Street, R.L. 1981 On the structure of turbulent flow over a progressive water wave: theory and experiment in a transformed, wave-following co-ordinate system. *Journal of Fluid Mechanics* **105**, 87–117.

Jessup, A.T., Zappa, C.J. & Yeh, H. 1997 Defining and quantifying microscale wave breaking with infrared imagery. *Journal of Geophysical Research: Oceans* **102** (C10), 23145–23153.

Katsaros, K.B. & Ataktürk, S.S. 1992 Dependence of wave-breaking statistics on wind stress and wave development. In *Breaking Waves*, pp. 119–132. Springer.

Khait, A. & Shemer, L. 2018 On the kinematic criterion for the inception of breaking in surface gravity waves: Fully nonlinear numerical simulations and experimental verification. *Physics of Fluids* **30** (5), 057103.

Lee, J.H., Monty, J.P., Elsnab, J., Toffoli, A., Babanin, A.V. & Alberello, A. 2017 Estimation of kinetic energy dissipation from breaking waves in the wave crest region. *Journal of Physical Oceanography* **47** (5), 1145–1150.

Longuet-Higgins, M.S. 1992 Capillary rollers and bores. *Journal of Fluid Mechanics* **240**, 659–679.

Peirson, W.L. & Banner, M.L. 2003 Aqueous surface layer flows induced by microscale breaking wind waves. *Journal of Fluid Mechanics* **479**, 1–38.

Peregrine, D. H. 1983 Breaking waves on beaches. *Annual Review of Fluid Mechanics* **15** (1), 149–178.

Perlin, M., Choi, W. & Tian, Z. 2013 Breaking waves in deep and intermediate waters. *Annual review of fluid mechanics* **45**, 115–145.

Qiao, H. & Duncan, J.H 2001 Gentle spilling breakers: crest flow-field evolution. *Journal of Fluid Mechanics* **439**, 57–85.

Raffel, M., Willert, C. E., Scarano, F., Kähler, C. J., Wereley, S. T. & Kompenhans, J. 2018 *Particle image velocimetry: a practical guide*. Springer.

Shemer, L. & Liberzon, D. 2014 Lagrangian kinematics of steep waves up to the inception of a spilling breaker. *Physics of Fluids* **26** (1), 016601.

Siddiqui, M.H.K. & Loewen, M.R. 2006 Detecting microscale breaking waves. *Measurement Science and Technology* **17** (4), 771.

Siddiqui, M.H.K. & Loewen, M.R. 2007 Characteristics of the wind drift layer and microscale breaking waves. *Journal of Fluid Mechanics* **573**, 417–456.

Siddiqui, M.H.K. & Loewen, M.R. 2010 Phase-averaged flow properties beneath microscale breaking waves. *Boundary-Layer Meteorology* **134** (3), 499–523.

Siddiqui, M.H.K., Loewen, M.R., Richardson, C., Asher, W.E. & Jessup, A.T. 2001 Simultaneous particle image velocimetry and infrared imagery of microscale breaking waves. *Physics of Fluids* **13** (7), 1891–1903.

Strand, O. 1993 An experimental investigation of stratified two-phase flow in horizontal pipes. *Dr. Scient. Thesis, University of Oslo. Oslo, Norway* .

Sutherland, P. & Melville, W.K. 2013 Field measurements and scaling of ocean surface wave-breaking statistics. *Geophysical Research Letters* **40** (12), 3074–3079.

Sutherland, P. & Melville, W.K. 2015 Field measurements of surface and near-surface turbulence in the presence of breaking waves. *Journal of Physical Oceanography* **45** (4), 943–965.

Tennekes, H. & Lumley, J.L. 1972 *A first course in turbulence*. MIT press.

Terray, E.A., Donelan, M.A., Agrawal, Y.C., Drennan, W.M., Kahma, K.K., Williams, A.J., Hwang, P.A. & Kitaigorodskii, S.A. 1996 Estimates of kinetic energy dissipation under breaking waves. *Journal of Physical Oceanography* **26** (5), 792–807.

Tulin, M. P. & Landrini, M. 2001 Breaking waves in the ocean and around ships. In *23rd Symposium on Naval Hydrodynamics*, pp. 713–745. The National Academies Press.

Tzotzi, D. & Andritsos, N. 2013 Interfacial shear stress in wavy stratified gas-liquid flow in horizontal pipes. *International Journal of Multiphase Flow* **54**, 43 – 54.

Vollestad, P., Ayati, A.A., Angheluta, L., LaCasce, J.H. & Jensen, A. 2019 Experimental investigation of airflow above waves in a horizontal pipe. *International Journal of Multiphase Flow* **110**, 37–49.

Zhang, X. & Cox, C.S. 1999 Vortical motions under short wind waves. *Wind-driven air-sea interface. School of Mathematics, Uni. NSW, Sydney, Australia* pp. 277–284.

Paper IV

Microbreaking and airflow separation in stratified air-water pipe flow - PIV setup and initial results

Petter Vollestad, Atle Jensen

In *Proceedings of the 13th International Symposium on Particle Image Velocimetry* (2019), pp. 1435–1444.

IV

13th International Symposium on Particle Image Velocimetry – ISPIV 2019
Munich, Germany, July 22-24, 2019

Microbreaking and airflow separation in stratified air-water pipe flow - PIV setup and initial results

Petter Vollestad[1*], **Atle Jensen**[1]

[1] University of Oslo, Department of Mathematics, Oslo, Norway

[*] pettervo@math.uio.no

Abstract

Simultaneous two-phase PIV of stratified air-water pipe flow is performed in order to study the effect of microscale wave breaking on the airflow above waves. This paper focuses on the experimental setup used to acquire high quality PIV results of both the gas and liquid phase, and how the PIV system is triggered to ensure that the system acquires data of the leeward side of individual wave crests, which is of interest for the analysis. Some preliminary results illustrating airflow over breaking and non-breaking waves are included. The results indicate that at moderate air flow rates, active wave breaking has a stabilizing effect on the airflow above waves, reducing the sheltered region on the leeward side of the waves and the extent of the separated airflow region compared to non-breaking waves of similar steepness.

1 Introduction

Stratified gas-liquid pipe flow is relevant for several engineering applications, especially within the oil and gas sector. Recently, simultaneous two-phase PIV has been applied to study the stratified regime in air-water pipe flow (Ayati et al., 2014; Birvalski, 2015; Vollestad et al., 2019a). This has provided spatio-temporally and phase-averaged velocity profiles, enhancing our understanding of the stratified flow regime.

Vollestad et al. (2019b) studied the phenomenon of microscale wave breaking in the stratified wavy regime of two-phase pipe flow, using PIV in the liquid phase. Microbreaking, or microscale breaking waves are small scale wave breaking events, where surface tension prevents the jet formation and air entrainment characteristic of the more energetic spilling or plunging breakers (Babanin, 2011). As microscale breaking waves do not cause air entrainment, these are difficult to detect visually. The vorticity in the crest region detected by PIV has been found to be a good way of detecting active wave breaking (Siddiqui and Loewen, 2006; Vollestad et al., 2019b).

Wave breaking transfers momentum and energy to the underlying liquid flow (both mean flow and turbulence). Wave breaking may also modify the airflow above the waves, and hence both the form drag and shear stresses which make up the interface friction (Banner, 1990; Reul et al., 2008). Hence, understanding the effect of microscale breaking on the airflow above waves is assessed to be important in accurately describing the momentum transfer between the two phases in gas-liquid pipe flow. For this reason we wish to extend the PIV system used by Vollestad et al. (2019b) to capture both the signs of small scale breaking in the liquid phase, and the simultaneous airflow in the gas phase.

In this paper, details of the PIV system and some instantaneous velocity profiles obtained are presented. The aim of the PIV system is:

- Obtain high quality, simultaneous PIV data of the gas and liquid phase of two-phase pipe flow.
- Simultaneously with the PIV acquisition; obtain interface elevation measurements along a region exceeding the dominant wavelength. To correlate wave statistics with wave breaking and airflow separation.
- Trigger the PIV system so that the leeward side of the crest (of interest for the analysis) is consistently within the PIV field of view as data is acquired.

2 Experimental setup

The experiments were conducted in the hydrodynamics laboratory, at the University of Oslo. The experimental setup consists of a 31 meter long, 10 cm diameter, transparent acrylic pipe. The fluids used are air and water at atmospheric pressure. A PIV measurement section was placed 26 meters from the pipe inlet (see figure 1). In this paper we focus on the PIV measurement section and the results stemming from it. Further details on the experimental setup is provided by Ayati et al. (2014); Vollestad et al. (2019b).

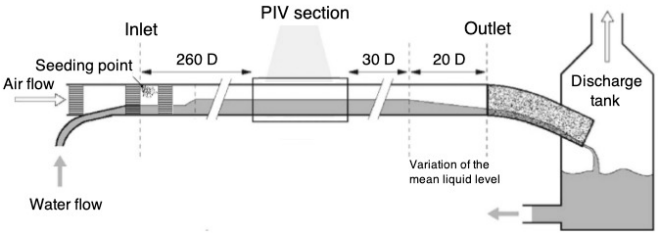

Figure 1: Overview of experimental setup.

2.1 PIV setup and processing

Simultaneous two-phase PIV (S2P-PIV) in pipes was first performed by Ayati et al. (2014), using the same flow loop and an experimental setup closely matching the setup used in the present work. While Ayati et al. (2014) demonstrated the applicability of S2P-PIV in gas-liquid pipe flow, a number of changes to the experimental setup was necessary to increase the accuracy close to the interface, and to obtain simultaneous information of the full wave profile, as well as the velocity field directly below and above the spilling region of microscale breaking waves.

A 147 mJ double pulse ND:YAG laser illuminated the centerplane of the pipe from above, while three cameras were applied to evaluate the velocity fields and the interface elevation (η) along the centerplane. The position and field of view (FOV) of the three cameras are illustrated in figure 2. The two PIV cameras are PCO.4000 cameras (4008x2672 pixels), fitted with 100 mm lenses. The liquid phase PIV camera was fitted with a 1.6x teleconverter, ensuring that the FOV of the liquid phase camera was approximately half of the gas phase camera. As a high downwards/upwards looking angle was necessary for the gas and liquid phase cameras respectively (due to the crescent shape of the waves), these were fitted with scheimpflug adapters, allowing the entire centerplane of the pipe to be in focus. A 'large-field-of-view' (LFV) camera (Nikon D7200, 6000x4000 pixels, fitted with a 28 mm lens) was applied to detect the interface over a section exceeding the dominant wavelength (λ_p) in the system (for the flow rates of interest λ_p varied from 0.2 to 0.3 m). For efficient interface detection Rhodamine B was added to the water at a concentration of $5 * 10^{-5}$ g/l, and the LFV camera was fitted with a filter closely matching the light emitted from the Rhodamine (B+W 041 red/orange filter). An example image from the LFV camera is presented in figure 5 a). An optical correction box half filled with water was placed around the pipe (see figure 2 c). Prior to the experiments a coordinate system was placed within the PIV section, and imaged by all cameras. The coordinate system is a combination of regular (Δx = 10 mm, Δy = 15 mm), and irregular (Δx and $\Delta y \approx$ 2-3 mm) spaced dots. The coordinate system is similar to the coordinate system used by Ayati (2015), but has been extended to account for the FOV of the LFV camera. When imaging the coordinate system by the liquid phase PIV camera the pipe was filled with water. To ensure that the coordinate system did not move as the pipe was filled with water, a circular mounting frame was designed (see figure 2 d). This included a mini lift jack that could be tightened to keep the coordinate system in a fixed location as water was introduced to the pipe.

While the two PIV cameras acquired double images (one image per laser pulse), the LFV camera was set to trigger before the first laser pulse, and had an exposure time which exceeds the Δt of the PIV acquisition, i.e. the LFV camera is double exposed. During the short Δt of the laser pulses the interface would move less than 0.1 mm, which is a negligible fraction of the overall wavelength.

As the velocity of the gas phase is approximately one order of magnitude higher than the liquid phase (excluding the spilling region of microscale breaking waves), care must be taken in setting a suitable Δt in the PIV acquisition. As seen in figure 2, the FOV of the gas-phase PIV camera is approximately twice the

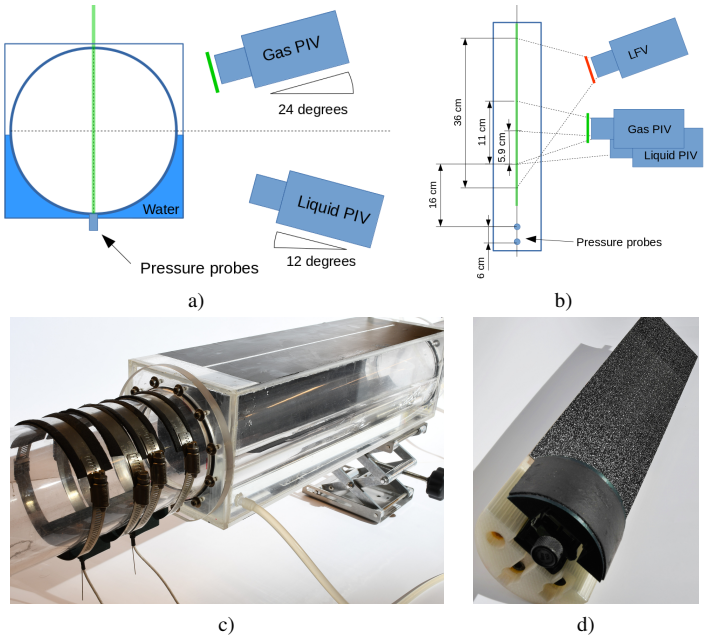

Figure 2: a-b) Overview of PIV setup. a) Seen in the streamwise direction. LFV camera located behind the gas-phase PIV camera. b) Seen from above. Green transparent line represents laser light sheet. Filters used indicated on cameras. Green: Midopt BP525 Light Green Bandpass Filter. Red: B+W 041 red/orange filter. c) Pipe section including pressure probes and optical correction box. d) Coordinate system on cylindrical mounting plate.

width of the liquid phase PIV camera, hence the maximum displacement (evaluated in pixels/Δt) of the gas-phase particles were found to be 4-5 times higher than the maximum displacement of the liquid particles. Δt was set to ensure that the gas phase particles had a maximum displacement of 18-20 px, while the liquid phase particles had a maximum displacement of 4-5 px outside the spilling region. In the spilling region of microscale breaking waves the liquid particle displacement could be up to 10 px.

Particles

The gas phase was seeded with small water droplets, generated by a high-pressure atomizer. The particles were introduced at the pipe inlet, and honeycomb flow straighteners were positioned behind the seeding point to damped out disturbances introduced by the seeder. Water is used to seed to airflow to ensure that we do not influence the surface tension of the liquid phase, and hence the characteristics of the wave formation/growth/breaking. According to the manufacturer, 72 % of the droplets are smaller than 6 μm, and the particles have been found to exhibit a stokes number well below 1 for the flow rates of interest (Ayati et al., 2014). The gas phase particles as seen in the PIV images is presented in figure 3 c).

In previous analysis of the experimental setup (Sanchis and Jensen, 2011; Ayati et al., 2014; Ayati, 2015; Vollestad et al., 2019b), 20-50 μm polyamide particles have been used as seeding particles in the liquid phase. Initial analysis using polyamide particles showed that light reflections near the interface of actively breaking waves dominated the light from the gas-phase particles near the interface. This is seen in figure 4 a). It is believed that this is caused by light scattering on the turbulent interface of an actively breaking wave. Due to the high downwards looking angle of the gas-phase PIV camera, light emitted from polyamide particles ”behind” the centerplane of the pipe obstructed the gas-phase PIV images in the spilling region of the wave.

In order to avoid this issue, fluorescent particles made from a commercially available acrylic paint (Lefranc & Bourgeois, Fluorescent light orange) were used in the liquid phase, and a green bandpass filter

centered at 532 nm (Midopt BP525 Light Green) was added to the gas-phase PIV camera. Particles made from the same paint was also used by Birvalski (2015). It was found necessary to remove the smallest particles from the paint/water mixture, as the high density of very small (sub μm) particles in the paint obstructed the view of the cameras, and significantly reduced the signal-to-noise ratio of the liquid phase images. The larger particles were extracted in a two-stage settling process, where approximately 20 mL of paint was added to 10 L of water. This mixture was left to settle for 12-16 hours, which allowed the larger particles to sink to the bottom. The water (including the smallest particles) was removed, and the process was repeated. After this process most of the particles were observed to be in the range of 5-20 μm diameter. An image of the particles under the microscope and as seen in the PIV images is presented in figure 3 a) and b) respectively.

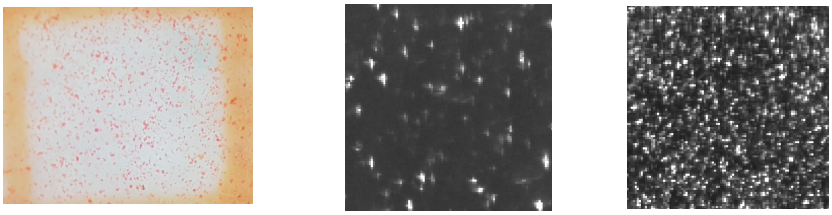

a) b) c)

Figure 3: a) Image of liquid phase particles under the microscope, 1 mm^2 FOV. b-c) 100x100 pixels raw image of particles as seen in the experiments, for the liquid (b) and gas phase (c)

Including the fluorescent particles and green bandpass filter to the gas-phase camera significantly improved the quality of the imaging of the gas-phase near the interface, which can be seen comparing figure 4 a) and b).

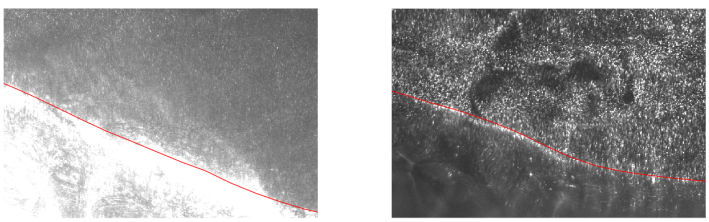

a) b)

Figure 4: Example gas-phase PIV images using polyamide particles in the liquid phase (a), and fluorescent liquid particles in combination with bandpass filter (b). Both images shows an actively breaking wave, zoomed in at the spilling region. Red line indicate detected interface.

Image processing

The gas-liquid interface was detected from the LFV camera by dividing the image into vertical sections, and scanning the image sections from top to bottom, using a combination of sobel edge-detection and a threshold value to detect the interface. An example image and interface is presented in figure 5 a). The interface was transferred to the gas and liquid PIV images using the coordinate transforms (figure 5 b-c), and the regions below/above respectively were masked out and omitted from the PIV analysis (figure 5 d-e).

As the laser light is directed from above, and hence penetrate the wavy gas-liquid interface, care must be taken in directly applying the liquid phase images for PIV. For several of the images acquired, strong light reflections were observed at the interface in the spilling region of the wave. In order to avoid that these

bright regions dominated the cross-corrolation and impacted on the PIV results, an algorithm was created for detecting and masking out coherent regions of high light intensity in the near the interface. An example of the process is presented in figure 6. Capillary ripples riding in front of the dominant wave components were found to scatter the light in the liquid phase, as seen in figure 5 b). By applying a median filter and subtracting from the original image, these variations in light intensity were reduced (see image 5 d).

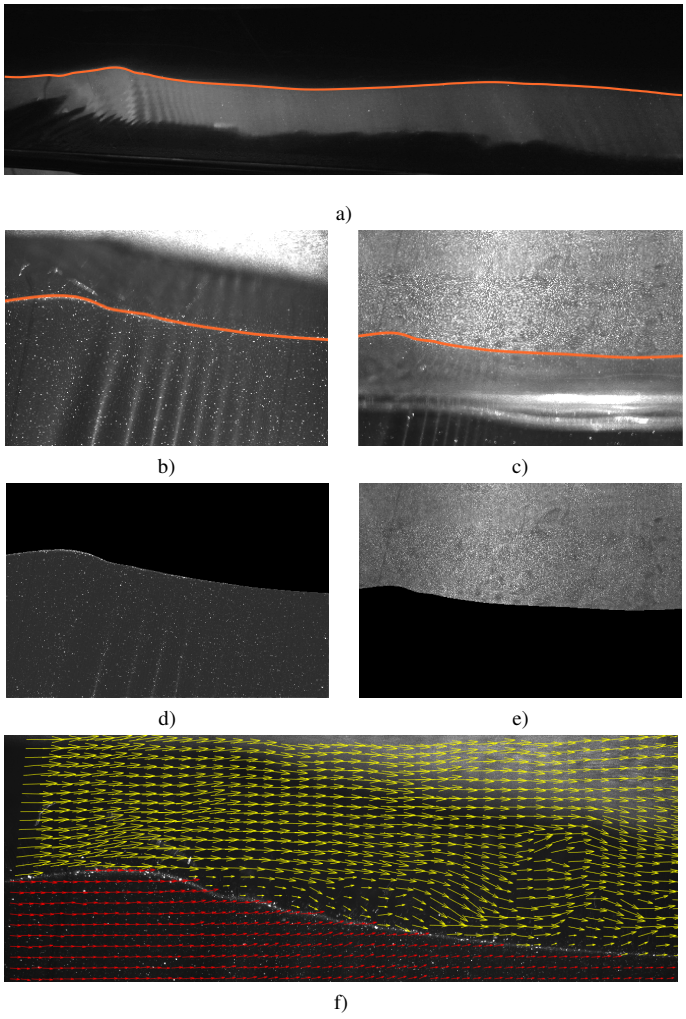

Figure 5: a-e) Example of interface detection and image pre-processing for PIV. a) Image and detected interface from the LFV camera. b-c) Raw image from the liquid (b) and gas-phase (c) camera respectively. d-e) Masked liquid (d) and gas (e) image used in cross-correlation. f) Vector field of gas (yellow arrows) and liquid (red arrows), superimposed on liquid phase PIV image. Showing 1/2 vectors in the gas phase, and 1/4 vectors in the liquid phase.

The cross-correlation was performed in Digiflow by Dalziel Research Partners, using a cascade of cross-correlation passes, with a final subwindow size of 32x32 pixels in the liquid phase, and 52x26 pixels in the

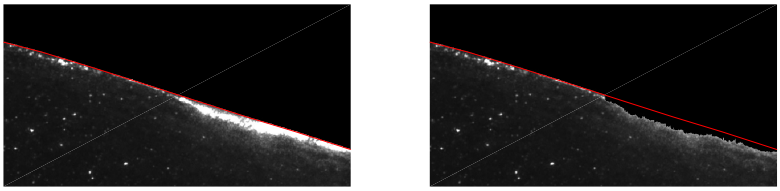

a) b)

Figure 6: Illustration of removal of high intensity regions observed in the spilling region of microscale breaking waves. Red line: detected interface.

gas phase, using 50 % overlap. This translates to a spatial resolution of 0.24x0.24 mm^2 in the liquid phase, and 0.75x0.38 mm^2 in the gas phase. Spurious vectors were detected by local median filtering and replaced by cubic interpolation (Raffel et al., 2018).

2.2 Trigging of PIV system

Due to limitations in the data transfer rate, the PIV cameras could only acquire new double images every three seconds. We are interested in acquiring images of the leeward side of the waves, to detect signs of microscale wave breaking (Vollestad et al., 2019b). If the PIV images were acquired at a fixed rate, only a small fraction (approximately 10 %) of the images would include the full leeward side of the wave, necessary to classify the wave as either actively breaking or non-breaking according to the criterion by Vollestad et al. (2019b).

In order to limit the measurement time, and the amount of data recorded, a method to trigger the PIV system to acquire data of value to the investigation was devised. Two pressure probes (Kulite XTL-190) were mounted flush to the pipe bottom, upstream of the PIV section (position indicated in figure 2). The pressure was sampled at 2000 Hz, and normalized by a normalization filter, based on the previous 30 seconds of data. The output from the normalization filter is denoted p_n. p_n is centered at zero, and has a standard deviation of one. Neglecting pressure variations in the air-phase and dynamic pressure fluctuations, the pressure variations at the pipe bottom is directly related to the liquid height. When a pressure peak (associated with a wave crest) fulfills the criterion $\sigma < p_n$ (where σ is a threshold value, chosen as 1.4-1.6 depending on the flow rate combination), a valid wave crest is detected. At this point a cross-correlation of the previous one second of data between the two pressure probes is performed, to estimate the wave propagation speed c. The wave speed is used to calculate a trigger delay, $\Delta t_{trigger} = \Delta x/c$ (where Δx is the distance to the PIV section), ensuring that the PIV system is triggered when the crest and the leeward side of the wave is within the liquid phase PIV FOV. The time development from detection of a valid crest is illustrated in figure 7.

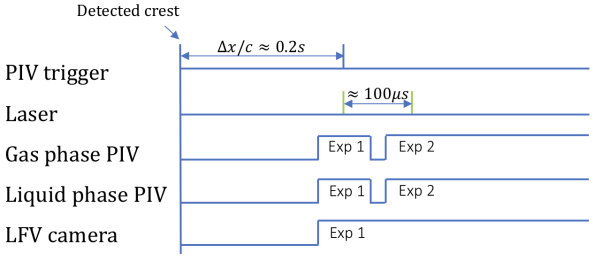

Figure 7: Schematic view of the trigging of the PIV setup, from the time a valid wave crest is detected by the trigger system.

As the propagation speed of individual waves is observed to vary in time, the triggering is not 100 % accurate. In figure 8 a) the distance from the prescribed crest position (Δx from the downstream pressure

probe), and the crest position found from the LFV interface detection for 1000 waves is presented. In table 1 the fraction of crests within ± 10, 20 and 30 mm of the target is presented. The dominant wavelength is approximately 20 cm, hence only 10 % would fall within ± 10 mm if the images were acquired at a fixed rate.

As the trigger will not activate for $\sigma < p_n$, the system introduces a bias for detecting the larger waves in the system. This bias is illustrated in figure 8 b). Here the distribution of crest heights detected by wave gauges (measuring all waves passing the measurement section) and the PIV system (measuring waves triggering the PIV system) are compared. As can be seen, the waves under analysis by the PIV system represent the larger waves in the system, and the large majority of the detected waves fulfill $\sigma\eta_{rms} < \eta_c$, where η_c and η_{rms} is the crest height (relative to the mean water level) and the rms of the interface elevation fluctuations respectively. Extracting the larger waves in the system is reasonable, as the smallest waves are very seldom found to be in a state of active breaking (Vollestad et al., 2019b), and hence will not contribute to the statistical analysis investigating the effect of breaking.

The method for assessing active wave breaking by Vollestad et al. (2019b) requires that the region θ = 20° to 80° , where θ is the wave phase determined by a zero-crossing procedure (from 0° at the crest to 360° at the following crest), is within the liquid phase PIV FOV. The trigger method is found to ensure that this is the case for typically 70 % of all waves found to trigger the system, increasing the number of useful images acquired by a factor seven compared with acquiring at a fixed rate.

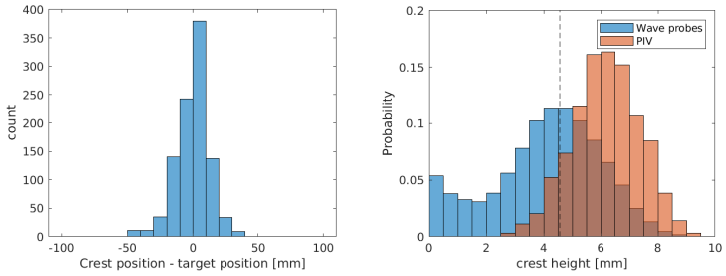

a) b)

Figure 8: Trigger statistics for U_{sl} = 0.1 m/s, U_{sg} = 1.95 m/s. a) Number of wave crests observed at 10 mm bins away from the target position. b) PDF of crest height observed by wave gauges (measuring all waves) and the PIV system (triggered at peak $p_n > 1.6$). Dashed vertical line represents $\sigma\eta_{rms}$.

Fraction of crests within +/- 10 mm from center	62.3 %
Fraction of crests within +/- 20 mm from center	90 %
Fraction of crests within +/- 30 mm from center	96.9 %

Table 1: Results from peak pressure probe triggering and peak detection

3 Example results and discussion

In this section some initial results from the analysis of one experimental case is presented and discussed. The experimental case considers gas and liquid superficial velocities (U_{sg}/U_{sl}) of 1.85 and 0.1 m/s respectively. This is slightly above the onset of microscale breaking found by Vollestad et al. (2019b). Approximately 10% of the waves passing the measurement section are in a state of active breaking. Due to space limitations, a full description and analysis of the results is not included in this paper, but will be addressed in a future publication.

Figure 9 a)-b) presents instantaneous velocity fields in the gas (showing velocity vectors and vorticity contours) and liquid phase (showing vorticity contours), superimposed on the gas-phase PIV images for two waves, denoted wave *A* and *B* respectively. The full wave profile (defined from zero-up crossing to the next zero-up crossing) from the LFV camera is presented in figure 9 c).

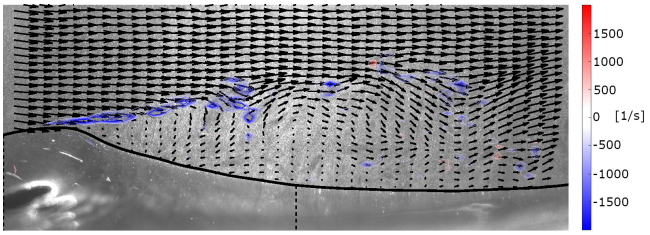

a) Wave *A*: Non-breaking wave

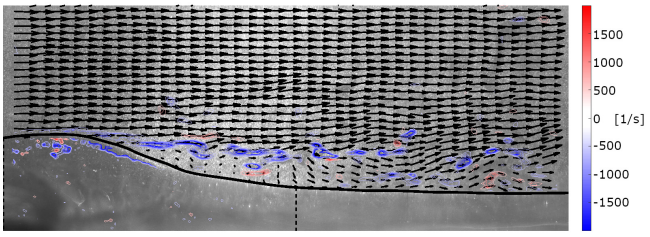

b) Wave *B*: Microbreaking wave

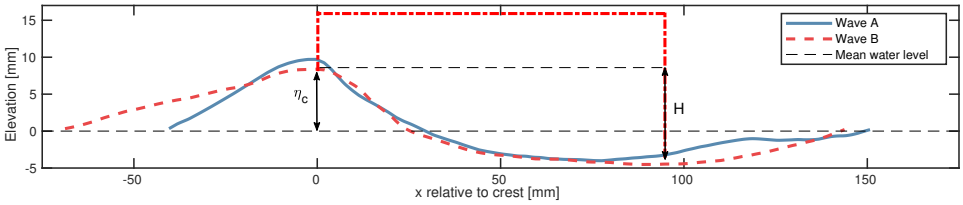

c) Wave profile of wave *A* and *B*

Figure 9: a-b) Velocity vectors in gas phase and vorticity contours ([s^{-1}]) in both gas and liquid phase superimposed on gas phase PIV image. Liquid vorticity multiplied by five for visibility. Showing 1/2 vectors in the gas phase. Vertical dashed lines indicate borders of liquid phase FOV. c) Wave profile from LFV camera for wave *A* and *B*. Crest height (η_c), wave height (H) and ROI (red dashed-dotted line) illustrated for wave *B*.

We observe that above wave *A* the airflow separates, as the shear layer is seen to leave the interface, resulting in a significant sheltered region including regions of backflow on the leeward side of the wave. For wave *B*, the signs of airflow separation are much more moderate. In the liquid phase we observe that the vorticity level is fairly constant along the wave profile of wave *A*, while for wave *B*, large coherent regions of high vorticity if observed on the leeward side of the wave, and directly below the crest. This indicates that vorticity is generated by a spilling region, and swept backwards relative to the propagating wave. The wave is found to be in a state of active breaking following the criterion by Vollestad et al. (2019a). The state of breaking can also be inferred from the images of the liquid interface. For wave *A* we observe capillary ripples extending all the way to the crest, while for wave *B* the capillary ripples are displaced downstream of the spilling region, indicating that the wave is in a state of active breaking.

Table 2 summarizes some properties of the two waves. ak is the wave steepness, evaluated as $\pi H/\lambda$, where H and λ is the wave height and length respectively, and ε_{crest} is the front-face steepness, evaluated as $\Delta y/\Delta x$ from the crest to the zero-down crossing. Also listed in table 2 is the fraction of vectors within a region of interest (ROI) where the horizontal velocity is negative. The ROI is chosen from the crest to the trough in the horizontal direction, and from the interface and to a height $2 * \eta_c$ (η_c is the crest height) above the mean water level in the vertical direction. The ROI for wave *B* is illustrated in figure 9 c). The results presented in figure 9 a-b) clearly show that while significant regions above the leeward side of wave

Wave	Microbreaking	ak	ε_{crest}	Fraction $u < 0$ in ROI
A	No	0.22	0.34	0.27
B	Yes	0.19	0.34	0.02

Table 2: Properties of the two waves presented in figure 9.

A is propagating against the dominant flow direction, this effect is much more moderate for wave B. This is reflected in the results in table 2, as 27% and 2% of the vectors within the ROI is observed to propagate against the dominant flow direction for wave A and B respectively.

In figure 10 a scatter plot of the fraction of the ROI with $u < 0$ versus ε_{crest} is presented for 1000 waves. Breaking and non-breaking waves (identified by the method of Vollestad et al. (2019b)) are indicated by red crosses and black circles respectively. We observe that backflow first occurs as ε_{crest} exceeds ≈ 0.1, and is moderate until $\varepsilon_{crest} > 0.2$. For high front-face steepness, backflow is occurring in a significant fraction of the ROI for both breaking and non-breaking waves, but the results indicate that the separated flow region on average is larger above non-breaking than breaking waves. Wave A and B also show this trend, but it is worth noting that they represent somewhat extreme cases of high/low sheltering for the relatively high front-face steepness of $\varepsilon_{crest} = 0.34$.

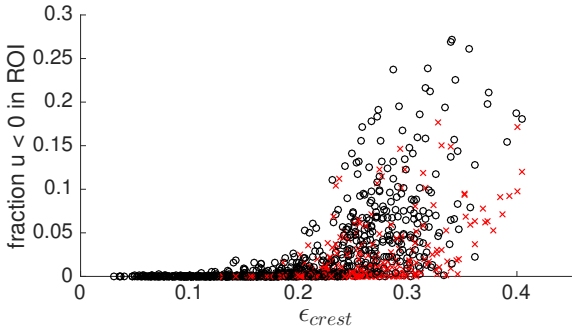

Figure 10: Scatter plot of the fraction of velocity vectors within the ROI where $u < 0$ vs ε_{crest} at $U_{sl} = 0.1$ m/s, $U_{sg} = 1.85$ m/s. o: Non-breaking wave. x: Microscale breaking waves.

Airflow separation has traditionally been linked with the onset of wave breaking (Banner, 1990), hence it is somewhat surprising to see that for a fixed front-face steepness, active wave breaking has the effect of reducing the extent of the separation bubble. There are different mechanisms that can explain this observation. As the waves break the interface geometry changes, and the actively breaking waves are observed to have a more rounded crest shape compared to the steep, non-breaking waves (this can be observed comparing wave A and B in figure 9), allowing for flow expansion without separation near the crest. As the wave breaks, the liquid spills forward at a speed exceeding the wave propagation speed, and the airflow speed close to the interface. Hence, wave breaking induces a shear force on the airflow, working against the airflow separation structures.

For this moderate flow rate we observe that microscale wave breaking has the effect of modifying the airflow pattern above waves of similar geometrical properties. Airflow separation is known to enhance the form drag over waves, as it drastically increases the pressure field asymmetry relative to the wave profile (Banner, 1990), and to reduce the shear stresses in the sheltered region. To assess the overall effect of the intermittent wave breaking and airflow separation on the momentum transfer between the phases we would need measurements of the pressure field at the interface, which is outside the scope of the present study.

Acknowledgements

The authors wish to acknowledge the strategic research initiative EarthFlows at the Faculty of Mathematics and Natural Sciences at the University of Oslo. Laboratory Head Engineer Olav Gundersen is gratefully

acknowledged for the assistance he provided for the experimental work.

References

Ayati AA (2015) *Dynamics of stratified gas/liquid pipe flow*. Ph.D. thesis from the University of Oslo

Ayati AA, Kolaas J, Jensen A, and Johnson GW (2014) A PIV investigation of stratified gas-liquid flow in a horizontal pipe. *International Journal of Multiphase Flow* 61:129–143

Babanin A (2011) *Breaking and dissipation of ocean surface waves*. Cambridge University Press

Banner ML (1990) The influence of wave breaking on the surface pressure distribution in wind-wave interactions. *Journal of Fluid Mechanics* 211:463–495

Birvalski M (2015) *Experiments in stratified gas-liquid pipe flow*. Ph.D. thesis from TU Delft, Delft University of Technology

Raffel M, Willert CE, Scarano F, Kähler CJ, Wereley ST, and Kompenhans J (2018) *Particle image velocimetry: a practical guide*. Springer

Reul N, Branger H, and Giovanangeli JP (2008) Air flow structure over short-gravity breaking water waves. *Boundary-layer meteorology* 126:477–505

Sanchis A and Jensen A (2011) Dynamic masking of PIV images using the radon transform in free surface flows. *Experiments in fluids* 51:871–880

Siddiqui MHK and Loewen MR (2006) Detecting microscale breaking waves. *Measurement Science and Technology* 17:771

Vollestad P, Ayati AA, Angheluta L, LaCasce JH, and Jensen A (2019a) Experimental investigation of airflow above waves in a horizontal pipe. *International Journal of Multiphase Flow* 110:37–49

Vollestad P, Ayati AA, and Jensen A (2019b) Microscale wave breaking in stratified air-water pipe flow. *Physics of Fluids* 31:032101

Paper V

Experimental investigation of intermittent airflow separation and microscale wave breaking in wavy two-phase pipe flow

Petter Vollestad, Anis Awal Ayati, Atle Jensen

Published in *Journal of Fluid Mechanics* **878** (2019), pp. 796–819.
DOI: 10.1017/jfm.2019.660. Reprinted with permission.

V

Experimental investigation of intermittent airflow separation and microscale wave breaking in wavy two-phase pipe flow

P. Vollestad[1,*], A.A. Ayati[1], A. Jensen[1]

[1] *Department of Mathematics, University of Oslo, 0316 Oslo, Norway*

[*] *Corresponding author: pettervo@math.uio.no, +47 48 14 72 76*

Abstract

We perform an experimental analysis of co-current, stratified wavy pipe flow, with the aim of investigating the effect of small scale wave breaking (microscale breaking) on the airflow. Particle image velocimetry (PIV) is applied simultaneously in the gas and liquid phases. Active wave breaking is identified by high levels of vorticity on the leeward side of individual waves, and the statistics of the airflow above breaking and non-breaking waves are extracted from the gas-phase velocity fields.

Keeping the liquid superficial velocity constant ($U_{sl} = 0.1$ m/s), we consider two experimental cases of different gas flow rates. The lowest flow rate ($U_{sg} = 1.85$ m/s) is slightly higher than the onset of microscale breaking, while the higher flow rate ($U_{sg} = 2.20$ m/s) is within the regime where wave breaking is observed to be frequent, and the root-mean-square interface elevation η_{rms} is independent of gas flow rate.

Results show that for the lowest gas flow rate considered, active wave breaking has a stabilizing effect on the airflow above the waves, reducing the sheltered region on the leeward side of the wave and the turbulence above the wave crest compared with non-breaking waves at similar steepness. At the higher gas flow rate the effect of active wave breaking is found to be small, and the main geometrical properties of the waves are found to dominate the evolution of the separated flow region.

Keywords: gas/liquid flows, wave breaking, wind-wave interactions

1. Introduction

Airflow over water waves represents a challenging problem relevant both in nature and for engineering applications, such as stratified two-phase pipe flows, which is the focus of this work. Considering wind over waves, two of the most characteristic features for the liquid and gas phases, respectively, is wave breaking and airflow separation. Wave breaking occurs when fluid elements at the surface overtake the general waveform, resulting in increased turbulence in the liquid phase and a transfer of momentum and energy from the waves to the underlying flow (Jessup *et al.*, 1997; Banner & Melville, 1976). Airflow separation over surface waves is characterized by increased turbulence in the air phase as the shear layer separates from the interface, and a significant displacement of the streamlines relative to the wave shape. This results in a distribution of pressure and shear forces along the wave profile which deviate significantly from the non-separated case (Weissman, 1986). Analysis of these phenomena in the pipe flow literature are scarce, hence we refer to the air-sea literature for a background to the understanding of wave breaking and airflow separation.

Banner & Melville (1976) and Gent & Taylor (1977) considered separation above water waves as *"the occurrence, in a frame of reference moving with the waves, of a streamline leaving the water surface"*. This requires the surface velocity of the interface to match the wave speed, which is the criterion for incipient wave breaking. Hence, it was concluded that airflow separation may only occur

in conjunction with wave breaking. This criterion has been applied by researchers modelling drag on the sea surface (Kudryavtsev & Makin, 2001). However, early flow visualization techniques indicated that airflow patterns resembling the separated flow over solid obstacles may occur over non-breaking waves (Kawai, 1981, 1982; Weissman, 1986). According to Weissman (1986), the separation criterion utilized by Gent & Taylor (1977) and Banner & Melville (1976) is not appropriate when the surface is moving, as airflow separation over moving boundaries may have stagnation points away from the wall. As described by Weissman (1986); *"the "separation" we are concerned with is that of the shear layer closest to the surface..."*. Buckley & Veron (2016) considered the airflow as separating *"if the near-surface, high vorticity layer characteristic of an attached boundary layer is ejected away from the water surface and the surface vorticity is near zero or negative"*. A similar criterion was also applied by Reul *et al.* (2008) and Sullivan *et al.* (2018*b*).

Applying the definition of (shear layer) separation by Weissman (1986), Buckley & Veron (2016) and Reul *et al.* (2008), it has been documented both experimentally (Veron *et al.*, 2007; Tian *et al.*, 2010) and numerically (Sullivan *et al.*, 2018*b*) that separation may occur over non-breaking waves. Wave breaking has been found to be a sufficient, but not a necessary, condition for airflow separation (Tian *et al.*, 2010; Sullivan *et al.*, 2018*b*).

Wave breaking is separated into categories related to the severity and visual characteristics of the breaking process. Babanin (2011) divides wave breaking into plunging, spilling and microbreaking. Microbreaking, or microscale breaking is a weak form of wave breaking, where surface tension prevents the jet formation and air entrainment into the liquid phase as the wave breaks (Tulin & Landrini, 2001; Jessup *et al.*, 1997; Siddiqui & Loewen, 2006; Vollestad *et al.*, 2019*b*). Microscale breaking waves are short (wavelength of the order of a few decimeters), wind generated waves with amplitudes up to a few centimeters. In the present work we focus our attention on these small scale breaking waves.

We consider stratified wavy two-phase pipe flow. These flows have traditionally been modelled using a simple two-fluid model, which in addition to a modified single-phase correlation for the wall friction, relies on a parametrization of the interface friction factor (Ullmann & Brauner, 2006). The interfacial friction factor has typically been established through correlation studies based on pressure drop and liquid hold-up measurements (see e.g. Tzotzi & Andritsos 2013), yielding little physical insight into the mechanisms that govern the momentum exchange at the interface. Recently, stratified gas-liquid pipe flow has been analyzed using particle image velocimetry (PIV) in the centerplane of the gas and liquid phase (Ayati *et al.*, 2014, 2016; Birvalski *et al.*, 2015, 2016). These studies have provided spatio-temporally and phase-averaged flow fields, and hence valuable experimental data for model validation of more complex numerical models, and new insight into the dynamics of the two phases. Previous analysis of the experimental setup considered in this work (Vollestad *et al.*, 2019*a*) has shown that intermittent airflow separation is a frequent event as the gas flow rate in increased into the amplitude saturation regime described by Ayati *et al.* (2015), and microscale wave breaking has been observed when the superficial gas velocity $U_{sg} \geq 1.8$ m/s, for a superficial liquid velocity $U_{sl} = 0.1$ m/s (Vollestad *et al.*, 2019*b*) (the superficial velocity of phase k is $U_{sk} = \dot{m}_k/(\rho_k A)$, where $\dot{m}_k$ and ρ_k is the mass flow rate and density of phase k, while A is the cross-sectional area of the pipe). Microscale wave breaking was found to influence the liquid phase down to a depth of approximately 1 cm below the crest (approximately one significant wave height), increasing the turbulent dissipation rate below the crest by a factor 3-4 compared with non-breaking waves (Vollestad *et al.*, 2019*b*). These results are consistent with observations of microscale breaking waves in wind-wave tanks (Siddiqui & Loewen, 2007, 2010), indicating that the main features of microscale breaking waves in two-phase pipe flow are similar to the processes occurring in the ocean.

When small scale wind waves go from incipient to active breaking, a thin spilling region is generated on the leeward side of the wave crest, resulting in increased turbulence and vorticity in

the liquid phase. The present understanding of how active breaking influences the airflow field above waves and airflow separation is however far from complete (Sullivan *et al.*, 2018*b*). While previous analysis of two-phase pipe flow has documented that both airflow separation and microscale wave breaking occurs for sufficiently high gas flow rates, the link between the two has not previously been investigated in a pipe flow setup.

Analyzing airflow over waves by PIV in a rectangular wind-wave tank, Reul *et al.* (2008) found that the separation induced by breaking waves is stronger and more consistent than separation over non-breaking waves. Reul *et al.* (2008) performed measurements over waves ranging from microbreaking to plunging, the claim is not specific for microscale breaking waves. Banner (1990) evaluated the pressure and velocity field over small scale incipient and actively breaking waves, using a slope exceedance threshold to distinguish between breaking and non-breaking waves. Banner (1990) reports that while there is a significant phase shift of the pressure field also for unbroken steep waves, active wave breaking results in an increased (order 100 %) phase shift and form drag above the wave profiles. Similar results were found by numerical analysis by Maat & Makin (1992), who concluded that the increased local roughness in the spilling region enhanced the asymmetrical surface pressure pattern. Recently, Sullivan *et al.* (2018*b*) performed large eddy simulations (LES) of airflow above wave profiles taken from the experiments of Banner (1990). Example wave profiles of incipient and actively breaking waves ($ak = 0.25$, 0.28, $c/u_* = 1.58$, 1.23 for incipient and active breaking respectively) were investigated. Based on parameter tuning of the numerical model they found that the wave steepness, not the enhanced surface drift caused by wave breaking, was the critical property inducing large form drag over the actively breaking waves, indicating that the geometrical properties of the waves (and not the state of wave breaking) dictates the surface drag. Recent two-fluid direct numerical simulations (DNS) by Yang *et al.* (2018) have shown that while a plunging breaker will significantly impact the airflow field, a spilling breaker (initial steepness $ak = 0.35$) under relatively strong wind forcing ($c/u_* = 3.7$) does not significantly influence the airflow as the wave transitions from a smooth unbroken wave form to a spilling breaker. Simulations by Yang *et al.* (2018) indicate that the form drag remains essentially constant as the wave evolves into an active spilling breaker.

In this work we perform simultaneous two-phase PIV, to obtain 2-D velocity fields in both the gas and liquid phases. The technique was first applied by Ayati *et al.* (2014) for two-phase pipe flow. The novelty of this work lies in the simultaneous assessment of active wave breaking and evaluation of the airflow above individual waves. Wave breaking is assessed by the method of Vollestad *et al.* (2019*b*), evaluating the root-mean-square (rms) vorticity in the liquid phase on the leeward side of the crest. Statistics of the flow field over breaking and non-breaking waves at two different gas flow rates are examined. The goal is to investigate how active wave breaking affects the airflow above waves compared with non-breaking waves of similar steepness. Understanding the effect of small scale wave breaking and its link to airflow separation in stratified two-phase pipe flow is assessed to be an important step in quantifying the physical processes responsible for the momentum exchange at the interface between the two phases. While the closed pipe geometry impacts the flow, making a direct comparison with the processes occurring in the ocean inaccurate, the results obtained in the present work may also provide insight into the processes occurring in an open system, as the underlying mechanisms (wave breaking and airflow separation) are the same. The simultaneous assessment of active wave breaking and airflow separation above microscale breaking waves has, to the authors' knowledge, not previously been documented for either an open or closed air-water system.

This paper is organized in six sections (including this introduction). In section 2 the experimental setup is presented. In section 3 the experimental cases and methodology are presented. Results are presented in section 4. Instantaneous flow fields are presented in section 4.1, while statistics of the airflow field above breaking and non-breaking waves are presented in section 4.2. A detailed

analysis of waves within a narrow steepness band is performed in section 4.3. Finally, a discussion and concluding remarks are presented in section 5 and 6.

2. Experimental setup

The experiments were conducted at the Hydrodynamics Laboratory, at the University of Oslo. The experimental setup consists of a 31 meter long, horizontal, transparent, acrylic pipe with an internal diameter $D = 10$ cm. An overview of the experimental setup is presented in figure 1. Air and water were supplied at the inlet by a frequency regulated fan and pump respectively. Here, honeycomb flow straighteners were placed to dampen turbulent fluctuations introduced at the inlet. The gas and liquid flow rates were measured using an Emerson MicroMotion Coriolis flow meter and an Endress Hauser Promass Coriolis flow meter respectively. At the pipe outlet the fluids were discharged to a tank (at atmospheric pressure), and recirculated. The differential pressure in the air phase was measured over a 12.4 meter section, using a smar LD301 differential pressure gauge.

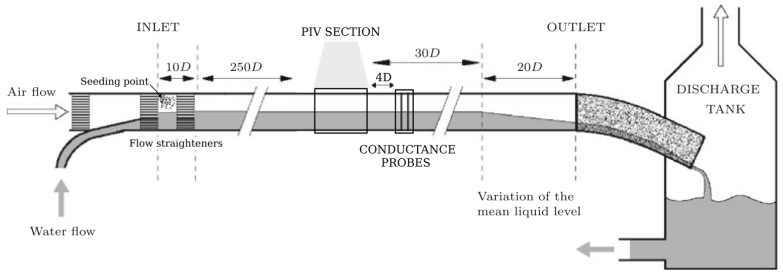

Figure 1: Schematic view of experimental setup.

A PIV section was placed $260D$ from the pipe inlet. Here, an optical correction box was placed around the pipe. The box was half-filled with water to reduce optical distortion of the liquid-phase PIV camera. A nonlinear coordinate transform was obtained for each of the cameras applied by imaging a coordinate system placed in the pipe centerline, using the coordinate system described in Ayati *et al.* (2015). PIV was conducted simultaneously in the centerplane of both phases. A 147 mJ ND:YAG laser (532 nm wavelength light) illuminated the centerplane of the PIV section from above. The head of the laser optics was placed 50 cm above the pipe centerline, creating a thin ($<$ 1 mm) laser sheet within the measurement section.

Three cameras were employed in the study. Their position and field of view (FOV) are shown in figure 2.

- Liquid phase PIV camera. PCO.4000 camera with 4008x2672 pixels. Fitted with a 100 mm lens and a 1.6x teleconverter. The camera is directed upwards at an angle of 12°.
- Gas phase PIV camera. PCO.4000 camera with 4008x2672 pixels. Fitted with a 100 mm lens. The camera is directed downwards at an angle of 24°. A high downwards looking angle was necessary as the crescent shape of the waves meant that the pipe wall was repeatedly wetted well above the mean water level.
- Large field of view (LFV) camera. A Nikon D7200 with 6400x4000 pixels. Fitted with a 28 mm lens. The camera was directed downwards at an angle of 30°, and looking upstream at an angle of approximately 31°.

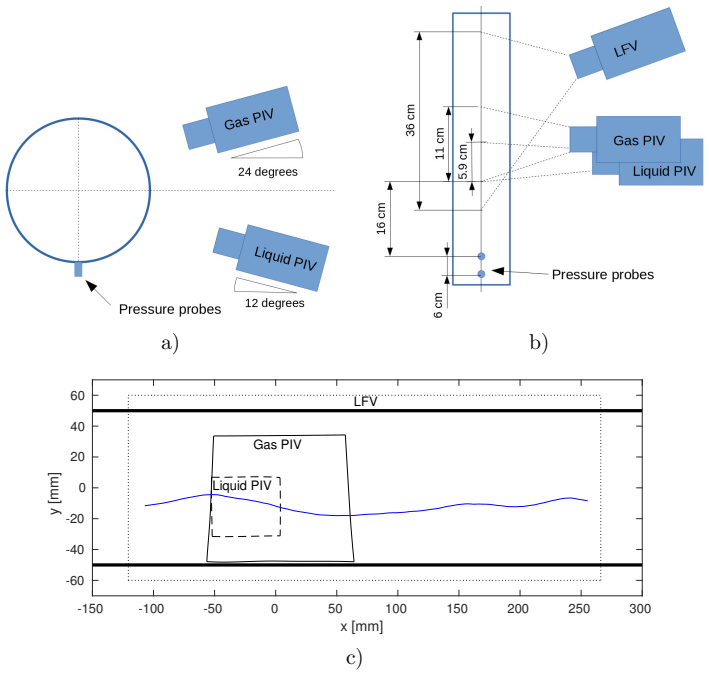

Figure 2: Schematic view of PIV measurement section. a) Looking downstream. b) Seen from above. c) FOV of all three cameras. Blue line represents an example interface profile (waves propagating to the right).

Due to the relatively high downward/upwards looking angle of the gas/liquid phase PIV cameras, these were fitted with Scheimpflug adapters, allowing the entire center plane of the pipe to be in focus.

The gas phase was seeded with small water particles, generated by a high-pressure atomizer. The particles were injected into the gas phase at the inlet. According to the manufacturer, 72 % of the droplets are below 6 μm, and it has previously been shown by Ayati *et al.* (2014) that the particles exhibit a Stokes number well below 1 for the flow rates of interest.

Initial analysis using polyamide particles in the liquid phase showed that light reflections from particles near the spilling region of microscale breaking waves influenced the gas-phase PIV images, causing unreliable results near the gas-liquid interface. This issue was overcome by using fluorescent particles in the liquid phase and fitting the gas-phase PIV camera with a bandpass filter centered at 532 nm (midopt BP525 Light Green Bandpass Filter). The liquid phase was seeded with fluorescent particles made from a commercially available acrylic paint (Lefranc & Bourgeois, Fluorescent light orange). Particles made from this paint were used also by Birvalski *et al.* (2015) to perform PIV in the liquid phase of two-phase pipe flow. The particles were extracted in a settling process, similar to the process described by Birvalski (2015). Visual inspection of the particles under the microscope revealed that the particle size typically ranged from 5 to 20 μm.

For efficient interface detection, Rhodamine B was added to the water at a concentration of $5 * 10^{-5}$ g/l. A filter closely matching the wavelength emitted from the rhodamine (B+W 041 red/orange filter) was added to the LFV camera. This removed the green signal from the droplets in the air phase, allowing for efficient interface detection from the LFV camera. The interface was detected by a thresholding technique, similar to the technique applied by Vollestad *et al.* (2019*b*), and transferred to the gas- and liquid-phase PIV images by applying a cubic coordinate transform.

By looking through many PIV images (gas and liquid), overlaid the detected interface, the accuracy of the interface detection and coordinate transform is assessed to be approximately 0.4 mm, similar to the PIV resolution.

Two pressure probes (Kulite XTL-190) were mounted flush to the pipe bottom (position indicated in figure 2). The probes measured the pressure at a frequency of 2000 Hz. The pressure was normalized by a normalization filter (output centered at 0 with standard deviation 1) based on the previous 30 seconds of data sampling. When a pressure peak (associated with a wave crest) above a threshold σ was detected by the downstream pressure probe, a cross-correlation of the previous one second of data was performed between the two probes, to estimate the wave speed. This estimate was used to evaluate a trigger delay to the PIV system, allowing the leeward side of the wave to be repeatedly present within the liquid phase PIV FOV as the PIV images were acquired (necessary for the analysis performed in this work). The pressure probe trigger system is described in more detail in Vollestad *et al.* (2019*b*).

The two laser pulses were triggered with a Δt of 100-120 μs (depending on the flow rate combinations applied). Note that while the PIV cameras acquired double images (one image per laser pulse), the LFV camera was set to trigger before the first laser pulse, and had an exposure time which was longer than the laser pulse Δt, i.e. the LFV image was double exposed. During the laser Δt, the waves would move less than 0.1 mm, which is a negligible fraction of the overall wave shape, and less than the accuracy of the interface detection.

A conductance wave gauge was placed 4 D downstream of the PIV section, measuring the interface elevation at 500 Hz. This consists of two double-wire probes of 0.3 mm diameter separated by 4 mm. The two probes were placed in the center of the pipe with a distance 6 cm in the streamwise direction. For more details on the wave gauges the reader is referred to Ayati *et al.* (2015).

PIV was performed with a cascade of sub-pixel passes, with a final interrogation window of 52x26 pixels in the gas phase, and 32x32 pixels in the liquid phase, using 50 % overlap. This translates to a spatial resolution of 0.75x0.38 mm^2 in the gas phase, and 0.24x0.24 mm^2 in the liquid phase. Spurious vectors were detected by standard methods based on a local median filtering (Raffel *et al.*, 2018), and replaced by cubic interpolation.

3. Methodology

3.1. Description of experimental cases

We consider two experimental cases, where the liquid superficial velocity is kept constant at U_{sl} = 0.1 m/s, while the gas superficial velocity (U_{sg}) is increased from 1.85 m/s to 2.20 m/s. These experimental cases were chosen as they appear in two different regimes in the flow map. As shown by Vollestad *et al.* (2019*b*), for this liquid flow rate the first interfacial waves are observed at U_{sg} = 1.3 m/s. η_{rms} (the rms of the interface elevation fluctuations) at the measurement section is observed to increase with U_{sg} until $U_{sg} \approx$ 2.0 m/s. At this gas superficial velocity a regime of "amplitude saturation" is observed, and the main characteristics of the wave field are relatively independent of the gas flow rate. This implies that an equilibrium between increased wind input and dissipation is reached, which is reminiscent of the equilibrium range of the ocean wave spectrum (Phillips, 1958, 1985). Vollestad *et al.* (2019*b*) found that the first evidence of wave breaking was observed at U_{sg} = 1.8 m/s. Increasing the gas velocity into the amplitude saturation regime was observed to increase both the frequency and intensity of the wave breaking events. Hence, for both experimental cases considered we expect to observe both breaking and non-breaking waves at the measurement section.

In order to observe a reasonable number of both breaking and non-breaking waves (needed to obtain reliable statistics) the lowest U_{sg} is set to 1.85 m/s rather than 1.8 m/s. The trigger

threshold σ was set to 1.6 for the $U_{sg} = 1.85$ m/s case and 1.4 for the $U_{sg} = 2.20$ m/s case. The trigger threshold results in a bias for detecting larger amplitude waves in the system, as the smaller waves will not trigger the PIV system. Setting a higher trigger threshold for the $U_{sg} = 1.85$ m/s case was necessary to observe a reasonable fraction of both breaking and non-breaking waves.

The main characteristics of the two experimental cases are presented in table 1, while the spectra (evaluated by the wave probes) are presented in figure 3. C_p is the characteristic wave speed evaluated by cross-correlation of the conductance wave probes, λ_p is the peak wavelength, evaluated at the peak of the spectrum and $\overline{h}$ is the mean water level in the center of the pipe, evaluated by the wave probes. This is used to evaluate the bulk gas and liquid velocities (U_{bg}/U_{bl}). The relationship between the superficial velocity of phase k and the bulk velocity is $U_{sk} = A_k U_{bk}/A$ where A and A_k are the pipe cross-sectional area and the area occupied by phase k. λ_p and $\overline{h}$ implies that $k_p h \approx 1.3 - 1$ for the two cases considered, and the waves can be classified as waves at intermediate depth. The wave age C_p/u_* indicates that the waves are young, wind-driven waves. The interfacial friction velocity u_* was estimated using a force balance over a 12.4 meter section of the pipe. Here the average pressure drop in the air phase was measured, and the wall friction was estimated by the Colebrook-White formulation. Subtracting the wall friction forces from the measured pressure drop yields an estimate of the interface friction τ_i, and the friction velocity is then evaluated as $u_* = \sqrt{\tau_i/\rho}$. Note that this is a global estimate of the wave age, and as the wave field develops along the pipe, deviations from the values listed in table 1 may occur locally. Further details on the development of the two-phase flow field with varying U_{sg} have been discussed by Ayati *et al.* (2015) and Vollestad *et al.* (2019*b*).

Table 1: Overview of experimental cases. N_{PIV} is the number of PIV velocity fields analyzed for each case.

U_{sl} $[m/s]$	U_{sg} $[m/s]$	η_{rms} $[mm]$	λ_p $[mm]$	C_p $[m/s]$	$\overline{h}$ $[mm]$	U_{bl} $[m/s]$	U_{bg} $[m/s]$	C_p/u_* $[-]$	N_{PIV} $[-]$
0.1	1.85	2.6	203	0.75	40.4	0.27	2.98	2.49	2395
0.1	2.20	3.4	230	0.82	38.2	0.30	3.39	2.12	2000

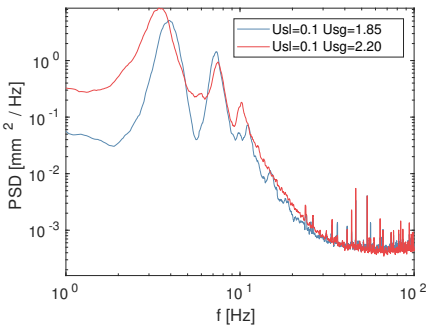

Figure 3: Frequency spectra from the waveprobes for the two experimental cases.

In the present work, measurements are performed in the pipe center plane, and flow variations in the lateral direction are not quantified. As discussed by Vollestad *et al.* (2019*b*) the flow rates under investigation are within the "2D wave" regime defined by Tzotzi & Andritsos (2013). The three-dimensionality of the wavefield (using the same two-phase flow loop) has previously been investigated by Strand (1993) and Smith *et al.* (2018). Strand (1993) used conductance wave probes at different cross-wise planes of the pipe and found that for the flow rates under investigation in the present work,

the normalized cross-correlation between the centerline and off-axis surface elevation exceeded 0.85 everywhere in the pipe. Smith *et al.* (2018) used X-ray tomography and found that the dominant wave components were well-described as two-dimensional for the flow rates of interest. Near the pipe walls the waves were observed to have a crescent shape, and slightly larger wave amplitudes were observed compared with the pipe centerline. This is in line with visual observations of the highest flow rate case in the present work. Example images of breaking and non-breaking waves in the same two-phase pipe flow configuration presented by Vollestad *et al.* (2019*b*) show that the waves retain their 2D shape also during breaking.

3.2. Regions of interest

Two "regions of interest" (ROIs) are implemented to monitor the velocity field in the gas and liquid phase, and to identify characteristic features of wave breaking and airflow separation respectively. These are denoted GROI and LROI for the gas and liquid phase ROIs. The ROI location relative to the wave profile is illustrated in figure 4 and described in more detail in the following sections.

The local wave phase θ is used to define the relative location along the wave. θ is determined based on a zero-crossing procedure. The crest/trough were assigned phases of 0° and 180° respectively, while the zero-down/zero-up crossings were assigned phases of 90° and 270°/-90°. Phases in between were linearly distributed. This is illustrated in figure 4.

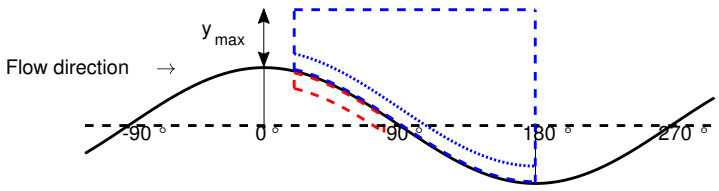

Figure 4: Illustration of the ROI's applied. Red dashed line: Liquid phase ROI to detect wave breaking. Blue dashed line: Gas phase ROI. Blue dotted line: Lower boundary of GROI applied when evaluating $\omega_{rms,g}$

3.2.1. Liquid-phase ROI

The LROI is defined for $20° < \theta < 80°$, from the interface and 3 mm into the liquid phase. The velocity field within the liquid-phase ROI is used to classify waves as either breaking or non-breaking based on the criterion by Vollestad *et al.* (2019*b*). Vollestad *et al.* (2019*b*) monitored the rms vorticity (denoted ω_{rms}) within the same ROI. Waves with $\omega_{rms} < 60\ s^{-1}$ were assessed to be non-breaking, while waves with $\omega_{rms} > 100\ s^{-1}$ were classified as active breaking. As we in the present study apply a spatial resolution closely matching the resolution used in Vollestad *et al.* (2019*b*), and hence resolve a similar fraction of the shear generated by wave breaking, the same criterion is used also here. The rms vorticity in the LROI is denoted $\omega_{rms,l}$ in the remainder of this paper.

Only waves where the full LROI was present in the liquid-phase PIV FOV are analyzed further. In table 2 the number of waves where the LROI was present in the liquid PIV FOV (N_{LROI}) and the number of breaking and non-breaking waves are presented. Note that waves with $60\ s^{-1} < \omega_{rms} < 100\ s^{-1}$ are classified as "intermediate", and not counted as either breaking or non-breaking. Further discussions on this methodology for distinguishing actively breaking and non-breaking waves is presented in Vollestad *et al.* (2019*b*).

Table 2: Number of waves found to be breaking/non-breaking in this study. N_{LROI} are number of waves with the full LROI present in the liquid PIV FOV.

U_{sl}	U_{sg}	N_{LROI}	N breaking	N intermediate	N non-breaking
0.1	1.85	1670	452 (27 %)	198 (12 %)	1020 (61 %)
0.1	2.20	1426	571 (40 %)	136 (10 %)	719 (50 %)

3.2.2. Gas-phase ROI

The GROI includes the region from $\theta = 20°$ to $180°$. If the full region is not present in the gas-phase FOV, the region from $\theta = 20°$ to the right edge of the FOV is applied as the GROI. The GROI extends to a height y_{max} above the crest (y_{max} is the crest height relative to the mean water level), i.e. $2 * y_{max}$ above the mean water level.

The purpose of the GROI is to monitor the velocity field for signs of airflow separation. When the shear layer separates from the interface, there is a significant increase in the vorticity away from the interface, and a sheltered region of low air velocity between the interface and the separated shear layer. Two individual measures are included in order to monitor these properties in the GROI:

- The characteristic critical height, $\overline{y_c}$ is calculated by the area within the GROI with $u < C_p$, divided by the horizontal extent of the GROI. Hence, $\overline{y_c}$ represents the mean critical height (height where $u = C_p$) within the GROI. To remove the effect of wave amplitude we evaluate $\overline{y_c}/y_{max}$ as a normalized measure of the sheltering.
- To evaluate the increased vorticity, we extract the rms vorticity within the GROI, denoted $\omega_{rms,g}$. High values of $\omega_{rms,g}$ are assessed to be related to the detachment of the shear layer and increased turbulence away from the gas-liquid interface.

When evaluating $\overline{y_c}/y_{max}$ the GROI extends from the interface to its top border (region illustrated by dashed lines in figure 4). When monitoring $\omega_{rms,g}$, we omit the region closest to the interface (from the interface and 3 mm up), as we are interested in detecting signs of the high intensity shear layer separating from the interface, not shear which remains attached to the interface. Hence, the GROI for evaluating $\omega_{rms,g}$ is bounded from below by the dotted line in figure 4.

4. Results

4.1. Example instantaneous velocity profiles

Figure 5 presents instantaneous velocity fields for four waves (referred to as waves A - D). Figure 5 a) shows an example velocity field at $U_{sg} = 1.85$ m/s, while figure 5 b-d) are taken from the $U_{sg} = 2.20$ m/s experimental case. The figures present the velocity vectors in the air phase, along with vorticity contours in both the gas and liquid phase, overlaid the original gas-phase PIV image. Note that the liquid vorticity is multiplied by 10 for visibility.

For all waves the negative shear layer is seen to remain attached above the wave crest. At the leeward side of the crest the shear layer is seen to separate from the interface, depending on the gas flow rate and wave crest geometry. This effect is most pronounced for the two steepest waves (figure 5 c and d), but also for figure 5 b) a slight detachment of the shear layer, and a sheltered region of low-velocity air is observed on the leeward side of the crest. In figure 5 c) and d) regions of negative axial velocity are observed within the sheltered region.

The vorticity contours from the liquid-phase PIV is also included in figure 5 (superimposed on the gas-phase PIV image). In figure 5 b) and c) the vorticity is seen to be low, and evenly distributed along the wave profile, while in figure 5 a) and d) there are coherent regions of negative vorticity on the leeward side of the wave and below the crest. This indicates a turbulent spilling

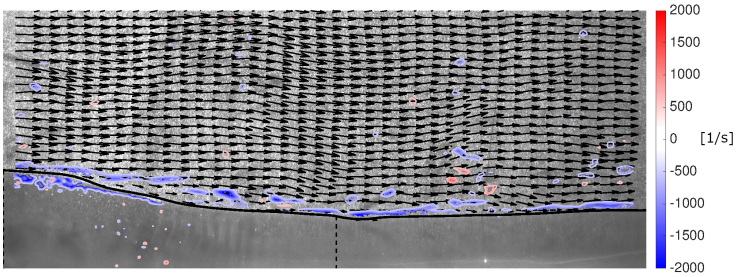

a) Wave A, $U_{sg} = 1.85$ m/s

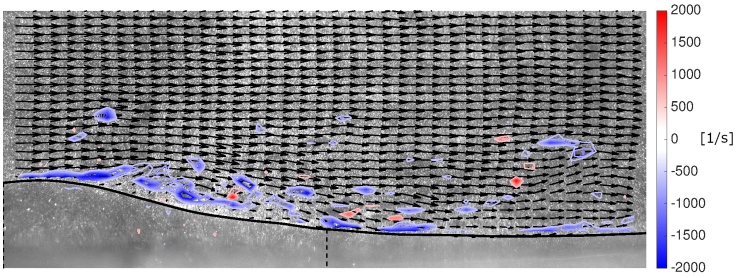

b) Wave B, $U_{sg} = 2.20$ m/s

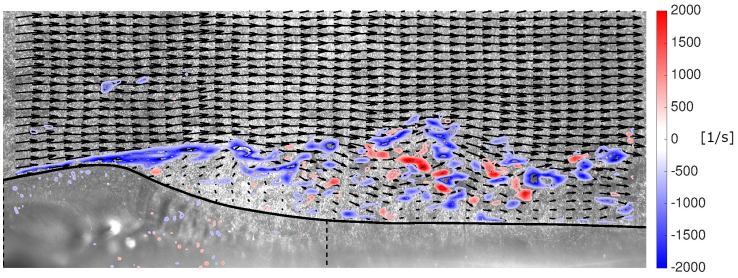

c) Wave C, $U_{sg} = 2.20$ m/s

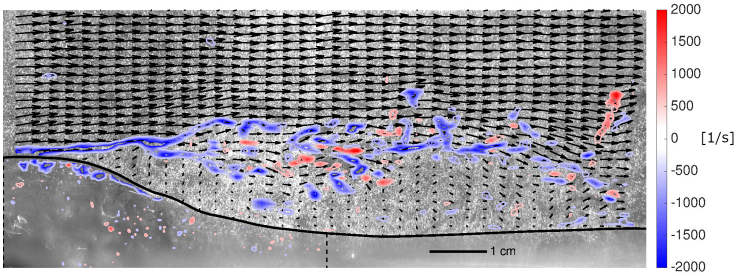

d) Wave D, $U_{sg} = 2.20$ m/s

Figure 5: Example velocity fields. Contours represent vorticity [s^{-1}]. NB: Liquid vorticity multiplied by 10 for visibility. Showing 1/4 vectors in the gas phase. Dashed vertical lines indicate borders of liquid phase PIV. Solid black line: Interface. Length scale included in figure d.

region caused by microscale wave breaking, and the waves are assessed to be in a state of active breaking according to the criterion presented in section 3.2. It can be noted that while the wave profile of figure 5 b) is fairly smooth, parasitic capillaries are observed on the leeward side of the wave in figure 5 c). These capillary waves were also observed by Vollestad *et al.* (2019*b*) for steep non-breaking waves in the same experimental conditions. When a wave transitions into an active state of breaking, fluid elements on the leeward side of the crest spill downwards and the capillary waves are displaced downstream of the spilling region (Vollestad *et al.*, 2019*b*).

The interfaces of the four waves shown in figure 5 are presented in figure 6. These were obtained from the LFV camera, and hence extend outside of the PIV FOV. Table 3 summarizes key parameters for the waves. Here we use the same notation as Reul *et al.* (2008): y_{max} and y_{min} are the maximum and minimum surface elevations, while λ is the wavelength. ϵ_{crest} is the crest front-face (leeward side) steepness ($|\Delta y/\Delta x|$ from the crest to the zero-down-crossing at $\theta = 90°$), while δ_{crest} is the crest windward side steepness ($|\Delta y/\Delta x|$ from θ = -90° to 0°). μ is the vertical asymmetry factor ($\mu = y_{max}/(y_{max} + |y_{min}|)$), while λ_v is the crest horizontal asymmetry factor ($\lambda_v = \epsilon_{crest}/\delta_{crest}$). The wave steepness ak is evaluated as $ak = \pi H/\lambda$, where H is the wave height ($H = y_{max} + |y_{min}|$).

From the data presented in table 3 it can be observed that there is only a moderate difference in the overall wave steepness ak comparing the three waves at U_{sg} = 2.20 m/s. The front face steepness ϵ_{crest} is however significantly higher for wave C and D.

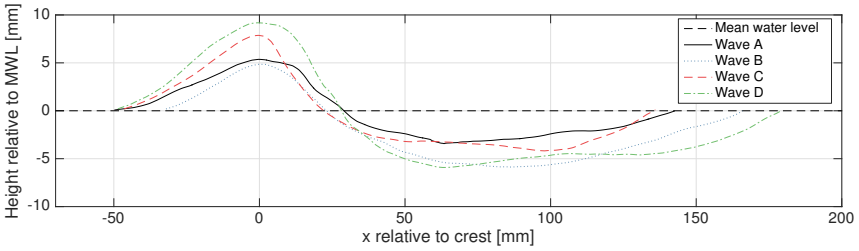

Figure 6: Interface elevation of the four waves displayed in figure 5. Crest positioned at x = 0.

Table 3: Overview of parameters describing the wave interface for wave A, B, C and D presented in figure 6.

Wave	y_{max} [mm]	y_{min} [mm]	λ [mm]	ϵ_{crest}	δ_{crest}	μ	λ_v	ak	Microbreaking
A	5.3	-3.4	193.0	0.19	0.11	0.61	1.73	0.15	Yes
B	4.9	-5.9	198.0	0.21	0.15	0.45	1.40	0.17	No
C	7.9	-4.2	182.5	0.35	0.17	0.65	2.06	0.21	No
D	9.2	-5.9	227.5	0.32	0.20	0.61	1.60	0.21	Yes

Table 4 presents the results for the parameters discussed in section 3.2. It can be seen that $\omega_{rms,l}$ varies by a factor four from the non-breaking to breaking cases, and that following the criterion presented in section 3.2, wave A and D are in a state of active breaking, while B and C are non-breaking.

The normalized critical height is seen to increase through wave A-D, from close to 0 for wave A to 0.8 for wave D. This is in accordance with the visual impression obtained from figure 5, as the sheltered region below the separated shear layer is seen to increase from wave A to D. We observe that $\omega_{rms,g}$ for wave A is significantly lower than the three other waves. This is to be expected, as wave A is from the U_{sg} = 1.85 m/s case, where the shear on the gas-liquid interface is lower, and as the shear layer is seen to remain attached along the wave profile. While $\overline{y_c}/y_{max}$ is maximum

for wave D, $\omega_{rms,g}$ is higher for wave C. Comparing figure 5 c) and d) the region of high intensity shear is seen to be somewhat thicker above wave C, indicating a higher degree of turbulent mixing.

Table 4: Overview of results from the ROI analysis for the four waves.

Wave	$\omega_{rms,l}$ $[s^{-1}]$	$\omega_{rms,g}$ $[s^{-1}]$	$\overline{y_c}$ [mm]	$\overline{y_c}/y_{max}$ [-]
A	168.6	268	0.1	0.02
B	43.9	560	1.0	0.21
C	44.6	739	4.1	0.52
D	176.4	689	7.4	0.80

The results in this section provide some indications of the importance of the crest geometry to the structure of the airflow. However, analyzing the effect of individual wave profile parameters and the effect of breaking requires a statistical approach.

4.2. Airflow statistics over breaking and non-breaking waves

In this section, statistics of $\overline{y_c}/y_{max}$ and $\omega_{rms,g}$ above breaking and non-breaking waves are presented. To isolate the effect of active wave breaking from the geometrical properties of the waves, it is necessary to keep at least one of the geometrical properties of the waves constant, as the wave geometry obviously has a significant impact on the airflow.

Reul *et al.* (2008) characterized the extent of the separated region by the air velocity, crest height and ϵ_{crest}. Here, we isolate the air velocity by comparing each of the experimental cases individually. As the vertical extent of the GROI used to evaluate $\omega_{rms,g}$, and $\overline{y_c}/y_{max}$ is scaled by the local crest height, ϵ_{crest} is chosen as the geometrical property of the wave to keep constant. Note that the average wave profile of breaking and non-breaking waves with the same ϵ_{crest} will vary, as wave breaking modifies the geometrical properties of the waves. Hence, completely isolating the effect of active wave breaking from the geometrical properties of individual waves is not possible. The variations on the overall wave form for breaking and non-breaking waves at constant ϵ_{crest}, and their effect on the results are discussed in section 5.

Breaking and non-breaking waves were evaluated individually, and binned in ϵ_{crest} intervals of 0.05. For each ϵ_{crest}-interval with more than five observations the mean value, standard deviation and 95 % confidence interval of the mean value (evaluated by the t-distribution) of $\overline{y_c}/y_{max}$ and $\omega_{rms,g}$ are evaluated. Results are presented in figure 7.

The results in figure 7 show that both $\omega_{rms,g}$ and $\overline{y_c}/y_{max}$ are strongly correlated with ϵ_{crest}. As expected, increased ϵ_{crest} is seen to result in increased turbulence and larger areas of sheltered airflow on the leeward side of the crest. It can be noted that all waves with $\epsilon_{crest} < 0.1$ are found to be non-breaking, while the steepest waves at $U_{sg} = 2.20$ m/s are found to be breaking. The shaded area represents the standard deviation around the mean value, and significant deviations around the mean value are observed both for breaking and non-breaking waves.

Results for the $U_{sg} = 2.20$ m/s case show that the breaking and non-breaking cases are more or less overlapping. The 95 % confidence intervals are everywhere overlapping, indicating that while there are some indications that $\omega_{rms,g}$ is higher for breaking waves within the steepness interval of $0.1 < \epsilon_{crest} < 0.25$, these results are not considered statistically significant.

At $U_{sg} = 1.85$ m/s there is a significant difference in the statistics above breaking and non-breaking waves. In the interval $0.2 < \epsilon_{crest} < 0.35$, the non-breaking waves are observed to result in significantly higher $\omega_{rms,g}$ and $\overline{y_c}/y_{max}$. This indicates that within this steepness interval, active wave breaking reduces the intensity of shear layer separation, as both the sheltered region and the turbulence generated by the separated shear layer are reduced. This is a somewhat surprising result as wave breaking is typically assessed to enhance the airflow separation above waves.

150

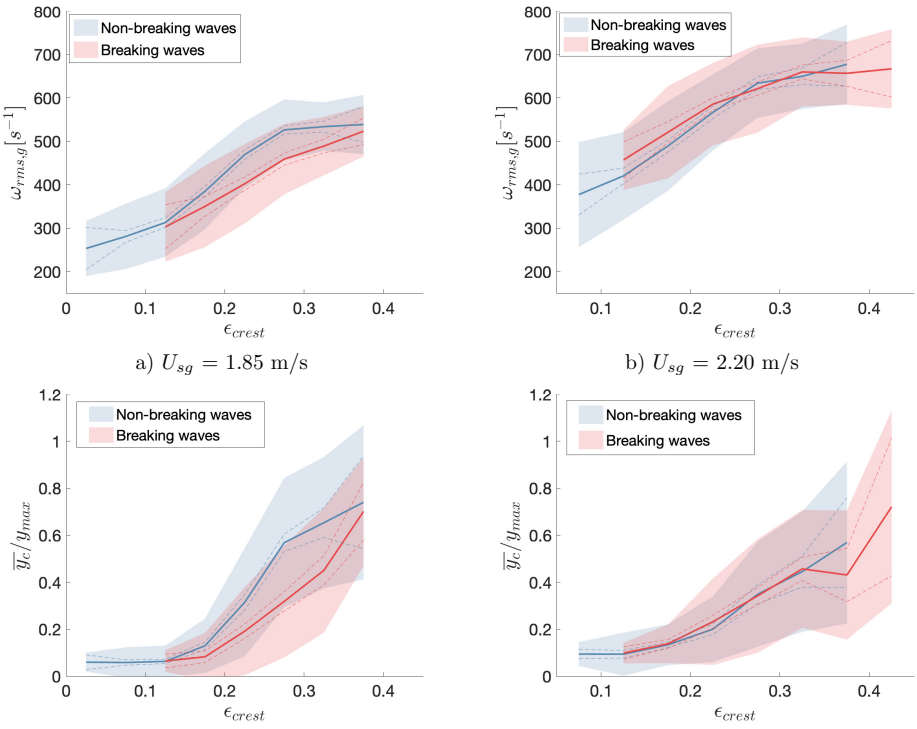

a) $U_{sg} = 1.85$ m/s b) $U_{sg} = 2.20$ m/s

c) $U_{sg} = 1.85$ m/s d) $U_{sg} = 2.20$ m/s

Figure 7: Statistics of $\omega_{rms,g}$ (a, b) and $\overline{y_c}/y_{max}$ (c,d) as a function of ϵ_{crest}. Thick full line: mean value, dashed line: 95 % confidence interval of mean value, shaded color: mean value ± standard deviation. $U_{sg} = 1.85$ m/s (a, c), and $U_{sg} = 2.20$ m/s (b, d).

While the results presented in this section are indicative of the effect of active wave breaking for the cases considered, further analysis of the experimental data is needed to understand how the variations in $\omega_{rms,g}$ and $\overline{y_c}/y_{max}$ observed for the $U_{sg} = 1.85$ m/s case manifest in the average flow field above breaking and non-breaking waves.

4.3. Analysis of effect of breaking for $0.225 < \epsilon_{crest} < 0.325$

In this section we perform an analysis of the velocity fields above breaking and non-breaking waves within the steepness interval $0.225 < \epsilon_{crest} < 0.325$, i.e. within the interval where we, in section 4.2, observed a reduced sheltering due to active wave breaking in the $U_{sg} = 1.85$ m/s case. The analysis is performed both for the $U_{sg} = 1.85$ and 2.20 m/s cases, to further describe the effect of active wave breaking observed in section 4.2. In section 4.3.1 a conditional phase-averaging of the velocity fields is performed, while in section 4.3.2 the spectra above breaking and non-breaking waves are analyzed.

While ϵ_{crest} is kept constant, other properties of the waves will vary slightly comparing breaking and non-breaking waves. The mean properties of the waves under investigation are presented in table 5. It is observed that while the average front-face steepness ϵ_{crest} is equal, the average crest height y_{max} and wave height H for non-breaking waves are somewhat higher than for the breaking waves. These variations will be discussed in section 5.

Table 5: Mean properties of the four averaging cases under investigation.

U_{sg}	State	$\overline{\epsilon_{crest}}$ [-]	$\overline{y_{max}}$ [mm]	$\overline{H}$ [mm]	$\overline{\lambda}$ [mm]	$\overline{ak}$ [-]
1.85	non-breaking	0.27	6.5	11.1	181	0.19
1.85	breaking	0.27	6.1	10.5	181	0.18
2.20	non-breaking	0.27	7.5	13.0	258	0.16
2.20	breaking	0.27	7.1	12.1	222	0.17

4.3.1. Phase-averaged results

A conditional phase-averaging of the gas and liquid phases is performed. The wave-following coordinate system is described in Appendix A. The coordinate system in the liquid phase is the same as the coordinate system employed by Vollestad *et al.* (2019*b*) to evaluate phase-averaged statistics of the liquid phase of microscale breaking waves, while the wave-following coordinate system in the gas phase is similar to the coordinate system used by Vollestad *et al.* (2019*a*), analyzing airflow over waves.

Figure 8 and 9 present the phase-averaged horizontal velocity ($\langle u \rangle$) for the $U_{sg} = 1.85$ and 2.20 m/s cases respectively. Breaking and non-breaking waves are averaged individually. Due to the limited FOV of the PIV cameras and the triggering applied (ref. section 2), the region where we can obtain reliable phase-averaged velocity profiles is limited to approximately -10° $< \theta <$ 180° for the gas phase and -10° $< \theta <$ 120° for the liquid phase. Here more than 100 data points are used in the evaluation of each phase-averaged quantity. In the range 20° $< \theta <$ 80° (LROI), more than 200 data points are obtained (number decreasing with distance from LROI). While the phase-averaged velocity profiles are not fully converged, the main flow features, such as the extent of the sheltered region, are assessed to be qualitatively converged, as performing the averaging with half of the available data resulted in only minor deviations from the results presented in figure 8 and 9, and no qualitative change in the results or conclusions related to the phase-averaged flow fields.

The results are overlaid on average interface (evaluated individually for breaking and non-breaking waves) detected by the LFV camera. Isocurves of constant velocity are included in the gas-phase velocity field. The critical height (where $\langle u \rangle = C_p$) is illustrated by a red dashed line.

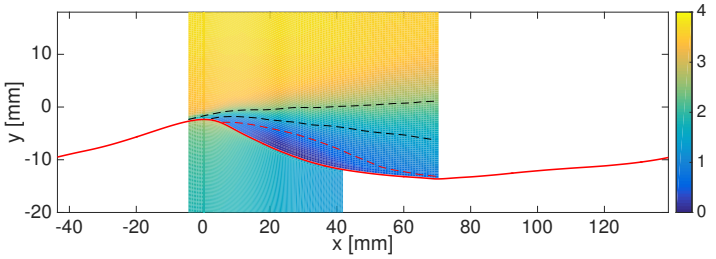

a) $U_{sg} = 1.85$ m/s, non-breaking

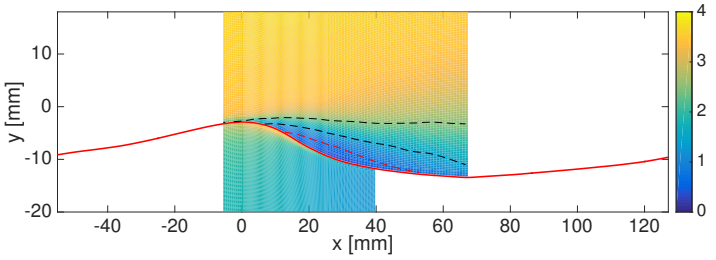

b) $U_{sg} = 1.85$ m/s, breaking

Figure 8: Phase-averaged results for the horizontal velocity $\langle u \rangle$, converted to (x, y)-coordinates by applying the mean interface elevation for each case. Gas-phase results plotted for -10° $< \theta <$ 180° . Liquid phase horizontal velocity multiplied by 5 for visibility. Colorbar in [m/s]. Full red line indicate mean interface elevation. Red dashed line represent the critical height, where $\langle u \rangle = C_p$. Black dashed lines represent isocurves at 1.5 and 2.5 m/s.

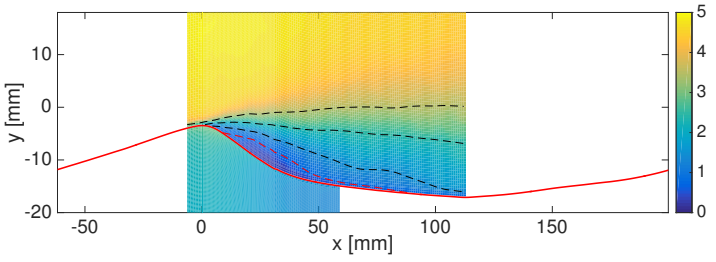

a) $U_{sg} = 2.20$ m/s, non-breaking

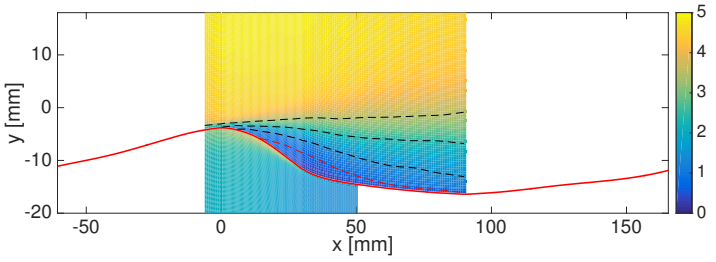

b) $U_{sg} = 2.20$ m/s, breaking

Figure 9: Phase-averaged results for the horizontal velocity $\langle u \rangle$, converted to (x, y)-coordinates by applying the mean interface elevation for each case. Gas-phase results plotted for -10° $< \theta <$ 180° . Liquid phase horizontal velocity multiplied by 5 for visibility. Colorbar in [m/s]. Full red line indicate mean interface elevation. Red dashed line represent the critical height, where $\langle u \rangle = C_p$. Black dashed lines represent isocurves at 1.5, 2.5 and 3.5 m/s.

The results in figure 8 show that the airflow is more sheltered in the lee of the non-breaking waves compared with the breaking waves. While the critical height is seen to detach from the interface close to the crest for the non-breaking case, the detachment occurs later over breaking waves, and the area where $\langle u \rangle < C_p$ is significantly reduced. It can be noted that while the peak horizontal velocity in the liquid phase of the non-breaking wave is centered below the crest, the peak is shifted towards the leeward side of the breaking waves. This is a clear indication of the spilling region observed below breaking waves. One interpretation of the results is that the spilling motion of the liquid on the leeward side of the wave reduces the shear on the gas flow, or even helps accelerate the gas close to the surface as the spilling is initiated, thus reducing the sheltered region on the leeward side of the wave.

The results presented in figure 9 show that the effect of breaking is less pronounced for the U_{sg} = 2.20 m/s case compared with the lower gas flow rate case. Again the critical height is seen to detach from the interface somewhat further downwind on the wave profile for the breaking case, but the sheltered area (here evaluated as the area limited by $\langle u \rangle < C_p$) is very similar, comparing the breaking and non-breaking cases.

In figure 10, streamlines of the phase-averaged velocity fields, observed in a frame of reference moving with the characteristic wave speed C_p, are presented for the U_{sg} = 1.85 m/s case. For both the breaking and non-breaking wave cases a clear "cat's eye" structure is observed on the leeward side of the crest. This illustrates that as the waves propagate in the streamwise direction, they experience a co-moving pocket of air in its front, displacing the streamlines in the outer flow relative to the wave profile. In table 6 the location of the cat's eye center (θ_c, ξ_c, where ξ_c is the height above the interface) and the area under the critical height y_c are summarized for all four averaging cases. The results show that while the sheltered area below non-breaking waves is slightly larger compared with the breaking waves at U_{sg} = 2.20 m/s, the effect is much more pronounced for the lower gas flow rate, and the area below the critical height is observed to be three times larger for the non-breaking waves at U_{sg} = 1.85 compared with breaking waves of similar ϵ_{crest}. These results are consistent with the results obtained in section 4.2, where it was found that $\overline{y_c}/y_{max}$ was significantly reduced as a result of breaking for the U_{sg} = 1.85 m/s case.

Gent & Taylor (1977) included an increased surface drift velocity to numerically analyze the effect of wave breaking on the extent of the cat's eye center. Analyzing a strongly forced wave ($c/u_* \approx 1.5$) they found that the effect of the increased surface drift was to reduce the elevation of the cat's eye center by approximately 30 %. While this is qualitatively in agreement with the results observed for the U_{sg} = 1.85 m/s case, the waves considered by Gent & Taylor (1977) had an even lower wave age than the cases considered in this work, hence the U_{sg} = 2.20 m/s case should be the more comparable. However, here we do not observe any significant change in the elevation of the cat's eye center.

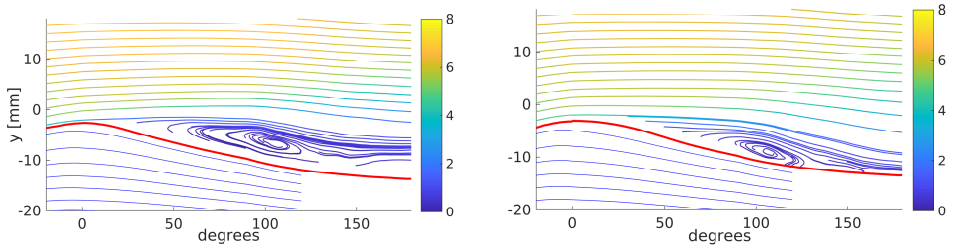

a) Non-breaking b) Breaking

Figure 10: Streamlines of phase-averaged velocity fields seen in a frame of reference moving with the characteristic wave speed C_p ($\langle \mathbf{u} \rangle - C_p$) for the U_{sg} = 1.85 m/s case. Gas-phase streamlines colored by $0.5(\langle u \rangle^2 + \langle v \rangle^2)$ $[m^2/s^2]$.

Table 6: Phase-averaged results. θ_c and ξ_c are the wave phase and height above the interface of the cat's eye center.

U_{sg} [m/s]	State	θ_c (degrees)	ξ_c [mm]	Area where $\langle u \rangle < C_p$ [mm^2]
1.85	Non-breaking	107	4.4	150
1.85	Breaking	108	2.1	49
2.20	Non-breaking	83	3.5	113
2.20	Breaking	96	3.5	103

The tangential velocity u_t along the interface was evaluated for each PIV velocity field, and phase-averaged similarly to the horizontal and vertical velocity components. Due to limitations in the spatial resolution and the accuracy of the interface detection, we are not able to evaluate the tangential shear in the viscous sublayer. Instead we evaluate the average tangential velocity over the two velocity vectors closest to the interface, in both the gas and liquid phases, and compute $\Delta u_t/\Delta y$ across the interface. While this does not provide the shear stresses directly, the results are indicative of the development of the shear stress along the wave profiles. Results are presented in figure 11. Note that the results are plotted for -10° $< \theta <$ 120°, as reliable phase-averaged velocities in both the gas and liquid phases are required.

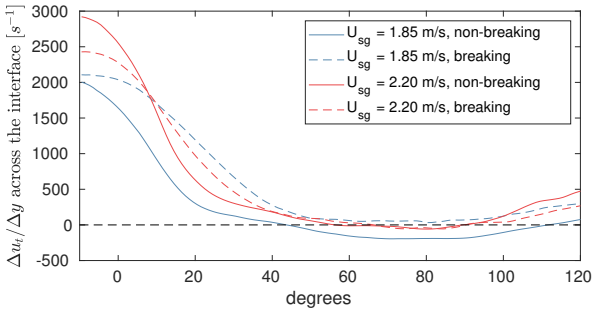

Figure 11: $\Delta u_t/\Delta y$ over the interface, plotted in the interval -10° $< \theta <$ 120°.

The results presented in figure 11 indicate that the shear stress at the interface varies considerably between the four averaging cases. The value of $\Delta u_t/\Delta y$ drops off faster for the non-breaking compared to the breaking waves, and for the non-breaking waves at $U_{sg} = 1.85$ m/s the results shows that there is a significant region of the wave profile (50° $< \theta <$ 110°) where the liquid on average travels faster than the overlying air, and will exert a force on the gas phase in the streamwise direction.

From figure 11 we also can observe that the velocity gradient across the interface at the crest is higher for non-breaking than breaking waves at $U_{sg} = 2.20$ m/s. Analyzing the phase-averaged velocity fields, it was found that the main reason for this discrepancy was a higher gas velocity close to the interface for the non-breaking waves, not an increased liquid velocity caused by wave breaking. The reason for this behavior is not completely understood, but it might be related to the somewhat higher crest height of the non-breaking waves compared with the breaking waves under investigation (ref. table 5), as the lower amplitude breaking waves may to a larger degree be sheltered by upwind waves. It is also possible that local interface variations on the windward side of the waves are the reason for these deviations, as the phase-averaged interface profiles indicate that the non-breaking waves are locally steeper close to the wave crest of the windward side compared with the breaking waves. This may result in a higher acceleration of the flow near the crest for non-breaking compared with breaking waves at $U_{sg} = 2.20$ m/s.

The momentum flux at the interface is governed both by shear stresses and form drag. As the experimental setup does not facilitate measurements of the pressure along the interface, we are not able to infer the overall change in the momentum flux as a result of active breaking. As we consider young waves the critical height is located within the inner region, where the turbulent eddies are in local equilibrium (Belcher & Hunt, 1993, 1998). In this region the turbulent shear stresses displace the streamlines asymmetrically, and the phase shift of the pressure field cannot be inferred directly from the location of the cat's eye (Kihara *et al.*, 2007).

From the air-sea literature it is well established that form drag contributes to the majority of the wind stress at the wave ages considered in this work (Banner & Peirson, 1998; Sullivan *et al.*, 2018*b*,*a*). While the pipe walls will influence the pressure distribution relative to the pressure field above waves in an open system, it is considered likely that this will also be the case for the current experimental investigation. Hence, the total momentum flux may well be higher for non-breaking compared with breaking waves at $U_{sl} = 1.85$ m/s, despite the reduced shear stress.

4.3.2. Spectra above breaking and non-breaking waves

The results in section 4.2 showed that $\omega_{rms,g}$ was higher over non-breaking than breaking waves at $U_{sg} = 1.85$ m/s. This is assessed to be related to increased turbulence intensity on the leeward side of the wave. To further investigate the turbulence above breaking and non-breaking waves, the wavenumber spectra of the horizontal velocity fluctuations are evaluated above breaking and non-breaking waves individually. Again we limit the cases under investigation to a steepness interval of $0.225 < \epsilon_{crest} < 0.325$. The horizontal velocity 1 mm above the wave crest is extracted for each wave. The periodogram is evaluated for each velocity profile and the mean of the periodogram is used to estimate the horizontal velocity spectra. Results are presented in figure 12.

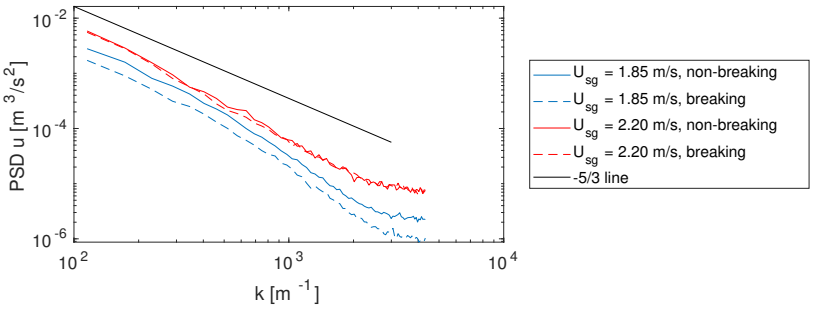

Figure 12: Power spectral density of the horizontal velocity component (PSD u), evaluated 1 mm above the crest of each wave observed with $0.225 < \epsilon_{crest} < 0.325$.

From the spectra it can be observed that at $U_{sg} = 1.85$ m/s, the airflow is more fluctuating over non-breaking than breaking waves. At $U_{sg} = 2.10$ m/s the spectra over breaking and non-breaking waves are seen to be more or less equal. This was also observed when the spectra were evaluated at a fixed height (y = 5 mm).

These results are consistent with the results obtained in section 4.2, and indicate that active wave breaking has the effect of reducing the turbulence levels above the wave trough for moderate wind speeds. We relate this to a reduction in the frequency and/or extent of airflow separation on the leeward side of the crest, which could be a result of a change in the wave geometry as the waves transition from non-breaking to breaking, and/or of the spilling motion induced by wave breaking (this will be discussed in section 5). At the higher airflow rate considered ($U_{sg} = 2.20$ m/s), the effect is not observed, and again we conclude that active wave breaking does not significantly influence

the airflow above waves at $U_{sg} = 2.20$ m/s.

5. Discussion

In this study efforts have been made to isolate the effect of wave breaking, by comparing breaking and non-breaking waves with similar geometrical properties (with focus on ϵ_{crest}). However, completely isolating the effect of the turbulent spilling region of the liquid is not possible, as wave breaking modifies the interface of the waves. In figure 13 the phase-averaged interface for the four averaging cases analyzed in section 4.3 is presented. Results are presented for θ in the range of -20° to 180°.

Figure 13 shows that while the waves are evaluated within a narrow ϵ_{crest}-band, there is a distinct difference in the average interface shape of breaking and non-breaking waves. The non-breaking waves are observed to be somewhat taller, with a higher local steepness close to the wave crest compared with the breaking waves at similar ϵ_{crest}. The more rounded profile of the breaking waves may help explain why we observe a reduced sheltered region on the leeward side of the breaking waves at $U_{sg} = 1.85$ m/s, as the more gentle slope of the interface may facilitate flow expansion without separation close to the crest. A more direct explanation for the observations made is that the spilling motion of the liquid (observed in the phase-averaged velocity profiles presented in figure 8 and 9) reduces the interfacial shear on the leeward side of the wave, preventing flow separation. Isolating these effects (the spilling motion induced by breaking and the change in wave shape also due to breaking) is not possible when considering naturally occurring wind-generated waves. Numerical analysis or controlled experiments with artificially generated waves are necessary to evaluate which of these effects is dominant in reducing the sheltered region behind breaking waves at the lower gas flow rate.

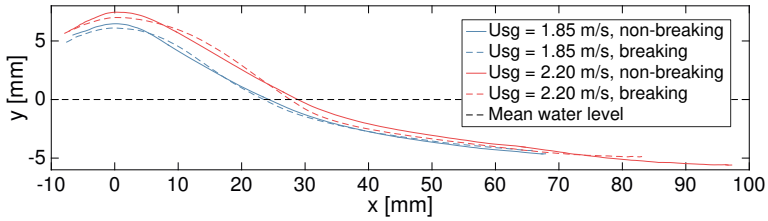

Figure 13: Mean interface of averaging cases, interval from θ = -20° to 180° converted to world coordinates.

It is important to note that all the results in the present work are obtained from, and only valid for, the centerplane of a two-phase pipe flow configuration. The closed pipe geometry induces lateral velocity variations which are not found in open wind-wave tanks, and the wave-coherent pressure variations at the upper pipe wall will be reflected down, modifying the wave-coherent pressure field relative to airflow over waves in an open channel. However, in the trough-to-crest region of the pipe centerline (where we focus our attention) the airflow is primarily influenced by the gas-liquid interface (as the distance to the pipe walls is much larger than the distance to the interface), and the lateral variations are much smaller than in the cross-sections near the pipe walls. As the relationship between active wave breaking and airflow separation has not previously been investigated in a pipe flow configuration, and as the wave breaking process and airflow above waves in pipes have previously been found to have many features similar to air-sea interactions (Vollestad *et al.*, 2019*a*,*b*), it is considered expedient to compare (in a qualitative manner) the results obtained in this work with studies conducted in an open channel.

Numerical results by Sullivan *et al.* (2018*b*), simulating wind over waves representing incipient and active breaking, indicate that the overall wave steepness, not the increased drift velocity or

the local steepness variations between incipient and actively breaking waves, is the main parameter controlling the form drag. The simulations by Sullivan *et al.* (2018*b*) are for a wave age which is even lower than the $U_{sg} = 2.20$ m/s case, hence the effect of active wave breaking observed for the $U_{sg} = 1.85$ m/s case is not necessarily in contradiction with the numerical results by Sullivan *et al.* (2018*b*). The results in this work indicate that the effect of wave breaking is relatively more important to the overlying airflow at lower gas flow rates.

Reul *et al.* (2008) attributed the change in the separated flow region to the front face steepness (ϵ_{crest}). It is interesting to note their figure 10, depicting two waves at $c/u_* \approx 2.6$ (closely matching the U_{sg} 1.85 m/s case). While the airflow clearly separates over one wave at incipient breaking ($\epsilon_{crest} = 0.52$), it remains attached over the other wave profile ($\epsilon_{crest} = 0.28$), which appears to be in a state of active wave breaking. While Reul *et al.* (2008) observe a clear correlation between both the horizontal and vertical extent of the separation bubble with ϵ_{crest} (which one can expect also from the results presented in section 4.2 in the present work), there is considerable scatter in the results, and the results for the $U_{sg} = 1.85$ m/s case in the present work could indicate that the state of breaking, as well as the crest front face steepness, influences the extent of the separated zone. This was however not investigated by Reul *et al.* (2008).

Investigating the effect of wave breaking on even lower gas flow rates would be of interest. However, as the first signs of microscale wave breaking is observed at $U_{sg} = 1.80$ m/s (Vollestad *et al.*, 2019*b*), this would require a different experimental setup.

6. Concluding remarks

In this work we have performed simultaneous two-phase PIV with the aim of detecting the influence of microbreaking on the airflow above waves in stratified gas-liquid pipe flow. Using the criterion for separating actively breaking and non-breaking waves by Vollestad *et al.* (2019*b*), we analyze the effect of active wave breaking from microscale breaking waves on the airflow structure.

Results show that at the lowest gas flow rate considered ($U_{sg} = 1.85$ m/s), wave breaking has a stabilizing effect on the airflow above the waves, reducing the extent of the separated flow region and the turbulence above the waves. Hence, the effect of airflow separation is reduced over actively breaking waves at this moderate flow rate. At $U_{sg} = 2.20$ m/s the effect of wave breaking is observed to be more moderate. The results indicate that the region in the flow map where active wave breaking significantly influences the air flow field in two-phase pipe flow is relatively small.

While a direct application of the results is restricted to a two-phase pipe flow configuration, the results can also be related to phenomena occurring in the ocean. The impact of wave breaking on the airflow is still a topic under investigation, and the present work adds new insight into the coupling between small scale wave breaking events and airflow separation at high wind forcing.

Acknowledgement

The authors wish to acknowledge the strategic research initiative EarthFlows at the Faculty of Mathematics and Natural Sciences at the University of Oslo. Laboratory Head Engineer O. Gundersen is gratefully acknowledged for the technical assistance he provided for the experimental work.

Appendix

Appendix A: Phase-averaging procedure

The wave-following coordinate system applied is illustrated in figure 14. The wave phase θ (evaluated by the zero-crossing procedure described in section 3.2) is used together with a wave-following ζ-coordinate to obtain a wave-following coordinate system. The ζ-coordinate is implemented slightly differently in the two phases. In the liquid phase, ζ_l is evenly distributed over 100

points from the lower part of the PIV velocity field (at y = -28 mm) to the interface. This is similar to the wave-following coordinate system applied by Vollestad *et al.* (2019*b*). In the gas phase the wave amplitude is a critical parameter, impacting on the extent of the sheltered region. For this reason the ζ_g-coordinate is normalized by the wave crest height. ζ_g is evenly distributed over 100 points, from the interface to a height $5 * y_{max}$ above the interface. This ensures that points in the trough-to-crest region are sampled at the same relative height above the interface, ensuring a more physical phase-averaged value in this region. This coordinate system is similar to the coordinate system applied by Vollestad *et al.* (2019*a*), evaluating the phase-averaged properties of airflow above waves.

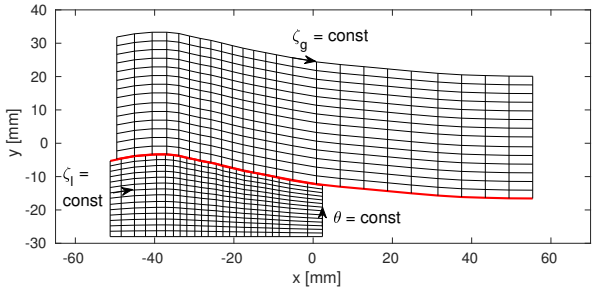

Figure 14: Example coordinate system. Only a small fraction of the gridlines included. Red line: interface.

The horizontal and vertical velocity components of breaking and non-breaking waves are sampled individually, and averaged at constant (θ, ζ)-coordinates to obtain the phase-averaged velocities $\langle u \rangle$ and $\langle v \rangle$. When performing the averaging, the average interface elevation (based on the LFV camera) is also evaluated. When presenting the phase-averaged results the (θ, ζ)-coordinates are transformed into (θ, y)- or (x, y)-coordinates (depending on the application) based on the mean interface.

References

Ayati, A. A., Kolaas, J., Jensen, A. & Johnson, G. W. 2014 A PIV investigation of stratified gas-liquid flow in a horizontal pipe. *International Journal of Multiphase Flow* **61**, 129–143.

Ayati, A. A., Kolaas, J., Jensen, A. & Johnson, G. W. 2015 Combined simultaneous two-phase PIV and interface elevation measurements in stratified gas/liquid pipe flow. *International Journal of Multiphase Flow* **74**, 45–58.

Ayati, A. A., Kolaas, J., Jensen, A. & Johnson, G. W. 2016 The effect of interfacial waves on the turbulence structure of stratified air/water pipe flow. *International Journal of Multiphase Flow* **78**, 104–116.

Babanin, A. 2011 *Breaking and dissipation of ocean surface waves*. Cambridge University Press.

Banner, M. L. 1990 The influence of wave breaking on the surface pressure distribution in wind-wave interactions. *Journal of Fluid Mechanics* **211**, 463–495.

Banner, M. L. & Melville, W. K. 1976 On the separation of air flow over water waves. *Journal of Fluid Mechanics* **77** (04), 825–842.

Banner, M. L. & Peirson, W. L. 1998 Tangential stress beneath wind-driven air–water interfaces. *Journal of Fluid Mechanics* **364**, 115–145.

Belcher, S. E. & Hunt, J. C. R. 1993 Turbulent shear flow over slowly moving waves. *Journal of Fluid Mechanics* **251**, 109148.

Belcher, S. E. & Hunt, J. C. R. 1998 Turbulent flow over hills and waves. *Annual Review of Fluid Mechanics* **30** (1), 507–538.

Birvalski, M. 2015 *Experiments in stratified gas-liquid pipe flow*. TU Delft, Delft University of Technology.

Birvalski, M, Tummers, M. J., Delfos, R. & Henkes, R. A. W. M. 2015 Laminar-turbulent transition and wave-turbulence interaction in stratified horizontal two-phase pipe flow. *Journal of Fluid Mechanics* **780**, 439–456.

Birvalski, M., Tummers, M. J. & Henkes, R. A. W. M. 2016 Measurements of gravity and gravity-capillary waves in horizontal gas-liquid pipe flow using PIV in both phases. *International Journal of Multiphase Flow* **87**, 102 – 113.

Buckley, M. P. & Veron, F. 2016 Structure of the airflow above surface waves. *Journal of Physical Oceanography* **46** (5), 1377–1397.

Gent, P. R. & Taylor, P. A. 1977 A note on separation over short wind waves. *Boundary-Layer Meteorology* **11** (1), 65–87.

Jessup, A. T., Zappa, C. J. & Yeh, H. 1997 Defining and quantifying microscale wave breaking with infrared imagery. *Journal of Geophysical Research: Oceans* **102** (C10), 23145–23153.

Kawai, S. 1981 Visualization of airflow separation over wind-wave crests under moderate wind. *Boundary-Layer Meteorology* **21** (1), 93–104.

Kawai, S. 1982 Structure of air flow separation over wind wave crests. *Boundary-Layer Meteorology* **23** (4), 503–521.

Kihara, N., Hanazaki, H., Mizuya, T. & Ueda, H. 2007 Relationship between airflow at the critical height and momentum transfer to the traveling waves. *Physics of Fluids* **19** (1), 015102.

Kudryavtsev, V. N. & Makin, V. K. 2001 The impact of air-flow separation on the drag of the sea surface. *Boundary-layer meteorology* **98** (1), 155–171.

Maat, N. & Makin, V. K. 1992 Numerical simulation of air flow over breaking waves. *Boundary-Layer Meteorology* **60** (1-2), 77–93.

Phillips, O. M. 1958 The equilibrium range in the spectrum of wind-generated waves. *Journal of Fluid Mechanics* **4** (4), 426–434.

Phillips, O. M. 1985 Spectral and statistical properties of the equilibrium range in wind-generated gravity waves. *Journal of Fluid Mechanics* **156**, 505–531.

Raffel, M., Willert, C. E., Scarano, F., Kähler, C. J., Wereley, S. T. & Kompenhans, J. 2018 *Particle image velocimetry: a practical guide*. Springer.

Reul, N., Branger, H. & Giovanangeli, J.-P. 2008 Air flow structure over short-gravity breaking water waves. *Boundary-layer meteorology* **126** (3), 477–505.

Siddiqui, M. H. K. & Loewen, M. R. 2006 Detecting microscale breaking waves. *Measurement Science and Technology* **17** (4), 771–780.

Siddiqui, M. H. K. & Loewen, M. R. 2007 Characteristics of the wind drift layer and microscale breaking waves. *Journal of Fluid Mechanics* **573**, 417–456.

Siddiqui, M. H. K. & Loewen, M. R. 2010 Phase-averaged flow properties beneath microscale breaking waves. *Boundary-Layer Meteorology* **134** (3), 499–523.

Smith, L., Kolaas, J., Jensen, A. & Sveen, K. 2018 Investigation of surface structures in two phase wavy pipe flow by utilizing x-ray tomography. *International Journal of Multiphase Flow* **107**, 246–255.

Strand, O. 1993 An experimental investigation of stratified two-phase flow in horizontal pipes. *Dr. Scient. Thesis, University of Oslo. Oslo, Norway* .

Sullivan, P. P., Banner, M. L., Morison, R. P. & Peirson, W. L. 2018*a* Impacts of wave age on turbulent flow and drag of steep waves. *Procedia IUTAM* **26**, 174–183.

Sullivan, P. P., Banner, M. L., Morison, R. P. & Peirson, W. L. 2018*b* Turbulent flow over steep steady and unsteady waves under strong wind forcing. *Journal of Physical Oceanography* **48** (1), 3–27.

Tian, Z., Perlin, M. & Choi, W. 2010 Observation of the occurrence of air flow separation

over water waves. In *ASME 2010 29th International Conference on Ocean, Offshore and Arctic Engineering*, pp. 333–341. American Society of Mechanical Engineers.

Tulin, M. P. & Landrini, M. 2001 Breaking waves in the ocean and around ships. In *23rd Symposium on Naval Hydrodynamics*, pp. 713–745. The National Academies Press.

Tzotzi, C. & Andritsos, N. 2013 Interfacial shear stress in wavy stratified gas-liquid flow in horizontal pipes. *International Journal of Multiphase Flow* **54**, 43 – 54.

Ullmann, A. & Brauner, N. 2006 Closure relations for two-fluid models for two-phase stratified smooth and stratified wavy flows. *International journal of multiphase flow* **32** (1), 82–105.

Veron, F., Saxena, G. & Misra, S. K. 2007 Measurements of the viscous tangential stress in the airflow above wind waves. *Geophysical Research Letters* **34** (19).

Vollestad, P., Ayati, A. A., Angheluta, L., LaCasce, J. H. & Jensen, A. 2019*a* Experimental investigation of airflow above waves in a horizontal pipe. *International Journal of Multiphase Flow* **110**, 37–49.

Vollestad, P., Ayati, A. A. & Jensen, A. 2019*b* Microscale wave breaking in stratified air-water pipe flow. *Physics of Fluids* **31** (3), 032101.

Weissman, M. A. 1986 Observations and measurements of air flow over water waves. In *Wave dynamics and radio probing of the ocean surface*, pp. 335–352. Springer.

Yang, Z., Deng, B.-Q. & Shen, L. 2018 Direct numerical simulation of wind turbulence over breaking waves. *Journal of Fluid Mechanics* **850**, 120–155.

Paper VI

Modification of the airflow structure due to wave breaking on a submerged topography

Petter Vollestad, Atle Jensen

Under review

VI

Paper VII

A note on PIV measurements of dilute air-sand pipe flow

Petter Vollestad, Atle Jensen

In preparation

Appendices

Appendix A

Velocity profiles from stereoscopic PIV measurements

In paper I, the bulk of the results from the stereoscopic PIV measurements are presented in the form of contour and vector plots. While this is suitable for a qualitative description of the flow phenomena under investigation, more detailed numerical results are valuable if the results are to be used for validation of CFD codes.

In figure A.2, the mean axial velocity U and in-plane velocity components V and W are shown (normalized by U_{sg}) along lines of constant y-coordinates. The profiles are evaluated along lines of y = -20, -10, 0, 10, 20, 30 and 40 mm in the pipe, bounded by $r \leq 45$ mm (indicated in figure A.1). Figure A.3 presents the turbulent kinetic energy (normalized by u_{wf}^2, the estimated wall friction factor) evaluated along the same lines.

The results in figure A.2 and A.3 presents the same data as presented in figure 11 and 13 a) and b) found in paper I, but should be more suitable for quantitative comparison with model results.

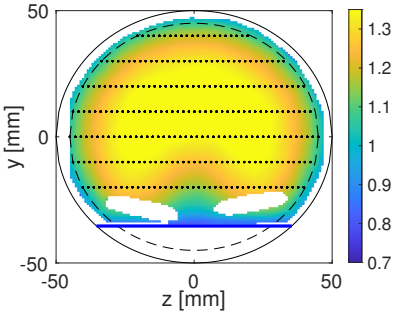

Figure A.1: Contour plot of U/U_{sg} for the U_{sg} = 7.20 m/s, flat interface case. Dotted lines illustrate lines where the mean velocity components and turbulent kinetic energy is extracted, and presented in figure A.2 and A.3. Dashed line indicate r = 45 mm, full line indicate pipe walls (r=50 mm).

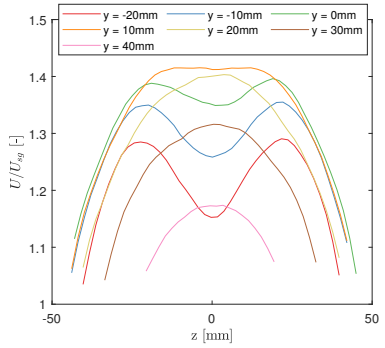

a) U/U_{sg}, $U_{sg} = 7.20$ m/s case

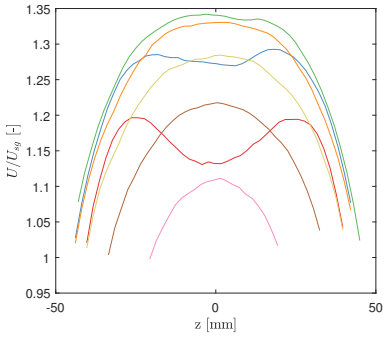

b) U/U_{sg}, $U_{sg} = 11.50$ m/s case

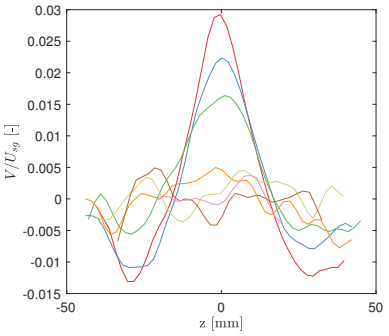

c) V/U_{sg}, $U_{sg} = 7.20$ m/s case

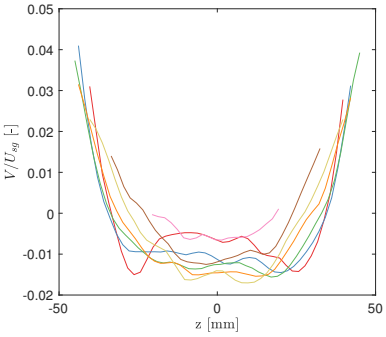

d) V/U_{sg}, $U_{sg} = 11.50$ m/s case

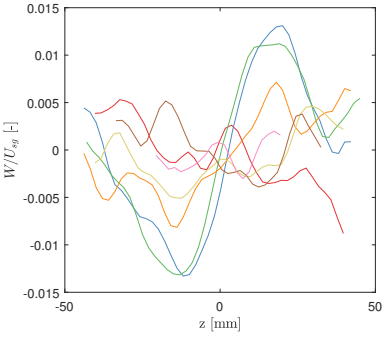

e) W/U_{sg}, $U_{sg} = 7.20$ m/s case

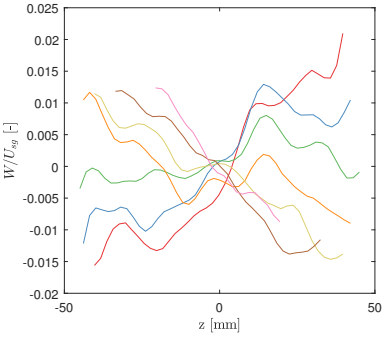

f) W/U_{sg}, $U_{sg} = 11.50$ m/s case

Figure A.2: Mean flow results for the two experimental cases under investigation with the stereoscopic PIV setup in paper I, evaluated along lines of constant y-coordinate.

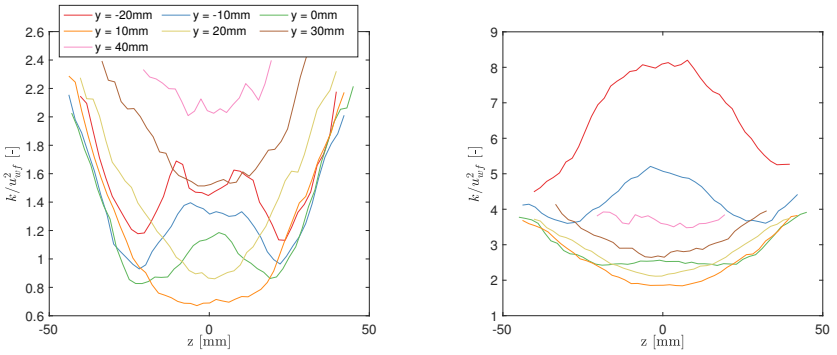

a) k/u_{wf}^2, $U_{sg} = 7.20$ m/s case b) k/u_{wf}^2, $U_{sg} = 11.50$ m/s case

Figure A.3: k/u_{wf}^2 for the two experimental cases under investigation with the stereoscopic PIV setup in paper I, evaluated along lines of constant y-coordinate.